# Behavioral Model and Predistortion Algorithm to Mitigate Interpulse Instabilities Induced by Gallium Nitride Power Amplifiers in Multifunction Radars

Carlos G. Tua-Martinez

Dissertation submitted to the faculty of the Virginia Polytechnic Institute and State University in partial fulfillment of the requirements for the degree of

Doctor of Philosophy
in
Electrical Engineering

Amir I. Zaghloul
Timothy Pratt
Donald E. Mullins
Richard M. Buehrer
Luiz A. DaSilva
Terry L. Foreman

November 16, 2016
Blacksburg, VA

Keywords: behavioral modeling, GaN MMIC, power amplifiers, multifunction radar system, moving target indicator, predistortion, electrothermal memory effects

# Behavioral Model and Predistortion Algorithm to Mitigate Interpulse Instabilities Induced by Gallium Nitride Power Amplifiers in Multifunction Radars

Carlos G. Tua-Martinez

## ABSTRACT

The incorporation of Gallium Nitride (GaN) Power Amplifiers (PAs) into future high power aperture radar systems is certain; however, the introduction of this technology into multifunction radar systems will present new challenges to radar engineers. This dissertation describes a broad investigation into amplitude and phase transients produced by GaN PAs when they are excited with multifunction radar waveforms. These transients are the result of self-heating electrothermal memory effects and are manifested as interpulse instabilities that can negatively impact the coherent processing of multiple pulses. A behavioral model based on a Foster network topology has been developed to replicate the measured amplitude and phase transients accurately. This model has been used to develop a digital predistortion technique that successfully mitigates the impact of the transients. The Moving Target Indicator (MTI) Improvement Factor and the Root Mean Square (RMS) Pulse-to-Pulse Stability are used as performance metrics to assess the impact of the transients on radar system performance and to test the effectiveness of a novel digital predistortion concept.

# Behavioral Model and Predistortion Algorithm to Mitigate Interpulse Instabilities Induced by Gallium Nitride Power Amplifiers in Multifunction Radars

Carlos G. Tua-Martinez

## GENERAL AUDIENCE ABSTRACT

The incorporation of Gallium Nitride (GaN) Power Amplifiers (PAs) into future radar systems is certain, and will present new challenges to radar engineers. This dissertation describes a broad investigation into signal transients produced by GaN PAs when they are excited with a wide variety of RF pulsed waveforms. These waveforms are representative of those used by a radar system to conduct multiple functions or missions. The transients are primarily the result of changes in the GaN PA gain due to self-heating, and are manifested as differences in consecutive pulses. These pulse-to-pulse differences negatively affect the ability of a radar system to extract information from a received echo. A behavioral model based on a Foster network topology has been developed to replicate the measured signal transients accurately. This model has been used to develop a digital predistortion technique that successfully counteracts the transients mitigating the impact of the transients. The Moving Target Indicator (MTI) Improvement Factor and the Root Mean Square (RMS) Pulse-to-Pulse Stability are used as performance metrics to quantify the effect of the transients on radar system performance and to test the effectiveness of a novel digital predistortion concept.

# Dedication

To my wife Madeline, for her encouragement and support from the beginning. She was there when I decided to enroll in the Master's Program of the Bradley Department of Electrical and Computer Engineering, and years later for the Ph.D. Program. She has been there for me, motivating me and allowing me the time and space to work towards finishing my Ph.D. I am blessed to have her in my life. I owe my success to her. I also dedicate this work to my parents Gustavo and Haydee, my sister Vanessa and my infant sons Carlos and Gustavo. Their pride in my accomplishments is my driving force.

# Acknowledgement

I would like to thanks my advisory committee members for their understanding and support. My thanks to Dr. Mullins, for standing in at short notice. Thanks to Dr. Pratt and Dr. Zaghloul for understanding that, I had a responsibility to my employer at the same time that I was working on my PhD, and for giving me free range to choose a topic I really enjoyed. Sincere gratitude to Dr. Pratt for understanding the importance of my research early into the process, and for his numerous technical and editorial reviews of my Ph.D. work.

To the people of NSWC Dahlgren Division for their support. Special thanks to Dr. Foreman for his advice and reassurance. Thanks are also due to Mr. Stapleton for his support, backing and being so readily accessible, and for providing laboratory access to equipment and materials that made this research possible. Thanks to my friends and coworkers Mr. Wallace and Mr. Diaz-Santos, you provided praise and motivation as well as helped me hone in my ideas and improve my explanations.

# Table of Contents

# Table of Figures

# List of Tables

# Chapter 1. Introduction

Gallium Nitride (GaN) technology in being adopted in the design and fabrication of Power Amplifiers (PA) for future radar systems. This combined with the ability of these radars to dynamically schedule a wide variety of waveforms introduces a transient effect in the transmitted waveforms. The transmitted waveforms are distorted, defeating the premise of identical pulse-to-pulse characteristic in a radar's Coherent Processing Interval (CPI), a.k.a. dwell time. A GaN PA produces a transient response when excited with multifunction radar waveforms. This transient has duration in the order of a few milliseconds and can severely limit the effectiveness of Moving Target Indicator (MTI) radars to suppress clutter. Appendix A provides a short explanation of Moving Target Indicator signal processing. Most modern surveillance radars use MTI processing to separate moving targets (such as aircraft) from stationary targets, known in radar parlance as clutter. MTI processing of radar returns allows the detection of moving targets in an environment in which stationary target returns can be thousands of times stronger than the wanted return. This is of particular importance in a military surveillance radar where enemy aircraft try to fly as low as possible in the hope that ground clutter masks their much smaller return.

## 1.1 Motivation

The motivation to pursue this line of research stems from testing, performed by the investigator, on S-Band Gallium Nitride (GaN) Power Amplifiers (PA) in support of the Digital Array Radar program [1]. One of the tests performed involved feeding the amplifier with different waveform pulse trains. A phase insertion push was observed whenever switching waveforms had significantly different pulse widths.

Figure 1-1 shows this phenomenon. The waveforms used in this example were radar pulses at 10% duty cycle; their only difference was the pulse width. The test alternated pulse trains composed of 10 microsecond pulse width to 100 microsecond pulse width and back. Figure 1-1 (a) shows a phase shift transient of approximately 2 degrees whenever the pulse width was switched from 10 to 100 microseconds. The phase shift transient lasted several milliseconds. Figure 1-1 (b) shows the phase shift transient that occurs when switching from 100 to 10 microseconds pulse width. The time constants in Figure 1-1 (a) and (b) look very similar, however, their phase shift takes an opposite direction.

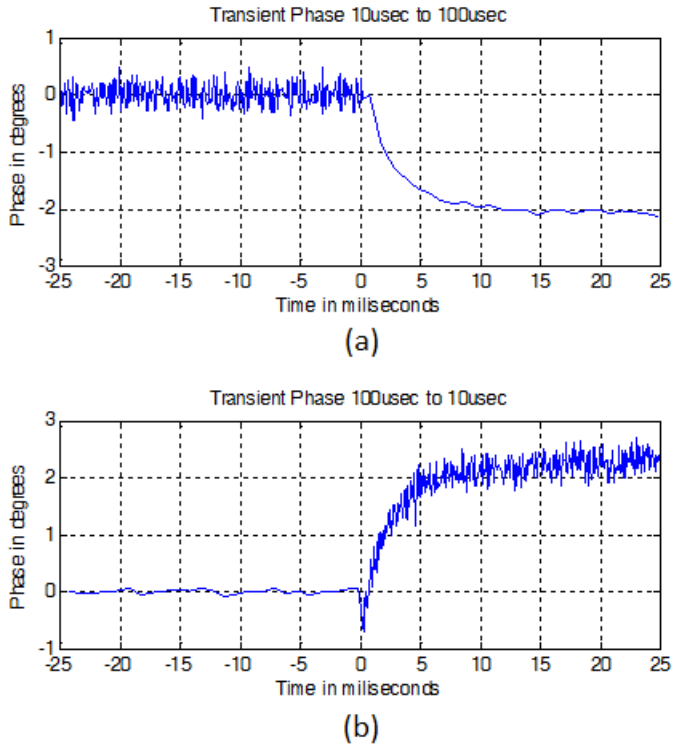


Figure 1-1: Phase shift transient following switching of widely different pulse width waveforms; a) 10 microsecond to 100 microsecond pulse-width transition, b) 100 microsecond to 10 microsecond pulse-width transition.

The signal noise visible in Figure 1-1 is due to the low Signal to Noise Ratio (SNR) in the collected data set. As part of this research a novel amplifier characterization technique was

developed. The technique uses Digital Signal Processing (DSP) to improve amplitude and phase measurements accuracy and precision.

Linear phase shift is expected on moving platforms, and is routinely corrected. The exponential shape of the amplitude and phase transient introduced by the PA is not expected. Not being aware of this transient can lead to unpredictable results, since the radar performance could degrade whenever multifunction waveforms are introduced. Amplitude and phase stability is of paramount importance to MTI and Doppler radar performance. Clutter rejection is greatly affected by minute pulse-to-pulse changes in amplitude and phase.

## 1.2 Background

Future Digital Array Radar (DAR) systems will be multifunction in design, supporting a diverse set of missions or functions, each requiring a specialized set of waveforms. Each waveform is specifically designed with its own duty cycle, pulse width, and requirements for optimal performance. The multifunction capabilities can cover a wide selection of functions [2] such as air traffic control, volume surveillance, and dedicated tracking among others; all of these functions can potentially be executed simultaneously. In general, long pulses are used for distant surveillance, short pulses for close in tracking or maritime navigation.

The DAR architecture also offers the potential for increased dynamic range when compared to more conventional systems due to the use of a distributed receiver/exciter architecture [3]. This allows for higher clutter cancellation ratios, and improves MTI and Pulse Doppler processing. Many processes taking place in a DAR depend on maintaining phase stability over a Coherent Processing Interval (CPI), and over extended periods of time (hours).

### 1.2.1 GaN MMIC in Future Radar Systems

New radar designs are incorporating GaN Monolithic Microwave Integrated Circuit ( MMIC) PA technology into their final amplification stage. This is due to a high power density

that exceeds 4 W/mm, high efficiency, and high breakdown voltage. GaN PAs represent the state-of-the-art in terms of power density and efficiency, making them appropriate for radar applications. Thus, their properties at a system level need to be well understood.

Active phased arrays use solid state PAs in their final amplification stage. The field has been dominated primarily by two technologies {i.e., the Silicon (Si) Laterally Diffused Metal Oxide Semiconductor (LDMOS) and the Gallium Arsenide (GaAs) Field Effect Transistor (FET)}. LDMOS has a lower cost than GaAs technology; however, its maximum frequency of operation is typically limited to less than 3.5 GHz. GaAs FETs can be used to much higher frequencies (above 100 GHz [4]).

MMIC development began in the 1960s [5]. The primary users of this technology at the time were involved in military and space applications. MMICs allow for a complete Radio Frequency (RF) design, often with inputs and outputs matched to a 50 ohm load. They have several advantages over designs using discrete components, including smaller size, reproducibility, and reliability.

Fielded active phased array radar systems almost exclusively use GaAs MMICs in their final amplification stage. Historically, MMICs always referred to a GaAs FET MMIC; however, this is no longer the case due to the introduction of the GaN MMIC in the mid-2000s [6]. The GaN MMIC has emerged as the best option to replace GaAs for high power aperture radars [7-9]. GaN semiconductors have more favorable properties than other technologies such as Si LDMOS or the GaAs Metal Semiconductor Field Effect Transistor (MESFET) [10, 11]. GaN devices have a higher breakdown voltage, which allows for a large drain voltage and leads to high output impedance per watt of RF power. GaN technology allows for easier matching and lower loss matching circuitry.

GaN reliability is very promising [12-14], with Accelerated Life Testing (ALT) predictions in excess of five million hours and degradation mechanisms consistent with source

metal intermixing [12]. Overall, the introduction of GaN MMICs in future radar systems is certain.

## 1.3 Problem Statement

Phase stability is necessary to achieve a high clutter cancellation ratio, which enhances the target detection capability in a cluttered environment. Testing of solid state GaN PAs showed that, under multifunction conditions including irregular radar pulse trains, the pulse-to-pulse stability assumption is not valid [15, 16]. These instabilities manifest as amplitude and phase transients and are caused by electrical and electro-thermal memory effects. Other potential instabilities have been reported, such as irregular pulse train burst [17], different pulse power due to staggered Pulse Repetition Frequency (PRF) [18], and long-time (hundreds of seconds) amplitude and phase drift due to device temperature changes [19].

Amplitude and phase (complex gain) transients have been observed to occur over time scales of several milliseconds on CPIs where the duty cycle or pulse width varies from the previous CPI. The time varying complex gain impacts the effectiveness of stationary clutter rejection in Pulse Doppler radars, which presents a significant problem. For example, MTI processing is highly sensitive to instability in the system [20].

## 1.4 Research Objectives

The purpose of this dissertation is to:

1. Explain the origin of the instability in GaN PAs; the self-heating electro-thermal memory effect is identified as the key mechanism that causes the observed transients.
2. Explain the developed measurement technique; the technique measures change in the amplifier's gain during normal operation.

3. Assess how the instability impacts clutter rejection and system pulse-to-pulse stability; Moving Target Indicator (MTI) radar processing technique and Root Mean Square (RMS) Pulse-to-Pulse (P2P) Stability metrics are used to accomplish this.
4. Propose a behavioral model; a Foster network topology is use to model the transients observed in the device.
5. Propose a method for mitigation; a digital predistortion technique was developed to counteract the amplifier's behavior in reference to the radar system master oscillator.

The concept behind the behavioral model is to replicate the observed amplitude and phase transients, which represents a change in the amplifier gain and insertion phase. The model delivers a single complex number value per pulse in a radar sequence. Characterizing these amplitude and phase transients requires a set of sophisticated equipment capable of exciting a PA with multifunction radar waveforms and collecting data for processing. An instrumentation radar and test set-up [15], hereafter referred to as the PA test set-up, is used to study the observed transients.

A literature review of behavioral models and predistortion techniques [21-36] did not reveal any existing model that can be directly applied to the effects observed within the context of multifunction radar waveforms. This dissertation proposes a new behavioral model and parameter extraction technique that can be used to model electrical and electro-thermal memory effects in multifunction radar systems.

Most predistortion algorithm designs involve the linearization of the PA's response to reduced spectral regrowth, adjacent channel interference, intermodulation products, and inter-symbol interference in communication systems. The maximum output power and high efficiency required for high power aperture radars run counter to these goals. This dissertation proposes a new digital predistortion technique to predistort individual pulses within a CPI to counteract the memory effect producing amplitude and phase transients, while maintaining the desired power

efficiency. The predistortion was implemented and tested using the PA test set-up and the developed behavioral model. The MTI Improvement Factor and the Root Mean Square (RMS) Pulse-to-Pulse (P2P) Stability methods were used to quantify the effectiveness of the predistortion. These two metrics offer different insight into system stability.

A digital predistortion algorithm and methodology is presented that corrects instabilities that are induced by radar power amplifiers during normal radar operations. These instabilities are generated when the power amplifiers are excited by dissimilar radar waveforms. The digital predistortion algorithm presented effectively cancels the instabilities in respect to the radar's coherent master oscillator.

## 1.5 Research Significance

This research is in regards to an algorithm that mitigates the interpulse (pulse-to-pulse) instabilities generated by radar's power amplifiers when excited with multifunction radar waveforms. Currently the only method practiced to mitigate these instabilities is adding extra pulses as fill pulses until the transients diminish. This reduces the impact on the radar's stability thus maintaining sensitivity. However, this approach is costly. The received echo signals due to these extra pulses are discarded before processing, since they don't have the required stability. RF energy is wasted reducing the overall efficiency of the system. The time expended in the transmission of the extra pulses cannot be used for the purposes of search or tracking of legitimate targets. This problem is expected to become more prevalent with the use of more dynamic multifunction waveforms. The fill pulse technique can strain the scheduler as more radar resources (time and energy) will be used to mitigate the transients.

Other approaches can help mitigate the problem by sampling the transmitted pulse, or by using coherent-on-receive techniques. These techniques cannot eliminate the distortion present in ambiguous clutter return. Ambiguous clutter returns result from unwanted targets located beyond the radar range; this range is a function of the Pulse Repetition Frequency of the radar.

For maximum performance the transient must be mitigated before the pulse is transmitted, thus it must be a solution intrinsic to the radar exciter and transmitter path.

## 1.6 Modern Radar Operations

An experiment was designed and implemented using the developed PA test set-up, where multifunction waveforms are feed to a Device Under Test (DUT) and the resulting processed data is used to characterize the amplifier. The experiment objective is to measure the amplifier complex gain during normal operating conditions. For modern multifunction radars, the normal operating condition implies that multiple diverse radar waveforms are transmitted in close succession. Also during normal radar operations, each CPI is considered independent; this means that coherent processing is performed only with data that belongs to a unique CPI.

Multifunction capabilities emerge from a radar's ability to rapidly change waveforms and arbitrarily steer the antenna beam. This means that at any given time the radar can change waveform and look angle to perform a different function. For example; the radar can be alternating between a surface search mode and an air search mode. These two functions call for significantly different waveforms. The surface search mode requires short pulses at a faster PRF, and targets echoes are expected to arrive from low elevation angles. The air search mode requires longer pulses and slower PRF, and targets echo are expected to arrive from any positive elevation angle.

The waveform characteristics used during the experiment must be representative of what a modern multifunction radar system can produce. Similar to modern multifunction radars, the experiment also requires the capability to rearrange the waveforms' order. This facilitates characterizing the effects that different waveforms produce in the amplifier. The properties to be measured are the change in amplifier scalar gain and phase insertion, also known as complex gain. The desired outcome is to characterize the behavior, magnitude and duration of these changes.

## 1.7 Original Contributions

This dissertation compiles previously disclosed contributions as well as new unpublished contributions. Previous contributions have included the development of a measurement technique to investigate the impact of electrothermal memory effects on multifunction radars [15], as well as the analysis of the degraded performance of a radar transmit antenna pattern and signal processing due to memory effects [16]. The referenced papers presented the results of two different GaN PA designs, showing the behavior, duration, and magnitude of the amplitude and phase transients. The results presented in this dissertation expand on that by adding the results of a third GaN PA design, in addition to a new behavioral model and predistortion technique.

The results presented here show a consistent behavior with previously reported results and results from a more recent study by Delprato 2014 [37]. The work in [37] evaluates the pulse-to-pulse stability of a GaN High-Electron-Mobility Transistor (HEMT) amplifier. They conducted circuit simulation that included RC-network to model electrothermal effects, and a one-trap drain-lag circuit to model trappings. The characteristic waveform used in the paper of eight pulses of 50 microseconds long at 20 % duty cycle is followed by silence. This is parallel to the concept of multifunction radar waveforms introduced in [15, 16], and further developed in this dissertation. However, instead of transmitting a different waveform, the silence function being executed could be for example a received only mode, blanking zone for safety, electromagnetic interference reduction, or a primary-power management concept on a large power-aperture radar system. In essence multifunction waveforms as well as pulse train bursts cause transients effects that affect the pulse-to-pulse stability and thus radar performance.

An important assumption in radar processing is that every pulse in a CPI is identical. When radar waveforms are synthesized for transmission, only a single pulse is created and is then repeated for a number of times until the CPI is completed. This research challenges this assumption and proposes the use of predistortion as a means to compensate for the observed transients in amplitude and phase.

## 1.8 Organization of dissertation

This dissertation is organized in eight Chapters. Chapter 1 discusses the motivation and importance of the research, in particular the importance of GaN technology in future radar systems. Chapter 2 discusses the memory effects present in a typical pulsed radar Solid State Power Amplifier (SSPA), identifying self-heating as the root cause of the observed transients, as well as a discussion of behavioral models. Chapter 3 describes the measurement technique developed to characterize the amplifier, as well as introducing the concept of interpulse instability and the MTI Improvement Factor (Cancellation Ratio) used as a metric to assess the impact of the transient on radar systems performance. Chapter 4 describes the development of the Power Amplifier Test set-up used to conduct the experiment, analyze data and implement the digital predistortion. Chapter 5 presents measurement results for a power amplifier submitted to multifunction radar waveform. Chapter 6 proposes a new behavioral model and parameter extraction technique. Chapter 7 proposes a novel concept of digital predistortion for individual pulses in a CPI. Chapter 8 is the conclusion.

# Chapter 2. Literature Review

This chapter describes various mechanisms for memory effects, as well as behavioral model techniques used to model amplifier behavior. These were studied under the context of a multifunction radar, in terms of characteristic time constant and pulse envelope frequency. The causes of the observed amplitude and phase transients are memory effects that ultimately affect the characteristics of a semiconductor due to the history of its input signal. The most prominent sources of memory effects and their relationship to the observed transient effect are discussed in Section 2.1; these are self-heating, bias network, charge trapping and matching network. The characteristic time constants of the transient effects, the technology maturity and device design points to the self-heating memory effect as the root cause of the observed transient effect. Various behavioral modeling techniques are discussed in Section 2.2. These techniques are studied to evaluate the feasibility of using them to mitigate the memory effects. The correction to memory effect requires a dependency to past waveforms. Within the research's scope, these dependencies have time spans of several milliseconds. This long time span is nonconforming to typical behavioral modeling techniques discussed, and thus requires the development of a new behavioral model.

## 2.1 Memory Effects in Solid State Power Amplifiers (SSPA)

As defined herein, memory effects are changes in the amplifier's gain and phase insertion due to previous radar CPIs. The previous CPI influence spans several milliseconds. This is significantly different than the scenarios applicable to a communication system, where the primary concerns are the spectral purity of the output signal, linearity, spectral regrowth, and adjacent channel interference [35, 38-40]. Conversely, the focus for radar systems is maximizing

output power and efficiency [8, 13, 41]. Memory effects are produced by many factors [42], including self-heating, biasing network, charge trapping, and matching networks.

Figure 2-1 shows a block diagram of a conceptual Field Effect Transistor (FET) power amplifier designs. Signals are routed in and out of the amplifier via transmission lines with 50-ohm characteristic impedance. Input and output matching network are used to match the low characteristic impedance of the FET to the much higher impedance of the transmission line. The biasing network provides precisely tuned voltages as well as large DC power into the transistor for proper operation. Semiconductor properties including its purity affect the charge trapping and thus the device performance. The transistor's thermal stackup design and implementation, as well as the semiconductor properties affect the degree of self-heating experienced by the device. Some transistor's architecture can allow electrical feedback loops to be formed within the transistor or though the biasing network. Each element and its corresponding memory effect is discussed in more detail in the next subsections.

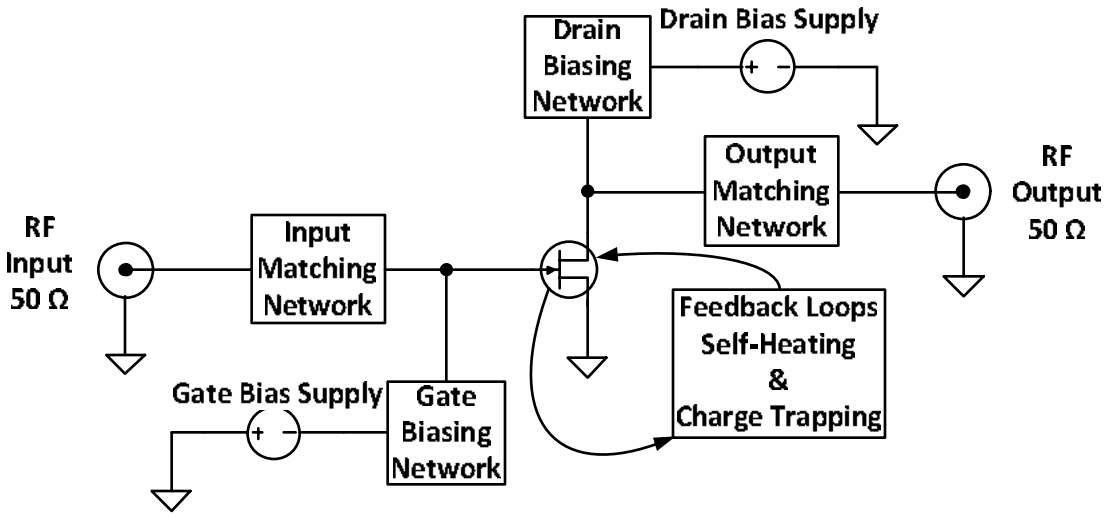


Figure 2-1: Block diagram for a conceptual FET power amplifier design. Mechanisms for memory effects include; 1) self-heating, 2) biasing network, 3) charge trapping and 4) input and output matching network.

### 2.1.1 Self-heating

Self-heating refers to an unavoidable increase in temperature inside a device due to heat dissipation which is typically viewed as an increase in channel or junction temperature over the package temperature. Figure 2-2 (a) shows a thermal diagram of a FET, where its channel temperature is ($T_C$) degrees above the ambient temperature ($T_A$). The temperature increase is determined by the dissipated power inside the chip and the thermal properties of the layers that form the packaged transistor and how it is attached to a heat sink. Figure 2-2 (b) shows a simplified thermal model typically used to describe the multiple layer scenario, and facilitated by virtue of the analogy between Fourier's Law and Ohm's law.

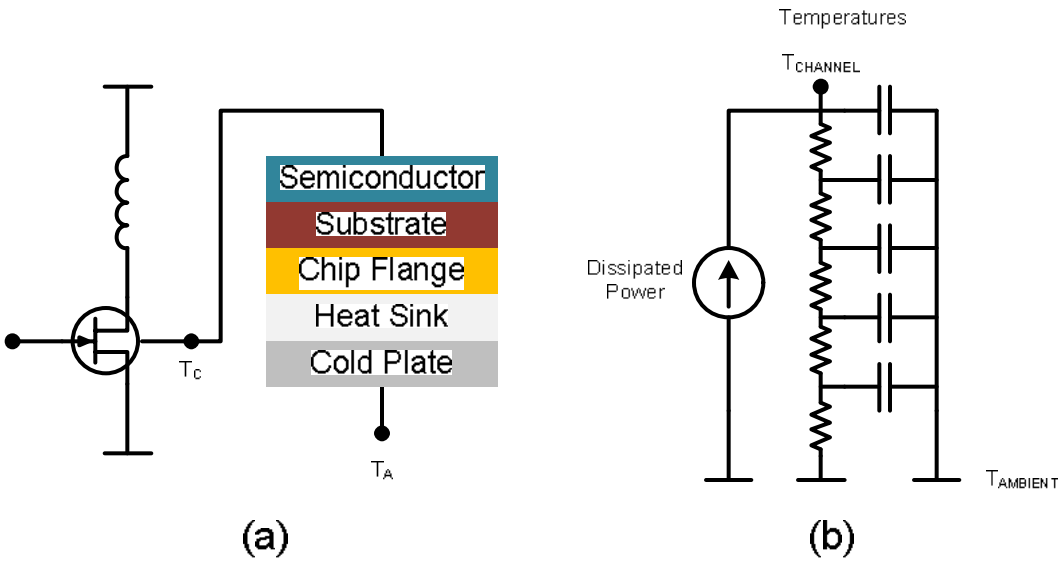


Figure 2-2: Thermal model of self-heating mechanism; (a) heat generated within the transistor elevates the channel temperature, (b) a simplified thermal model shows how the dissipated power within the semiconductor layer increases the channel temperature by representing each layer as an electrical time constant.

The circuit shown in Figure 2-2 (b) is in general impractical to be used in circuit simulations. The reason is the time-span of the several time-constants. The thermal time constants can range from nanoseconds in the semiconductor layers to several minutes at the cold

plate. Instead, a simplified circuit with perhaps one thermal resistance and capacitance is used, as shown in Figure 2-3. Where the parameter $I_{th}$ is a function of the instantaneous power dissipated within the FET. The instantaneous power dissipation is computed as the product of the drain current ($I_{DS}$) and the drain voltage ($V_{DS}$). $R_{th}$ is the equivalent thermal resistance, and $C_{th}$ is the equivalent thermal capacitance. The FET's drain current is in turn a function of the instantaneous gate to source voltage ($V_{GS\_int}$), drain to source voltage ($V_{DS}$) and the channel temperature ($T_C$).

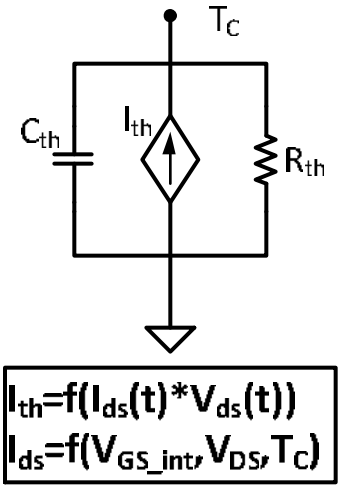


Figure 2-3: Simplified thermal circuit used in small signal models. The drain current ($I_{DS}$) is a function of the channel temperature ($T_C$). Parameter $I_{th}$ is a function of the instantaneous dissipated power, $R_{th}$ is the equivalent thermal resistance, and $C_{th}$ is a the equivalent thermal capacitance.

The rapid temperature cycling that occurs inside the device [43, 44] alters its gain and linearity [45]. The device channel (junction for BJT) temperature changes as a function of the pulse envelope frequency, which is typically below 20 kHz. The device bias class is an important factor in the channel temperature fluctuation. In the case of pulse radar amplifiers, the biasing point of choice is class AB.

Figure 2-4 shows a compact GaN HEMT model used by CREE [46], based on a 13-element MESFET model developed in [47]. The figure is shown for illustration purpose only, additional information about the definition of all the parameters can be found in CREE [46]. The model is an electrical circuit often simulated within dedicated RF and electronic design automation software such as the Keysight's Advanced Design System (ADS) or the AWR's Microwave Office. Additional information about large-signal models can be found in [48].

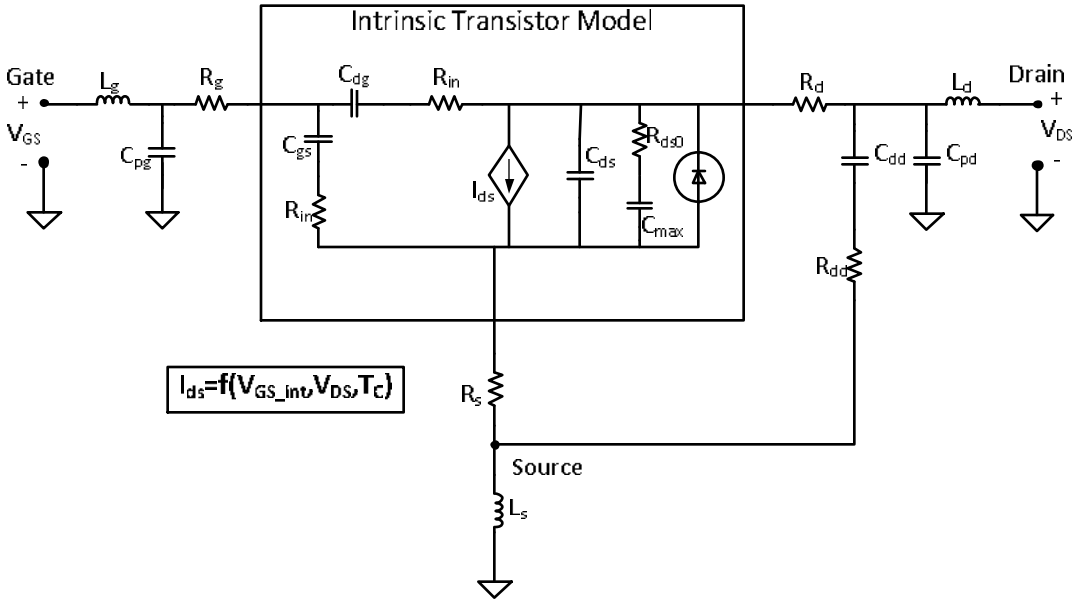


Figure 2-4: Large-signal model for a CREE GaN HEMT; the drain current ($I_{ds}$) is a function of the gate ($V_{GS\_int}$) and drain voltage ($V_{DS}$) as well as the channel temperature ($T_c$).

The properties of semiconductor materials and devices change with temperature [49-58]. For example, the thermal resistance and the specific heat of GaN [59] and Silicon Carbide (SiC) increase with rises in temperature. Indeed, the large-signal model has a negative feedback between the channel temperature and the drain current. For a given biasing point, the drain current decreases as a function of the channel temperature, resulting in a drop in output power; equivalent to a drop in device gain. The high thermal conductivity of SiC, 130 W/(m•K) [60] allows for rapid heat transfer from the channel to the case. This, combined with the high power

density of the GaN devices, suggests that there is a significant difference in channel temperature between the ON and OFF states of a pulsing device [36, 61].

### 2.1.2 Bias Network

The biasing network is used to properly energize the device while stopping the propagation of RF into the power supply lines [62]. The biasing network influences the memory effects observed in PAs [33, 36, 63-65]. Left unattended, voltage fluctuations in the device drain can be a major contributor to memory effects, due to a non-zero bias to power supply impedance. The biasing network requires low impedance at the pulse envelope frequencies to avoid envelope dependent voltage changes at the device's gate and drain.

Figure 2-5 shows a well-designed drain biasing network circuit, taken from [66], similar to those used to energize FETs. Following the power supply, a capacitor bank (C1) is used to store energy and to decouple the envelope frequency from the power supply. It is beneficial to select capacitors with low internal resistance to reduce the voltage droop that occurs during high loads. Due to physical constraints, the capacitor bank is located away from the amplifier circuit. The inductor L1 must be selected for minimum impedance and lowest resistance. L1 may also include stray inductance inherent in the wire or PCB trace that connects the capacitor bank to the device. Connected at the FET is a decoupling capacitor C2. C1 and L2 resonate at the RF frequency, presenting a high impedance to the voltage source. The inductor L2 is in series with a close-in energy storage capacitor C3, and thus must have low impedance at the pulse envelope frequency. The properties for the close in energy storage capacitor are of large capacity, low inductance and very low resistance. The use of high capacity energy storage electrically close to the device drain mitigates the memory effect, thus eliminating this mechanism as a major contributor to the observed amplitude and phase transient. The capacitors used can be a combination of parallel plate, multilayer ceramic and solid tantalums, depending on the desired properties.

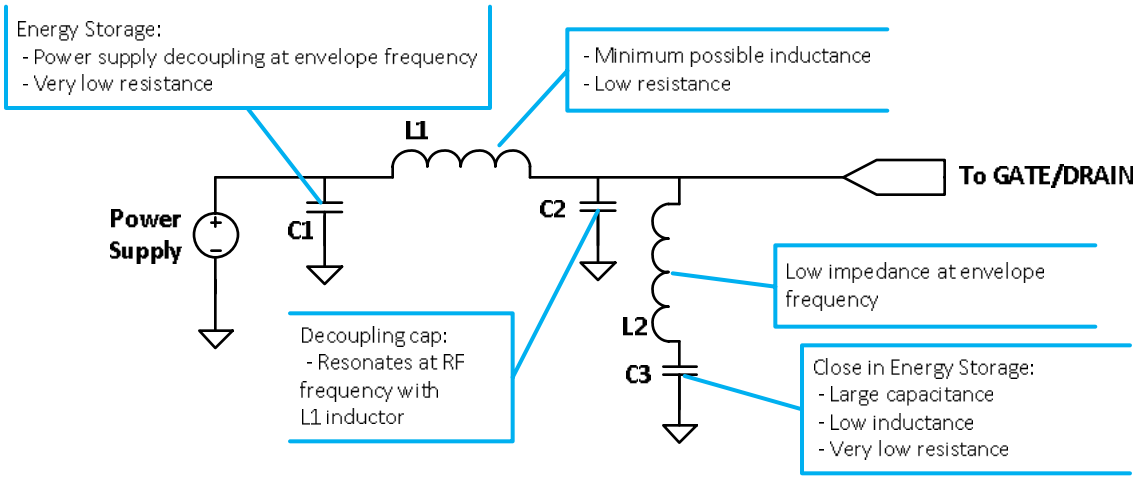


Figure 2-5: Drain biasing network is designed to reduce memory effects by using filters to prevent feedback mechanism.

### 2.1.3 Charge Trapping

Charge trapping is a phenomenon that influences the performance of GaN devices [67-70] by introducing parasitic charges that limit high frequency output power [71]. The trappings responsible for degradation in the microwave performance of Aluminum Gallium Nitrate (AlGaN)/GaN devices are located at the surface and in the underlying semiconductor buffer layers [71, 72]. Charge trapping is associated with a recoverable reduction in drain current and thus power output over time. The time-constant associated with charge trapping depends on the process used to build the device and can vary widely with temperature, ranging from microseconds to minutes [73]. Trapping results in parasitic capacitances, which interact with other equivalent resistance in the device. The trap occupancy and temperature will affect the parasitic capacitance, and thus the traps' time constants.

Figure 2-6 shows a circuit used to model drain-lag trapping. The drain-to-source current is a function of the models' intrinsic voltage, the drain-to-source voltage and the channel

temperature. The time-constant for charging and discharging is asymmetric. The traps are emptied when the drain voltage is removed, and are filled when the drain voltage is applied to the device.

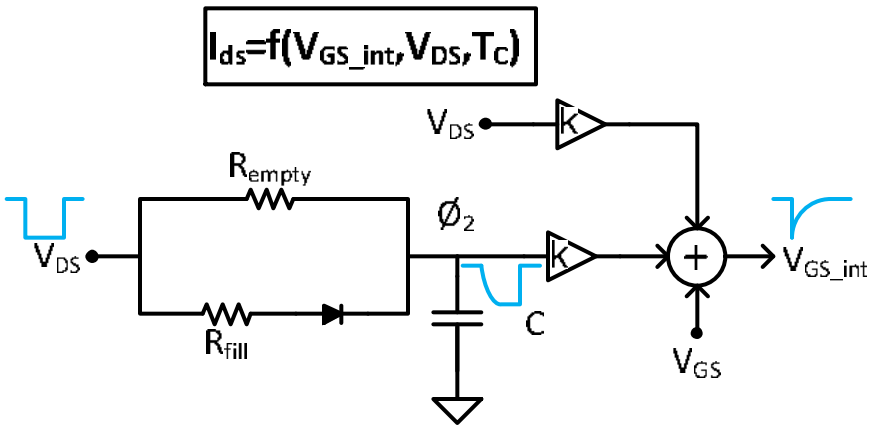


Figure 2-6: Drain-Lag Model for trapping mechanism. The trap emptying and trap filling circuits have different time constants.

Trapping effects have been largely eliminated due to modern device manufacturing processes [74], and the fact that gate and drain voltage are kept at a constant bias. Therefore, this mechanism is regarded as a minor contributor to the observed amplitude and phase transients.

### 2.1.4 Matching Network

As a convention, RF power amplifiers are matched to 50 ohms, and this is applied to most RF and wireless devices. The prominent exceptions to this are the cable TV and satellite communication industries that use 75 ohm. Matching networks are circuitry built at the input and output of transistors to match the impedances of the device to a load, allowing for maximum power transfer and minimum reflected power. Matching is also used to reduce (terminate) the number of harmonics produced by the inherent transistor non-linearity.

Figure 2-7 shows a block diagram for a transistor's input and output matching network. In general, transistor impedance is very low, in the order of a few ohms. The input circuit is a

High Pass Hi-to-Low matching network, and the output is a High Pass Low-to-Hi matching network. This example is one of multiple approaches used to design a matching network. In practice, the lump element design is abandoned in favor of a microstrip circuits design.

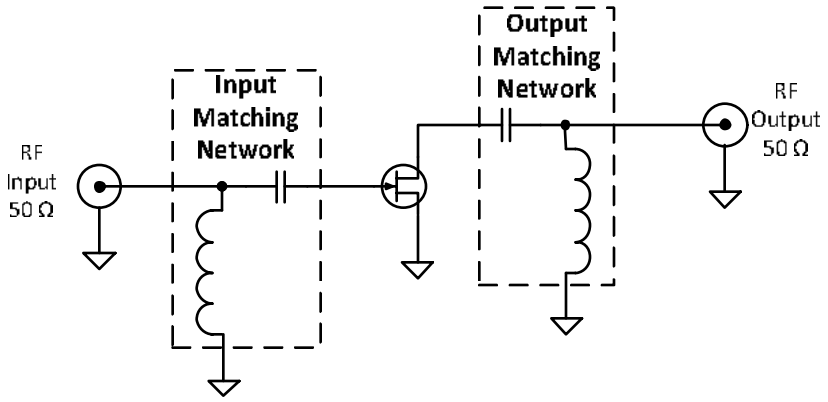


Figure 2-7: Block diagram for a simple input and output matching network. This example uses high pass filters to match the low impedance of a FET to the standard 50 ohm input and output impedances.

Clearly, the matching network is a filter, thus its impedance and response is frequency dependent. The matching network and its interaction with the FET will cause high frequency dispersion memory effects. These memory effects are of short duration, up to several nanoseconds, and therefore are of no concern in this investigation.

For example the data sheet for the CREE CGH40120P GaN HEMT provides a transistor source (input) impedance of 1.09-j5.9 ohms and load (output) impedance of 3.06-j3.82 ohms at 3 GHz. For ideal matching to 50 ohms, the input matching network requires component values of 0.4 nH and 37.9 pF. Conversely, the output matching network requires component values of 0.7 nH and 6.5 pF. This rudimentary example illustrates typical values for matching network impedances and thus time constants.

Figure 2-8 illustrate the various memory effect mechanisms and their interaction with a GaN HEMT model. At the center in the lower part of the model is the intrinsic transistor model

surrounded by the wire bond, which in turn is connected to the matching networks. At the upper part of the figure, the biasing network for the gate is on the left side of the circuit and for the drain is on the right side. The self-heating and trapping memory effect models are located in the top center.

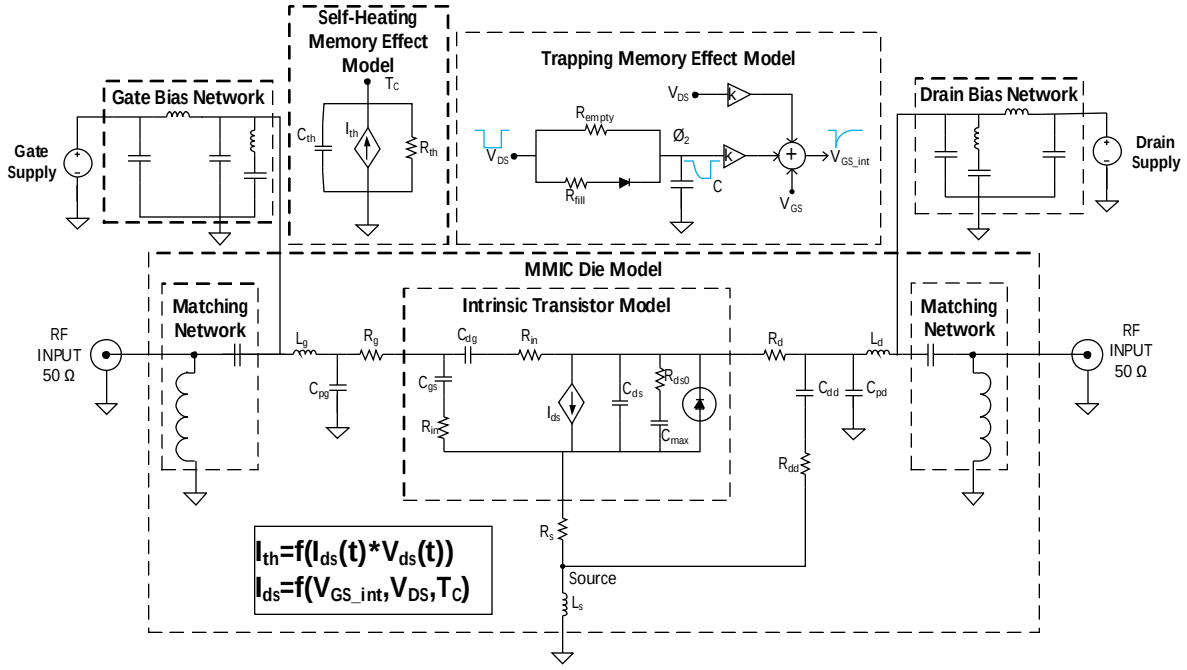


Figure 2-8: Equivalent circuits for electro-thermal and electrical memory effects mechanism interacting with a GaN HEMT power amplifier model. The four major memory effects, self-heating, biasing network, charge trapping and matching network are represented.

Proper design practices and test conditions can mitigate and isolate different mechanism allowing the investigator to focus on the effects of one mechanism versus another. As far as this research is concerned, the effect of self-heating was chosen as the most important memory mechanism that affects pulse to system stability. The matching network memory effect mechanism was dismissed as their associated time constants are of short duration in the order of nanoseconds. The Biasing network mechanism is mitigated due to the location of high

capacitance energy storage in close proximity to the device drain. The trapping mechanism is mitigated by keeping the gate and drain voltage source energized (no drain pulsing). Thus, the self-heating mechanism is the main contributor for the observed amplitude and phase transient.

## 2.2 Behavioral Models for Power Amplifiers

Behavioral modeling is a technique used to produce approximations of real systems operation. It is applied at a high level of abstraction, where the internal properties of the system or physical attributes are unknown or too difficult to analyze. As technology advances, the complexity of modern systems increases, making it harder to quantify their behavior. In addition, it becomes harder to observe their internal processes. A behavioral model is a mathematical function used to map or describe the relationship of a system output to its input. Most often, the behavior relates to measurement data, but it can also relate to simulated data or system operation. The mathematical nature of the models results in an infinite number of possible model formulations.

The development and evaluation of a behavioral model requires the selection of a mathematical domain. Depending on the model's hierarchy, the mathematical representation may take place on the frequency domain, time-domain at the carrier frequency, or as time-domain envelope analysis. A behavioral model is developed based on input stimulus and its corresponding output. A properly developed model is valid for the range of stimulus used in its development. However, deviating from this stimulus can render the model useless. Behavioral models are developed from measured or simulated data, often by fitting polynomials functions to a dataset to train Artificial Neural Networks (ANN). Thus, it is necessary to pay attention in the adaptation of behavioral models.

There has been a significant amount of work done in developing behavioral models for amplifiers [21, 24-26, 28-36, 75]. These models are used in many scenarios, from circuit design aids to the development of predistortion techniques, and are most often tailored to communication systems, with little mention of applicability to pulse radar waveforms [24] and

no mention of multifunction radar waveforms.

The thermal feedback mechanism of amplifiers has been studied [24] where envelope transient analysis is used to predict the impact of the thermal effects in pulsed RF modes. The behavioral electrothermal model is implemented in the time domain. The model is intended for the design of single pulse amplifiers for radar applications, and does not deal with multiple pulses, or multifunction waveforms.

Volterra series analysis is often used to represent a nonlinear input-output system. The classical Volterra-series can only be used to characterize weakly nonlinear systems [28] due to difficulties in applying the technique in practice. Other approaches such as reduced Volterra series can characterize more pronounced nonlinear systems. However, solid state PAs used in radars are routinely driven into compression (1 to 6 dB), to maximize output power and increase efficiency, thus limiting the number of behavioral models that can be used.

A behavioral model approach tailored towards communication systems using a Volterra-based modeling is presented in [34]. One interesting concept from this paper was the proposal of a model with two widely separated time-constants. This approach is intuitively logical as many PAs are composed of multiple stages, each with its own properties that can be affected by temperature. The time constants discussed are between 1 to 10 microseconds. These are of interest to this investigation; the time constants that are being observed in GaN amplifiers are from dozens of microseconds to milliseconds. The longer time constant is also suspected to be related with the amplifier drain biasing network. Biasing networks have large capacitor banks for energy storage. The power supply also becomes part of the biasing circuit; a large capacitor bank is needed to limit the power supply noise from affecting the PA's behavior.

A commonly used approximation to the heat transfer problem on transistors is a second order differential equation. From this, an expression is developed [36] to calculate dynamic junction temperature. This expression is used to construct an electro-thermal model for PAs. The model was used to design a predistortion function to compensate for effects due to temperature changes in the junction. Thermal self-heating is the most relevant long term

memory effect in this investigation, as this affects the junction temperature of the transistors resulting in amplitude and phase transients.

Memory effects induced by thermal coupling and bias circuits [31] have been studied. The test used an intermodulation distortion signal applied together with a two-tone signal to the input of the amplifier. The amplitude and phase of the test signal is adjusted until the third order intermodulation (IM3) products at the output of the amplifier are cancelled. The technique provides information to help in the design of amplifiers and associated predistortion circuits. The technique has limited usability for the time constants of interest in this investigation, and to pulse amplifiers.

A model was developed [32], which tracks the signal-induced changes of PAs. This model uses previously developed models, but changes parameters that depend on the long term memory estimates. The average input signal level over a window is used to track the average input power and self-heating. This result is used to change parameters of the behavioral model. Their work was focused on a model that will help predict the behavior of an amplifier to bursty data transmissions. Memory length in the order of milliseconds is of great interest to this investigation; furthermore the moving average concept to track self-heating will be adopted.

Memory depth is an important issue for behavioral models. It relates to the amount of data needed to produce a valid output. An increase in memory depth is invariably linked to an increase in mathematical operations, thus increasing its complexity. Work done by [35] attempts to reduce complexity by proposing a systematic approach to determine the memory lag and memory depth of the model. These two parameters are identified from measurements, and are used in memory polynomial and real-valued time-delay neural networks to model the amplifier and digitally synthesize baseband predistortion to correct for memory effects. Linearization of the models was assessed by looking at the spectral regrowth (adjacent channel leakage ratio) for a 4-carrier Wideband Code Division Multiple Access signal.

## 2.3 Chapter Summary

A GaN PA, being the Device Under Test (DUT) used during this investigation, was biased with a constant gate and drain voltage, limiting trapping charge and discharge mechanisms. A large energy storage capacitor located electrically close to the drain terminal reduces the drain bias network memory effect [33]. This allows for the isolation of self-heating as the root cause of the amplitude and phase transients observed. Due to the time constants associated with a radar's CPI, only self-heating was of interest during this investigation.

Memory effects have been shown to be closely linked to the biasing network [33] and self-heating of amplifiers [36, 45]. Thermal analysis of power GaN amplifiers shows that thermal resistance significantly changes depending on operating conditions, and can change quite rapidly with duty cycle selection [43] and that prolonged off time before a pulse train [61] directly affects the device gain, affecting insertion phase due to Amplitude Modulation to Phase Modulation (AM-PM) conversions.

# Chapter 3. Measurement Technique to Characterize RF Power Amplifiers During Multifunction Radar Conditions

This chapter explains the methodology used to characterize RF power amplifiers, the experimental framework and the minimum capability required for the execution of the experiment. The new context of multifunction radar operations using GaN technology requires the development of a measurement technique to characterize the amplifier. The implementation of the measurement technique is complex and requires a complicated arrangement of instrumentation for proper execution. The technique discussed here is the first developed to address the issue of interpulse instability produced by GaN power amplifiers when excited with multifunction radar waveforms. The technique was first disclosed in [15]; a manuscript by this author further developing this work has been accepted for publication by the IEEE Transactions on Microwave Theory and Techniques [76]. Recently Delprato 2014 [17] evaluated the pulse-to-pulse stability of a GaN HEMT amplifier. They conducted circuit simulation that included RC-network to model electrothermal effects, and a one-trap drain-lag circuit to model trappings. The characteristic waveform used in the paper, is parallel to the concept of multifunction radar waveforms in [15, 16, 76], and further developed in this dissertation. However, instead of transmitting a different waveform, the silence function being executed could be, for example, a receive only mode, blanking zone for safety or electromagnetic interference reduction, or a primary-power management concept on a large power-aperture radar system. In essence, multifunction waveforms as well as pulse train bursts cause transients effects that affect the pulse-to-pulse stability and thus radar performance.

## 3.1 Experiment Design

The conditions a power amplifier experiences during normal operation need to be replicated. These conditions, introduced in Chapter 1, are that multiple diverse radar waveforms are transmitted in close succession. Waveform characteristics change significantly from one waveform to another. In Chapter 2 we learned that memory effects have associated time constants. The time constants studied in this research have duration of dozens of microseconds to milliseconds; the influence of earlier waveforms can last for several milliseconds. This is fundamental in establishing a time-span in which a past waveform affects the present waveform. The experiment must capture all of these conditions in a well-defined and repeatable fashion. The waveform characteristics used during the experiment must be representative of what a modern multifunction radar system can produce. The experiment also requires the capability to rearrange the waveform order. This facilitates characterizing the effect that different waveforms produce in the amplifier.

The properties intended to be measured are the change in amplifier scalar gain and insertion phase, also known as complex gain. The desired outcome is to characterize the behavior, magnitude and duration of these changes over the duration of a waveform, and establish a relationship between this behavior and past conditions.

There are at least three conditions necessary to characterize the amplifier behavior:

1. Replicate multifunction radar waveforms: This condition is necessary to satisfy the experiment's premise. The amplifier complex gain changes as a function of previous waveforms fed to the amplifier. Creating several different waveforms will help to establish a meaningful relationship between waveform parameters and the observed transients.
2. Measure the amplifier complex gain for any pulse within a Waveform: Due to memory effects, the amplifier complex gain will change over time. Therefore, the amplifier introduces distortion to every transmitted pulse. The actual gain is very

dynamic, even across a pulse. This investigation looks into the average gain per pulse.

3. Measure the complex gain over multiple consecutive pulses: The amplifier behavior is found by examining the differences between multiple consecutive pulses. A record must be keep to associate the observed behavior with a particular waveform sequence.

### 3.1.1 Multifunction Operations:

Figure 3-1 illustrates the concept of multifunction operations. In this example, multiple waveforms are scheduled to be transmitted by the radar. From left to right, the radar will transmit CPI 1, then CPI 5, then CPI 6, and so on. Examining waveforms CPI 1 reveals that it is composed of 32 pulses, each with a duration of 10 microseconds and a duty cycle of 8%. Conversely, waveforms CPI 2 is composed of eight pulses, each with a duration of 50 microseconds and a duty cycle of 2%. In this example, we can assume that the properties for CPI 1 were selected to comply with a surface-search function, while the properties for CPI 2 were selected for an air-search function. The transmission of CPI 1 and CPI 2 is therefore representative of a multifunction waveforms sequence. Although there are many possible combinations of multifunction waveforms, to include portion where no transmission occurs, the above scenario is used throughout this dissertation to introduce the processing techniques and present results.

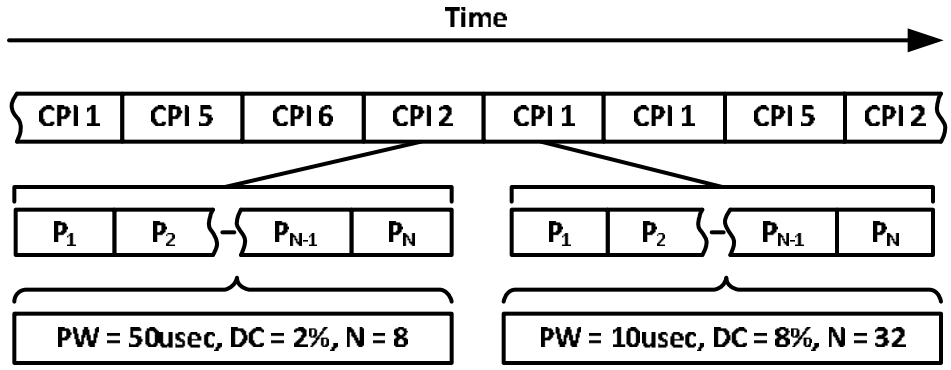


Figure 3-1: Example of a Multifunction Waveform Sequence. Different waveforms are transmitted consecutively. Some of these waveforms properties can vary significantly. Their interaction causes long term memory effect in the amplifier, distorting future waveforms.

Radar system engineers design waveforms with specific properties (such as pulse width, duty cycle) depending on the required function. A pulse can have arbitrary length, shape, modulation and duty cycle. Each pulse within a waveform is repeated for a specified number of times. Multifunction operation requires the use of waveforms where duty cycle or pulse width varies from a previous waveform. Consequently, the experiment requires the creation of arbitrary pulses for each waveform. A minimum of two waveforms are required to test the concept of multifunction operations.

### 3.1.2 Waveform Library File:

The information required to construct the waveforms is stored in a Waveform Library File (WLF). The WLF contains a list of the waveforms to be synthesized during a test event. The number of entries in the waveform file is arbitrary, but should be kept small to conserve system resources and reduce the number of possible waveform combination while conducting an experiment. A description of the properties required for each entry in the WLF is listed in Table 3-1. Each waveform must have a unique waveform name, and have independent and arbitrary values for the following properties: Pulse Modulation, Modulation Bandwidth, Pulse Width, Pulse Duty Cycle and Number of Pulses in a waveform.

Table 3-1: Description of waveform properties

| Property Name: | Description: |
|---|---|
| Waveform Name | A unique name to distinguish a waveform during a test event. The name is used to rearrange the order in which waveforms are played back. |
| Pulse Modulation | Pulses are modulated with conventional techniques, such as Pulsed CW, LFM or silence |
| Modulation Bandwidth | Bandwidth of modulated pulses, in hertz |
| Pulse Width | The pulse length, specified in seconds |
| Pulse Duty Cycle | Duty factor for individual pulses, specified in percentage |
| Number of Pulses | Number of pulses in a waveform |

The combined time for all pulses in a waveform is known as the Coherent Processing Interval (CPI), also known as dwell time. The CPI is a group of pulses used to extract information about a target. Figure 3-2 shows a hypothetical waveform containing $\boldsymbol{N}$ pulses. Ideally, each pulse has identical properties of pulse width, duty cycle and modulation. The property specifies the number of times a pulse is repeated to complete a radar's CPI. At any time during normal radar operations, only individual pulses are transmitted. There are no other signals being transmitted in between pulses.

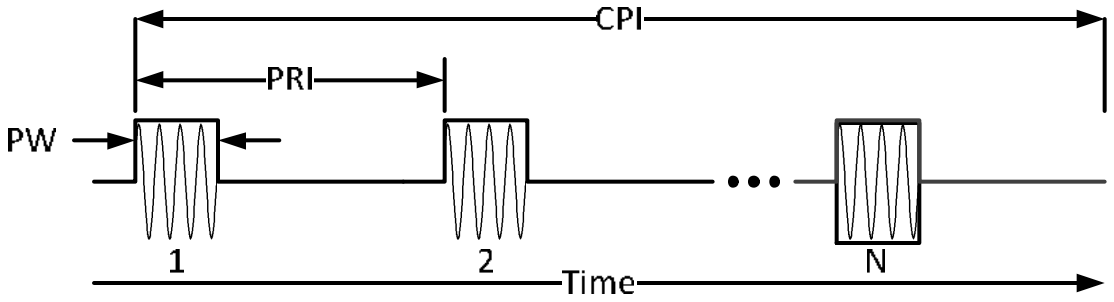


Figure 3-2: Illustration of the construction of a Coherent Processing Interval. Multiple pulses of identical characteristics are transmitted consecutively. Each pulse has duration PW, the spacing between pulse edges is the PRI.

The experiment must have provision to modulate pulses. Pulse modulation is ubiquitous in modern pulse Doppler radars. Pulse modulation is used to increase the bandwidth of the transmitted signal. This additional bandwidth is used to increase range resolution via pulse compression. The reason is that target detection depends on the energy of the radar pulse that reaches the target. The pulse energy is $\boldsymbol{E = Pt}$, where $\boldsymbol{P}$ is the root mean square power of the pulse and $\boldsymbol{t}$ is the pulse duration. Early radars used large $\boldsymbol{P}$ and small $\boldsymbol{t}$ to obtain good detectability and range resolution. For radars with solid-state amplification, the pulse power is not high when compared with more conventional amplifiers such as Traveling Wave Tubes (TWT), Klystrons or other vacuum-electronics devices. With lower $\boldsymbol{P}$ available from solid-state transmitters, $\boldsymbol{t}$ must be increased to compensate for lower $\boldsymbol{P}$. To obtain the same range resolution, pulse compression must be used. However, the examples presented in this dissertation use Pulsed CW (unmodulated pulses) for clarity.

### 3.1.3 Waveform of Interest:

To study the effect of one waveform on another, the concept of Waveform of Interest (WOI) is introduced. This waveform is treated differently than all other waveforms, and is the only one that will be collected for analysis. Due to the envisioned predistortion algorithm, this waveform synthesis requires the creation of all of the pulses in the waveform, instead of repeating an identical pulse. This will allow for the predistortion of each individual pulse in a

waveform. This also means that reproducing the waveform will occupy more system resources such as memory, as well as increasing the data transfer time between Radar Controller and the Radar Exciter.

Figure 3-3 shows the waveform synthesis concept. In this example, the WLF contains four entries; CPI 1, CPI 2, CPI 3 and CPI 4. Due to the implementation complexity, several programming objects are created to contain the waveform properties and the appropriate digital IF waveform that later will be loaded into the Radar Exciter. Refer to Chapter 4 and Appendix B for a more detailed explanation. CPI 1, CPI 2 and CPI 3 were synthesized as conventional waveforms, where only a single pulse needs to be created for each waveform. CPI 4 was selected as the WOI. In this instance, each pulse is created and assigned to a Waveform Object.

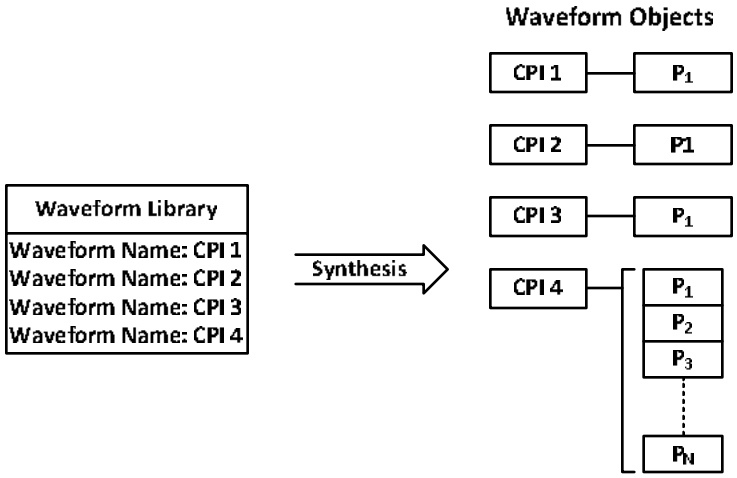


Figure 3-3: WLF Synthesis, showing the concept of Waveform of Interest. Multiple waveforms are created in memory. Each waveform has unique properties. For the selected WOI (CPI 4), each pulse in synthesized.

The duration of CPI that precede the WOI must be set to assure that only the memory effect from the previous waveforms will affect the WOI. This reduces the number of condition needed to be mapped, as part of the parameter extraction for the behavioral model. Figure 3-4 illustrate the concept, where the combination of waveforms is limited. The combination of

waveforms necessary to characterize and document the amplifier behavior is reduced to simply the WOI preceded by another waveform.

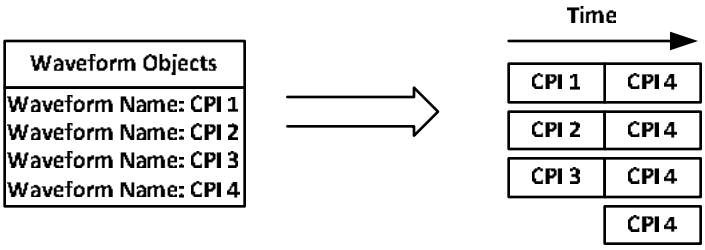


Figure 3-4: Effective Memory-Length Waveform Playback Sequence; limiting the length of the multifunction waveform sequences. The amplifier conditions needs to be reduced in order to facilitate a mapping of the recorded conditions into the behavioral model.

### 3.1.4 Data Collection and Storage:

Data collection requires the digital sampling of the amplifier's input and output. It also requires the storage of information regarding the WOI and the sequence being fed to the amplifier. The stored data should include information about the multifunction waveform sequence used during data capture, including its properties and others derived from the experiment implementation. The information collected must be sufficient to characterize the amplifier and repeat the test at a later time. The developed predistortion algorithm relies on knowing the operating conditions of the amplifier to calculate the predistortion coefficients; this is explained in Chapter 7.

For every pulse in the WOI a sample of the input signal to the amplifier must be collected. This is the reference used to establish changes in the amplifier's scalar gain and phase insertion. Figure 3-5 illustrate the input signal $x(t)$ being amplified and distorted by the amplifier resulting in the output signal $y(t)$. A sample of the amplified signal $y(t)$ must also be

collected. The amplifier has a transfer function described by $G$. For a stable input signal $x(t)$, any changes in the amplifier's transfer function will be reflected at the output signal $y(t)$.

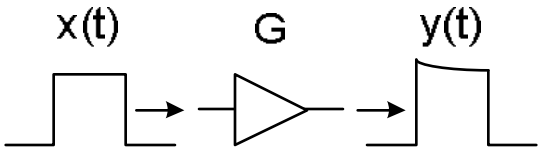


Figure 3-5: Signal x(t) is amplified and distorted, resulting in y(t).

The input signal $x(t)$ and the output signals $y(t)$ are RF signals, at a carrier frequency between 2.9 and 3.4 GHz. The signal need to be digitized and frequency translated into baseband complex signals (Inphase (I) and Quadrature (Q) components), before processing. These signals are digitally represented by $x[k]$ and $y[k]$, were k in the index of the sampled data. Refer to Chapter 4 for more information about how this is accomplished.

## 3.2 Cross-correlation as System Identification Tool

An important signal processing function used in Pulse Doppler radars is pulse compression. It is accomplished by performing a cross-correlation between the received radar echo and a reference. Cross-correlation is ubiquitous in practically all modern radars. The cross-correlation maximizes the signal to noise ratio and is also used in a system identification technique [77] known as the Wiener-Hopf equation.

The Wiener-Hopf equation makes use of autocorrelation matrix and cross correlation to estimate a system's transfer function. One of the conditions for this is the assumption that the system is asymptotically stable. Thus, this technique is ideal to characterize the amplifier complex gain on a pulse-to-pulse basis.

The complex gain of the amplifier is found by relating the digital representation of its output signal $y[k]$ to its inputs $x[k]$. In modern radar systems, the reference signal is synthesized rather than sampled. This assumes the system clock-source is highly stable. Due to the instrument grade quality of the clock-sources available for this study, the experiment requires sampling both signals $x[k]$ and $y[k]$. This mitigates clock-source instabilities that may otherwise disturb the results. A calibration process performed during the implementation of the experiment allows to scale both signal so that their power level is known.

### 3.2.1 Pulsed Signals

The signals $x[k]$ and $y[k]$ are in the baseband I/Q domain, and are expressed as shown in equations (1) and (2):

$$x[k] = \begin{cases} A_x \exp(j\phi_x) & k = 0,1,2,\text{L},N_S - 1 \\ 0 & \textit{elsewhere} \end{cases} \tag{1}$$

$$y[k] = \begin{cases} A_y \exp(j\phi_y) & k = 0,1,2,\text{L},N_S - 1 \\ 0 & \textit{elsewhere} \end{cases} \tag{2}$$

where, $A_x$ and $A_y$ are the pulse amplitude envelope for $x[k]$ and $y[k]$ respectively. $\phi_x$ and $\phi_y$ are the pulse phase envelope for $x[k]$ and $y[k]$ respectively. $k$ is the index for the sampled data. $N_S$ is the number of data points collected, excluding times when no signal is present. This will ensure that the complex gain of the amplifier is calculated when a valid signal is being feed to the amplifier.

The amplifier complex gain is defined in equation (3).

$$G = \frac{A_y \exp(j\phi_y)}{A_x \exp(j\phi_x)} = \frac{A_y}{A_x} \exp\left(j\left(\phi_y - \phi_x\right)\right) \tag{3}$$

The gain can be further separated into amplitude in decibels (4) and phase in degrees (5).

$$G_{dB} = 20Log_{10}\left|\frac{A_y}{A_x}\right| \tag{4}$$

$$G_{\deg} = \frac{180}{\pi}\left(\phi_y - \phi_x\right) \tag{5}$$

### 3.2.2 Sample Autocorrelation

The sample autocorrelation function is shown in equation (6):

$$r_{xx}(m) = \begin{cases} \dfrac{1}{N_S}\displaystyle\sum_{n=0}^{N_S-m-1} x[n+m]\,x^*[n], & m \geq 0, \\ r_{xx}^*(-m), & m < 0. \end{cases} \tag{6}$$

where, $r_{xx}(m)$ is the autocorrelation of $x[k]$, and $m$ is the index for lag with integer values $-N_S < m < N_S$.

The amplitude and phase of the signal $x[k]$ remains constant throughout the duration of the pulse. The phase component $\phi_x$ of the autocorrelation cancels out. The sample autocorrelation function can then be solved explicitly as shown in equation (7) and (8):

$$r_{xx}(m) = \begin{cases} A_x^2\left(1 - \dfrac{m}{N_S}\right), & m \geq 0, \\ A_x^2\left(1 + \dfrac{m}{N_S}\right), & m < 0. \end{cases} \tag{7}$$

$$r_{xx}(m) = A_x^2\left(1 - \left|\frac{m}{N_S}\right|\right), \quad -(N_S - 1) \leq m \leq (N_S - 1) \tag{8}$$

### 3.2.3 Sample Cross-Correlation

The sample cross-correlation function is shown in equation (9):

$$r_{xy}(m)=\begin{cases}\dfrac{1}{N_S}\displaystyle\sum_{n=0}^{N_S-m-1}x[n+m]\,y^*[n], & m\geq 0,\\ r_{xy}^*(-m), & m<0.\end{cases} \tag{9}$$

The phase components $\phi_x$ and $\phi_y$ of the cross-correlation are maintained. Equation (10) shows the cross-correlation between $x[k]$ and $y[k]$. The signal amplitude and phase are written explicitly into the sample cross-correlation function.

$$r_{xy}(m)=\begin{cases}\dfrac{1}{N_S}\displaystyle\sum_{n=0}^{N_S-m-1}A_x\exp(j\phi_x)\,A_y\exp(-j\phi_y)\,f(n,m), & m\geq 0,\\ r_{xy}^*(-m), & m<0.\end{cases} \tag{10}$$

$$f(n,m)=\big(u[n+m]-u[n+m-N_S]\big)\big(u[n]-u[n-N_S]\big) \tag{11}$$

where *f(n,m)* is a unit step function that sets the limits where $r_{xy}(m)$ is different from zero. After simplification, the result of the sample cross-correlation is shown in equation (12):

$$r_{xy}(m)=\begin{cases}A_xA_y\exp\big(j(\phi_x-\phi_y)\big)\left(1-\dfrac{m}{N_S}\right), & m\geq 0,\\ A_xA_y\exp\big(-j(\phi_x-\phi_y)\big)\left(1+\dfrac{m}{N_S}\right), & m<0.\end{cases} \tag{12}$$

### 3.2.4 Wiener-Hopf Equation

The Wiener-Hopf equation is used to get an estimate of *G*. The Wiener-Hopf equation states that:

$$r_{xy}(m) = \sum_{k=0}^{S} g(k)\, r_{xx}(m-k) \tag{13}$$

where, $r_{xx}(m)$ is the autocorrelation of $x[k]$, $g(k)$ is the Finite Impulse Response (FIR) filter coefficients of a system and $r_{xy}(m)$ is the cross correlation of $x[k]$ and $y[k]$. Substituting the sample correlation function values into the Wiener-Hopf equation (13) for $m = 0,1,2,\mathrm{L}\,,S$, gives:

$$\begin{aligned}
r_{xy}(0) &= g(0)r_{xx}(0) + g(1)r_{xx}(-1) + g(2)r_{xx}(-2) + \mathrm{L} + g(S)r_{xx}(-S) \\
r_{xy}(1) &= g(0)r_{xx}(1) + g(1)r_{xx}(0) + g(2)r_{xx}(-2) + \mathrm{L} + g(S)r_{xx}(1-S) \\
r_{xy}(2) &= g(0)r_{xx}(2) + g(1)r_{xx}(-1) + g(2)r_{xx}(0) + \mathrm{L} + g(S)r_{xx}(2-S) \\
&\mathrm{M} \\
r_{xy}(S) &= g(0)r_{xx}(S) + g(1)r_{xx}(S-1) + g(2)r_{xx}(S-2) + \mathrm{L} + g(S)r_{xx}(0)
\end{aligned} \tag{14}$$

Rewriting these results in matrix form:

$$\begin{bmatrix} r_{xy}(0) \\ r_{xy}(1) \\ r_{xy}(2) \\ \mathrm{M} \\ r_{xy}(S) \end{bmatrix} = \begin{bmatrix} r_{xx}(0) & r_{xx}(-1) & r_{xx}(-2) & \mathrm{L} & r_{xx}(-S) \\ r_{xx}(1) & r_{xx}(0) & r_{xx}(-1) & \mathrm{L} & r_{xx}(1-S) \\ r_{xx}(2) & r_{xx}(1) & r_{xx}(0) & \mathrm{L} & r_{xx}(2-S) \\ \mathrm{M} & \mathrm{M} & \mathrm{M} & \mathrm{O} & \mathrm{M} \\ r_{xx}(S) & r_{xx}(S-1) & r_{xx}(S-2) & \mathrm{L} & r_{xx}(0) \end{bmatrix} \begin{bmatrix} g(0) \\ g(1) \\ g(2) \\ \mathrm{M} \\ g(S) \end{bmatrix} \tag{15}$$

$$r_{xy} = R_{xx} g \tag{16}$$

where $R_{xx}$ is the autocorrelation matrix. The elements of the filter $g(0), g(1), \mathrm{K}, g(S)$ can be solved by matrix inversion:

$$\mathrm{g} = R_{xx}^{-1} r_{xy} \tag{17}$$

$$\begin{bmatrix} g(0) \\ g(1) \\ \vdots \\ g(S) \end{bmatrix} = R_{xx}^{-1} \begin{bmatrix} r_{xy}(0) \\ r_{xy}(1) \\ \vdots \\ r_{xy}(S) \end{bmatrix} \tag{18}$$

For the sampled signals $x[k]$ and $y[k]$, the amplifier acts as an all pass filter. The amplifier will distort the shape of the pulse, meaning that the complex gain changes slightly thorough the pulse progression (intrapulse distortion). However, the interest in this investigation is to characterize the difference between consecutive pulses (interpulse distortion). Therefore, the amplifier's transfer function is treated as a single complex gain coefficient as shown in equation (3). This means that the size of the filter $g$ is only one tap; $g = g(0)$.

The autocorrelation matrix is then simplified to $R_{xx} = r_{xx}(0)$. The matrix system is then reduced to:

$$g(0) = \frac{r_{xy}(0)}{r_{xx}(0)} \tag{19}$$

### 3.2.5 Amplifier Gain and Phase Insertion

The results from equation (19) state that we only need to calculate $r_{xx}(0)$ and $r_{xy}(0)$ to calculate the mean complex gain of the amplifier over a pulse. Thus, the sample autocorrelation is reduced to equation (20) and the sample cross-correlation is reduced to equation (21):

$$r_{xx}(0) = A_x^2 \tag{20}$$

$$r_{xy}(0) = A_x A_y \exp\left(j\left(\phi_x - \phi_y\right)\right) \tag{21}$$

The filter coefficient $g(0)$ is calculated to be:

$$g(0) = \frac{A_y}{A_x} \exp\left( j\left(\phi_x - \phi_y\right)\right) \tag{22}$$

Recalling the amplifier complex gain in equation (3), the amplifier complex gain is the complex conjugate of $g(0)$:

$$G = \frac{A_y}{A_x} \exp\left( j\left(\phi_y - \phi_x\right)\right) = g^*(0) \tag{23}$$

$$\text{G} = \frac{r_{xy}^*(0)}{r_{xx}(0)} \tag{24}$$

Recalling equation (4), the amplifier scalar gain in decibels is then found by evaluating equation (25):

$$G_{dB} = 20Log_{10}\left|\frac{r_{xy}^*(0)}{r_{xx}(0)}\right| \tag{25}$$

Recalling equation (5), the amplifier phase insertion in degrees is then found by evaluating equation (26):

$$G_{\text{deg}} = -\frac{180}{\pi} Arg\left(r_{xy}(0)\right) \tag{26}$$

## 3.3 Analysis of Amplifier Behavior

The result from the cross-correlation method is the conjugate of a single filter coefficient $g^*(0)$ for each pulse in the WOI. The complex number $g^*(0)$ contains information about the amplifier's average scalar gain and insertion phase during a processed pulse. The amplifier behavior is then expressed as the change in scalar gain and insertion phase over the WOI

duration. Each computed $g^*(0)$ must be indexed to a pulse within in the WOI. Thus, for a WOI that contains N pulses, the complex gain $g^*(0)$ is indexed as follows:

$$G_{CC}(n) = \frac{r_{xy}^*(0,n)}{r_{xx}(0,n)} \tag{27}$$

where $G_{CC}(n)$ in the indexed complex gain $g^*(0)$ of the $n^{th}$ pulse in a the WOI. $r_{xx}(0,n)$ is the autocorrelation of the $n^{th}$ pulse in the WOI, and $r_{xy}^*(0,n)$ is the cross-correlation of the $n^{th}$ pulse.

With proper calibration and scaling, $g^*(0)$ results in the actual amplifier gain and insertion phase. The actual value of $g^*(0)$ will change depending on the frequency of operation and device flange temperature, making it difficult to visualize the amplifier behavior. This is overcome by normalizing the gain and applying a phase offset to the insertion phase. The first pulse in the $G_{CC}(n)$ response is used as reference. The normalized indexed amplitude is defined by equation (28), while the zeroed insertion phase is defined by equation (29).

$$A[n] = \left| \frac{G_{CC}(n)}{G_{CC}(1)} \right| \tag{28}$$

$$\phi[n] = Arg\left(G_{CC}(n)\right) - Arg\left(G_{CC}(1)\right) \tag{29}$$

Both the normalized gain $A[n]$ and zeroed insertion phase $\phi[n]$ can show trends across the duration of the WOI. The interpretation of $A[n]$ can have various equivalent meanings. By definition $A[n]$ is interpreted as a change in voltage gain. However, since the input signal has constant envelope from pulse to pulse, $A[n]$ can also be interpreted as a change in output power. The zeroed insertion phase $\phi[n]$, can only be interpreted as the change in the insertion phase. However, the insertion phase can be seen as a stretching effect in a transmission line, where a negative insertion phase implies the line is getting longer, or vice versa.

Throughout this research, the amplifier behavior is described to have an amplitude transient and a phase transient. The amplitude transient is defined as the normalized gain $A[n]$. The phase transient is defined as the zeroed insertion phase $\phi[n]$. The amplifier behavior is better appreciated in graphical form. The amplitude transient $A[n]$ is expressed in decibels as $20Log_{10}(A[n])$. The phase transient is expressed in degrees as $\phi[n]\times 180 \div \pi$.

Figures 3-6 and 3-7 shows an example of amplifier's behavior. Chapter 5 will cover in greater length the meaning and significance of these figures. Figure 3-6 illustrates the changes in scalar gain as a function of time. The abscissa corresponds to time, indexed at increments of the WOI Pulse Repetition Interval (PRI). The ordinate corresponds to the change in amplifier scalar gain in decibels. Notice that the first data point in normalized, the first gain calculation from the Wiener-Hopf method is used as reference. Each dot in the graph represents the change in amplifier's scalar gain experience by the amplifier over the duration of the WOI.

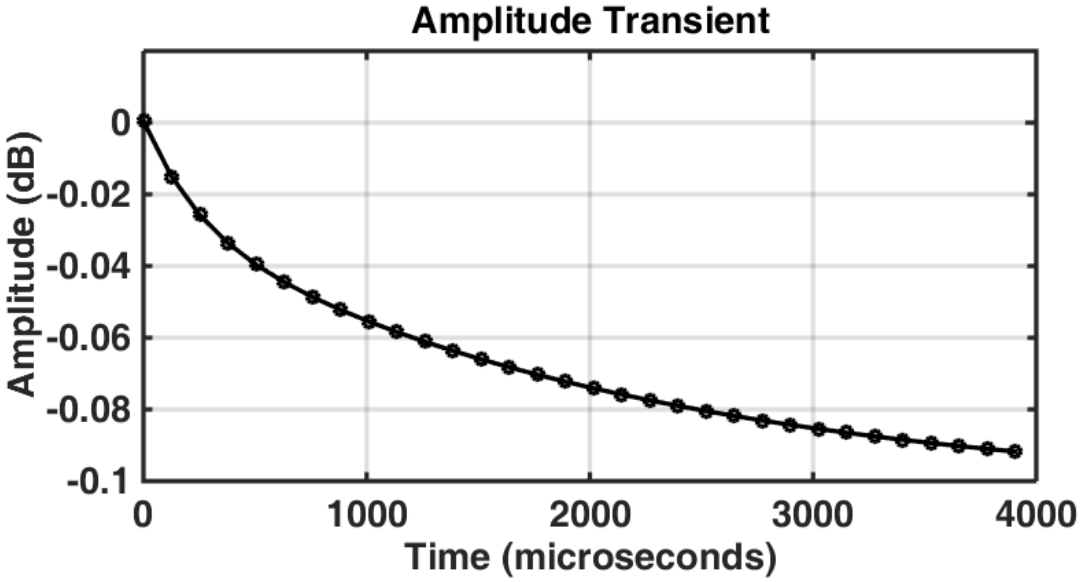


Figure 3-6: Example of amplifier behavior showing amplitude transient. The gain of the amplifier reduces over the duration of a CPI. Each data point represents a change in scalar gain, indexed at increments of the waveform's PRI.

Figure 3-7 illustrates the changes in insertion phase as a function of time. The abscissa corresponds to time, indexed at increments of the WOI Pulse Repetition Interval (PRI). The ordinate corresponds to the change in amplifier insertion phase. Each dot in the graph represents the change in amplifier's insertion phase.

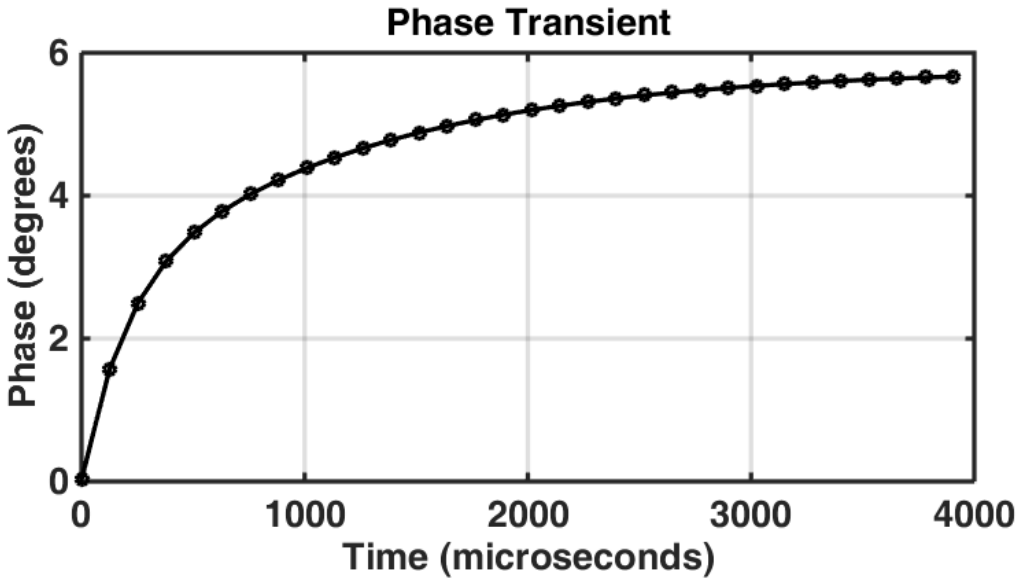


Figure 3-7: Example of amplifier behavior showing phase transient. The insertion phase of the amplifier increases over the duration of a CPI. Each data point represents a change in insertion phase, indexed at increments of the waveform's PRI.

### 3.3.1 Developed Algorithm

Figure 3-8 shows a flow diagram of the algorithm used to characterize the amplifier. A multifunction waveform-pair, selected from a WLF, is transmitted to the DUT. A select portion of this signals is used as the reference. The reference signal and a select portion of the amplified signal are sampled and digitized. Both signals are then digitally downconverted into baseband I/Q components. The Wiener-Hopf method (cross-correlation) is performed on the signals. The results are identified and indexed to its corresponding position within the CPI. The complex data

in each indexed peak can be further segregated into amplitude and phase, thus characterizing any pulse-to-pulse change in the DUT's complex gain.

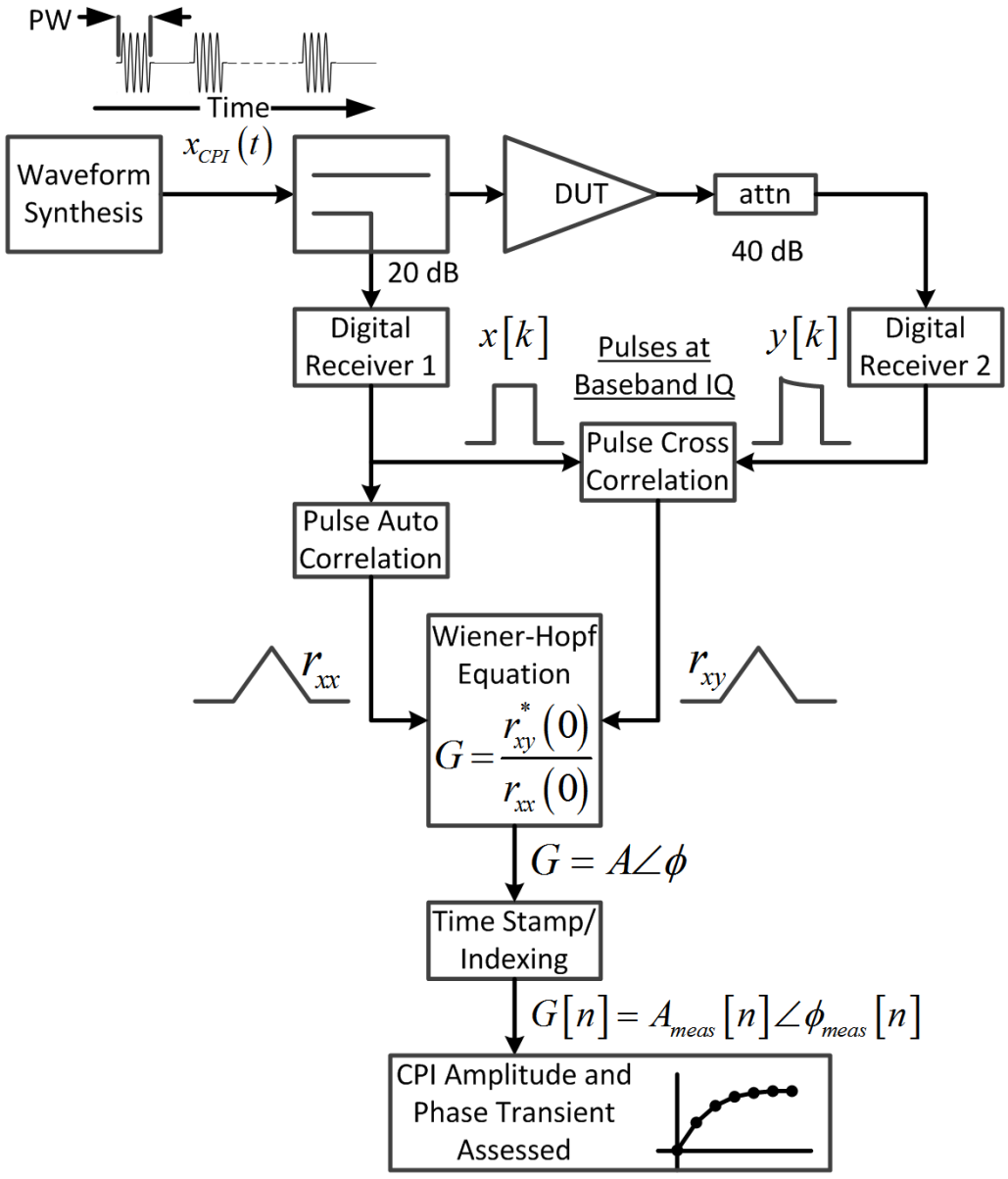


Figure 3-8: Block Diagram of Cross-Correlation Technique. Used as System Identification Tool.

## 3.4 Radar System Instability

The observed amplitude and phase transients are detrimental to radar system performance. This work uses an MTI single pulse canceller as the performance metric for evaluating the severity of the transients and to determining the effectiveness of predistortion implementation.

This dissertation uses an MTI single pulse canceller and a Root Mean Square (RMS) Pulse-to-Pulse (P2P) method as the performance metrics for evaluating the severity of the transients and for determining the effectiveness of predistortion implementation. These two metrics are used to visualize different aspect of the observed transients. The MTI method is helpful in characterizing the stability of adjacent pulses. The RMS P2P method is helpful in assessing the impact of individual pulses in the overall waveform stability.

### 3.4.1 MTI Improvement Factor

MTI Instability Limitation equations [78] are used to calculate the clutter improvement limitations. The limitations in MTI Improvement Factor due to pulse amplitude and phase changes are given by (30) and (31):

$$I = 20 \log_{10} \left( \left| \frac{A}{\Delta A} \right| \right) \tag{30}$$

$$I = 20 \log_{10} \left( \left| \frac{1}{\Delta \phi} \right| \right) \tag{31}$$

where $I$ is the limitation in MTI Improvement Factor given in decibels, $A$ is the pulse amplitude in volts, $\Delta A$ is the interpulse amplitude change also in volts, and $\Delta \phi$ is the interpulse phase change in radians per second. Combining (30) and (31) into vector form and replacing $A$ for $A[n]$ and $\phi$ for $\phi[n]$, is equivalent to an MTI two-pulse canceller given by:

$$IF\,[n] = -20\,Log_{10}\left(\left|A[n]\,e^{(i\phi[n])} - A[n-1]\,e^{(i\phi[n-1])}\right|\right) \qquad (32)$$

where $IF[n]$ is the MTI Improvement Factor (or cancellation ratio) of two adjacent pulses, $n$ is the index of the pulse within a CPI, $A[n]$ is the amplitude (volts), and $\phi[n]$ is the insertion phase (radians per second) of the $n^{th}$ pulse in a CPI.

### 3.4.2 MTI Improvement Factor Performance Contour

From equation (32), it is clear that the MTI Improvement Factor has dependencies in amplitude and phase. For a given amplitude instability, there is a phase instability that will result in identical MTI Improvement Factor coefficient. Figure 3-9 shows a contour plot for the MTI Improvement Factor, showing a relationship between amplitude instability and phase instability.

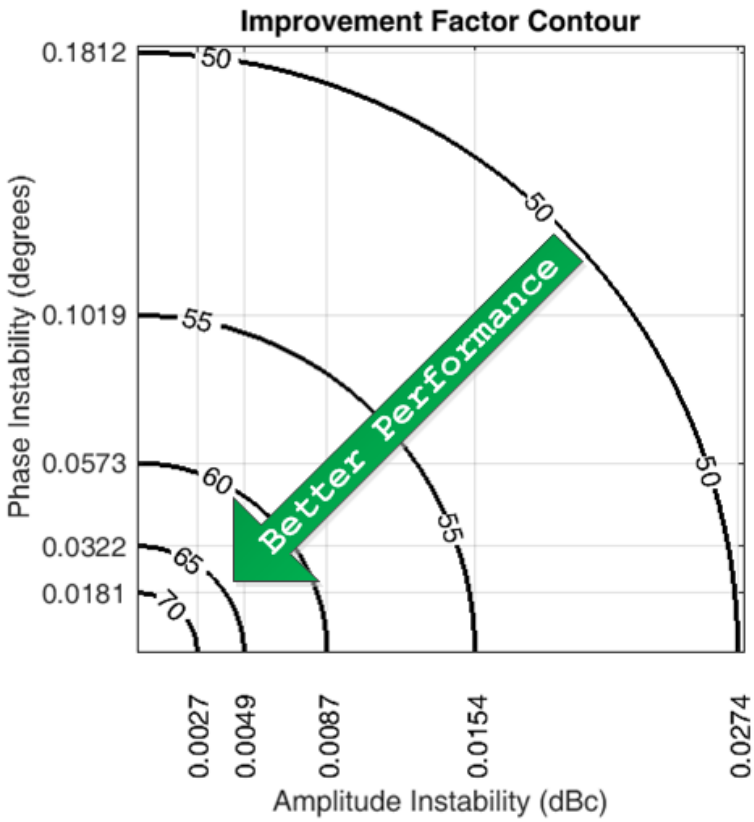


Figure 3-9: MTI Improvement Factor Contour. The contour shows a relationship between the amplitude instability and the phase instability. Better radar performance is achieved by reducing the systems instabilities. A larger value of Improvement Factor indicates better performance.

Taking as an example an MTI Improvement Factor of 55 dB; an amplitude instability of 0.015 dBc is equivalent to a phase instability of 0.1 degrees. The contour can help determine which instability, amplitude or phase, is more detrimental to radar performance. The smaller the instabilities, the better the radar will perform in cancelling stationary clutter. The actual system performance depends on many system-specific parameters, weather conditions, and the type of target among other thing.

For this dissertation, a threshold of 53 dB in MTI Improvement Factor is assumed, where an MTI Improvement Factor greater than 53 dB, calculated via equation (32), means that the

system has enough stability to operate. This value is typical of the MTI Improvement Factor achievable by air surveillance radar with rotating antennas. The pulse-to-pulse system stability requirement in this instance is better than 0.019 dBc or 0.128 degrees. If these two uncertainties are present at the same time, the improvement will be less than 53 dB. Thus to guarantee that the combined values meets the 53 dB requirements, the required pulse-to-pulse system stability requirement needs to be better than 0.007 dBc and 0.091 degrees.

### 3.4.3 MTI Improvement Factor vs. SNR

The previous subsection established a relationship between the amplitude and phase instability and MTI Improvement Factor given that the amplitude and phase instabilities are calculated from the derivative of the amplifier's amplitude $A[n]$ and phase $\phi[n]$ transients. The resulting MTI Improvement Factor is influenced by noise. It is therefore of interest to determine the relationship between SNR and MTI Improvement Factor. However, there are several processing techniques used in between the initial data capture of $x[k]$ and $y[k]$ and the resulting amplitude $A[n]$ and phase $\phi[n]$ transients. Each processing stage improves upon the initial SNR; refer to Chapter 5 for additional details.

For a noiseless process, the signal $A[n]\exp(i\phi[n])$ has an amplitude $A[n]$ equal to one and a phase $\phi[n]$ equal to zero. A simulation was conducted to illustrate the relationship between MTI Improvement Factor and SNR. The simulation was limited to changing the SNR of $A[n]$ as follows:

$$A[n] = 1 + \hat{N}[n] \tag{33}$$

where $\hat{N}$ is a complex random variable with a Gaussian probability function (circularly-symmetric complex normal), with variance $\sigma^2 = 10^{-SNR/10}$ and zero mean. The first two operations within equation (32) take the absolute of the difference between two adjacent signal

values. The probability distribution function is now a Rayleigh distribution, with variance equal to:

$$\sigma^2 \frac{4-\pi}{2} \tag{34}$$

and mean equal to:

$$\sigma\sqrt{\frac{\pi}{2}} \tag{35}$$

The resulting MTI Improvement Factor has a logarithmic Rayleigh distribution. Assuming no system noise or instabilities, the ideal value of $G_{CC}(n) = 1 \forall n$. This makes the ideal Improvement Factor infinite. Because digitized signals are corrupted by system noise the MTI Improvement Factor will therefore be limited. For a given SNR, the MTI Improvement Factor adopts a mean value:

$$IF = -20\, Log_{10}\left(\sigma\sqrt{\frac{\pi}{2}}\right) = SNR - 2\ dB \tag{36}$$

Figure 3-10 shows an error bar graph of the limit in the MTI Improvement Factor as a function of SNR. The bar shows the values of the MTI Improvement Factor with a confidence interval of 68.2%, where the *IF* is between +5.4 dB and -4.4 dB from the mean. The asymmetry is due to the Rayleigh probability distribution function.

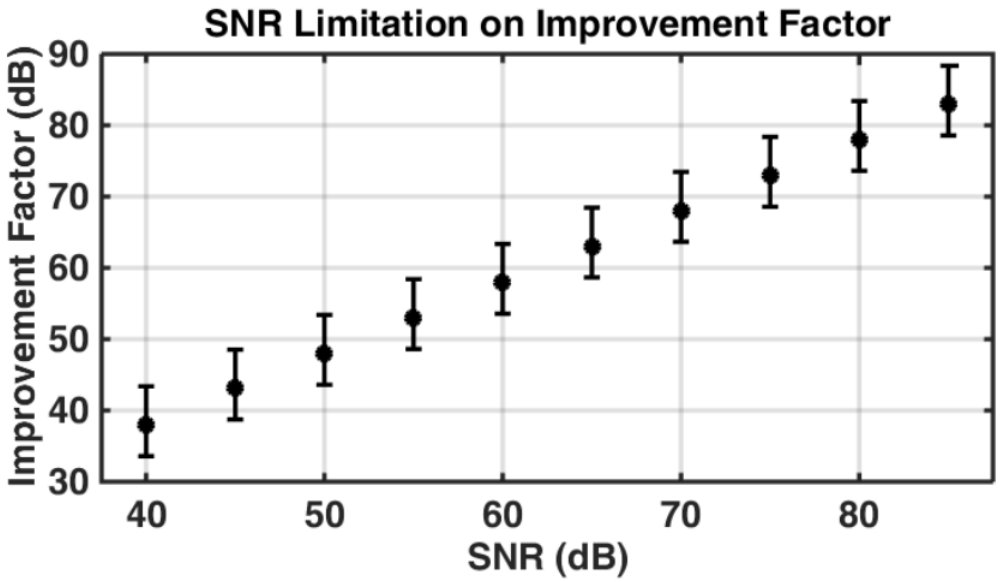


Figure 3-10: Limit in MTI Improvement Factor due to system SNR after cross correlation.

### 3.4.4 Accuracy of MTI Improvement Factor Measurement vs. SNR

The MTI Improvement Factor quantifies the residual power after subtracting two consecutive pulses. Equation (36) showed that for two consecutive pulses that are identical, their SNR limits their MTI Improvement Factor. The amplitude and phase transients are always asymptotically stable for the duration of a CPI; they decrease over time. Thus, as the transients reduce over time, the MTI Improvement Factor transitions from the limit imposed by the interpulse instability to the limits due to the SNR. The influence of the SNR over a measured MTI Improvement Factor was quantified with a simulation. In this instance, the signal $A[n]$ is constructed such that its ideal MTI Improvement Factor increases over time, from 30 dB to 85 dB.

The noise variance was set to achieve an SNR of 72 dB. This will set the SNR limit in MTI Improvement Factor to a mean value of 70 dB. As the signal progresses in time, its power residue due to instabilities decreases, but the residue due to noise remains (on average) the same. Eventually the residual noise will dominate, and no further Improvement Factor will be possible.

Figure 3-11 shows the simulation results. The red line (Ideal) shows the ideal MTI Improvement Factor increasing from 30 dB to 85 dB. The light blue line (IF) shows the simulated MTI Improvement Factor for the noisy signal. Its MTI Improvement Factor increases earlier in the simulation, but it plateaus later as it becomes influenced by noise. The black line (Mean) shows the mean value of (IF), limited to 70 dB as predicted by equation (36). The purple line (Upper 34.1 %) and the dark blue line (Lower 34.1 %) shows the boundaries of MTI Improvement Factor, where 68.2 % of the values for the MTI Improvement Factor are between the upper and lower bound.

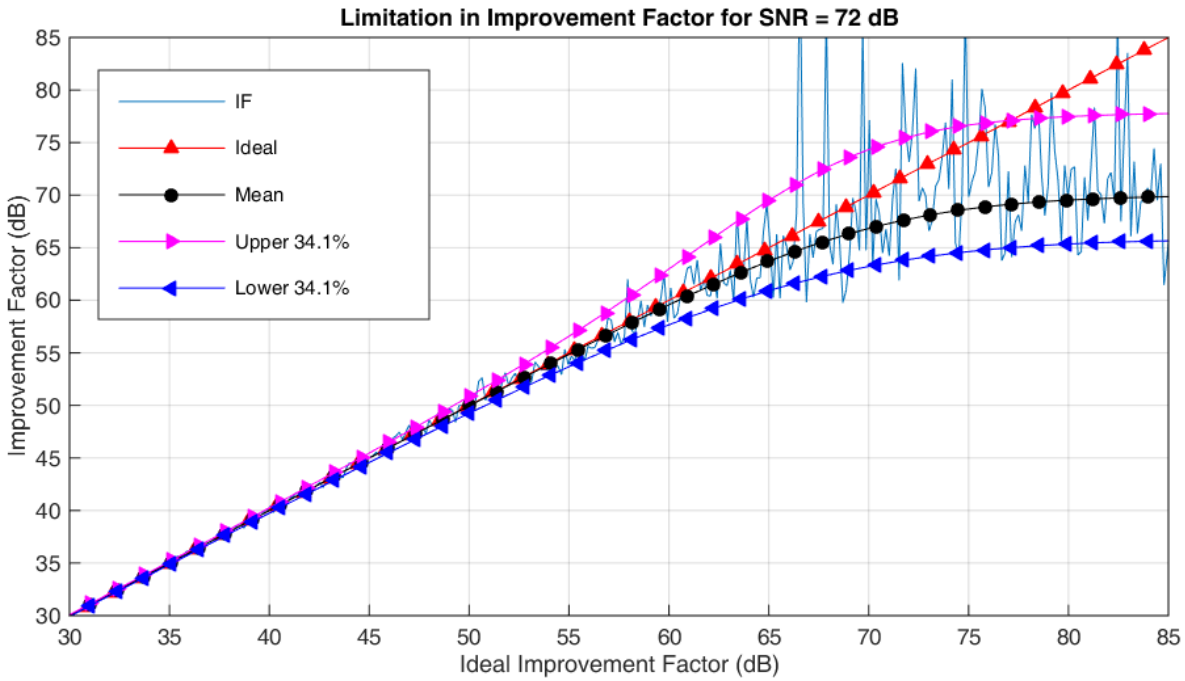


Figure 3-11: Effect of SNR on MTI Improvement Factor. The ideal MTI Improvement Factor is limited by noise.

Low values of Improvement Factor have a small deviation from the ideal value. As the Improvement Factor increases the deviation increases as well. For example, at a time where the ideal Improvement Factor is 52 dB, the measured value is expected to be 52 dB ± 1.0 dB. The graph clearly shows that the accuracy and precision of an MTI Improvement Factor measurement is impacted by the SNR.

A valid MTI Improvement Factor measurement requires an SNR several decibels above the expected Improvement Factor. Table 3-2 shows simulation results indicating the required SNR for a desired Improvement Factor precision. If an Improvement Factor measurement requires a precision of ± 1.0 dB or better, then the SNR must be at least 20 dB higher than the intended target Improvement Factor.

Table 3-2: Measurement Precision for MTI Improvement Factor measurement due to SNR.

| Excess SNR (dB): | Precision (dB): |
|---|---|
| 10 | ± 3.4 |
| 20 | ± 1.0 |
| 30 | ± 0.3 |
| 40 | ± 0.1 |

### 3.4.5 Root Mean Square Method to Quantify Pulse-to-Pulse Stability of a Radar Transmitter

Another important metric used to evaluate the pulse-to-pulse stability of radar system is referred to as the Root Mean Square [17, 79, 80]. In this method, the stability is calculated from the mean square error between successive pulses in a CPI (or pulse train burst).

Similar to the MTI Improvement Factor discussed above, the RMS method quantifies variations between consecutive pulses in a CPI. However, there are three main differences:

1) Whereas in the MTI method, the pulses are pulse-compressed following conventional radar processing techniques, the RMS method compares the entire pulse envelope

2) On the MTI method the stability for each consecutive pulse-pair is quantified separately, but on the RMS method the results is a combination of all of the pulses in the CPI.

3) The RMS method cannot utilize the pulse compression processing gain. Thus to improving the result accuracy requires additional data averaging.

The equations for pulse-to-pulse amplitude and phase stability [80] are below:

-Amplitude stability in dB:

$$S_A = -10 \times \log\left( \frac{\frac{1}{N-1}\sum_{n=1}^{N-1}\left(X_{n+1} - X_n\right)^2}{\bar{X}^2} \right) \tag{37}$$

$$\bar{X} = \frac{1}{N}\sum_{n=1}^{N} X_n \tag{38}$$

-Phase stability in dB:

$$S_\Phi = -10 \times \log\left( \frac{1}{N-1}\sum_{n=1}^{N-1}\left(\Phi_{n+1} - \Phi_n\right)^2 \right) \tag{39}$$

where, $S_A$ is the amplitude stability expressed in decibels, $S_\Phi$ is the phase stability expressed in decibels, $X_n$ is the pulse amplitude envelope for the $n^{th}$ pulse in the CPI with $N$ pulses, $\bar{X}$ is the average of all the pulses in a pulse train burst with $N$ pulses, and $\Phi_n$ is the pulse phase envelope in radians.

Phase is usually measured in degrees or radians, however, phase stability in expressed in decibels. The phase stability metric $S_\Phi$ uses the signal's phase envelope to compute differences between consecutive pulses. In the case of the amplitude stability, the amplitude is normalized by $\bar{X}^2$. The phase stability is not normalized; however, the range of phase differences between any two pulses is bounded to $\leq |2\pi|$.

## 3.5 Number of Observations to Achieve Desired Measurement Precision

The PA test set-up captures and processes the entire CPI. Each captured pulse is stored in memory for processing. The system measures minute changes in the DUT's complex gain that occur during the CPI. The differences in the DUT's complex gain observed were small; gain changes of 0.1% and phase changes of 0.05 electrical degrees had to be measured accurately. The system identification and analysis relies on being able to quantify small changes in the output signal $y[k]$ from one pulse to another. A desired SNR is one that will allow for the reliable measurement of the amplitude and phase that occurs in $y[k]$. The previous section showed that the SNR needed to measure the MTI Improvement Factor of 53 dB ± 1 dB is 73 dB. This translates to a required measurement precision of 0.002 dB in amplitude transient $A[n]$, and 0.013 degrees in insertion phase transient $\phi[n]$.

The SNR for the baseband I/Q domain signals $x[k]$ and $y[k]$ is approximately 48 dB. This is due to limitations in the surrogate Digital Receiver. Refer to Chapter 5 for more details. The deficit of 25 dB in SNR is overcome via cross-correlation and by averaging multiple data sets. The cross-correlation is expected to improve the SNR by at least 16 dB, improving $A[n]$ and $\phi[n]$ SNRs to 64 dB. The additional gain of nine decibels is obtained from averaging multiple observations.

The work done in [81] is used to determine the number of observations or data collections necessary to achieve the desired degree of precision in the amplitude and phase measurement. For large SNR and assuming a Gaussian distributed noise, the Cramer-Rao lower bound for the error in measuring signal magnitude and phase is simplified to the expressions in equations (40) and (41) respectively:

$$\sigma_A^2 = \frac{1}{N}\frac{A_0^2}{R_{SNR}} \tag{40}$$

$$\sigma_{\phi}^2 = \frac{1}{N}\frac{1}{R_{SNR}} rad^2 \tag{41}$$

where, $\sigma_A$ is the amplitude precision in volts, $A_0$ is the signal amplitude, $\sigma_{\phi}$ is the angular precision in radians per second, $N$ is the number of observations, and $R_{SNR}$ is the SNR for one observation.

$$R_{SNR} = 10^{64/10} = 2.5\times10^6 \tag{42}$$

Assuming $A_0 = 1$ and substituting known values on equation (40) yields:

$$\sigma_{Adb} = 20\log_{10}(1+\sigma_A) = 0.002\,dB \tag{43}$$

$$\sigma_A^2 = 5.3\times10^{-8} \tag{44}$$

$$N = \left\lceil \frac{A_0^2}{\sigma_A^2 R_{SNR}} \right\rceil = \left\lceil \frac{1}{(5.3\times10^{-8})\times(2.5\times10^6)} \right\rceil = 8 \tag{45}$$

Substituting $\sigma_{\phi}^2$ and $R_{SNR}$ in equation (41) yields:

$$\sigma_{\phi}^2 = \left(0.013\frac{\pi}{180}\right)^2 = 5.15\times10^{-8} \tag{46}$$

$$N = \left\lceil \frac{1}{\sigma_{\phi}^2 R_{SNR}} \right\rceil = \left\lceil \frac{1}{(5.2\times10^{-8})\times(2.5\times10^6)} \right\rceil = 8 \tag{47}$$

Table 3-3 summarize the results. The SNR after cross-correlation processing gain of 64 dB in not sufficient to provide the required precision. Al least eight captures (observations) are averaged to improve the SNR by 9 dB for a total of 73 dB. The processing gain achieved by integrating the coherent data captures is $10\log_{10}(N)$, where $N$ is the number of observations.

Table 3-3: Number of Observations for required Measurement Precision

| Parameter Description: | Value: |
|---|---|
| Initial SNR (Baseband I/Q) | 48 dB |
| Required amplitude precision | 0.002 dB |
| Required phase precision | 0.013 degrees |
| Cross-correlation processing gain | 16 dB |
| SNR after cross-correlation | 64 dB |
| Addition processing gain required | 9 dB |
| Number of observations | 8 |
| SNR after multiple observations | 73 dB |

## 3.6 Chapter Summary

The chapter put forward the concept of multifunction operations and explained how it can be exercised in a controlled manner. The amplifier characterization is accomplished by the use of the Wiener-Hopf equation as system identification tool, as well as utilizing signal processing techniques that are ubiquitous in modern radar systems. The MTI performance metric was introduced as a way to assess the system instability. The expected performance of the measurement system when system noise is present was examined in order to understand the required conditions to acquire valid measurements.

# Chapter 4. Overview of Power Amplifier Test Set-up

The objective of this chapter is to present an overview of the hardware and software designed to conduct the experiment. The experiment complexity emerges from the desired functionalities to: 1) replicate multifunction radar operations, 2) capture RF and DC signal for analysis, 3) capture supplementary data to document and replicate experiment, and 4) provide a mechanism for predistortion implementation.

Typical amplifier performance parameters, such as gain and 1 dB compression point are measured using a Vector Network Analyzer (VNA). VNAs measure complex (magnitude and phase) reflection and transmission coefficients; these are expressed as scattering parameters (S-parameters). The amplifier gain is given by the transmission coefficient $S_{21}$. To measure $S_{21}$, a signal is injected at port 1, and the resulting signal is measured at exiting port 2. Their relationship is shown in equation (48):

$$\mathrm{S}_{21} = \frac{b2}{a1} \tag{48}$$

where $S_{21}$ is the ratio of the voltage leaving port 2 ($b2$) over the incident voltage into port 1 ($a1$).

Some VNAs are capable of measuring the amplifier gain under pulsed conditions. However, for any given measurement, the pulse width and duty cycle is fixed. Their pulsing circuitry and data acquisition architecture does not support the transmission of multifunction radar waveforms. They cannot dynamically change waveforms. Therefore, it is not possible to observe these conditions using a typical Vector Network Analyzer (VNA).

The Power Amplifier (PA) test set-up was developed [15] to stimulate the PA with representative multifunction radar waveforms. The measured parameters are analogous to the $S_{21}$ scattering parameter in that both of the amplifier's input and output signals are digitally captured for analysis. This allows for the pulse amplitude and phase to be measured, and thus the amplifier complex gain can be assessed. The data capture contains and preserves a large instantaneous bandwidth; this is not available from conventional VNAs.

The PA test set-up was designed to respond similarly to a Digital Array Radar (DAR), where multiple independent channels are used to transmit and receive. However, data processing is done in non-real-time after data collection. Four receive channels and two transmit channels (exciters) were implemented. The hardware was designed to allow for the characterization of two amplifiers simultaneously, while being submitted to representative multifunction radar conditions. In addition, since each exciter can transmit a different waveform, this allows for the implementation and validation of predistortion.

There are two unique aspects about the test setup, the Scheduler and the Waveform of Interest (WOI):

1. The Scheduler: interleaves groups of pulses configured to form coherent processing intervals, mimicking notional multifunction radar conditions. A wide variety of waveforms can be added to the scheduler. Each waveform has its own modulation, bandwidth, pulse width, duty cycle and number of pulses.
2. The Waveform of Interest: defines the specific CPI in a set of multiple CPIs that is being implemented by the Scheduler whose data is captured for subsequent analysis. It is unique because the WOI will be instantiated N times, where N is the number of pulses in the CPI, instead of being repeated. This enables the predistortion of each pulse to be synthetized independently, a feature later used for the development of a predistortion algorithm explained it Chapter 7.

Multiple instruments and hardware were used in conjunction with custom design hardware. The complexity of the test setup required extensive software development to automate instrumentation, and to manage data capture and data analysis. It required the extensive creation and use of classes (object-oriented programming) and instrument drivers. The logistics of managing the instrumentation, scheduling multifunction waveforms, data capture and data storage, necessitated the development of a Graphical User Interface (GUI). All of the software was developed within the MATLAB™ environment.

## 4.1 Hardware Design and Functionality

After the initial design of the PA test set-up in 2012 [15], several improvements were made, including an enhanced digital receiver for greater instantaneous dynamic range; a faster data capture download capability; additional analog band pass filtering; digitization of the drain voltage and current waveforms; and easier data manipulation, processing, and analysis. Figure 4-1 shows a block diagram of the experiment implementation.

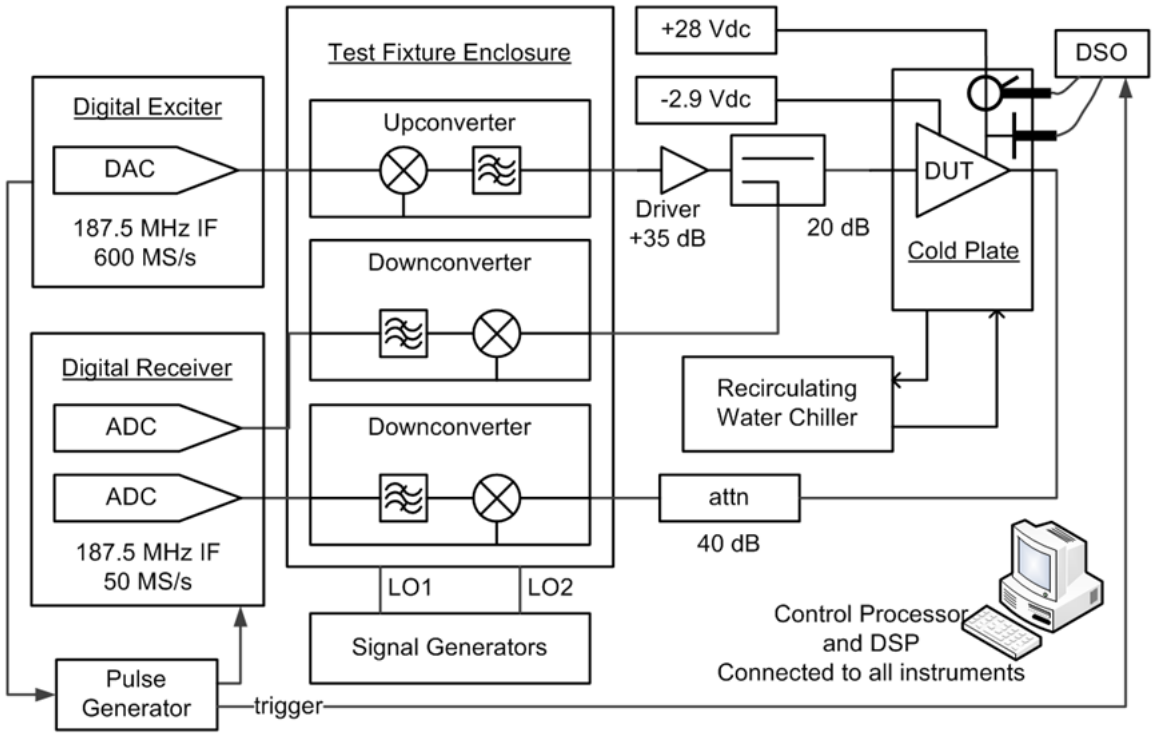


Figure 4-1: Block diagram of PA test set-up, shown configured to characterize a single amplifier.

The next subsections will briefly describe each of the instruments used to conduct the experiment, as well as custom-made hardware and supporting equipment. Refer to Appendix B for more information about the design and instrument selection. Figure 4-2 shows a picture of the hardware setup.

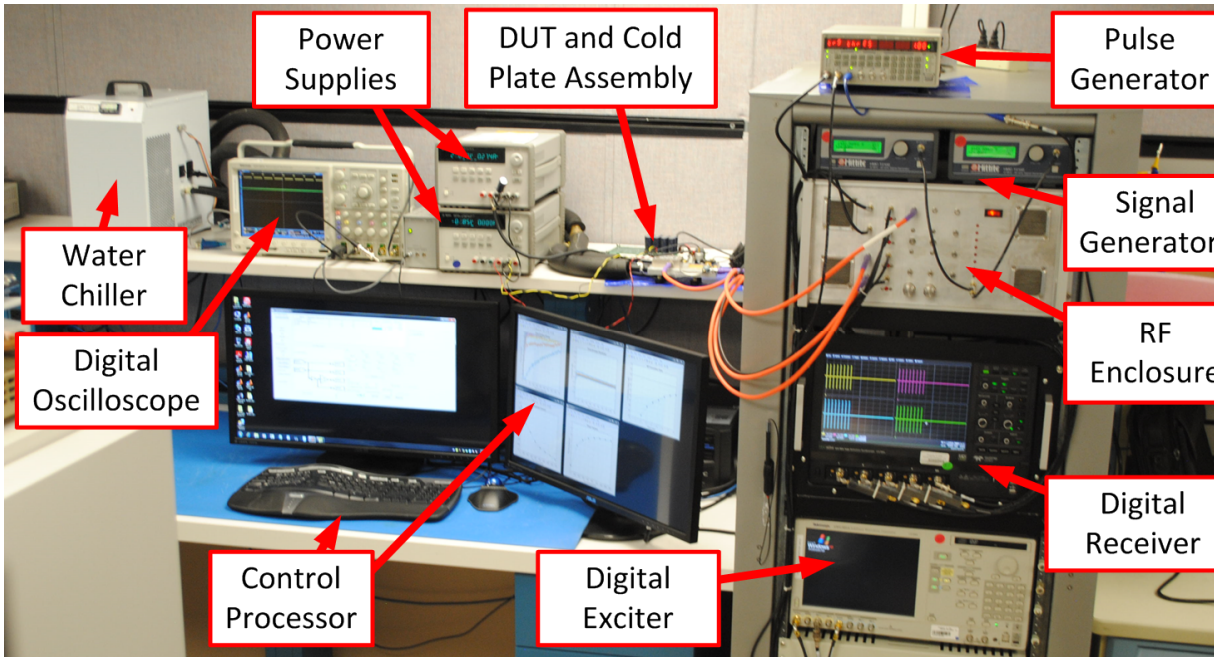


Figure 4-2: Photo of instrumentation used to build the PA test Fixture.

### 4.1.1 Control Processor and Digital Signal Processing (DSP):

The Control Processor is an industrial rack mounted personal computer running MATLAB™. All the functionality necessary to reproduce radar waveform, capture data and process the amplifier response was programmed into the Control Processor. It controls all the equipment and instrumentation via a GUI. The information required to construct the waveforms is stored in a Waveform Library File (WLF). The Control Processor synthesizes waveforms based on the specifications listed in the WLF. The GUI facilitates the creation of waveform sequences (including multifunction sequences), from the WLF. The Control Processor configures the instruments for data capture. The data is later transferred to the Control Processor for analysis and display. The Control Processor is also used to parameter fit the behavioral model, discussed in Chapter 6, and compute coefficients for predistortion, discussed in Chapter 7.

### 4.1.2 Radar Digital Exciter:

A Tektronix AWG5012 Arbitrary Waveform Generator (AWG) is used as a surrogate Radar Digital Exciter. The Radar Digital Exciter generates the radar waveforms synthesized and scheduled by the Control Processor. This instrument allows for the creation of pulses with arbitrary characteristics. This is a necessary feature for the envisioned predistortion technique that was developed to mitigate interpulse distortion. The analog outputs were designed to have an IF of 187.5 MHz. In addition, the instrument provides two digital outputs per analog channel. These are used to mark the beginning of a WOI, and as an amplifier enable signal.

### 4.1.3 Pulse Generator

A Stanford Research Systems Model DG645 Digital Delay Generator is used to coordinate the data capture trigger pulses. The instrument receives a marker signal from the Radar Digital Exciter indicating the beginning of a WOI. During data capture operations, the Control Processor configures the pulse generator to create a trigger pulse that is synchronized with the received marker signal. The trigger pulse is sent to the Digital Receiver and DC Bias Signaling Digitizer to initiate a capture.

### 4.1.4 RF Enclosure

Implementing the experiment requires at least the capture of a reference signal and the amplified signal. In practice, the signals needs to be frequency translated and conditioned for proper operation and data capture. These include gain adjustment to provide appropriate power level at the input to the amplifier under test as well as to maximize the available SNR for the digital receiver. In addition, a RF signal calibration path is used to by-pass the amplifier, and demonstrates that the observed amplitude and phase transients originate in the amplifier. The RF enclosure also includes mechanisms to implement and validate predistortion, refer to Appendix B for additional details.

#### 4.1.4.1 Up/Down-Converter Design

The operational frequency band chosen for this research was from 2.9 GHz to 3.4 GHz. This was due primarily to the availability of amplifiers designed to operate in that frequency range. Based on hardware limitations and an iterative design approach, the selected IF for the Radar Digital Exciter and the Radar Digital Receiver was set to 187.5 MHz. The design follows a dual stage superheterodyne architecture, with an instantaneous bandwidth of 150 MHz.

The first stage of the upconverter translates the signal generated by the Radar Exciter centered at 187.5 MHz to 1245 MHz, using a Local Oscillator (LO) tuned at 1435 MHz. The second stage, translate the signal at 1245 MHz to a selected frequency within the frequency band of operation. This stage LO is tuned within the frequency range of 4145 to 4645 MHz. The data presented in this dissertation was captured at 3200 MHz, unless otherwise noted. Conversely, the downconverter is the counter part of the upconverter.

#### 4.1.4.2 Switch Matrix

The Switch Matrix is a key part in the experiment implementation. It performs three RF signaling routing functions without physically perturbing the amplifier being tested. The Switch Matrix is used to route RF signals into the DUT and out to the 4-channel Radar Digital Receiver. The signal routing is controlled via mechanical RF switches, that are actuated by a Digital Interface card controlled over a USB. Chapter 7 will discuss in more detail the predistortion mechanism. The routing functions are listed below:

1) Calibration: where all of the signals are keep within the RF enclosure.

2) Amplifier testing and characterization: where signals are sent and received from the DUT.

3) Predistortion Implementation and Validation: where the Digital Exciter channels are swapped before their signals are routed to the DUTs. This mode is only valid if

predistortion coefficients were applied to the WOI; otherwise it will behave identically to the Characterization mode.

### 4.1.5 Radar Receiver

A four-channel Digital Storage Oscilloscope (DSO) is used as a surrogate Radar Digital Receiver. Initially a Tektronix DSO4034 oscilloscope was used as surrogate digital receiver. It was later replaced with a Teledyne-LeCroy HDO6054 digital oscilloscope in favor of improved vertical resolution and faster data download.

The Radar Digital Receiver digitizes signals after the down-converters. The instantaneous bandwidth of the downconverters was designed to support 150 MHz waveforms. To reduce the noise power present at the receiver input, the analog bandwidth was reduced to 20 MHz via band pass filters. All waveform signals are at a nominal Intermediate Frequency (IF) of 187.5 MHz and are digitized at a sampling rate of 50 mega samples per second. The resulting digital IF is 12.5 MHz. Digital Downconvertion (DDC) is later used to translate the digital IF into In-phase (I) and quadrature (Q) components.

### 4.1.6 DC Bias Signaling Digitizer

A Tektronix DSO4034 oscilloscope is equipped with an Agilent N2783A current probe to digitize the DUT's drain current waveform. The drain current waveform contains high frequency components due to the pulse signal's short rise and fall time, and ringing. The drain voltage waveform is also digitized. The two waveforms for $I_D$ and $V_D$ are saved along with the digitized RF waveforms. With the drain current and drain voltage, the DUT's power draw is approximated. The results are later used to compute the Power Added Efficiency (PAE).

### 4.1.7 Hardware Design Summary

The Control Processor synthesizes waveforms according to the specifications in the WLF. These waveforms are uploaded into the Digital Exciter (AWG) for scheduling and

transmission. The output of the Digital Exciter is frequency translated by the Up Converter into the RF band. There the signal is routed to multiple places. Some of the signals are sent directly to the Down Converters, others are routed to the Device Under Test. The amplifier output is routed into the Down Converters. A Digital Receiver digitizes the output after the down-converters. The four digital signals are transfered from the Digital Receiver Memory to the Control Processor, where they are stored for processing.

## 4.2 Device Under Test (DUT)

The DUT is a CREE CMPA2735075F High-Electron-Mobility Transistor (HEMT) MMIC capable of delivering more than 75 watts of peak pulse power between frequencies of 2.7 GHz and 3.5 GHz. The device is an N-type depletion-mode MOSFET. The design features two stages of reactively matched amplification. It offers a PAE greater than 50 % over the tested frequencies band of 2.9 – 3.4 GHz. It operates with a 28 VDC drain bias and a negative gate bias. The nominal dimensions for the MMIC chip as shown in the pictures below are 12.5mm wide by 12.5 mm deep by 4 mm high.

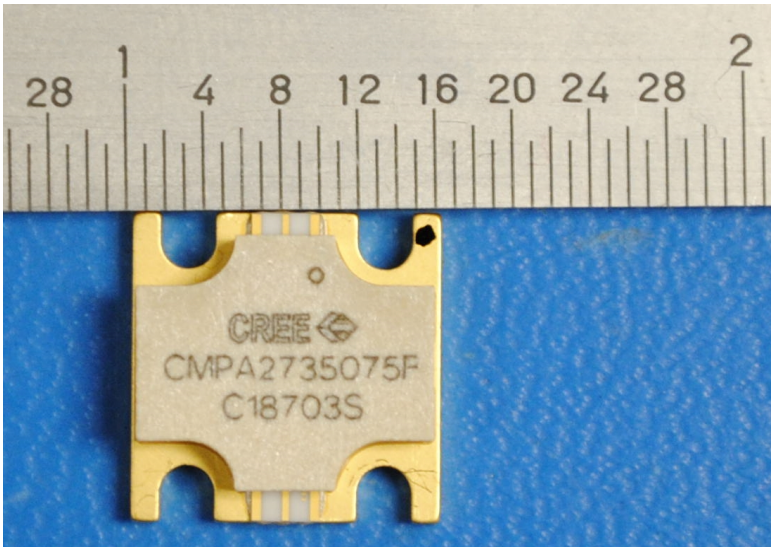


Figure 4-3: Photo of the CMPA2735075F GaN HEMT power amplifier; the MMIC is bonded to a copper tungsten flange. Rule is marked in 1/32 inch increments.

GaN MMIC PA technology is superior the Silicon (Si) Laterally Diffused Metal Oxide Semiconductor (LDMOS) and the Gallium Arsenide (GaAs) Field Effect Transistor (FET) technology, in terms of power output and efficiency. This due to GaN's high power density that exceeds 8 W/mm compared to just 1 W/mm for LDMOS and GaAs. GaN efficiency is also superior; typical figures for GaN exceed 50 % whereas LDMOS and GaAs are 30% efficient.

Figure 4-4 shows a MMIC mounted on a demonstration amplifier circuit (CMPA2735075F-TB). Notice the large energy storage (capacitor) at close proximity of the device drain. The figure also points out the location of the RF Input and Output, voltage and current test points.

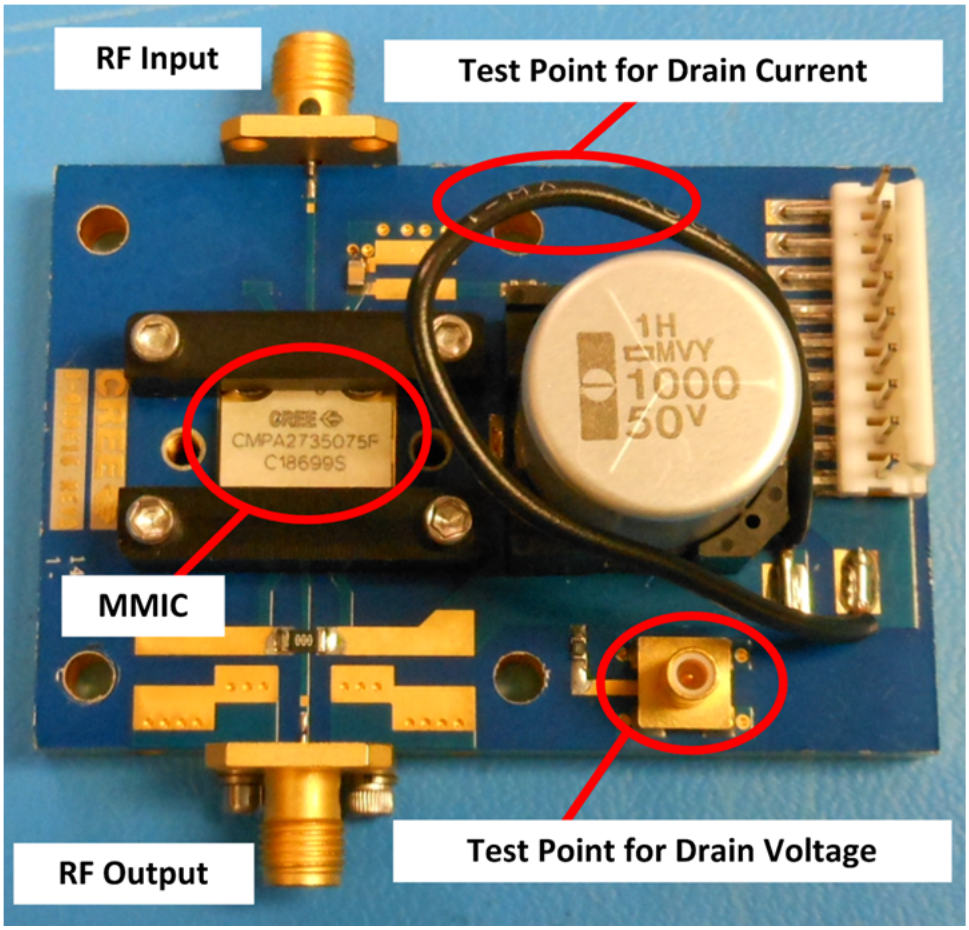


Figure 4-4: Picture of the CMPA2735075F GaN HEMT power amplifier; mounted on demonstration amplifier circuit CMPA2735075F-TB.

During testing, the demonstration circuit is bolted onto an aluminum cold plate. Figure 4-5 shows the demonstration amplifier circuit mounted on the cold plate. The cold plate temperature is controlled via a water recirculating chiller that is kept at a nominal 25 °C. The control processor can set the water temperature to a different value if desired. Also visible in the picture is a Mini-Circuit power amplifier Model ZVE-3W-83+ used to drive the RF input power to the power amplifier. In between the driver amplifier and the MMIC is a 20 dB coupler used to sample the signal after the driver amplifier. Clamping the drain current test point wire on the upper side of the picture is a high bandwidth current probe (Agilent N2783A). The probe is used to capture the MMIC drain current waveform. A high power attenuator is used to dissipate the output power before sampling the output signal.

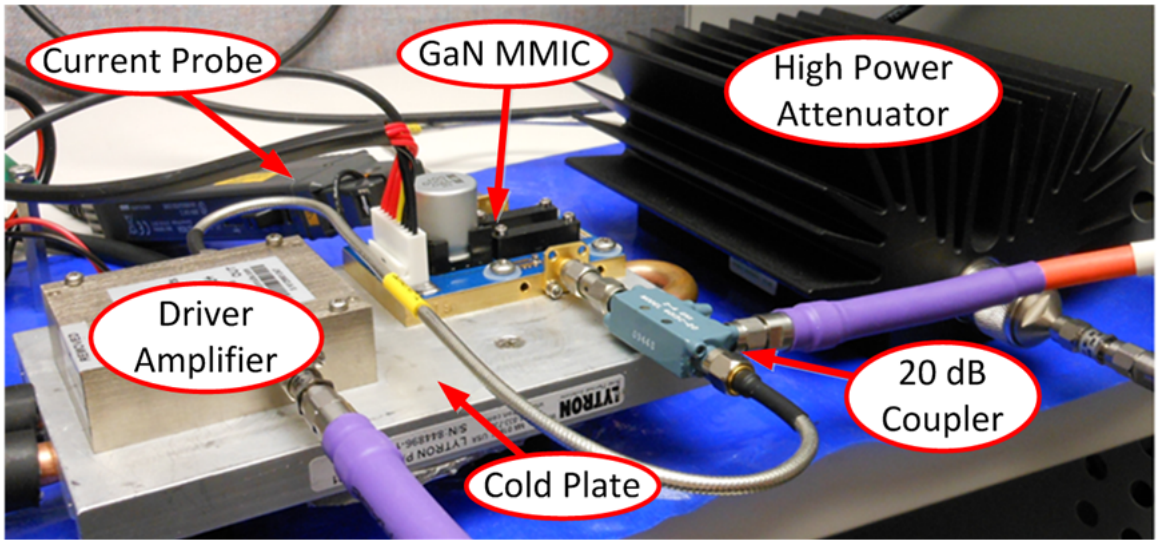


Figure 4-5: Picture of the CREE GaN HEMT MMIC Power Amplifier mounted on cold plate.

## 4.3 Software Design

All the software programming was implemented in MATLAB™. The software design consisted of two parts. The first part deals with controlling the instrumentation for data collection and storage. The second part deals with data analysis. Object oriented programming was used extensively to accomplish these two parts.

### 4.3.1 Instrument Control

Eight instruments and devices were used to construct the P.A. Test set-up. These includes two signal generators, one 8-bit digital output module used to configure the Switch Matrix, a recirculating water chiller, two oscilloscopes, an arbitrary waveform generator and a pulse generator. Several instrument drivers were created to interface with the instruments. The majority of the drivers were written by referencing the Standard Commands for Programmable Instruments (SCPI). The drivers provide a basic interface between the instruments and the control computer. However, the actions needed to take place between instrument and on the

various stages of data acquisition were very complex. Therefore, these instrument drivers were enhanced by using object oriented programming. The instrument ease of use was significantly improved as compared to typical drivers; it also reduces the length of the scripts needed to accomplish a task. The instrument control is absolute, in that any changes that needs to be made to the instrument configuration are automated.

### 4.3.2 Implementation of Waveform Library File

The waveforms entry within a Waveform Library File (WLF) have unique names. A unique name is of particular importance when uploading waveform into the Radar Exciter and scheduling the waveforms for playback. It is a direct requirement from the instrument used as Radar exciter. The unique name also helps in documenting a test event.

The test design and execution is started by creating a WLF. The file follows a Comma-Separated Values (CSV) format depicted as the example in Table 4-1. The example shows four waveforms, each with significantly different characteristics in term of pulse width and duty cycle. Each column specifies a desired property for the waveforms. Only one WLF is used per test event, but there is no set limit in the number of waveforms each file can have. Also any of the waveform listed in the WLF can be use as the Waveform of Interest (WOI). To change the WOI, a new test event needs to be initiated; this requires all waveforms to be cleared from memory.

Table 4-1: Waveform Library File Example

| index | name | modul | RF_GHz | IF_MHz | FS_MHz | BW_MHz | PW_usec | DC_perc | Npulses |
|---|---|---|---|---|---|---|---|---|---|
| **1** | **CPI1** | **CW** | **3.2** | **187.5** | **600** | **0** | **10** | **2** | **40** |
| **2** | **CPI2** | **CW** | **3.2** | **187.5** | **600** | **0** | **1** | **2** | **400** |
| **3** | **CPI3** | **CW** | **3.2** | **187.5** | **600** | **0** | **50** | **2** | **8** |
| **4** | **CPI4** | **CW** | **3.2** | **187.5** | **600** | **0** | **10** | **8** | **32** |

From the several fields in the WLF, the most important for the discussion of the example within this dissertation are the name, PW_usec, DC_perc and Npulses. A description for each of these fields in given below, more information can be found in Appendixes C and D.

***Name***: Every waveform within the WLF needs to have a unique name. The name is used primarily as a requirement to upload waveforms into the Radar Exciter.
***PW_usec***: Pulse width, specified in microseconds.
***DC_perc***: Pulse duty cycle, specified in percentage.
***Npulses***: Number of pulses in a waveform.

### 4.3.3 Graphical User Interface (GUI):

A graphical user interface was developed to facilitate the complex interaction with instruments, data collection and analysis, more information can be found in Appendix D. The interface allows for the loading of a WLF and the selection of the desired WOI. After the WLF is loaded into the computer memory, a table is populated with the waveform properties. After selecting a waveform as the WOI, several Waveform_Class objects are created, one for each waveform in the WLF. The exception is the WOI; each pulse within this waveform is assigned to a unique Waveform_Class object. The pulses are linked so that their order within the CPI is known. At this point all of the waveforms have been synthesized.

Once the waveforms are loaded into the Digital Exciter the number of pulses (**Npulses**) in any of the waveforms can be changed, with the exception of the WOI. Also the order of the waveforms can be altered at any time. WOI must always be in the selected sequence. WOI can be selected by itself, or with any combination of waveforms in the WLF.

The GUI provides the ability to input information relevant to the experiment. Four different fields can be changed based on particular test conditions. For example multiple amplifiers could be tested. The serial number for each amplifier or some other identifiable information and a test description can be typed directly into the GUI text edit boxes. Also a circuit diagram can be selected via a drop down menu. Every time data is saved, all of the user

inputs and all of the current states of the GUI are saved with the data, including the actual waveform sequence played back during the test.

At this point data collection is simplified to a single click on the Data Collection pushbutton. All of the necessary instrument setups and procedures are performed by the GUI and the underlying classes and scripts. This includes the control over the Switch Matrix, used to set the three modes discussed earlier.

Figure 4-6 shows multiple checkboxes designed to facilitate data collection, saving and analysis. The GUI also allows the display of process data on several different ways. Upon verifying that all test parameters are correct, the user can choose to automatically save captured data into uniquely named data files. The user can also choose to do multiple back-to-back data collections, select to automatically save all of the collection, or link each data collection to automatically analyze the data.

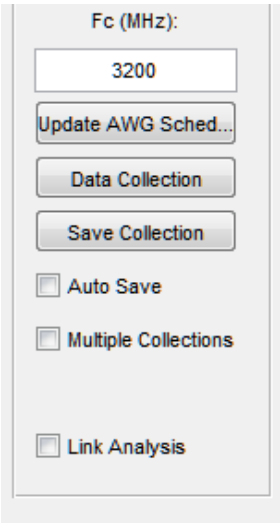


Figure 4-6: The GUI can be used for multiple data captures, data analysis and automatic saves.

The same GUI is used offline for data analysis. Any of the files saved with the GIU can be loaded for analysis. After selecting a saved file, all of the test descriptions, DUT serial number fields and block diagram are retrieved and displayed by the GUI.

### 4.3.4 Data Capture and Storage

There are several steps necessary to execute a successful data capture. These steps are managed by a "Data_Collection_Class.m" object. The Digital Receiver and Digital Storage Oscilloscope are configured to capture and digitize the RF and DC Waveforms including proper sampling rates and memory size. The Digital Receiver and DC Waveform Digitizer are armed to trigger on the edge of the trigger pulse sent by the Pulse Generator. The trigger pulse marks the beginning of the WOI. After verify that a successful trigger occurred, the data collected by the Digital Receiver and the DC Waveform Digitizer are then transferred into the Control Processor memory.

The raw data captured includes the entire WOI CPI, formed by pulses and the silence space in between pulses. The data is in the form of a digital IF centered at 12.5 MHz. The data undergoes digital downconversion and digital filtering resulting in digital baseband I and Q components.

For any single pulse in the WOI, there are six data sets, four digital receiver channels, and two for the DC waveforms (drain voltage and current). The data sets are parsed into "Waveform_Class.m" objects. Only the time in which the pulses was active in addition to a programmable amount of guard time is stored. The rest of the captured data is discarded, as it is just noise and no valid signal is present.

## 4.4 Signal Processing

The signal processing described in Chapter 3 was programmed into a "Data_Analysis_Class.m" object. The object facilitates the display of raw and processed data in

multiple forms for analysis. This object also executes the parameter extraction for the behavioral model discussed in Chapter 6. The Class object manipulates the data to provide; 1) pulse edge detection, 2) amplitude and phase pulse envelope information, 3) pulse auto-correlation and cross-correlation, 4) averaging multiple data captures (observations), and 5) calculate MTI Improvement Factor.

### 4.4.1 System Identification

The Control Processor performs signal processing similar to a Pulse Doppler radar. The major signal processing function used in the analysis was pulse compression, by performing a cross-correlation between the amplified signal and its reference. Section 3.2.4 Wiener-Hopf Equation showed how the correlation results are used to find the amplifier's scalar gain and phase insertion.

## 4.5 Chapter Summary

This chapter presented an overview of the hardware and software designed to conduct the experiment. It also introduced the DUT characterized and used throughout this dissertation. The experiment allows for the replication of multifunction radar operations as required by the experiment design introduced in Chapter 3. However, in order to replicate the experiment at a later time as required by the predistortion algorithm explained later in Chapter 7, many other details about the condition of the DUT and instrumentation were captured. The PA test set-up has enough built-in flexibility to test power amplifiers under a wide range of representative conditions.

# Chapter 5. Characterization of Power Amplifier Memory Effects and Assessment in Radar Performance

## 5.1 Characterization of measurement noise

Characterizing the amplifier's behavior starts by measuring the amplitude and phase of every pulse in a CPI. The accuracy of these measurements is dependent on the Signal to Noise Ratio (SNR). In addition, the MTI Improvement Factor performance metric quantifies the differences in amplitude and phase between neighboring pulses in a CPI. Therefore, the metric is also sensitive to SNR. This section details the SNR throughout the measurement system's data processing.

The analyzed signals are not transmitted into space, they are routed to the DUT via coaxial cables. Thus, the SNR is inherently high, in excess of 80 dB. The limiting factor in SNR is the dynamic range of the Digital Storage Oscilloscope (DSO) used as surrogate Digital Receiver.

The DSO uses a 12-bit Analog to Digital Converters (ADC) architecture, however, its effective bit count is in the order of nine to 10 bits, and is dependent on the signal level and frequency. This limits the available instantaneous SNR to no more than 60 dB. In addition, the thermal noise floor was adjusted to 6 dB (1-bit) above the ADC quantization noise. The maximum signal level was adjusted to stay approximately 1.5 dB below the ADC's full voltage scale. These two measures reduce spurs, but limited the SNR to no more than 52.5 dB, at 20 MHz bandwidth.

### 5.1.1 Digital Receiver

Figure 5-1 shows five pulses digitized by the digital receiver. A period of silence follows each pulse. The digital Intermediate Frequency (IF) was design to be at exactly 12.5 MHz, a quarter of the selected sampling frequency of 50 MSps. This is possible by phase locking all signal sources and the digital receiver.

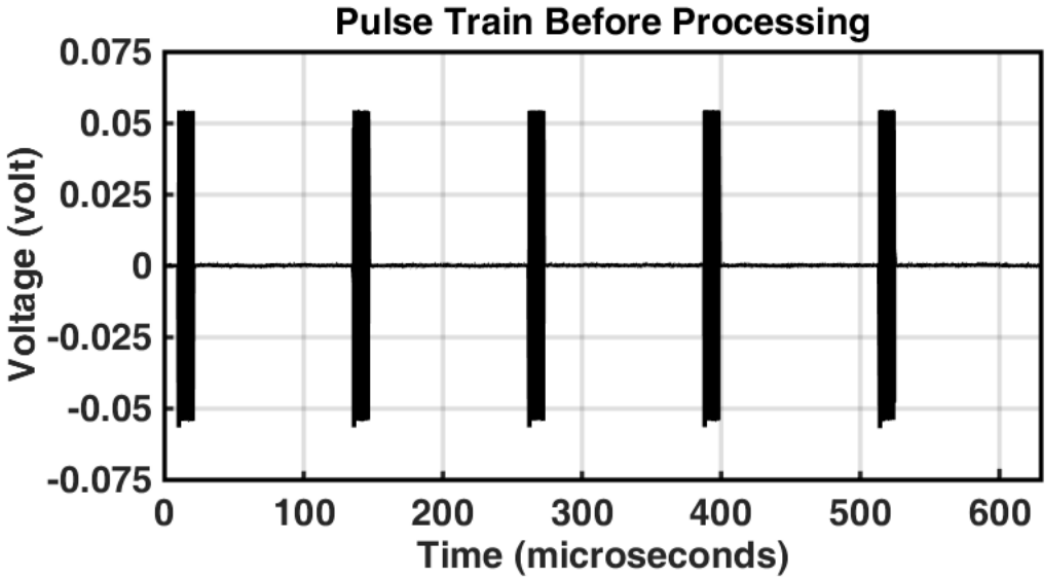


Figure 5-1: Pulses as captured by the digital oscilloscope (digital receiver).

The digital signal is further parsed into individual pulses, discarding all but a few microseconds of the silence before and after each pulse. At this point, the location of the pulses is known to within a fraction of a microsecond. This is enough to be certain that the pulse is being keep in its entirety before proceeding with Digital Down Conversion (DDC). Later on, envelope detection is used to locate the beginning of the pulse to within ± 50 nanoseconds.

The estimation of the SNR is found by taking the ratio of the pulse average power over the noise variance. In the example from Figure 5-1 the signal power is -6.5 dBm, while the noise power is -52.3 dBm, making the SNR approximately 45.8 dB. Table 5-1 shows the estimated SNR for each digital receiver channel, taken over multiple pulses. The difference between SNR

is attributed to the different signal levels at the input of the downconverters, and subsequently the input of the Digital Receivers.

Table 5-1: Digital Receiver SNR estimation

| Channel #: | SNR: |
|---|---|
| 1 | 41.7 dB |
| 2 | 42.5 dB |
| 3 | 52.5 dB |
| 4 | 47.3 dB |

### 5.1.2 Digital Down Conversion (DDC)

The SNR computed in Table 5-1 represent the digitized signal without any processing. To measure the pulse amplitude and phase, it is first necessary to DDC the digital IF at 12.5 MHz into baseband I and Q components. As part of the process, the signal is decimated by a factor of two, reducing sampling frequency to 25 MHz. The frequency response of the decimation filter is shown in figure 5-2. The 3 dB bandwidth of this filter is 5.8 MHz by design. The expected SNR improvement is therefore 6.3 dB.

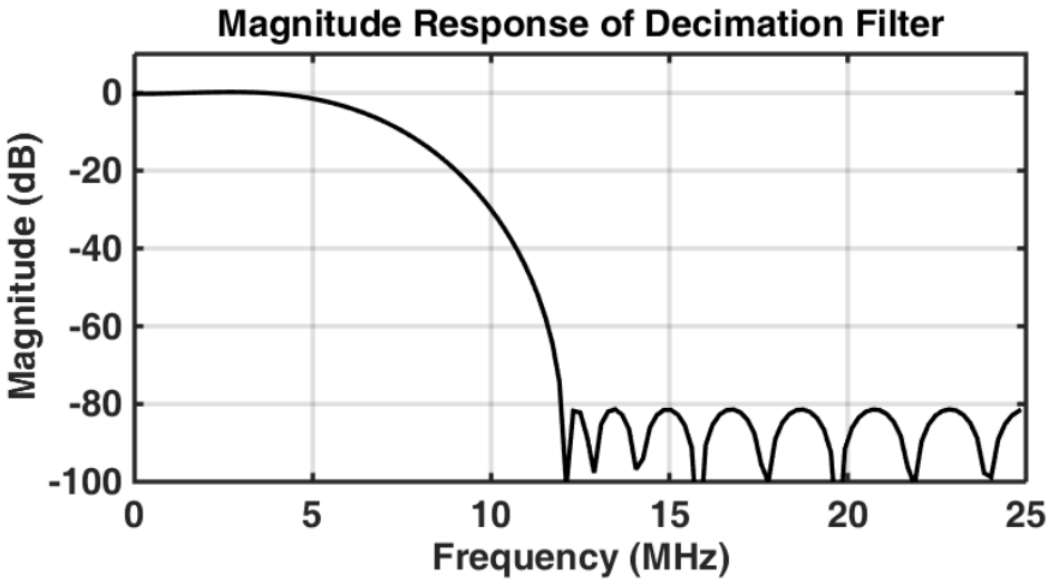


Figure 5-2: Magnitude Response of Decimation Filter.

The DDC processing improves the SNR. Table 5-2 shows the estimated SNR for each digital receiver channel. The table also lists the achieved SNR improvement. The discrepancies between the achieved and expected improvement is due to spurs and other systems noise.

Table 5-2: Digital Receiver SNR estimation, after Digital Down Conversion.

| Channel #: | SNR: | SNR Improvement: |
|---|---|---|
| 1 | 48.2 dB | 6.5 dB |
| 2 | 45.9 dB | 3.4 dB |
| 3 | 58.6 dB | 6.1 dB |
| 4 | 49.9 dB | 2.6 dB |

After DDC, all the information carried by the pulse is frequency translated to baseband I/Q components. This facilitates visualizing the pulse amplitude and phase envelope. Figure 5-3 shows the magnitude of the pulse envelope.

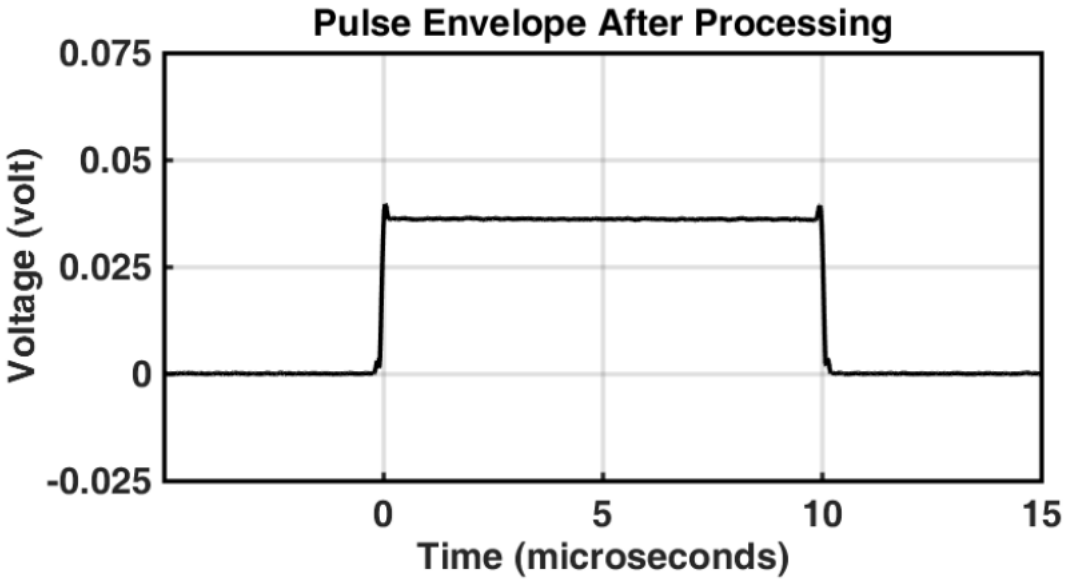


Figure 5-3: Magnitude of the pulse envelope after DDC.

Figure 5-4 shows the normalized magnitude in decibels. The measured signal level throughout the pulse duration is constant. For channel #2, the noise power is on average 45.9 dB below the signal power.

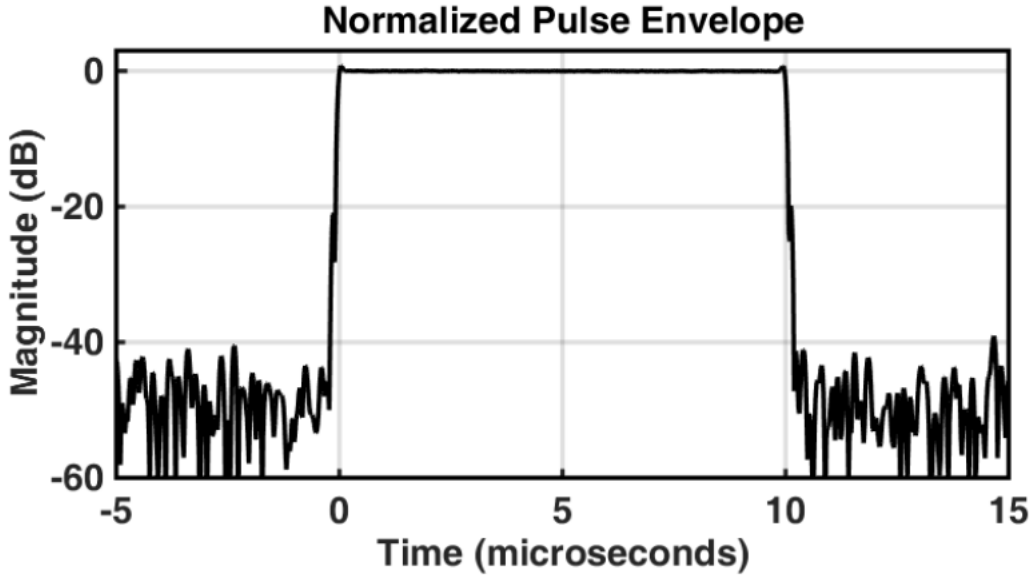


Figure 5-4: Normalized pulse envelope magnitude in decibels.

The waveform selection is an unmodulated pulse; its phase at baseband is therefore constant over its duration. Figure 5-5 shows the phase envelope. The constant phase is visible during the pulse duration of 0 to 10 microseconds. The figure also shows the no-signal (noise) phase, which is random and follows a uniform distribution.

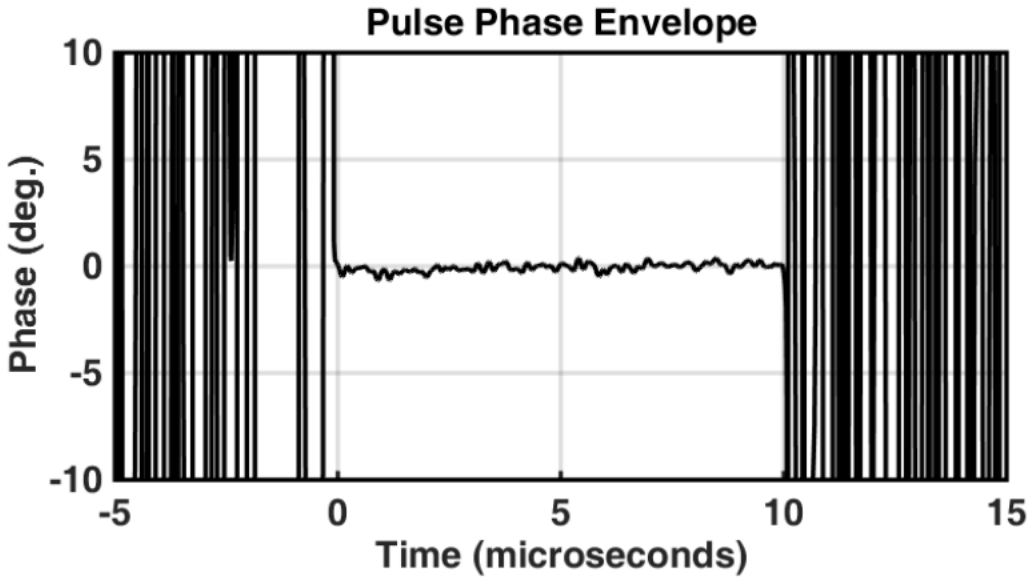


Figure 5-5: Pulse phase envelope in degrees.

### 5.1.3 Pulse Cross-Correlation

Figure 5-6 shows the resulting cross-correlation of the amplifier signal (channel 3) with the reference signal (channel 4). Only the data point needed for the system identification is stored for later use. This data point is the peak cross correlation value. As discussed in the Wiener-Hopf method, only one complex value is stored for each pulse in the WOI.

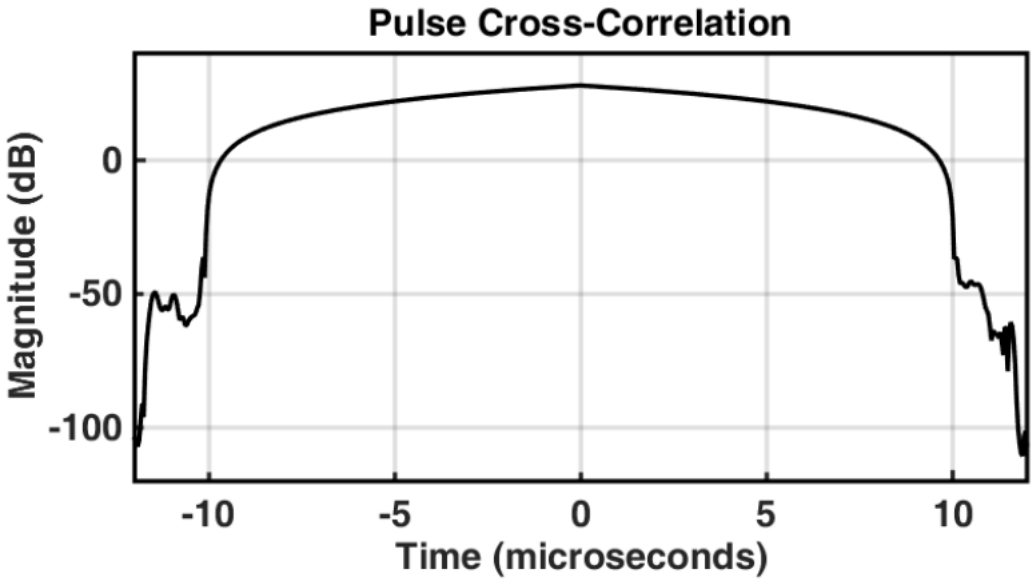


Figure 5-6: Cross correlation result of the pulse reference (channel 4) and the amplifier signal (channel 3).

For each pulse in a CPI, the result of the peak cross correlation value is stored. Since the interest is finding the differences between pulses, the peak cross correlation is normalized in reference to the first pulse in the sequence. The peak cross-correlation values are further decomposed into and amplitude component and a phase component.

Figure 5-7 shows the amplitude components for the peak cross correlation, expressed in magnitude decibels. The expected value for the magnitude is 0 dB. Figure 5-8 shows the phase components for the peak cross correlation, expressed in degrees. The expected value for the phase is zero degrees. Deviation from zero dB magnitude and zero degree phase indicates noise in the system.

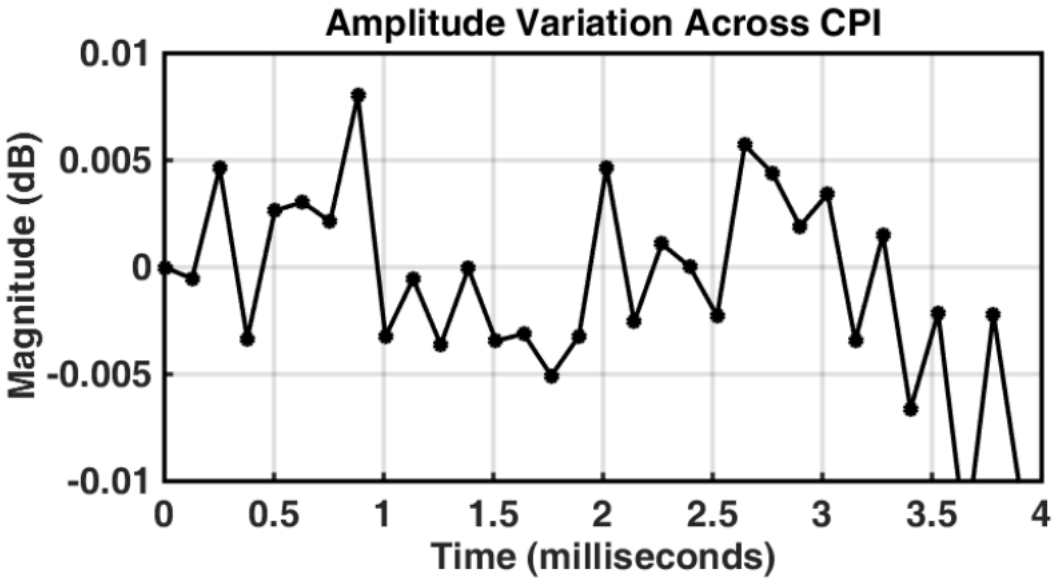


Figure 5-7: Amplitude variation across CPI for a single capture.

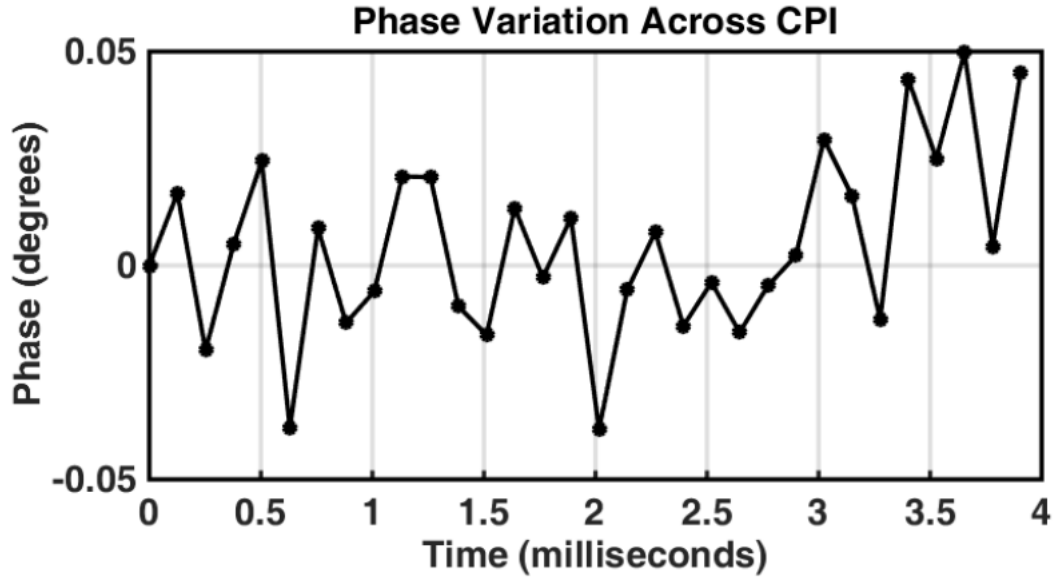


Figure 5-8: Phase variation across CPI

The noise power is estimated via a Direct Fourier Transform (DFT) method. Figure 5-9 shows the power spectral density of the normalized peak cross correlation result. The signal level is represented by the zero-frequency component. The noise power is spread across all frequencies. The signal power level normalized, thus calculated to be 0 dBc. The noise power is

the linear sum of all of the frequency bins (except zero). Compensating for the portion at zero-frequency the noise power is -63.9 dBc. The SNR at this stage of the signal processing is 65.6 dB.

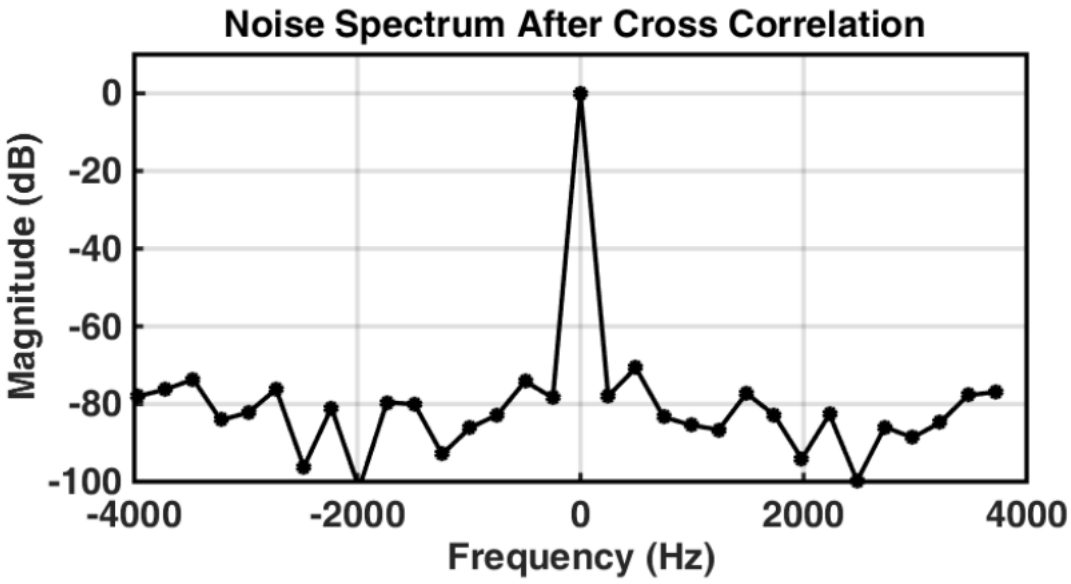


Figure 5-9: System noise spectrum after a single CPI peak cross correlation.

Figure 5-10 shows the MTI Improvement Factor limitation for the single data capture. The estimated SNR is 65.6 dB. Based in the analysis done in Chapter 3, Sections 3.4.3 and 3.4.4, the MTI Improvement Factor can be measured to 45.6 dB with a precision of ± 1 dB. The precision will deteriorate rapidly for larger MTI Improvement Factors. This falls short of the required 53 dB ± 1dB.

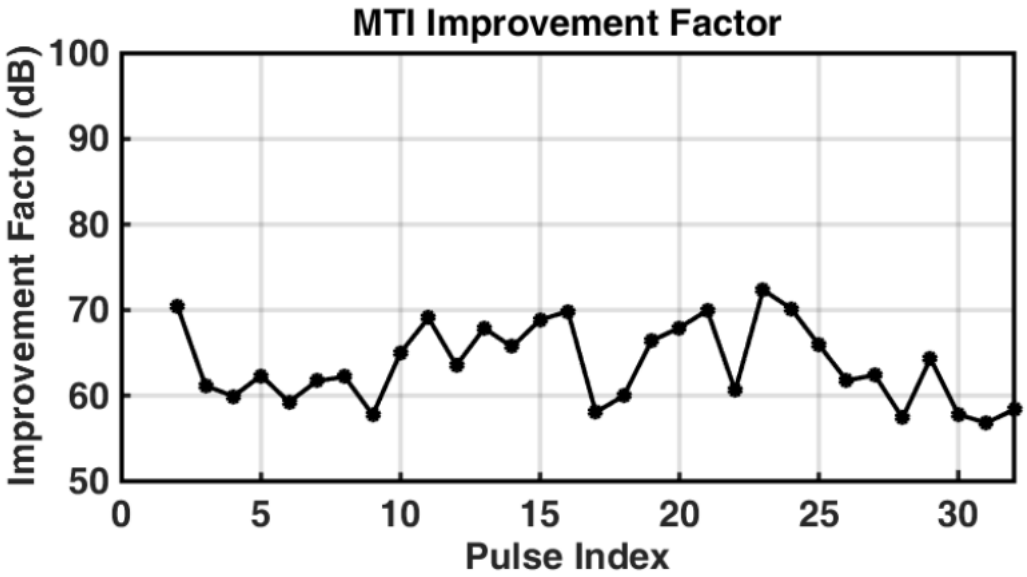


Figure 5-10: MTI Improvement Factor for single calibration waveform is limited by noise.

### 5.1.4 Averaging Multiple Captures

Processing multiple captures and averaging the results yields an improved SNR. The number of captures for this example was 40. Figure 5-11 shows the amplitude components for the peak cross correlation, expressed in magnitude decibels. Figure 5-12 shows the phase components for the peak cross correlation, expressed in degrees. For the 40 captures average, the deviation from the expected value is reduced, meaning that the system noise improved. Averaging multiple captures (observations) works in reducing the sample variance due to the cancelation of random components added to the signal. These components are primarily comprised of thermal noise.

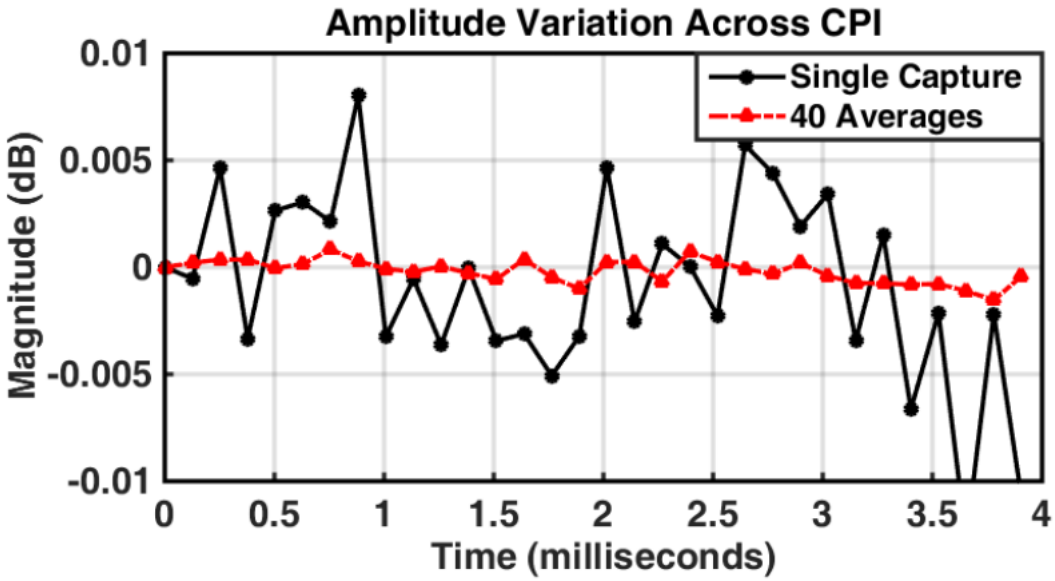


Figure 5-11: Amplitude variation from pulse to pulse across CPI for a single capture and for 40 averaged captures.

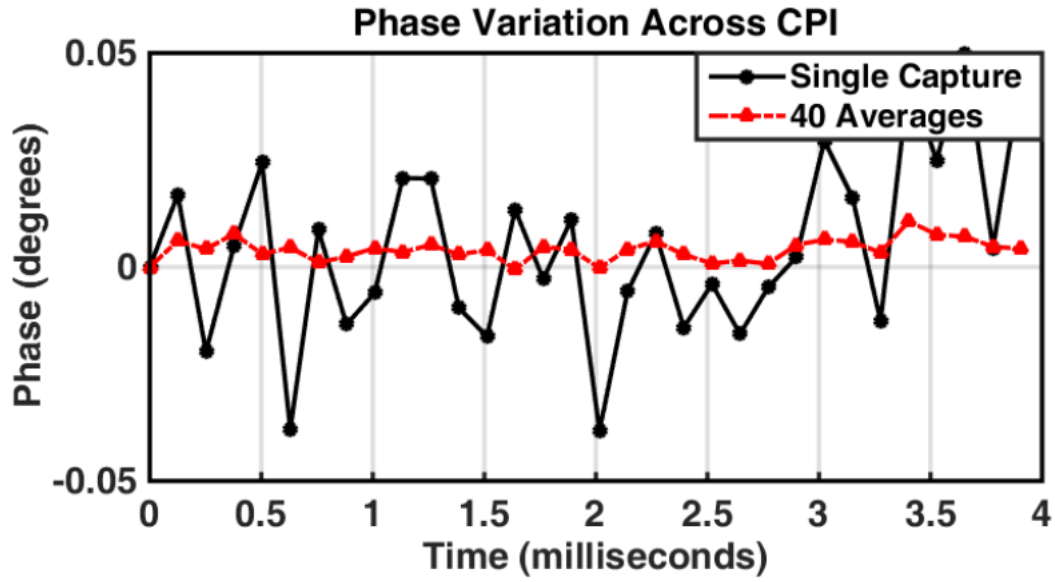


Figure 5-12: Phase from pulse to pulse across CPI for a single capture and for 40 averaged captures.

Figure 5-13 shows the power spectral density of the normalized peak cross correlation result, for both the single capture and the 40 averaged captures. Using the DFT method, the

estimated SNR for the single capture is 65.6 dB, after 40 averages the estimated SNR is 82.2 dB. This represents a SNR improvement of approximately 16.6 dB. This is 0.6 dB higher than the expected 16.0 dB. This discrepancy may be due to excess noise present in the first data, such as voltage supply noise.

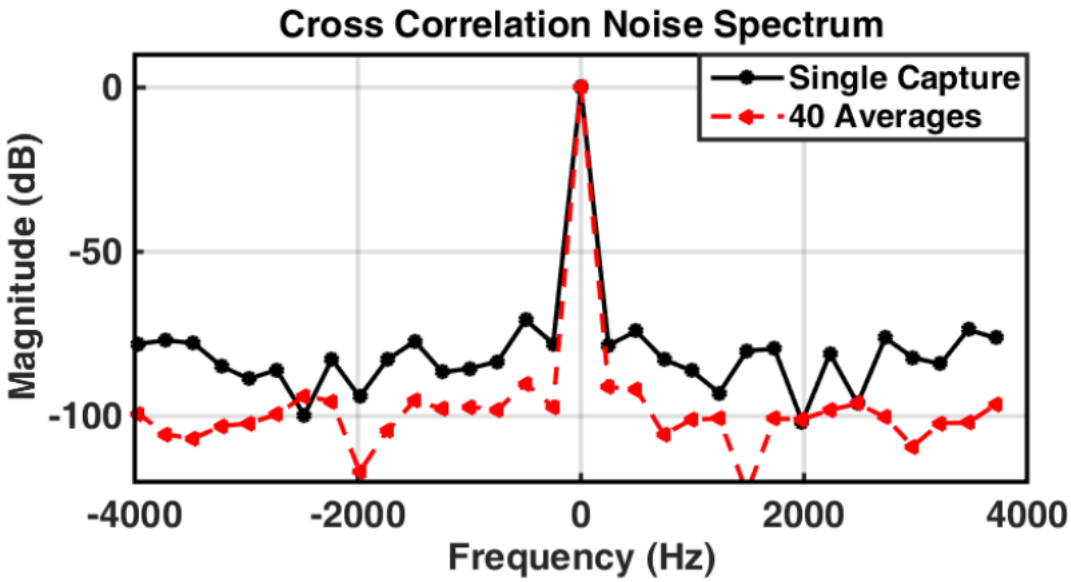


Figure 5-13: System noise spectrum for a single CPI capture and multiple averaged CPI captures.

Figure 5-14 shows the MTI Improvement Factor limit for the single capture data set and the 40 averages. The average MTI Improvement Factor for the single capture is 62.6 dB, while the average MTI Improvement Factor after averaging 40 captures increased to 82.4 dB.

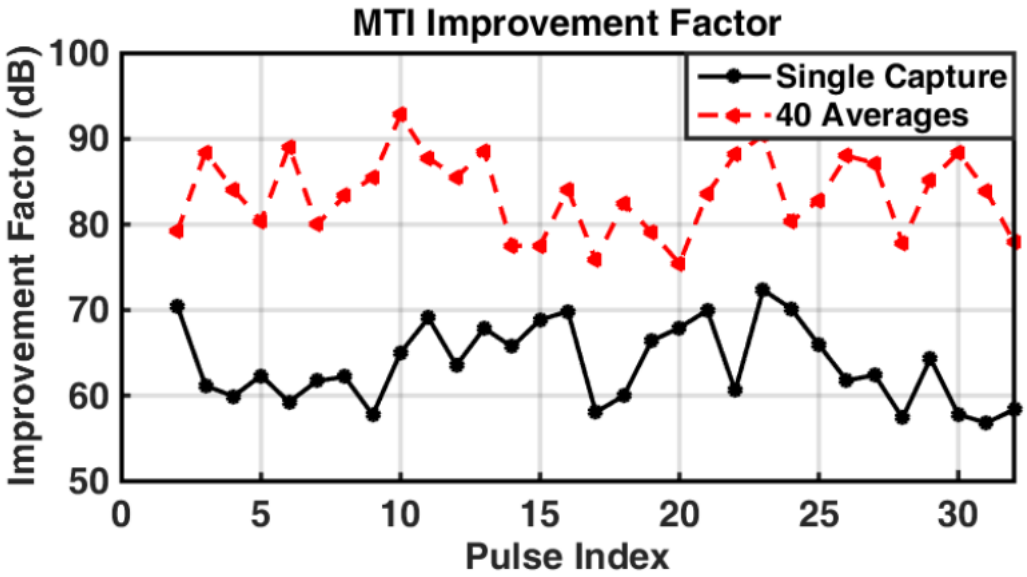


Figure 5-14: MTI Improvement Factor for a single CPI capture and multiple averaged CPI captures.

Table 5-3 summarizes the estimated SNR for all combinations of channel. After averaging 40 captures, and evaluating all possible combinations of channels for the cross correlation products, the expected minimum SNR is 78.3 dB, which is approximately 5 dB better than the required 73 dB.

Table 5-3: SNR estimation for the cross-correlation products for all possible combination of channels.

| Channels #: | SNR: | | |
|---|---|---|---|
| | Single Capture (dB): | Averaging 40 Captures (dB): | Improvement (dB): |
| 1 & 2 | 62.4 | 78.3 | 15.9 |
| 1 & 3 | 65.4 | 81.4 | 16.0 |
| 1 & 4 | 63.5 | 80.4 | 16.9 |
| 2 & 3 | 63.0 | 78.3 | 15.3 |
| 2 & 4 | 62.8 | 79.5 | 16.7 |
| 3 & 4 | 65.6 | 82.2 | 16.6 |

## 5.2 Amplifier Operating Point and System Calibration

The operating point selected for the power amplifier depends on many factors. These factors include device characteristics and applications. In this experiment, the operating points for drain voltage and current were set according to the manufacturer instructions. The input power was set to operate near maximum efficiency.

In radar applications, the goal is to maximize the output power and the efficiency, accomplished by calculating the Power Added Efficiency (PAE) while the RF input power into the device is increased. The PA test set-up can measure all the necessary parameters to calculate the PAE. The PAE will reach a peak after the device is well into compression and will then start to decrease. Due to the gain curve characteristics of the GaN device, the maximum PAE is several decibels into compression. This operating point is significantly different from typical communication applications where it is set to several decibels backed off from compression.

The AM/AM and AM/PM conversion was measured after the PAE calculation. Similarly to the PAE measurement, the input power to the device is varied while the output power is

measured, however the phase insertion of the device is also tracked. This information is necessary to implement amplitude corrections as part of the predistortion algorithm.

### 5.2.1 Single waveform calibration sequence

Table 5-4 shows the waveform parameters used to acquire data to characterize the amplifier behavior. CPI 1, referred here as the Waveform of Interest (WOI) is the waveform that was captured and analyzed. For simplicity in presenting the results, the RF frequency was tuned to 3.2 GHz.

Table 5-4: Waveform parameters used for calibration sequence.

| Parameter: | CPI 1<br>Waveform of Interest |
|---|---|
| Pulse Width (PW): | 10 microseconds |
| Duty Cycle (DC): | 8 % |
| Pulse Repetition Frequency (PRF): | 8 kHz |
| Coherent Processing Interval (CPI): | 4 milliseconds<br>(32 pulses) |

### 5.2.2 Results on Power Added Efficiency

Power Added Efficiency (PAE) defines as the ratio of the RF output power minus input RF power to the DC power used to drive the power amplifier. The PAE was calculated for several operating points along a range of input power, using equation (49):

$$PAE = 100 \times \frac{P_{RF\ out} - P_{RF\ in}}{P_{DC\ in}} \tag{49}$$

where, $P_{RFout}$ is the RF output power in watt, $P_{RFin}$ is the RF input power in watt, and $P_{DCin}$ in the DC input power in watt.

The efficiency was calculated from measured RF input and output power and measured DC power drawn. This calculation indicates the power dissipated by the device in the form of heat and how effectively the amplifier converts energy into usable RF power. Refer to Appendix D for more information about PAE. The input power was swept from 20 dBm to 30 dBm, while output power, and power draw was measured.

Figure 5-15 shows the RF output power versus the RF input power. The curve asymptotically approaches maximum power. This means that the GaN device is severely into compression. A dot along the curve marks the point in which the maximum PAE occurs. The output power at this point is 49.3 dBm, while the input power is 27.9 dBm, the amplifier power gain it therefore 21.4 dB.

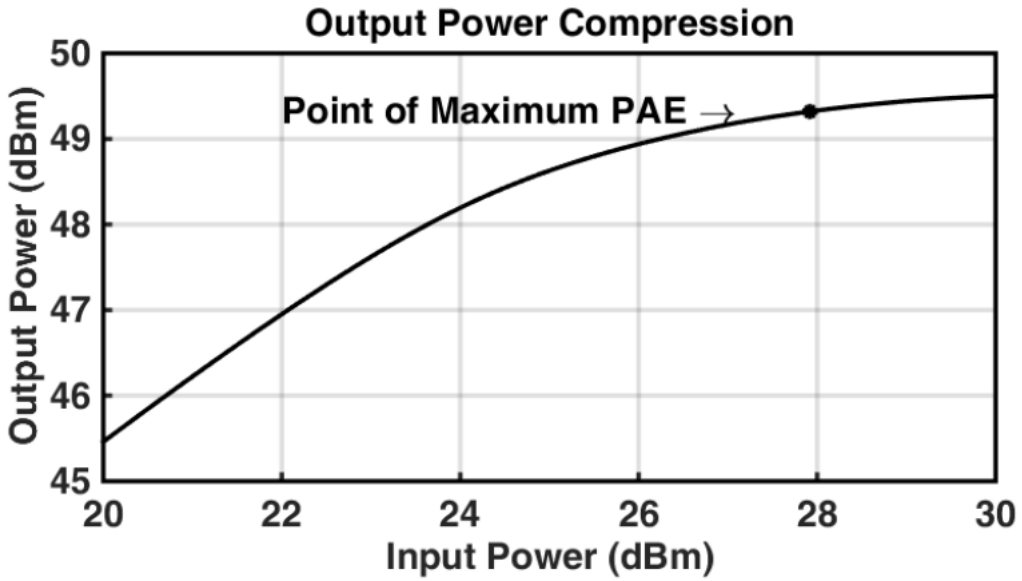


Figure 5-15: Device RF output power as a function of RF input power.

The asymptotically increasing RF output power in Figure 5-15 also means that the device gain is decreasing rapidly with increased input power. Figure 5-16 shows the gain as a function of input power. The device is well in the nonlinear region. In fact, the gain characteristics of GaN pulse amplifiers are peculiar in that their compression is much softer and deeper than amplifier based on GaAs or LDMOS technology.

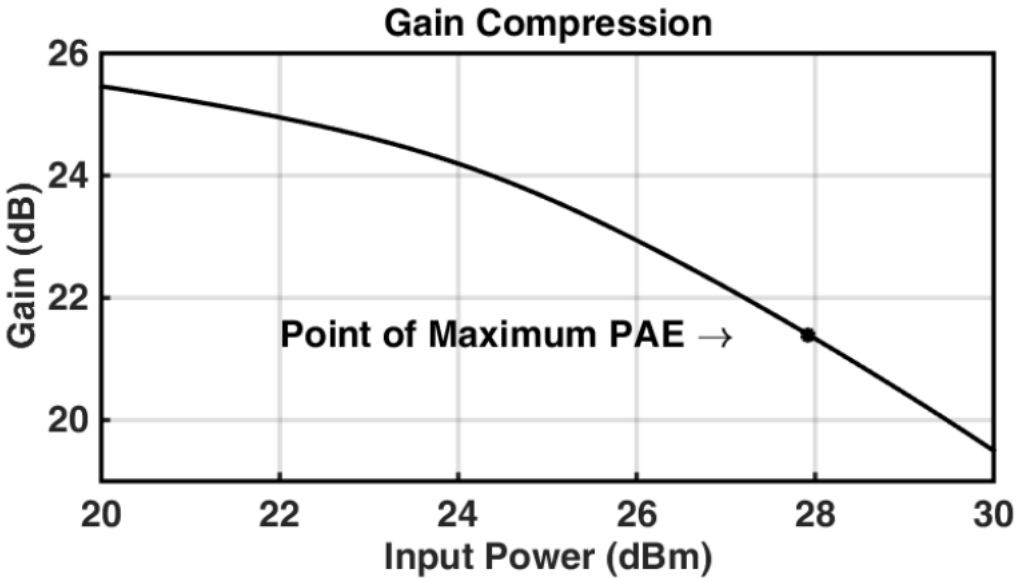


Figure 5-16: Device scalar gain as a function of RF input power.

Figure 5-17 shows the DC power drawn by the device as a function of the RF input power. A portion of the DC power supplied by the power source is converted into usable RF power, the balance is wasted as heat. The power drawn at maximum PAE is 171.3 watt.

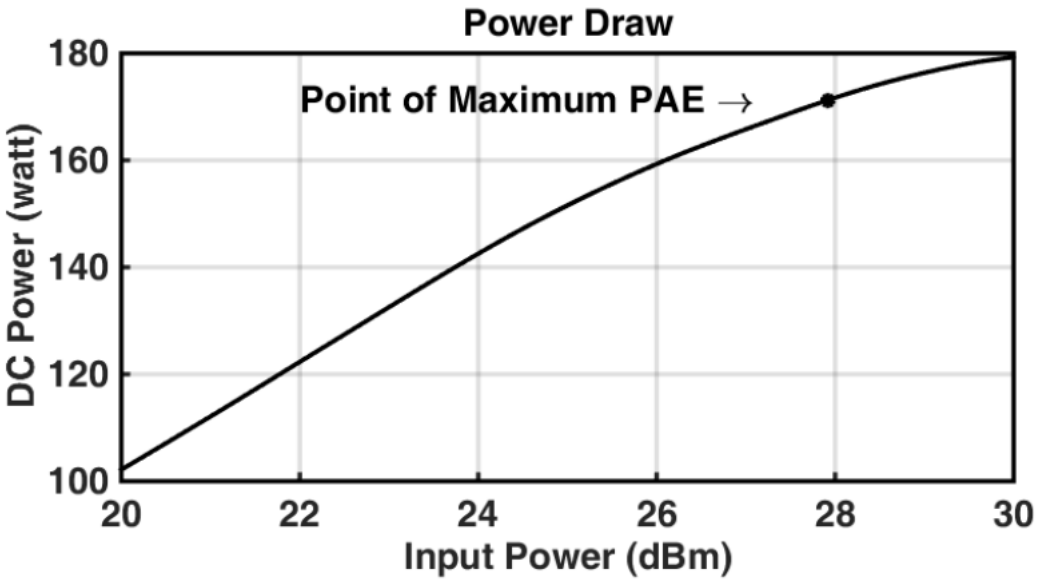


Figure 5-17: Drawn DC power as a function of RF Input power.

Figure 5-18 shows the portion of power that is being wasted as heat. This heat is generated within the GaN semiconductor channel, and majority of it is generated just under the gate finger. The power converted into heat while operating at maximum PAE is 86.4 watt.

Efficient heat dissipation is critical for the device longevity. The heat is generated in a small volume inside the device, (3.6 mm x 0.002mm x 0.05 mm). The device thermal stack up is designed to minimize the thermal resistance from the device channel (gate cells) to the chip flange, to quickly purge the heat out. To maintain a safe temperature at the device channel, the device is mounted to a cold plate or heat sink. In general the high power density and relatively large duty cycle used during normal radar operations demands the used of water-cooling to dissipate the generated heat.

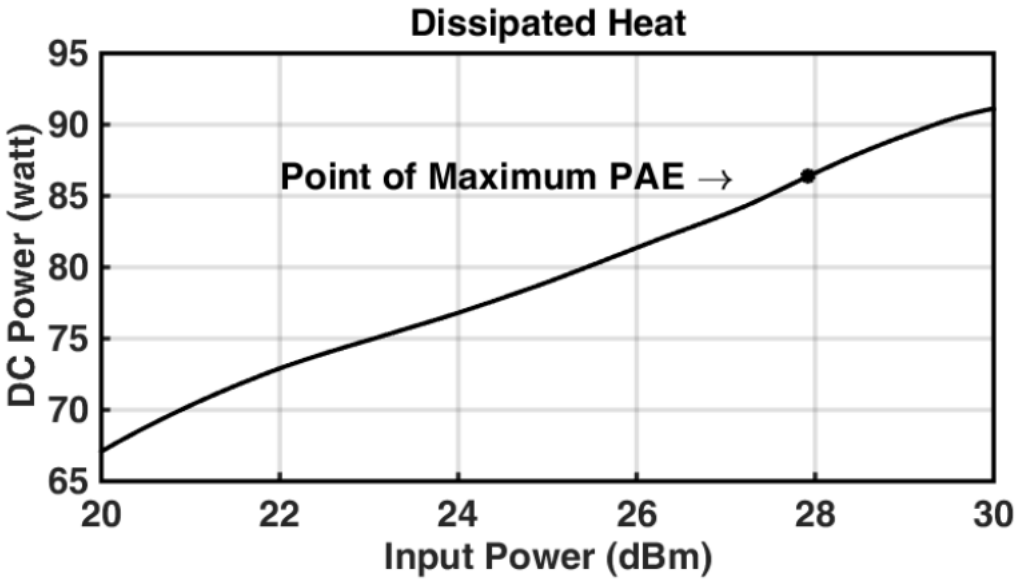


Figure 5-18: Power wasted as heat.

Figure 5-19 shows the resulting curve for the PAE. The PAE increases rapidly to a maximum, and then starts to decrease slowly. The maximum PAE is marked by the dot along the curve. The calculated maximum PAE is 49.6 %.

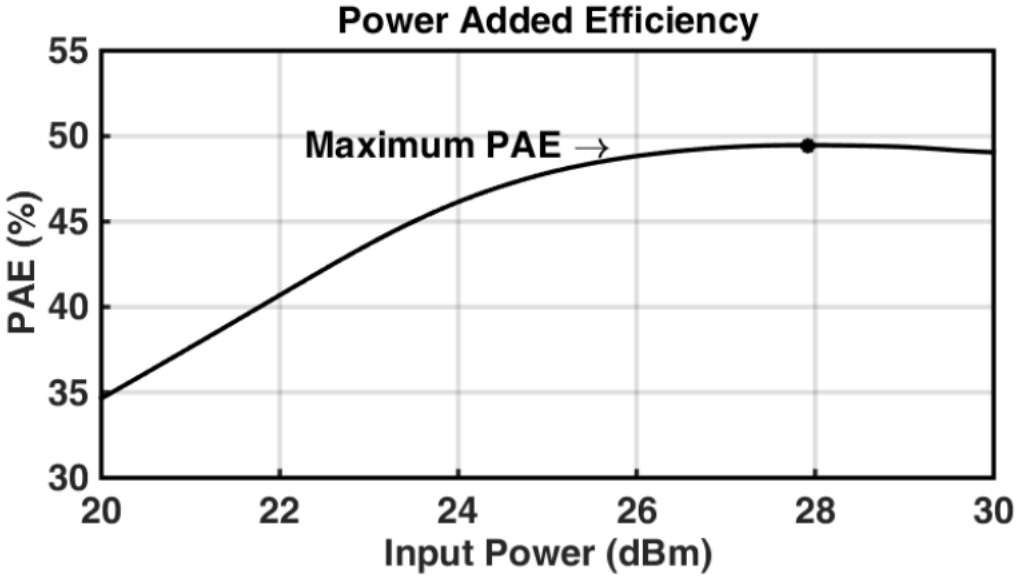


Figure 5-19: Calculated PAE as a function of RF Input Power

Table 5-5 summaries the finding for the maximum power added efficiency operating point. The operating point described in the table is only valid for a single device at a single operating frequency.

Table 5-5: Summary Results for maximum PAE

| Parameter: | Value: |
|---|---|
| Input Power: | 0.62 watts (27.9 dBm) |
| Gain: | 21.4 dB |
| Output Power: | 85.5 watts (49.3 dBm) |
| DC power draw: | 171.3 watts |
| DC heat dissipated: | 86.4 watts |
| Power Added Efficiency: | 49.6 % |

### 5.2.3 AM/AM and AM/PM Conversion

The AM to AM and AM to PM conversion are measures of amplifier distortion. This arises from the pulse power amplifier intrinsic non-linearity. The AM/AM and AM/PM conversion characterizes the changes in output power and insertion phase based on changes in input power. The amplifier non-linearities are well-behaved, meaning that the output power asymptotically reaches a maximum for an increasing input power. This was observed in Figure 5-15, where the input power is increased, while the output power increased at a smaller rate. The AM to AM conversion is equivalent to gain as a function of input power, shown in Figure 5-16. The AM to PM conversion relates to a change in amplifier insertion phase due to a change in input power.

During normal radar operations, pulses are not modulated in amplitude. Thus, AM/AM and AM/PM are generally of no concern. An exception is during calibration of active phased arrays. This is a lengthy process generally performed in antenna ranges. The details are outside

of the scope of this dissertation. For this research, the importance of characterizing the AM/AM and AM/PM conversion emerges from the envisioned pre-distortion algorithm, where each pulse within a CPI can potentially have a different amplitude and phase. Any desired change in output phase directly follows a change in the input phase, since the PM/PM has a one-to-one relationship. However, due to the AM/AM conversion, any desired correction in output power requires a non-linear change in input power. Furthermore, due to the AM/PM conversion, a change in input power will inevitably change the output phase.

Figure 5-20 shows the output power ($P_{out}$) versus input power ($P_{in}$) and the output phase ($\phi_{out}$) versus $P_{in}$. The nominal operating point (near maximum PAE) is used as the reference point for both curves. $P_{in}$ was swept from -8 dB to +2dB in reference to 27.9 dBm. $P_{out}$ vs. $P_{in}$ is represented by a solid line, with units on the left hand side axis indicate changes in output power in decibels. The curve established the relationship between the input and output power. $\phi_{out}$ vs. $P_{in}$ is represented by a dashed line, with units on the right hand side axis indicates changes in the amplifier insertion phase in degrees. The curve establishes the relationship between the input power and output phase.

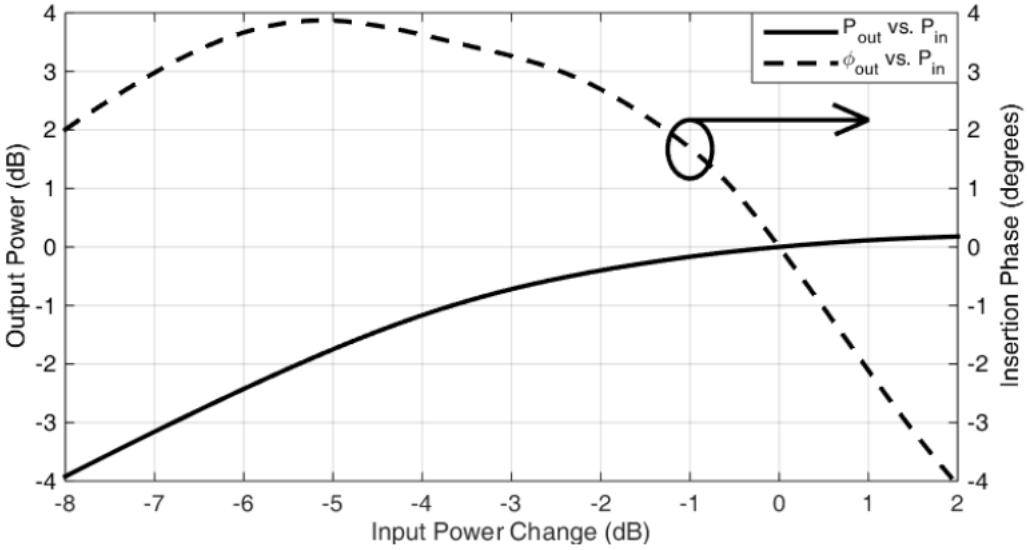


Figure 5-20: AM/AM and AM/PM conversion as a function of RF input power.

Both curves exhibit strong nonlinearities as a function of the $P_{in}$. For example to reduce the output power by 1 dB (from 49.3 dBm to 48.3 dBm) the input power must be reduced by 3.5 dB (from 27.9 dBm to 24.4 dBm). In this instance, the AM/AM is approximately 0.3 dB / dB. Conversely, the output phase changes by +3.4 degrees. In this instance, the AM/PM is approximately -0.97 degrees / dB.

Anticipating the use of predistortion requires understanding the effects that modulation conversion will have in its implementation. Should the predistortion algorithm change the input RF power into the device, this necessarily requires a correction in the signal phase. In addition, due to the selected operating point, the modulation conversion is highly non-linear. By reducing the range in which the modulation conversion is considered, the nonlinearity is approximated with a low order polynomial. Figure 5-21 shows the modulation conversion curves, now for an input power limited to ± 2 dB from the selected operating point.

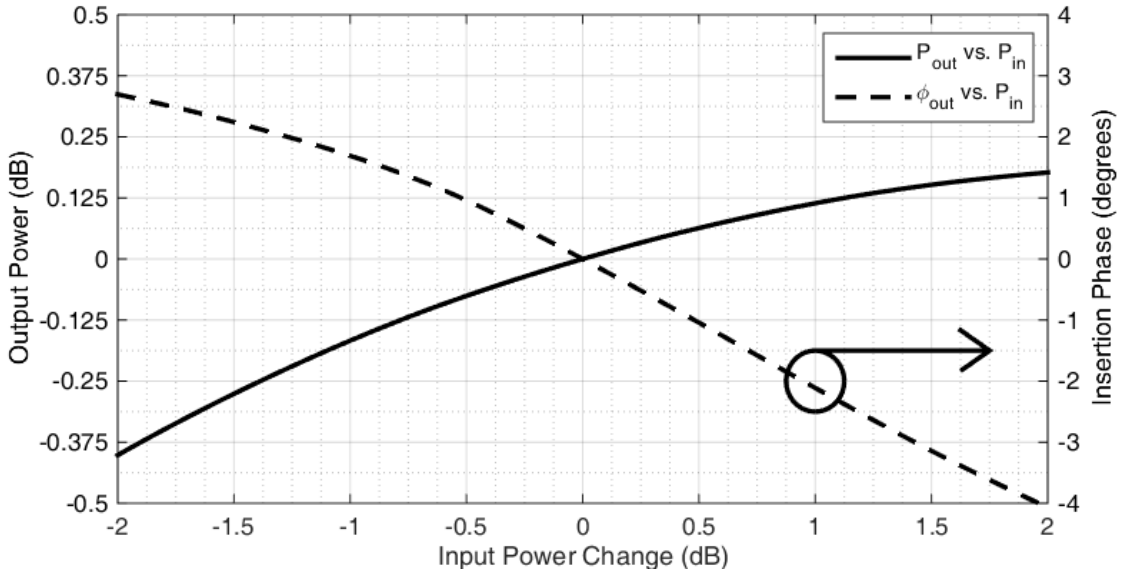


Figure 5-21: AM/AM and AM/PM modulation conversion as a function of RF input power, the range of input power was reduced to ± 2 dB.

The AM/AM slope at the immediate vicinity of the operating point is 0.14 dB / dB. This means that the output power will change by approximately 0.14 dB for every 1 dB change in input power. The AM/PM slope at the immediate vicinity of the operation point is -2.1 deg. / dB. This means that that the insertion phase changes by approximately -2.1 degrees for every 1 dB change in input power. A second order polynomial makes for a reasonable approximation to fit the AM/AM and AM/PM curves results in:

$$V_{out} = -0.2969V_{in}^{\ 2} + 0.7441V_{in} + 0.5528 \tag{50}$$

$$\phi_{out} = -0.1014V_{in}^{\ 2} - 0.0640V_{in} - 0.1651 \tag{51}$$

where, $V_{in}$ is the input rms voltage normalized to the nominal operating point. $V_{out}$ is the output rms voltage normalized to the nominal operating point. $\phi_{out}$ is the output phase in degrees.

## 5.3 Characterizing Amplifier Behavior

The goal of the experiment is to characterize the amplifier's scalar gain and insertion phase over the duration of a CPI. This is defined as the amplifier behavior, and is influenced by previous waveforms. If the same waveform is repeated in perpetuity, then the expected amplifier behavior will be constant. However, if a multifunction sequence is fed to the amplifier the memory effects will manifest causing a change in the amplifier behavior.

To demonstrate this phenomenon a series of examples is discussed. The examples will use the waveforms listed in Table 5-6. The table shows two waveforms with significantly different characteristics. First, each waveform sequence is fed to the amplifier. This is analogous to a single function radar mode, where a single waveforms is transmitted by the radar for several CPI's (dwells). Second, the waveform will be combined, repeating the sequence of CPI1 and CPI2. Data is captured and processed showing the effect that one waveform causes on the other waveform.

Table 5-6: Waveform parameters used in example.

| Parameter: | CPI 1 | CPI 2 |
|---|---|---|
| Pulse Width (PW): | 10 microseconds | 50 microseconds |
| Duty Cycle (DC): | 8 % | 2 % |
| Pulse Repetition Frequency (PRF): | 8 kHz | 400 Hz |
| Coherent Processing Interval (CPI): | 4 milliseconds<br>32 pulses | 20 milliseconds<br>8 pulses |

### 5.3.1 CPI 1 in Single Waveform Sequences

Figure 5-22 shows the first waveform sequence used. Notice that CPI 1 is repeated in perpetuity. Each CPI contains 32 pulses, each having identical properties because all of the pulses within the CPI are identical. This ensures that the device reaches thermal equilibrium.

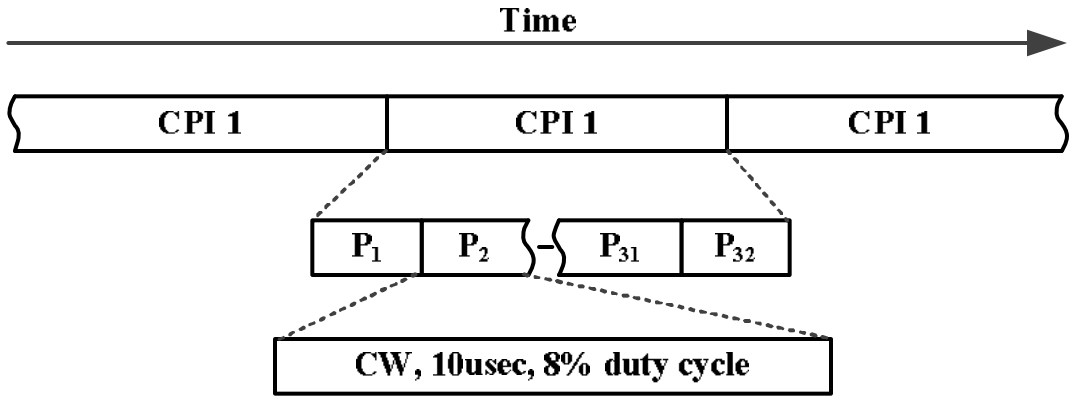


Figure 5-22: Single function sequence (CPI 1); a 10-microsecond pulse is repeated in perpetuity.

The characterization of the pulse envelope reveals distortions that are introduced to the transmitted signal. Figure 5-23 shows the power envelope of two consecutive pulses. Their amplitudes were normalized in reference to the first pulse. Notice that apart from system noise,

the pulses have identical shape and amplitude. The root mean square error is 0.005 V rms. Figure 5-24 shows the phase offset across the second pulse normalized to the first pulse. The root mean square error is 0.3 degrees rms. This is consistent with the available SNR discussed earlier in Section 5.1. Both Figures 5-23 and 5-24 show ringing in amplitude and phase, which is typical of Class AB high PAs. The important characteristic observed is that at steady state operation, any two consecutive pulses are identical in amplitude and phase.

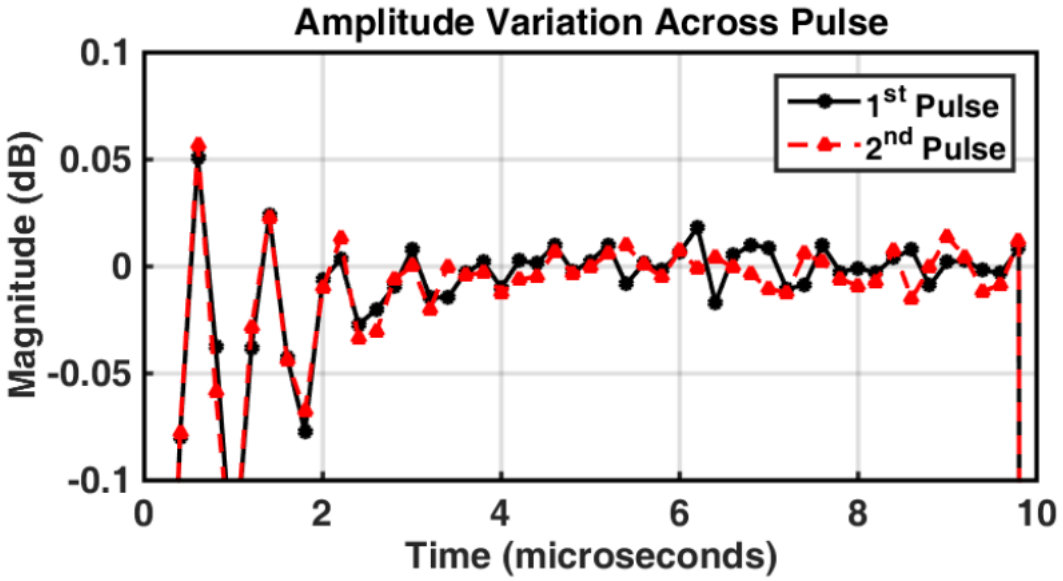


Figure 5-23: Amplitude variation across two consecutive pulses for CPI 1.

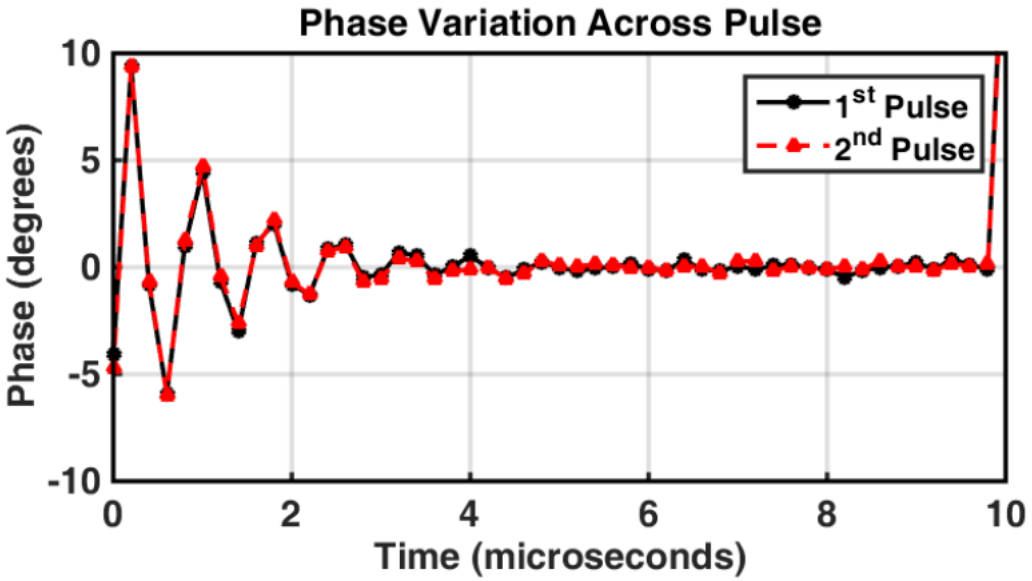


Figure 5-24: Phase variation across two consecutive pulses for CPI 1.

Following the procedure discussed in Chapters 2 and 3, Figures 5-25 and 5-26 show the amplitude and phase associated with the indexed cross-correlation peaks for the entire CPI 1 (WOI). Figure 5-25 shows the amplitude transient that occurs over the CPI. The figure shows 32 points at a periodic time interval that corresponds to the CPI's Pulse Repetition Interval (PRI). Each dot represents the change in the amplifier's scalar gain.

Figure 5-26 shows the phase transient that occurs over the WOI. Each dot represents the amplifier's insertion phase that resulted from the cross correlation technique. The first pulse in the sequence in used as the reference. Figures 5-25 and 5-26 show no observable amplitude or phase transients when a train of identical pulses is used; only system noise is observed. The physical meaning is that the amplifier experienced no appreciable change in complex gain.

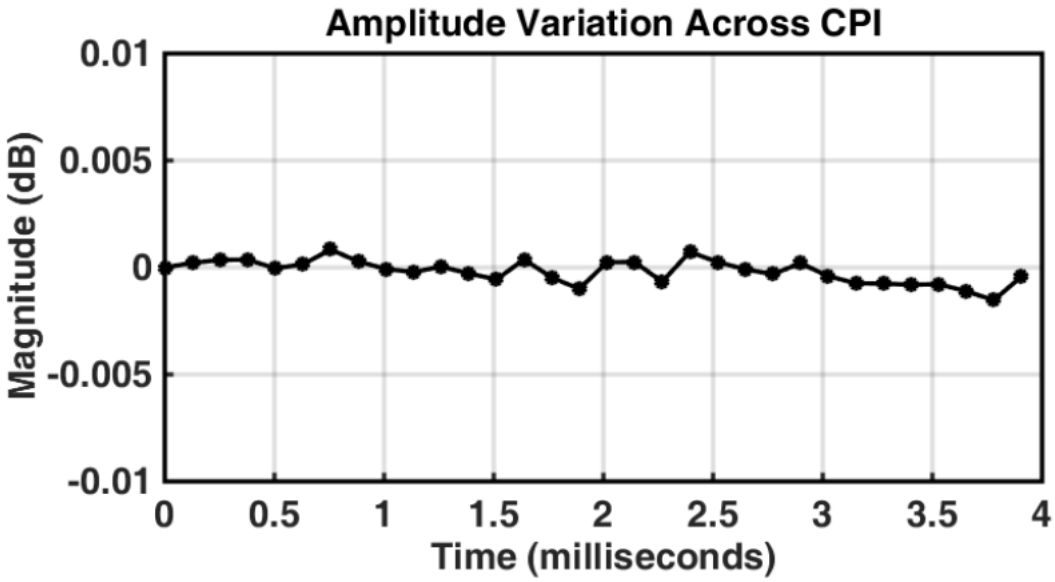


Figure 5-25: Magnitude of 40 averaged and normalized peak correlation results for CPI 1.

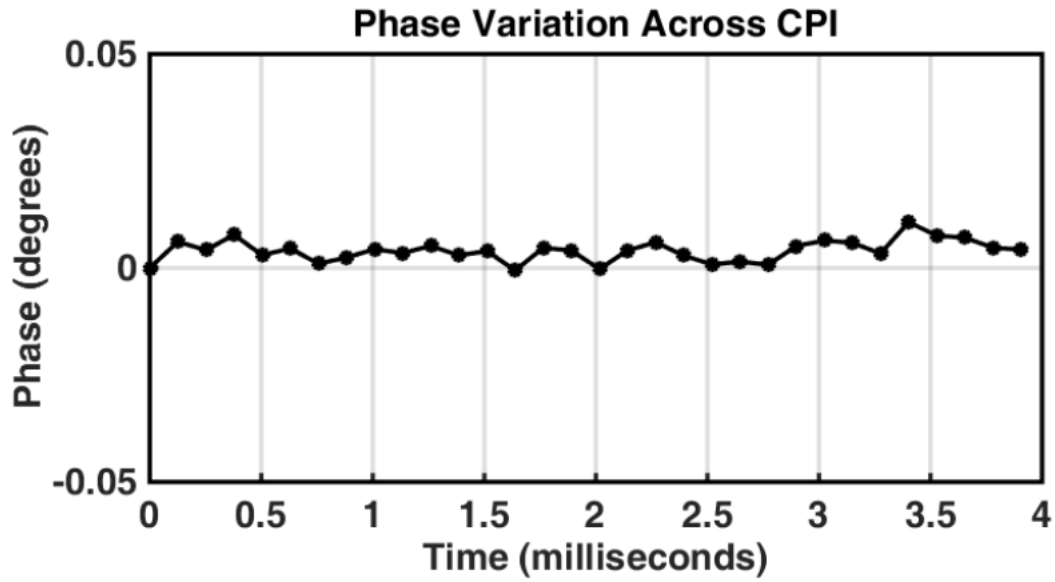


Figure 5-26: Phase of 40 averaged and normalized peak correlation results for CPI 1.

Figure 5-27 shows the DC power drawn by the amplifier during testing. The average power draw is 164.8 watts. The input power was estimated to be at 27.1 dBm (0.5 W), the

output power 48.9 dBm (78.5 W). The PAE was estimated to be 47.3 %. The PAE is slightly lower than the case for maximum PAE of 49.6 %.

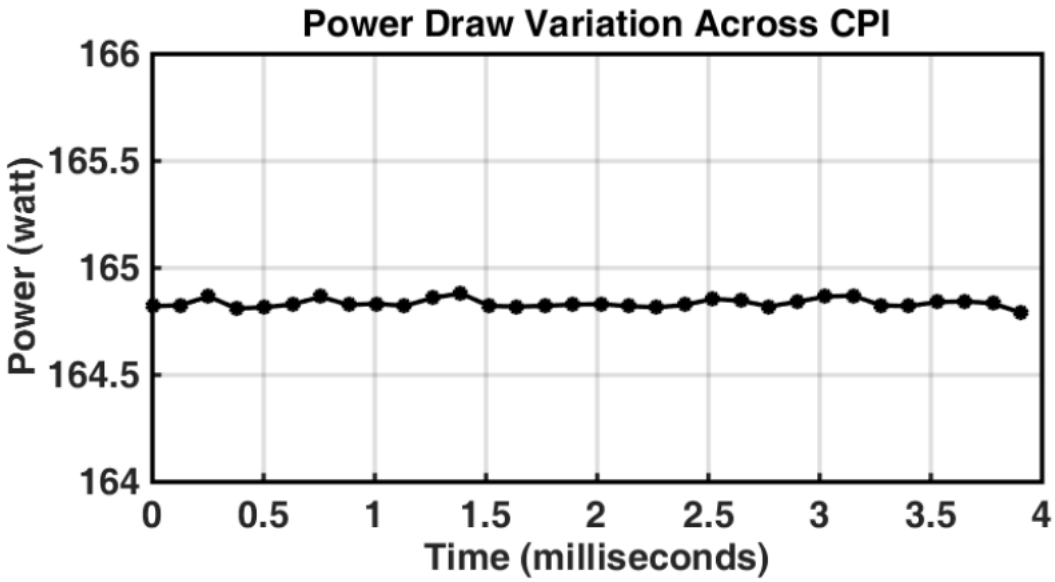


Figure 5-27: Amplifier DC power draw for each pulse in the single function sequence CPI 1.

Figure 5-28 shows the MTI Improvement Factor calculated from the amplitude and phase transient for several pulses in the waveform. The MTI Improvement Factor is limited by system noise to an average value of 82 dB.


Figure 5-28: CPI 1 Waveform MTI Improvement Factor limited due to SNR.

### 5.3.2 CPI 2 in Single Waveform Sequences

Figure 5-29 shows the second waveform sequence used, similar to the previous example. CPI 2 is selected as the WOI and repeated in perpetuity. Each CPI contains eight pulses, each having identical properties.

Figure 5-29: Single function sequence (CPI 2); a 50-microsecond pulse is repeated in perpetuity.

Figure 5-30 shows the power envelope of two consecutive pulses. The average amplitudes were also normalized in reference to the first pulse. Figure 5-31 shows the phase offset across the second pulse normalized to the first pulse. As previously shown, for a single pulse repeated in perpetuity, any two consecutive pulses are identical. The root mean square error is 0.006 V rms and 0.4 degrees.

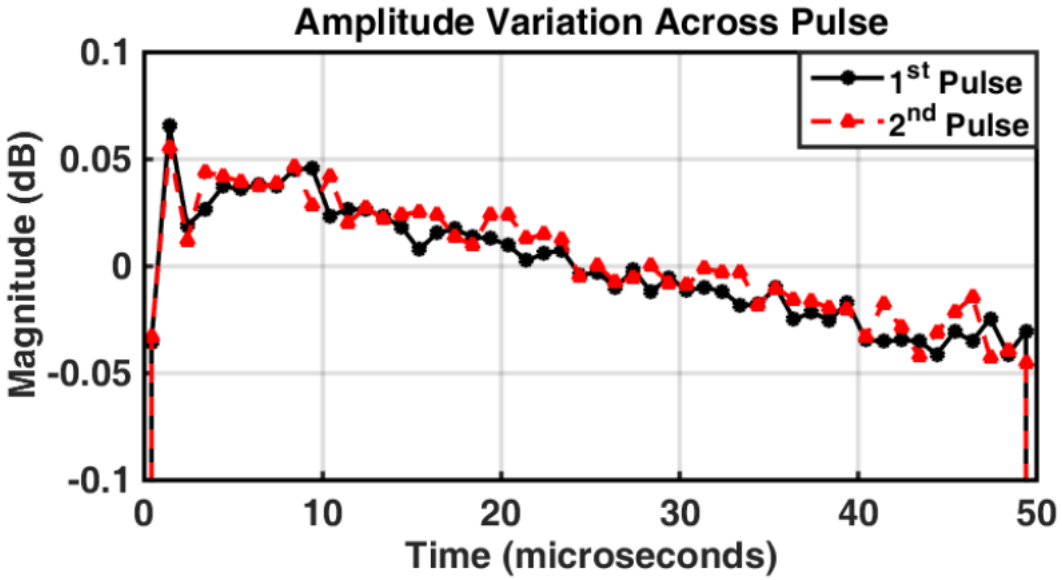


Figure 5-30: Amplitude variation across two consecutive pulses for CPI 2.

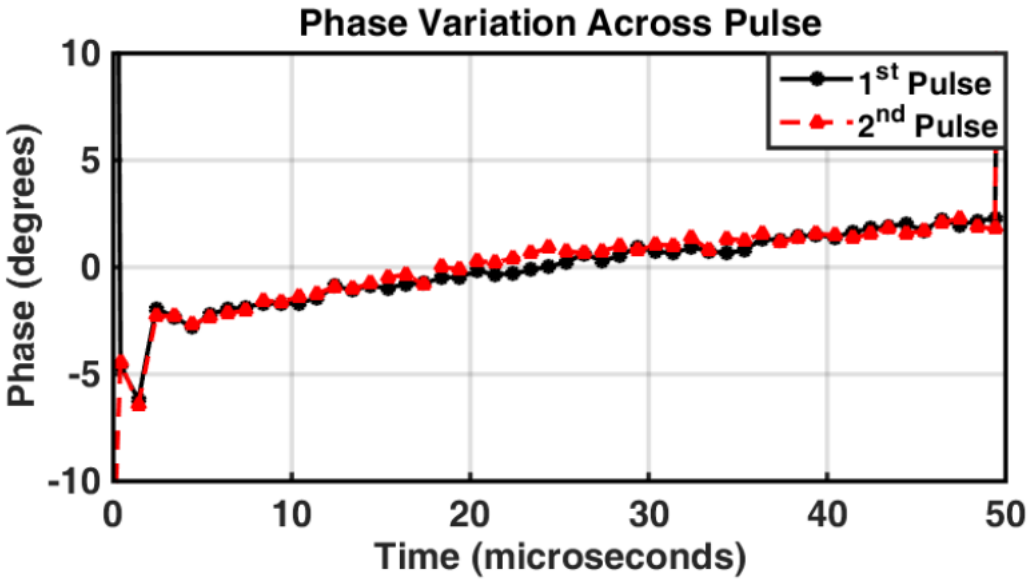


Figure 5-31: Phase variation across two consecutive pulses for CPI 2.

Figures 5-32 and 5-33 show the amplitude and phase associated with the indexed cross-correlation peaks for the entire CPI 2 (WOI). Figure 5-32 shows the amplitude transient that occurs over the CPI. The figure shows 8 points, one per pulse in the CPI, spaced by the Pulse Repetition Interval (PRI). Figure 5-33 shows the phase transient that occurs over the WOI. Each dot represents the amplifier's insertion phase that resulted from the cross correlation technique. Figures 5-32 and 5-33 show that the amplifier experienced no appreciable change in complex gain.

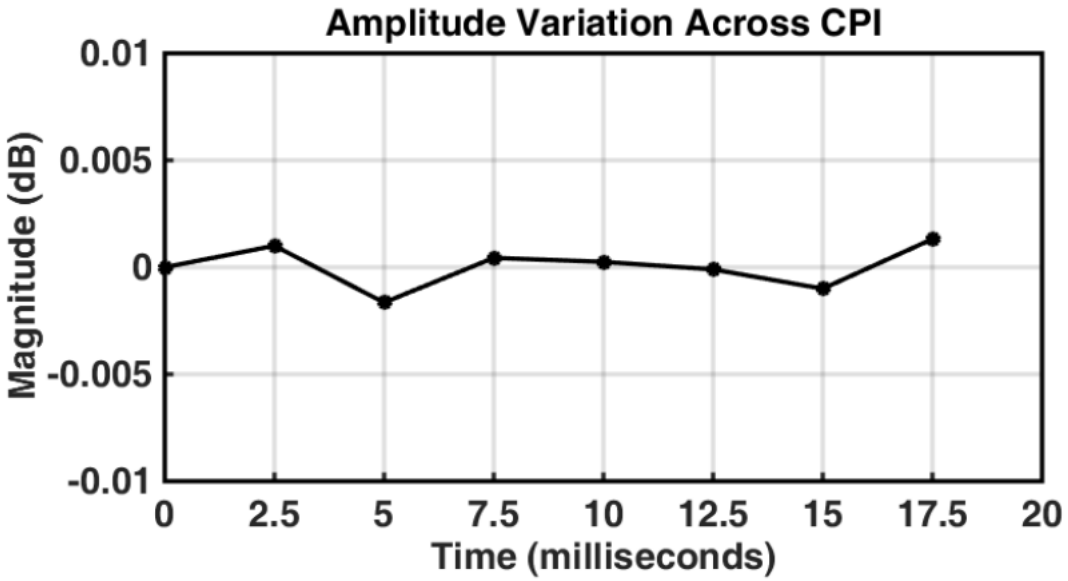


Figure 5-32: Magnitude of 40 averaged and normalized peak correlation results for CPI 2.

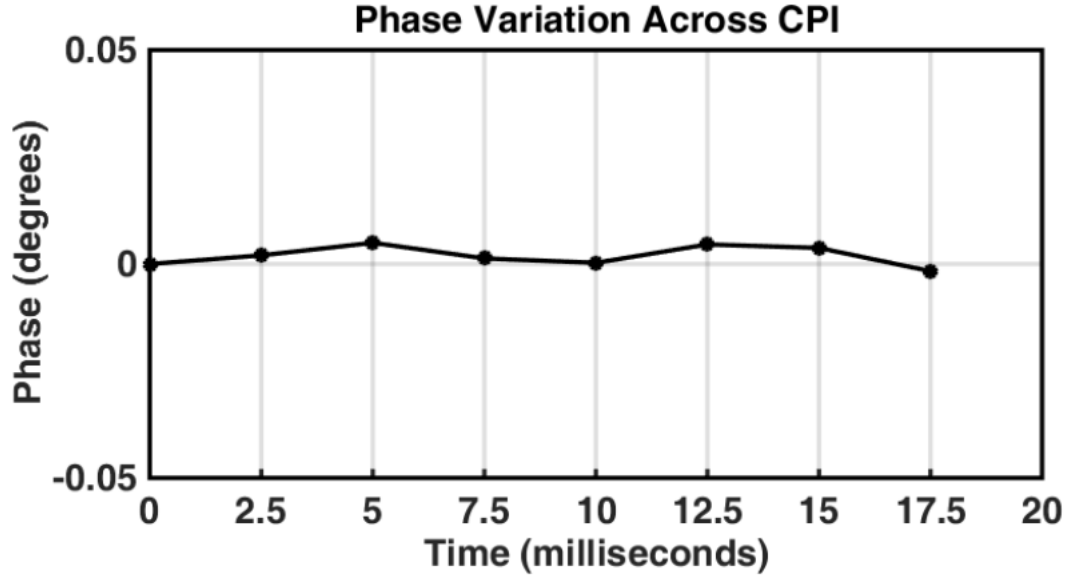


Figure 5-33: Phase of 40 averaged and normalized peak correlation results for CPI 2.

Figure 5-34 shows the DC power drawn by the amplifier during testing. The average power draw is 167.7 watts. The input power was estimated to be at 27.1 dBm (0.5 W), the output power 49.1 dBm (80.8 W). The PAE was estimated to be 47.9 %.

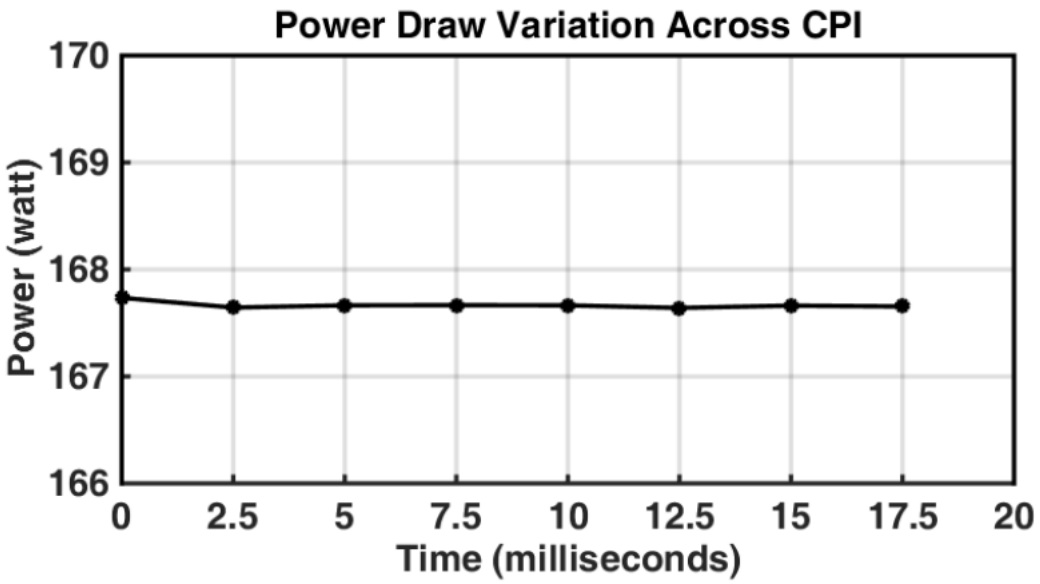


Figure 5-34: Amplifier DC power draw for each pulse in the single function sequence CPI 2.

Figure 5-35 shows the MTI Improvement Factor for several pulses in the waveform. The MTI Improvement Factor averages to 76 dB. The DFT method estimates the system SNR to be 78 dB.

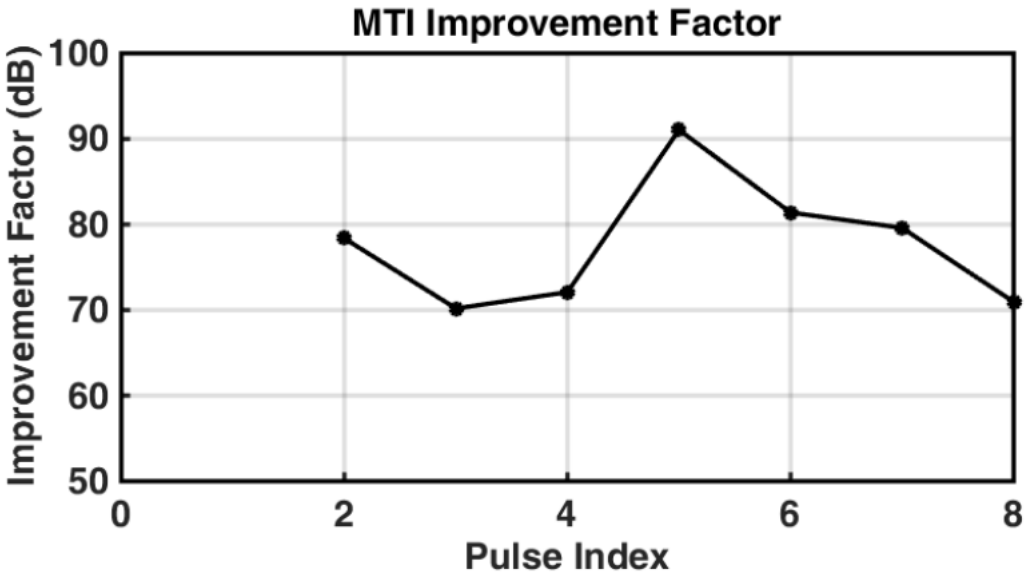


Figure 5-35: CPI 2 Waveform MTI Improvement Factor limited due to SNR.

### 5.3.3 Multifunction Waveform Sequence; observed amplifier behavior (CREE power amplifiers)

To emulate multifunction operations, the two CPIs listed in Table 5-6 are transmitted, one after the other in perpetuity. Figure 5-36 illustrate this concept. One at a time, each waveform is selected as the WOI and processed to observe the amplifier behavior. The following subsections show the results obtained.

Figure 5-36: Multifunction sequence.

#### *5.3.3.1 CPI 1 in Multifunction Sequence with CPI 2*

In this arrangement, CPI 1 is selected as the WOI. Following the procedure discussed earlier, Figures 5-37 and 5-38 show the amplitude and phase associated with the indexed cross-correlation peaks for the entire CPI 1 (WOI). Figure 5-37 shows the amplitude transient that occurs over the CPI. The figure shows 32 points at a periodic time interval that corresponds to the CPI's Pulse Repetition Interval (PRI). Each dot represents the change in the amplifier's scalar gain that occurs during the CPI. Figure 5-38 shows the phase transient that occurs over the WOI. Each dot represents the change in the amplifier's insertion phase.

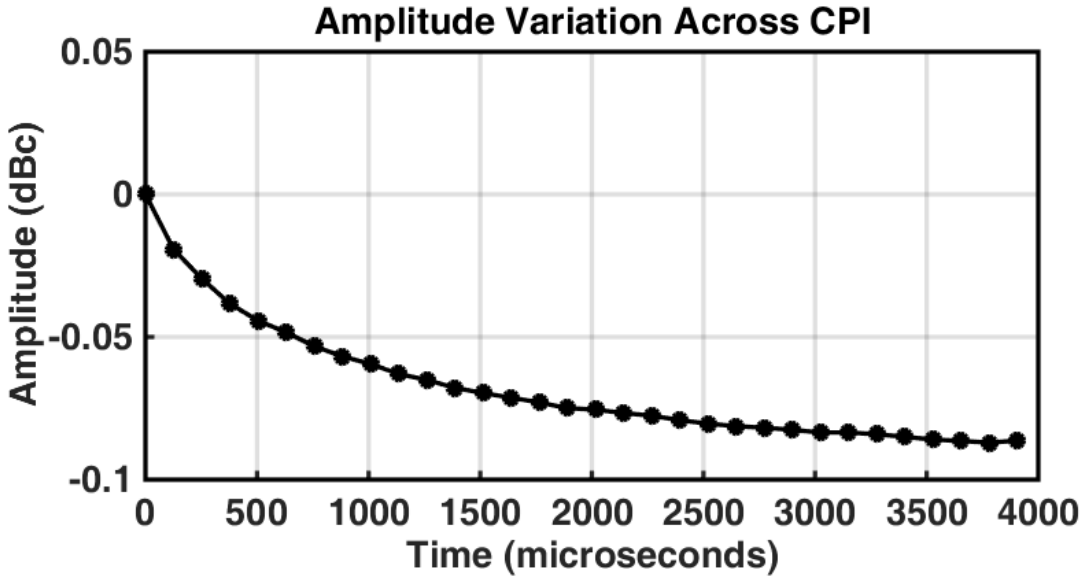


Figure 5-37: Scalar gain change during CPI 1 when preceded by CPI 2.

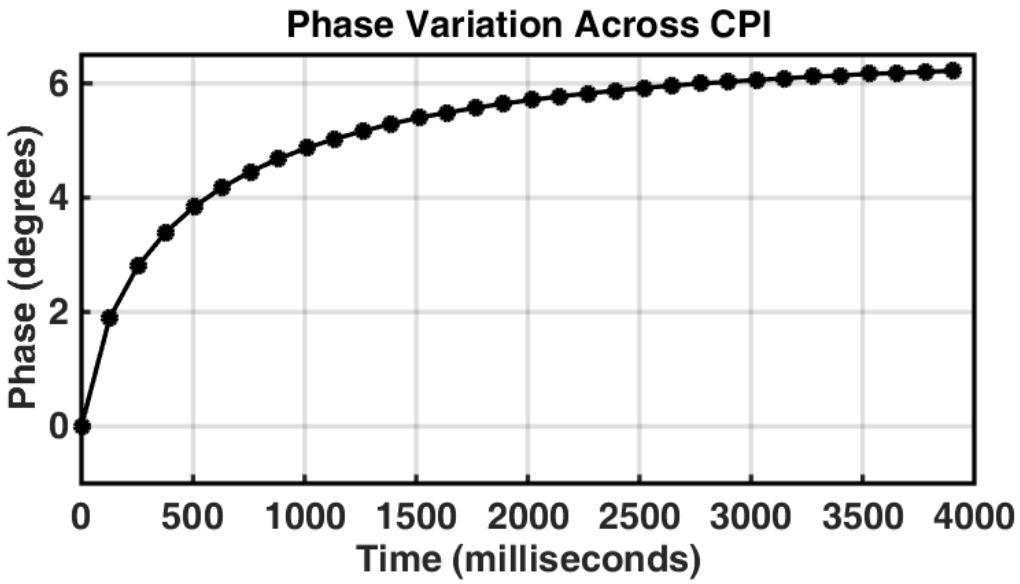


Figure 5-38: Insertion phase change during CPI 1 when preceded by CPI 2.

Figure 5-37 shows the amplitude transient, which causes a drop in scalar gain, and a drop in output power. If the amplifier's Power Added Efficiency stays constant during this period, it necessarily means that the power draw is reduced. This can be seen in the measured power draw on Figure 5-39. A comparison between the expected and measured power draw suggests that the PAE dropped only by 0.1% during the CPI 1, from 47.6% to 47.5 %. Earlier in Section 5.3.1 the PAE was estimated to 47.3%.

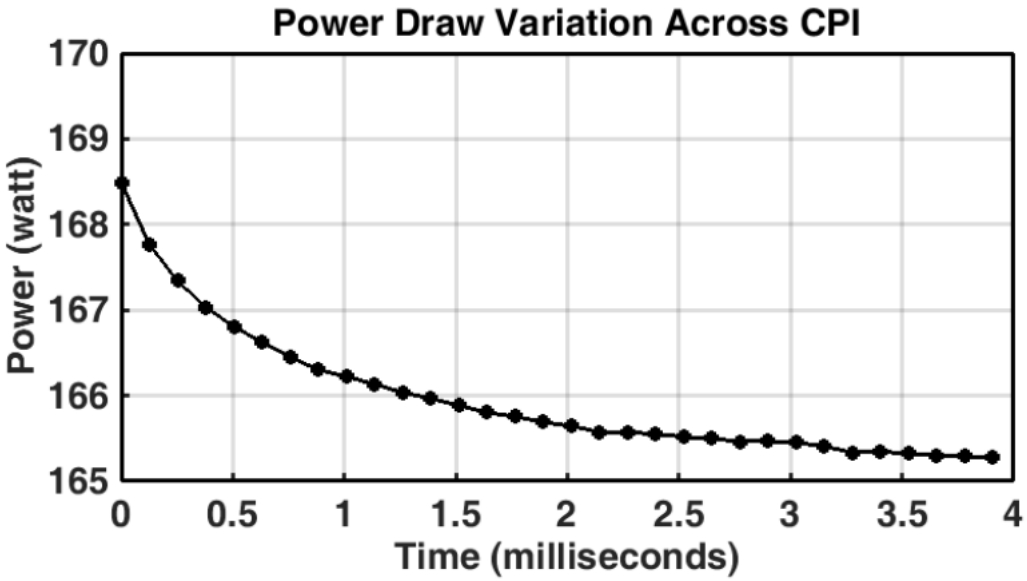


Figure 5-39: Power drawn transient during CPI 1 when preceded by CPI 2.

Figure 5-40 shows the MTI Improvement Factor limitation due to the transients. Earlier, for the single function CPI 1, the MTI Improvement Factor was shown to be limited by noise, with an average value of 82 dB. Now the MTI Improvement Factor is limited by the change in the amplifier scalar gain and insertion phase. The MTI Improvement Factor is sharply limited at the beginning of the CPI to more than four orders of magnitude worse than the limit due to SNR.

As an example, Figure 5-40 shows a threshold for the MTI Improvement Factor, set to 53 dB. If a radar system requirements call for enough system stability to achieve an MTI Improvement Factor of better than 53 dB, then the radar will not be in compliance with this requirement until after the twelfth pulse is transmitted. It took approximately 1.4 milliseconds for the transients to decay to an acceptable level.

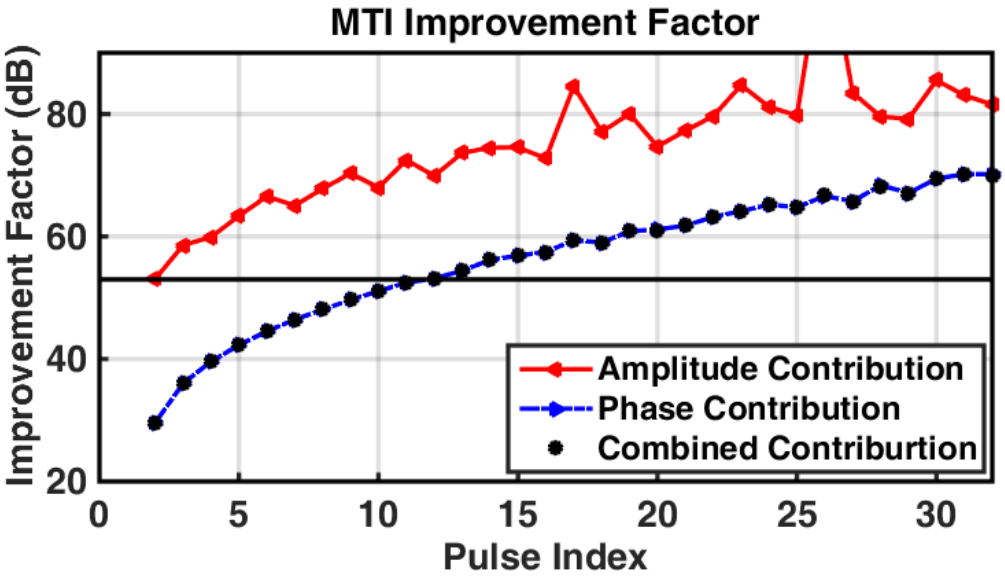


Figure 5-40: Limitation in MTI Improvement Factor due to amplifier behavior. The amplifier transmits CPI 1, but its complex gain is affected by multifunction operations, causing instabilities in CPI 1.

The amplifier's amplitude and phase transient is separated to observe the contribution to the MTI Improvement Factor. The graph shows that the instability introduced by the phase transient is several orders of magnitude worse than the amplitude transient. In this example, the instability introduced by the amplitude transient is of small enough magnitude to achieve the required MTI Improvement Factor at the beginning of the CPI.

#### *5.3.3.2 CPI 2 in Multifunction Sequence with CPI 1*

In this arrangement, CPI 2 is selected as the WOI. Using the test methods discussed earlier in Section 5.3, the results for scalar gain, insertion phase and power draw transients, as well as resulting MTI Improvement Factor are shown below.

Figures 5-41 and 5-41 show the amplitude and phase transient associated with the indexed cross-correlation peaks for the entire CPI 2 (WOI). Figure 5-41 shows the amplitude transient that occurs over the CPI. The figure shows 8 points at a periodic time interval that

corresponds to the CPI's Pulse Repetition Interval (PRI). Each dot represents the change in the amplifier's scalar gain that occurs during the CPI. Figure 5-42 shows the phase transient that occurs over the WOI. Each dot represents the change in the amplifier's insertion phase.

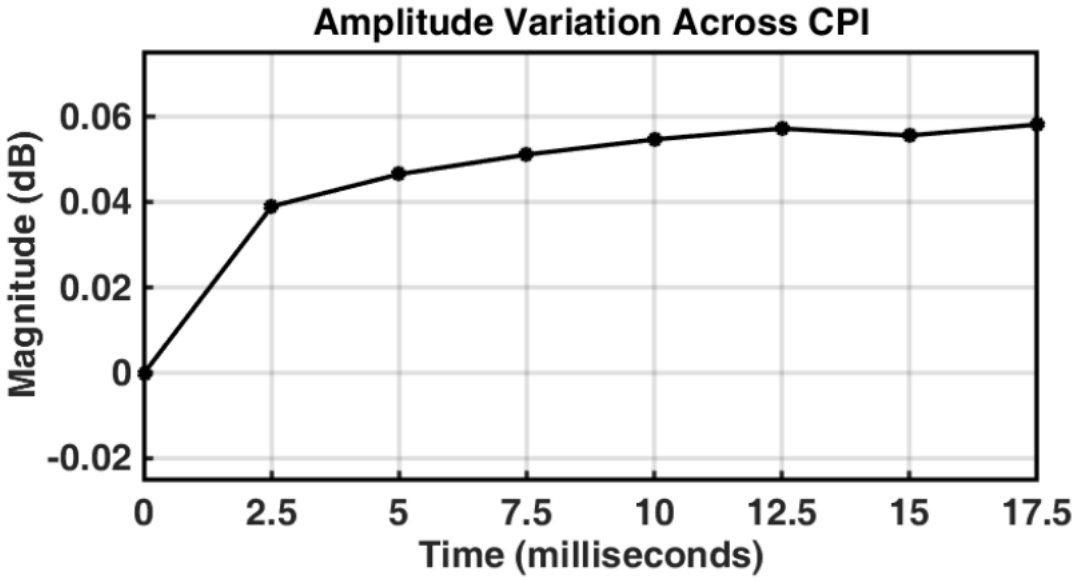


Figure 5-41: Scalar gain transient during CPI 2 when preceded by CPI 1.

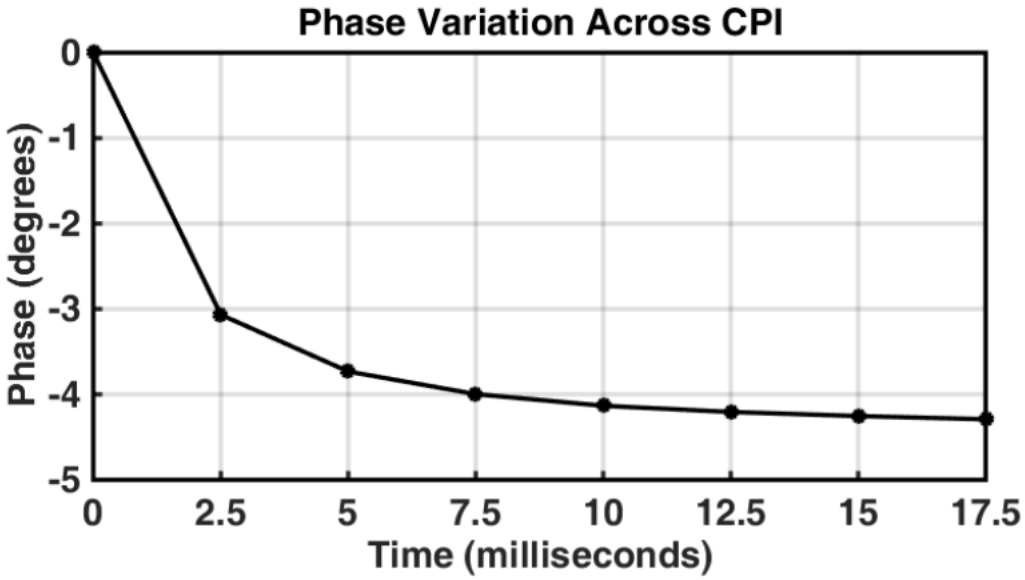


Figure 5-42: Insertion phase transient during CPI 2 when preceded by CPI 1.

Figure 5-43 shows the power draw variation over CPI2. The PAE increased by 0.1% during the CPI 2, from 47.8 % to 47.9 %.

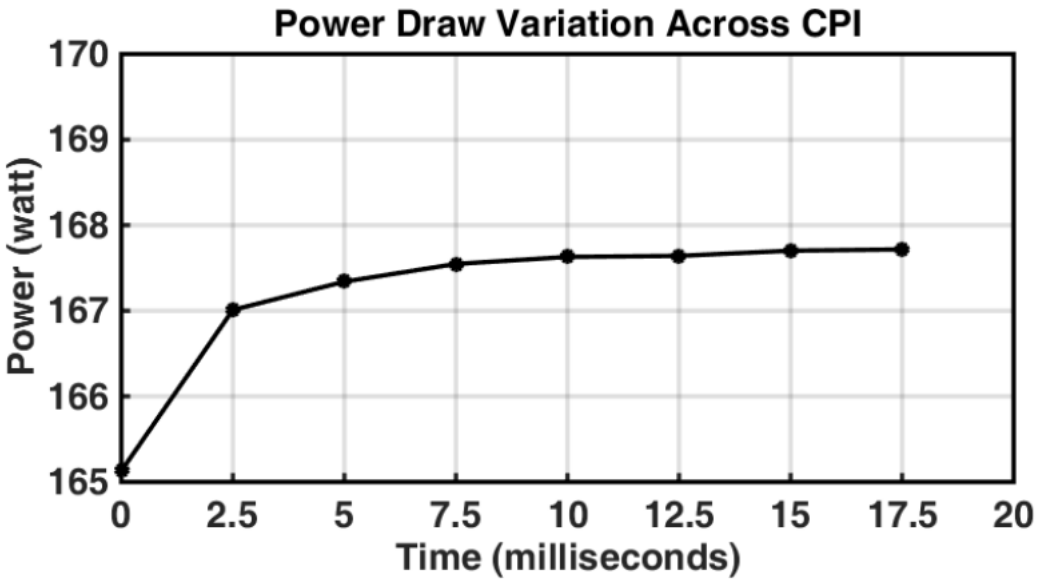


Figure 5-43: Power drawn transient during CPI 2 when preceded by CPI 1.

Figure 5-44 shows the MTI Improvement Factor limitation due to the transients. Earlier, for the single function CPI 2, the MTI Improvement Factor was shown to be limited by noise, with an average value of 78 dB. Following the requirement for a threshold of 53 dB, the radar will not be in compliance with this requirement until after the sixth pulse is transmitted. It took approximately 12.5 milliseconds for the phase transient to decay to an acceptable level.

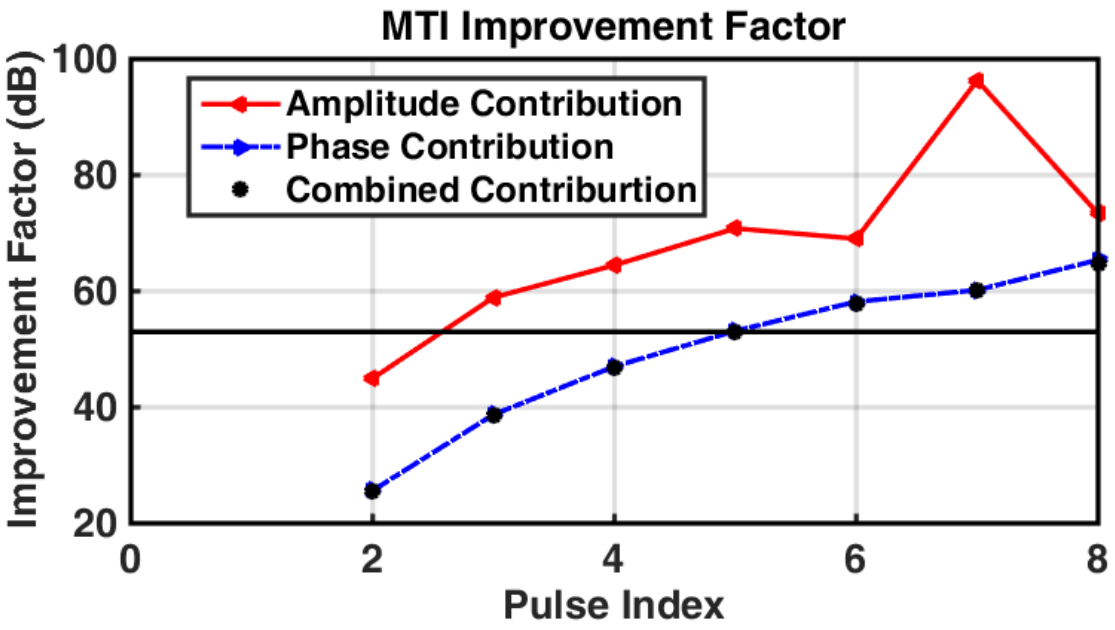


Figure 5-44: Limitation in MTI Improvement Factor during CPI 2 due to amplifier behavior, when preceded by CPI 1.

#### *5.3.3.3 Observed behavior for several multifunction sequences*

Section 5.3.3.1 showed the behavior of the amplifier complex gain when CPI 1 was preceded by CPI 2. The complex gain exhibits a similar behavior when other waveforms are used as preceding waveform to CPI 1. To demonstrate this, two sets of waveforms were selected for the test. Remembering that CPI 1 is formed by 32 pulses, each pulse is 10 microseconds in duration and the pulse repetition interval is 125 microseconds, corresponding to eight percent duty cycle. The first set of waveforms had equal duty cycle to CPI 1, and pulse widths of two, six, 10, 13, 36 and 50 microseconds. The second set of waveforms had equal pulse width to CPI 1, and duty cycle of two, five, eight, 12, 16 and 20 %. On both cases, the number of pulses within each waveform was adjusted to achieve a 20 millisecond CPI. Only eight captures per waveforms were processed.

##### 5.3.3.3.1 Multifunction sequences with equal duty cycle (8%)

Figure 5-45 shows the gain variation across CPI 1. In this instance, only the preceding waveform pulse width was changed. For preceding waveforms with pulse width of 36 or 50 microseconds, the gain transient is clearly visible. However, for pulse width smaller than 36 microseconds, the transient becomes difficult to see, due to limitations in SNR. The change in scalar gain is insignificant.

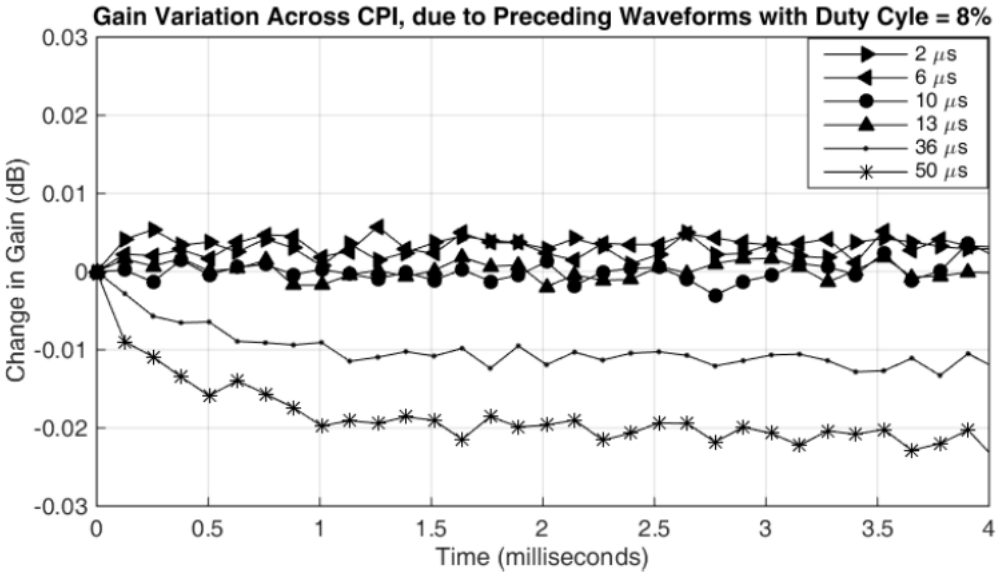


Figure 5-45: Gain variation across CPI 1 due to several preceding waveforms. The preceding waveform pulse width was changed among several values (two, six, 10, 13, 36 and 50 microseconds), the duty cycle was kept at a constant 8%.

Figure 5-46 shows insertion phase variations across CPI 1. In this instance, a phase change is observable in all combinations of pulse width tested. This is a significant find, since maintaining a constant duty cycle does not guarantees that transients are avoided. The premise has been that since the waveforms maintain a constant duty cycle, the dissipated heat and thus channel temperature remains constant. This however, this is not the case, due to nonlinearities in gain/temperature relationship.

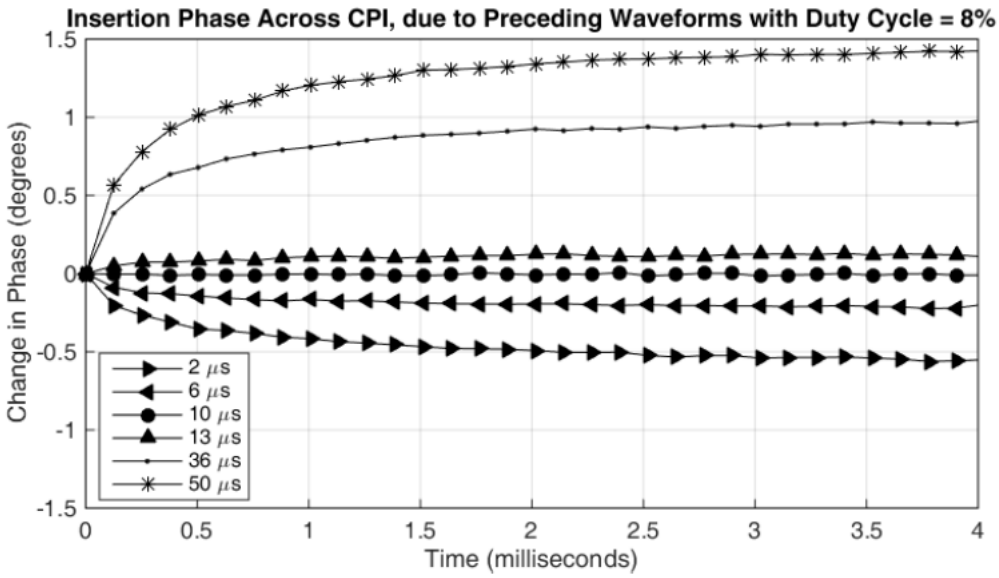


Figure 5-46: Insertion phase variation across CPI 1 due to several preceding waveforms. The preceding waveform pulse width was changed among several values (two, six, 10, 13, 36 and 50 microseconds), the duty cycle was kept at a constant 8%.

Figure 5-47 shows the MTI Improvement Factor for all the multifunction waveforms with constant duty cycle. Evaluating the 53 dB MTI Improvement Factor threshold, the preceding waveforms with 13, 36 and 50 microsecond pulse width produce transients that take from 3 to 5 pulses to decay to acceptable levels.

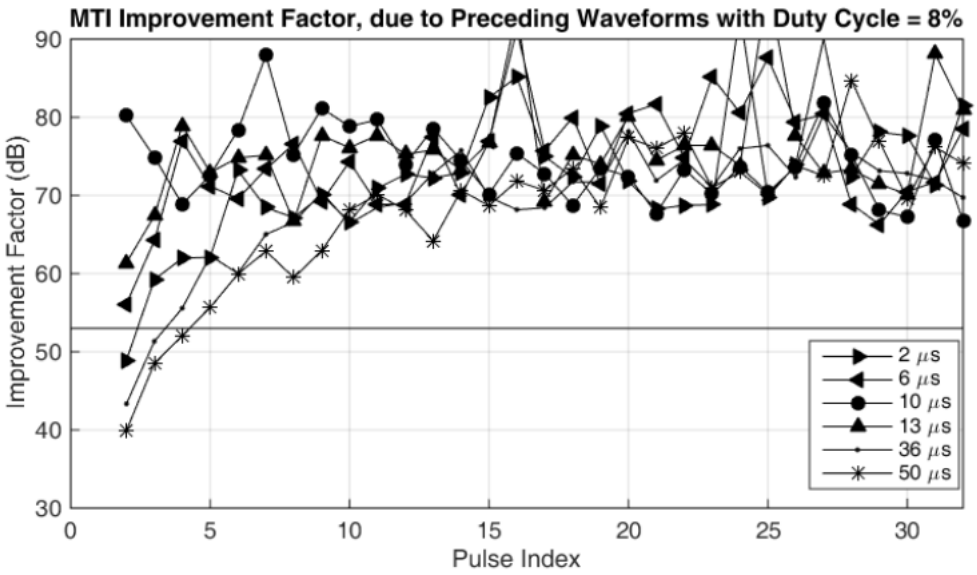


Figure 5-47: Limitation in MTI Improvement Factor due to amplifier behavior. Changes in duty cycle dramatically affect the achievable MTI Improvement Factor.

#### 5.3.3.3.2 Multifunction sequences with equal pulse width (10 microseconds)

Figure 5-48 shows the gain variation across CPI 1. In this instance, only the preceding waveform duty cycle was changed. A gain transient is clearly visible for all combinations of duty cycle. Figure 5-49 shows the insertion phase variations across CPI 1. Here the phase change is also observed in all combinations of duty cycle tested.

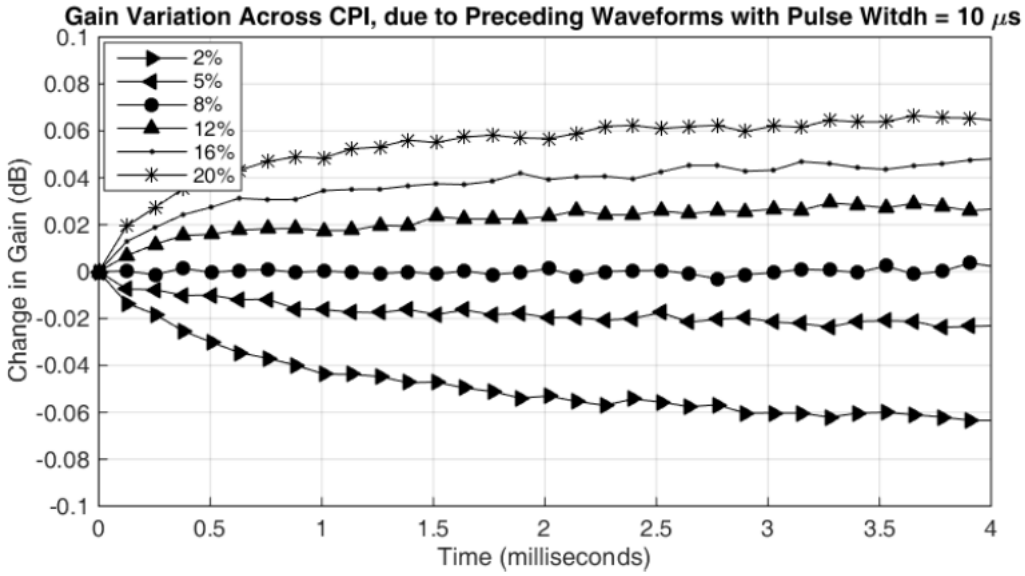


Figure 5-48: Gain variation across CPI 1 due to several preceding waveforms. The preceding waveform pulse width was kept at 10 microseconds, the duty cycle was changed among several values (two, five, eight, 12, 16 and 20 %).

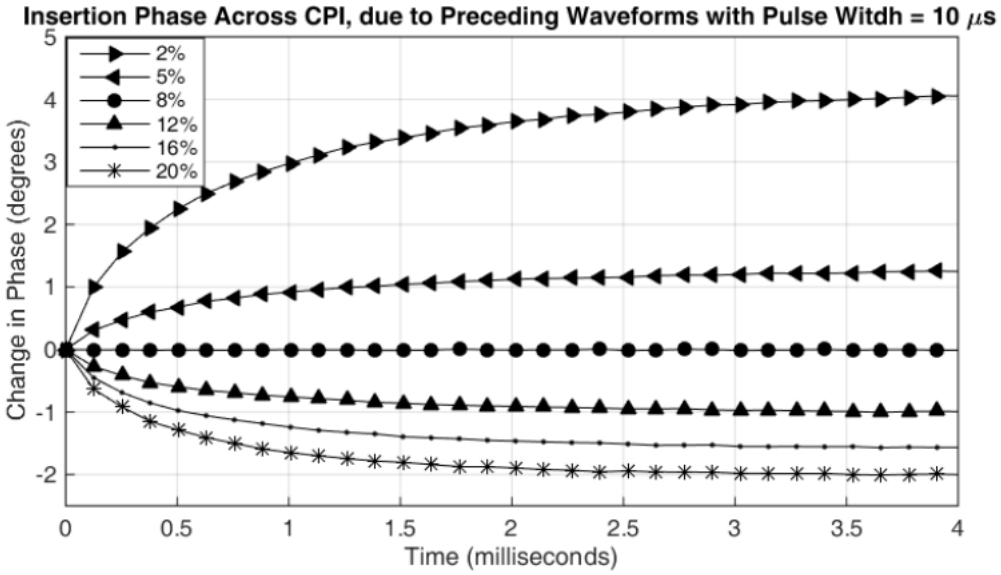


Figure 5-49: Insertion phase variation across CPI 1 due to several preceding waveforms. The preceding waveform pulse width was kept at 10 microseconds, the duty cycle was changed among several values (two, five, eight, 12, 16 and 20 %).

Figure 5-50 shows the MTI Improvement Factor for all the multifunction waveforms with constant pulse width. Evaluating the 53 dB MTI Improvement Factor threshold, indicates that all preceding waveforms with duty cycle different from CPI 1 introduce undesirable transients.

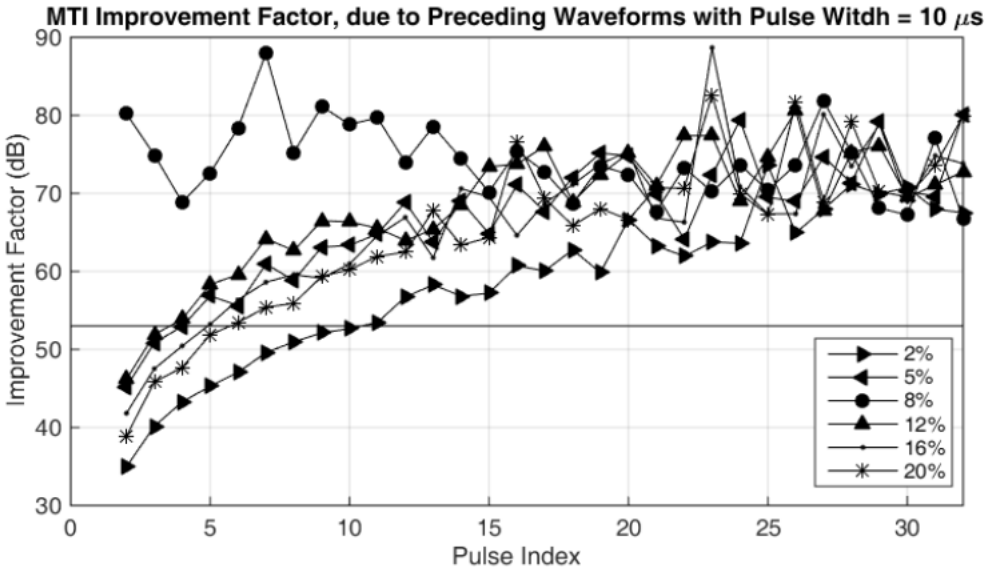


Figure 5-50: Limitation in MTI Improvement Factor due to amplifier behavior. The MTI Improvement Factor appears to be less sensitive to changes in the preceding waveform pulse width.

Thus far, the scalar gain and insertion phase transient has been characterized. The MTI Improvement Factor performance metric indicate that insertion phase disturbances are significantly more detrimental to radar performance than the gain transients are. Often the insertion phase transient limits the available Improvement Factor by 20 dB more than the limits imposed by the gain transient. This is a significant discrepancy.

## 5.4 Chapter Summary

The measurement system noise was quantified at various steps along the signal processing chain. This showed that the measurement system provides enough SNR to accurately characterize the amplitude and phase transients, and quantify a hypothetical radar system

instability.

The amplifier operating point was found and maintained throughout multiple data collection. This is a fundamental step to ensure that the amplifier is experiencing condition equivalent to those encountered during normal radar operations. A well defined operating point is very important during the characterization of the amplifier's AM/AM and AM/PM conversion, since the extracted coefficients are sensitive to input power, as well as the characterization of the amplifier's behavior for subsequent predistortion.

The amplifier behavior was observed for several combinations of waveforms. It was found that amplitude and phase transients are most sensitive to the preceding waveform's duty cycle, and that the phase transient is much more sensitive than the amplitude transient.

# Chapter 6. Development of a Behavioral Model

This Chapter introduces a new behavioral model intended to replicate the change in complex gain observed in the DUT based on the previous stimuli. The model presented is at the baseband envelope domain post pulse-compression (cross-correlation) level, which is appropriate for pulse radar applications. The model parameters are stored in a lookup table for later use. No information regarding either the device's internal design or its physics is needed to develop a model that will accurately describe the behavior of the DUT excited with a known stimulus.

Pulse radar waveforms are selected from a large library, and are almost exclusively constant envelope in order to maximize output power and efficiency. This investigation used known stimuli to excite the DUT to various states for parameter extraction. The behavioral model must predict the outcome of any possible combination of waveforms, within the dimensional space of the waveforms, tested with a memory window limited to 20 milliseconds. The memory window was determined experimentally, as this memory will depend on the behavior of the selected amplifier and the system-specific parameters.

## 6.1 Power Amplifier Behavior

In Chapter 5, multiple waveform were fed to the amplifier as a way to assess its behavior. The change in scalar gain and insertion phase clearly resemble a time decaying function that asymptotically approaches a steady state value. This steady state value is in reality the nominal gain and insertion phase of the device during WOI.

Chapter 2 established that these transients are primarily related to electrothermal memory effects and thus to thermal transients that occur within the device. With this idea in mind, it makes sense to seek for equations or circuit topologies typically used to fit and model thermal

transients.

### 6.1.1 Foster Network

A resistor-capacitor (RC) tank configuration (Foster Ladder Network topology) was chosen to model the observed behavior. The Foster topology is widely used as a thermal equivalent circuit to model system's thermal transient response. This is due to the analogy between Fourier's Law and Ohm's law, where the rate of heat flow ($Q$) is to current ($I$), temperature difference ($\Delta T$) is to voltage ($\Delta V$), thermal resistance ($\theta$) is to resistance ($R$) and thermal capacitance ($C$) is to capacitance ($C$). Figure 6-1 shows a Foster ladder network.

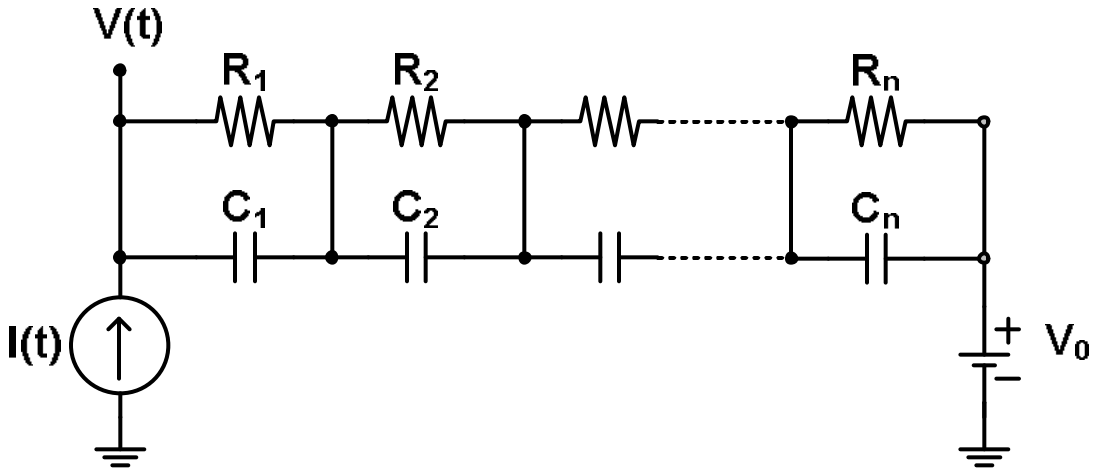


Figure 6-1: Foster network topology adopted to model amplifier behavior.

For a circuit with only two tank circuits (time-constants), the curve of temperature $V(t)$ is described by the following equation:

$$V(t) = R_1 I(t)\left(1-\exp\left(\frac{-t}{R_1 C_1}\right)\right) + R_2 I(t)\left(1-\exp\left(\frac{-t}{R_2 C_2}\right)\right) + V_0 \qquad (52)$$

where, $I(t)$ is the dissipated power in watts, and the resistance and capacitance are found via curve fitting techniques to replicate simulated or measured temperature profiles.

### 6.1.2 Adapting Foster Network as Behavioral Model

The properties intended to be modeled are the scalar gain change and the insertion phase change across a CPI. Each property is modeled separately. The gain change is modeled in volts, while the insertion phase is modeled in radians per second.

The first adaptation is to convert equation (52) into its discrete-time form:

$$V[n] = R_1 I[n]\left(1-\exp\left(\frac{-(n-1)}{PRF}\frac{1}{R_1C_1}\right)\right) + R_2 I[n]\left(1-\exp\left(\frac{-(n-1)}{PRF}\frac{1}{R_2C_2}\right)\right)+V_0 \tag{53}$$

Where, the sampling rate is chosen to be the CPI waveform Pulse Repetition Frequency (PRF). The pulse index *n* has values of *1,2,3,…,N*, were *N* is the number of pulses in the CPI.

Equation (53) is simplified by making $I[n]=1$, grouping all constants into a single variable *c*, and replacing the time constant $R_1C_1$ for $\tau_1$ and $R_2C_2$ for $\tau_2$:

$$V[n] = -P_1\exp\left(\frac{-(n-1)}{PRF}\frac{1}{\tau_1}\right) - P_2\exp\left(\frac{-(n-1)}{PRF}\frac{1}{\tau_2}\right)+c \tag{54}$$

### 6.1.3 Modeling Complex Gain Change

Throughout this dissertation, the complex gain transient is expressed as changes in scalar power gain in decibels, and changes in insertion phase in degrees. This was done by convention and for clarity.

The complex gain behavior results from evaluating equation (27) $G_{CC}(n)$. The value of $G_{CC}$ for the $n^{th}$ index is a complex number, which is later separated into its magnitude in volts and phase in radians per second. To model the gain transient, Equation (54) is rewritten to model $A[n]$:

$$\begin{aligned} A_m[n] = &-P_{1A}\exp\left(\frac{-(n-1)}{PRF}\frac{1}{\tau_{1A}}\right) \\ &-P_{2A}\exp\left(\frac{-(n-1)}{PRF}\frac{1}{\tau_{2A}}\right)+c_A \end{aligned} \tag{55}$$

where, $A_m[n]$ is the modeled transient gain change in volts, for the $n^{th}$ pulse in the CPI, $n = 1, 2, 3, \mathrm{K}, N$. $PRF$ is the correspondent CPI waveform pulse repetition interval. The time constants $\tau_1$ and $\tau_2$ are in the order of hundreds of microseconds and milliseconds, respectively. Variables *P's* and $c$ are a function of the preceding waveform's pulse width and duty cycle.

The insertion phase behavior exhibits a more complex behavior than the gain. The phase transient is better represented by adding a third time-constant stage to the Foster network. The insertion phase is then modeled by $\phi[n]$:

$$\begin{aligned} \phi_m[n] = &-P_{1\phi}\exp\left(\frac{-(n-1)}{PRF}\frac{1}{\tau_{1\phi}}\right) \\ &-P_{2\phi}\exp\left(\frac{-(n-1)}{PRF}\frac{1}{\tau_{2\phi}}\right) \\ &-P_{3\phi}\exp\left(\frac{-(n-1)}{PRF}\frac{1}{\tau_{3\phi}}\right)+c_\phi \end{aligned} \tag{56}$$

where, $\phi_m[n]$ is the insertion phase change in radians per seconds, for the $n^{th}$ pulse in the CPI. The time constants $\tau_1$, $\tau_2$ and $\tau_3$ are in the order of dozens of microseconds, hundreds of

microseconds and milliseconds, respectively. Variables *P's* and *c* are a function of the preceding waveform's pulse width and duty cycle.

## 6.2 Model Fitting and Validation

### 6.2.1 Fitting Data to Model

Recalling the transients discussed in Section 5.3.3.1 Figure 5-37, where CPI 2 preceded CPI 1, causing an amplitude and phase transient during CPI 1. CPI 1 is the collection of 32 pulses, each 10 microseconds long at eight percent duty cycle. CPI 2 is the collection of eight pulses, each 50 microseconds long at two percent duty cycle. Figure 6-2 shows the (power) gain transients for clarity of discussion, its corresponding voltage gain is shown in Figure 6-3.

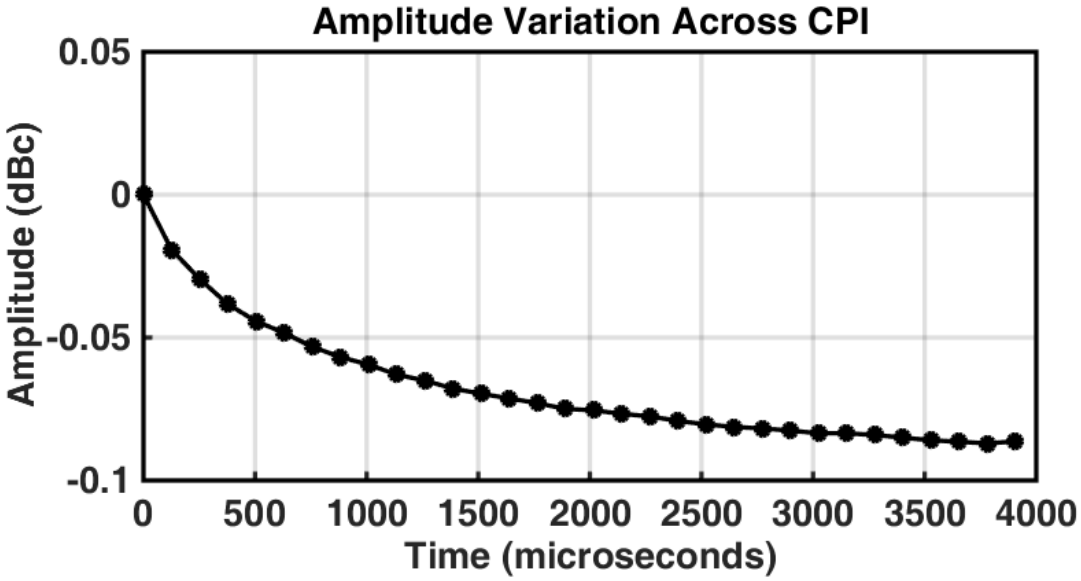


Figure 6-2: Recalling the scalar gain transients during CPI 1 when preceded by CPI 2.

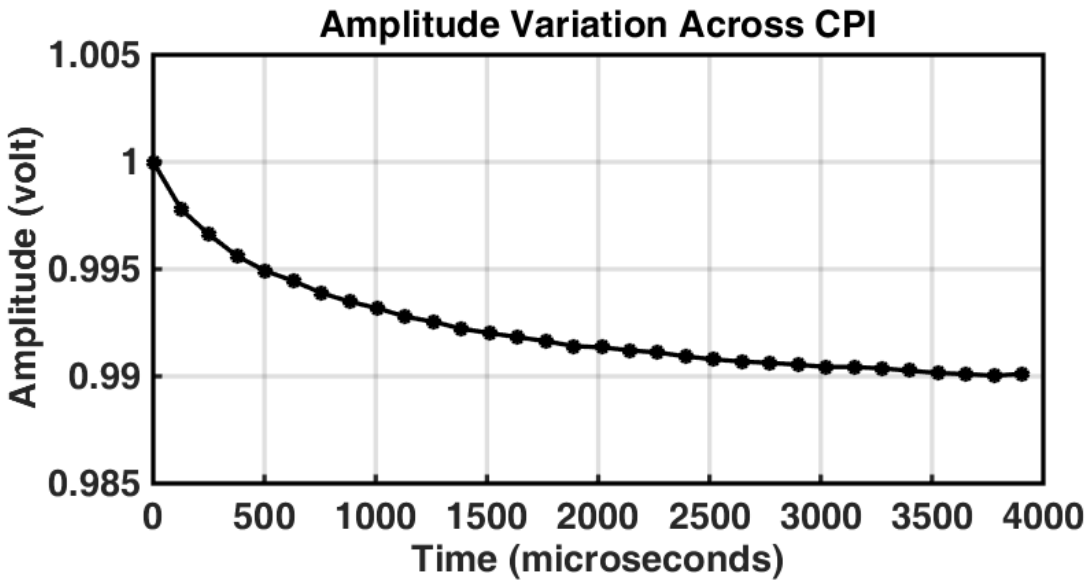


Figure 6-3: Scalar gain transients expressed in volts, during CPI 1 when preceded by CPI 2.

Equation (55) represents the normalized voltage gain, thus it is numerically solved to fit the trace data from Figure 6-3. To accelerate the numerical fitting, various initial estimates for $P_1$, $P_2$ and $c$ are found directly from the measured transient curves. Estimating initial values for the time constants $\tau_1$ and $\tau_2$ is more complex. However, experiments suggest that a good starting point is 250 microseconds for $\tau_1$ and 2 milliseconds for $\tau_2$.

To find the parameters for the gain change model $A_m[n]$, first the value of $c_A$ is approximated to one. It is refined by knowing that $A_m[1]$ is equal to 1 volt, and $A_m[32]$ is approximately equal to 0.99 volts. Figure 6-3 shows gain change has not reached steady state. Since the gain is decreasing, this tells us that the value of $c_A$ will be smaller than 0.99, however 0.99 is a good starting point. The other two coefficients, $P_{1A}$ and $P_{2A}$, contribute to the difference between the beginning of the CPI and the end. That difference is approximately -10 millivolts. A good starting point is found by equally dividing the contributions to approximately -5 millivolts each for $P_{1A}$ and $P_{2A}$. Numerically solving Equations (55) shows that $P_{1A}$ = -4.6

millivolts, $P_{2A}$ = -7.1 millivolts, and $c_A$ = 988.3 millivolts. The time constants are $\tau_{1A}$ = 261 microseconds and $\tau_{2A}$ = 1.88 milliseconds.

Following the steps described above, the insertion phase model $\phi_m[n]$ expressed in radians per second has parameters; $P_{1\phi}$= -16.3 mrad/s, $P_{2\phi}$ = -46.8 mrad/s, $P_{3\phi}$ = -48.4 mrad/s, and $c_\phi$ = 101.6 mrad/s. The time constants were $\tau_{1A}$ = 61 microseconds, $\tau_{2A}$ = 341 microseconds and $\tau_{3A}$ = 1.47 milliseconds.

### 6.2.2 Model Validation

The model was validated with a new set of measured data. The model error is the difference between the measured data and the model output. A quality number used for comparing the model to the measured data is the Normalized Mean Square Error expressed in decibels; shown in Equation (57):

$$NMSE_{dB} = 10 \times Log_{10}\left( \frac{\sum_{n=1}^{N} \left| y_{meas}[n] - y_{model}[n] \right|^2}{\sum_{n=1}^{N} \left| y_{meas}[n] \right|^2} \right) \tag{57}$$

where, $y_{meas}$ is the measured data (either $A[n]$ or $\phi[n]$) , kept in their linear domain (i.e. volts for $A[n]$). $Y_{mod}$ is the modeled data (appropriately $A_m[n]$ or $\phi_m[n]$).

Figure 6-4 shows the gain error (volts) between $A[n]$ and $A_m[n]$. The $NSME_{dB}$ quantity for this example is -81 dB for the model training data set. A new data set captured several days after the initial characterization showed an $NSME_{dB}$ of -73 dB. Although this represents a small decrease in fitness, this still shows the model is in excellent agreement with the measured data.

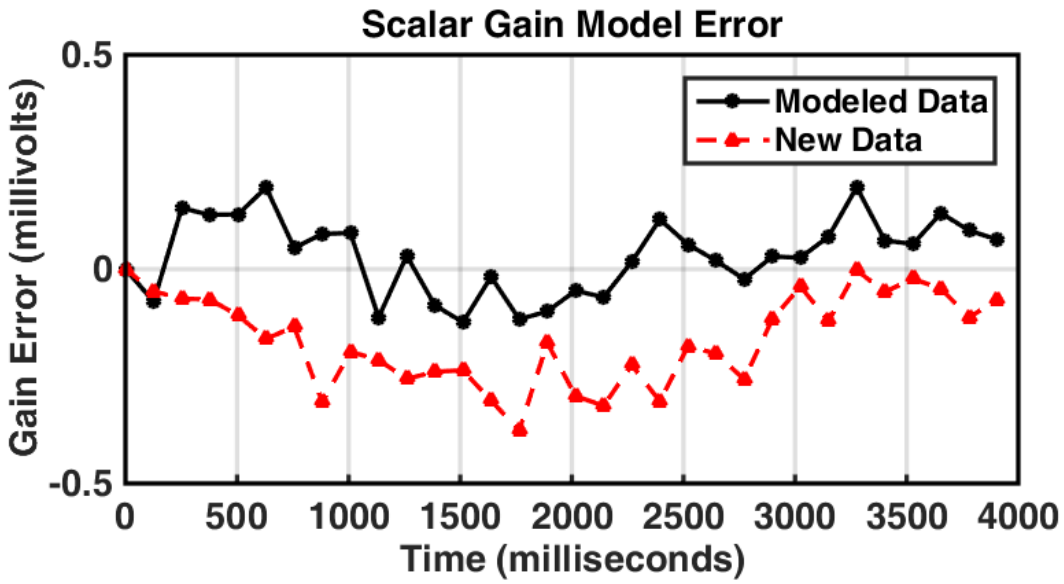


Figure 6-4: The gain error is the difference between the measured ($A[n]$) and modeled ($A_m[n]$) gain change, expressed in volts.

Figure 6-5 shows the phase error (degrees) between $\phi[n]$ and $\phi_m[n]$. The NMSE quantity for this example is $NSME_{dB}$ = -57 dB. This represents excellent agreement between the model and the measured data. The new data set showed a small decrease in fit, with an $NSME_{dB}$ of -44 dB. This is still a very good fit.

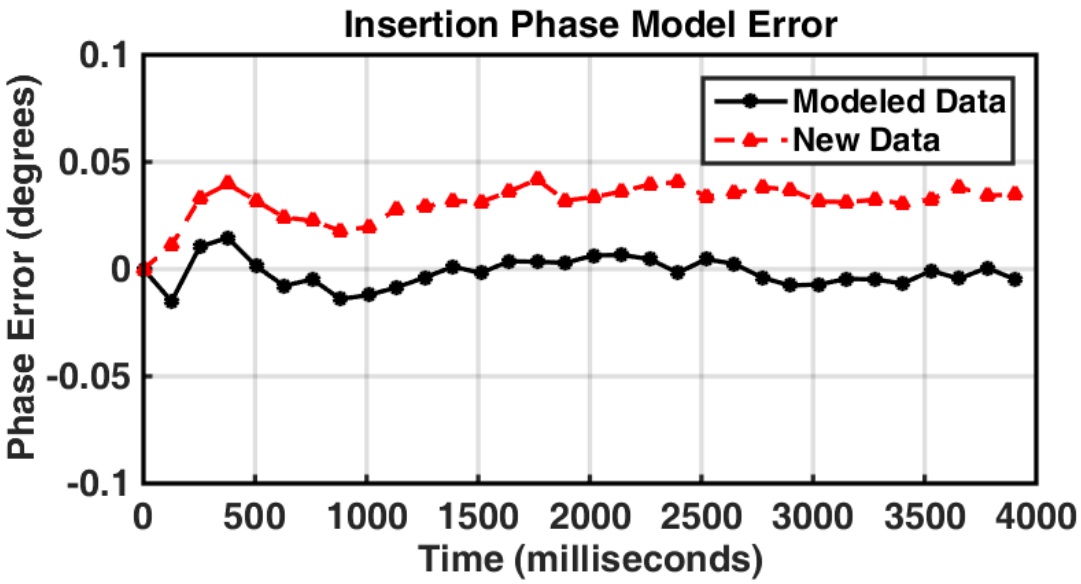


Figure 6-5: The phase error is the difference between the measured ($\phi[n]$) and modeled ($\phi_m[n]$) insertion phase change.

The $NMSE_{dB}$ showed excellent agreement between the behavioral model and the scalar gain and insertion phase transients. The model remains valid even after an extended period has passed. However, Figures 6-4 and 6-5 show a systematic error along the CPI. This indicates that the model cannot completely replicate the transients. In spite of this, the model is sufficiently accurate as demonstrated below.

A small error is desirable in order to use the model as part of a predistortion algorithm, and in radar performance prediction analysis. MTI and Doppler radars are highly sensitive to pulse-to-pulse stability [78, 80]. Recalling the results in Section 3.4.2, for the desired 53 dB threshold in the MTI Improvement Factor, the pulse-to-pulse system stability requirement needs to be better than 0.007 dBc and 0.091 degrees at all times. Assuming a perfect predistortion implementation, the gain error in Figure 6-4 shows difference between pulse-to-pulse to be at a maximum approximately 0.2 millivolts, or 0.002 dBc, a greater stability than the required 0.007 dBc. The phase error in Figure 6-5 shows a difference between pulse-to-pulse to be at a

maximum of 0.026 degrees, well below the required 0.091 degrees. Thus, the developed behavioral model is sufficiently accurate to be used in predistortion algorithm.

## 6.3 Parameter fit for multiple multifunction waveform sequence

The process discussed in section 6.2.1 was repeated for several different preceding waveforms (CPI 2), forced to last 20 milliseconds. The DUT used for this data collection is a different specimen from the DUT used to develop the behavioral model in Section 6.2.1 above. Several combinations of duty cycles (2%, 8%, 10%, 15% and 20%) and pulse widths (1, 8, 10, 20, 30, 40, 50 microseconds) were used, totaling 35 different waveforms that precede the WOI. To increase the SNR, in addition to the cross-correlation discussed earlier, 20 CPIs where captured and analyzed to extracts the transient response. The transient responses are not shown here; however, model parameters dependencies regarding pulse width and duty cycle were observed.

The next several Figures 6-6 thru 6-10 show a contour for each of the model parameters $P_{1A}$, $\tau_{1A}$, $P_{2A}$, $\tau_{2A}$ and $c_A$ characterized for $A_m[m]$. Each parameter has a single value per waveform combination, thus a total of 35 data points were calculated. These parameters were stored in a lookup table where a simple interpolation can be used to estimate parameters within the dimensional space of pulse width and duty cycle. Each contour figure was constructed by interpolating the appropriate parameters data points to an increased resolution Pulse Width (abscissa) and Duty Cycle (ordinate).

A preceding waveform with identical properties will not cause a transient. Consequently, the model parameters for proportionality $P_{1A}$ and $P_{2A}$ are forced to zero, the time constant $\tau_{1A}$ and $\tau_{2A}$ are interpolated using neighboring values and the offset constant $c_A$ is forced to one. The parameters value is highlighted in the contour plot with a red circle.

Figure 6-6 shows the values for the amplitude fit $P_{1A}$ parameter; the contour shows that whenever duty cycle or pulse width changes, $P_{1A}$ will change. However, these changes indicate a weak non-linearity as observed by the contour line slopes and line spacing remaining constant. In general, a larger magnitude value of $P_{1A}$ indicates a large transient, whereas a positive value indicates a cooler preceding waveform. The numbers illustrated on the lines indicate the calculated value for parameter $P_{1A}$. The red circle at a pulse width of 10 microseconds and a duty cycle of 8% indicates a $P_{1A}$ value of zero, as this is the point in which the preceding waveform is identical to the WOI.

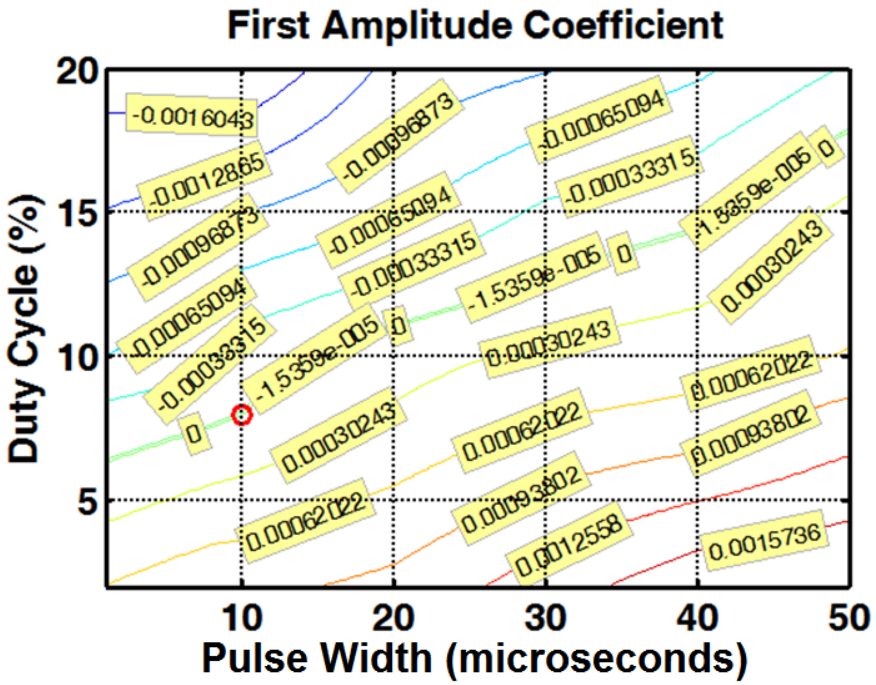


Figure 6-6: Contour for behavioral model $P_{1A}$ parameter; the contour shows a weak non-linearity of $P_{1A}$ with respect to duty cycle or pulse width changes. The numbers illustrated on the lines indicate the calculated value for parameter $P_{1A}$.

Figure 6-7 shows the contour for the first (and shorter) behavioral model time constant $\tau_{1A}$. The values remain near 250 microseconds; there is no noticeable change regardless of the

duty cycle or pulse width selected. The numbers illustrated on the lines indicate the calculated value for time constant $\tau_{1A}$.

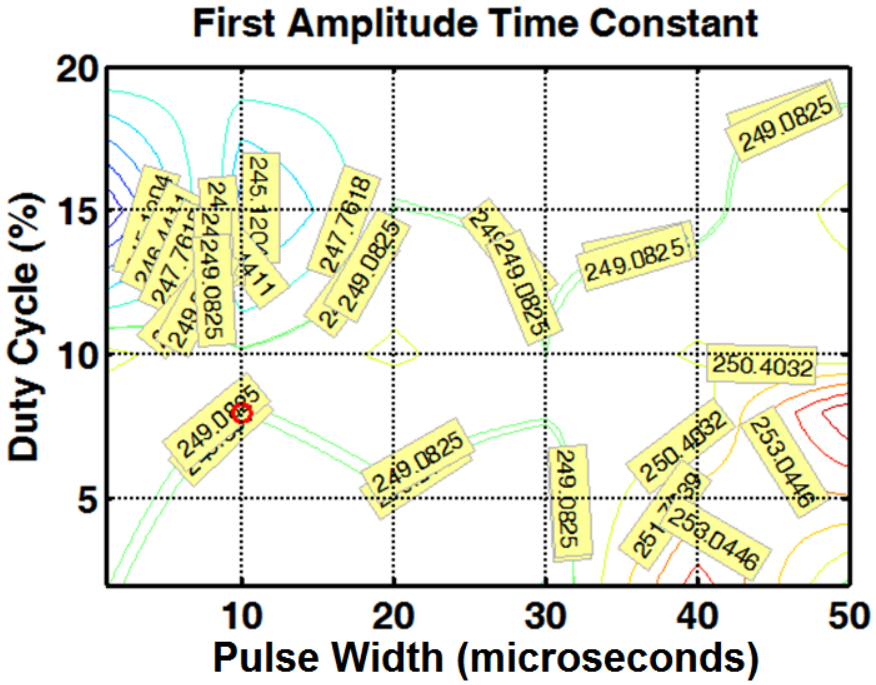


Figure 6-7: Contour for behavioral model $\tau_{1A}$ parameter; the contour shows the time constant value is stable, to approximately 250 microseconds, and does not changes significantly with either duty cycle or pulse width changes.

Figure 6-8 shows the values for the amplitude fit $P_{2A}$ parameter; the contour shows that whenever duty cycle or pulse width changes $P_{2A}$ will change. However, $P_{2A}$ has a greater dependency on duty cycle than pulse width, in particular when compared to $P_{1A}$. Furthermore, the relationship between duty cycle and $P_{2A}$ is non-linear, as seen by the increased spacing between lines for larger duty cycles.

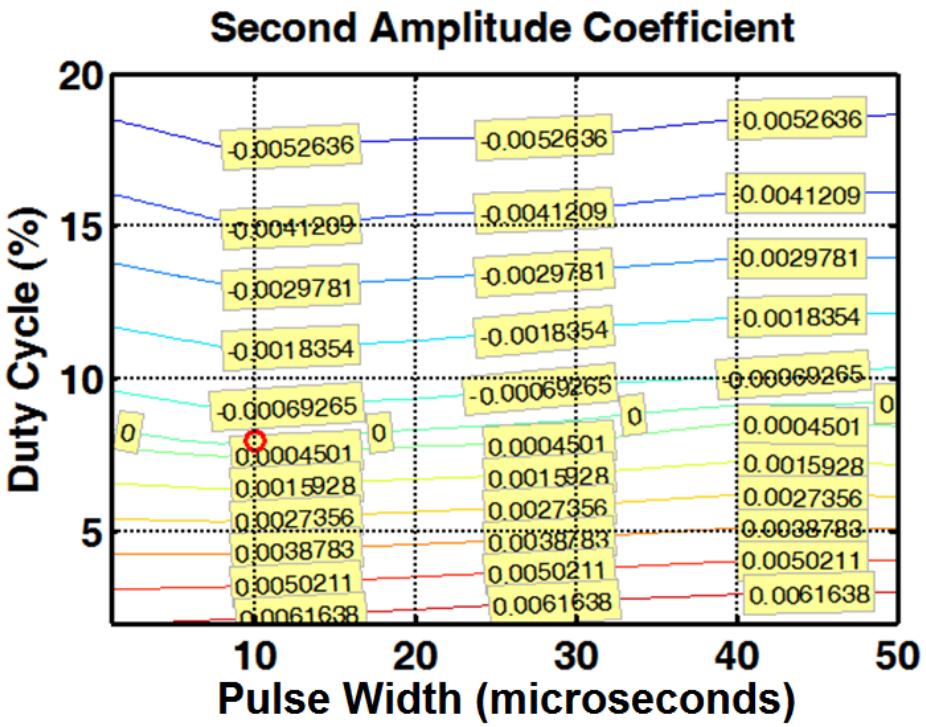


Figure 6-8: Contour for behavioral model $P_{2A}$ parameter; the contour shows that $P_{2A}$ has a strong dependency with duty cycle and a mild non-linearity.

Figure **6-9** shows the contour of the second (longer) time constant $\tau_{2A}$ of the behavioral model. The values remain in the vicinity of 2 milliseconds; there is no noticeable change in time constant regardless of the duty cycle or pulse width selected.

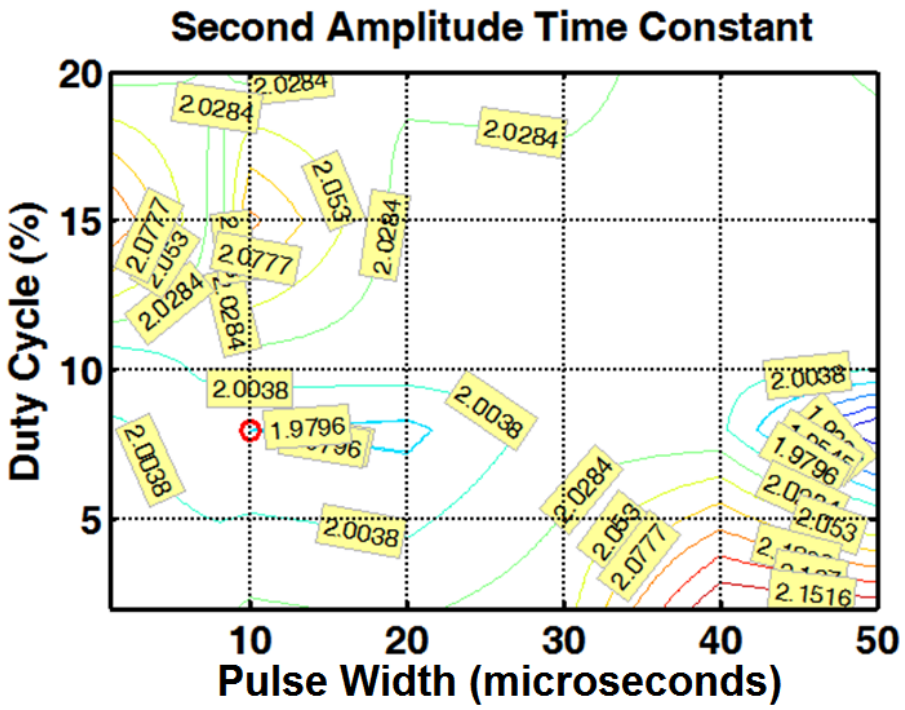


Figure 6-9: Contour for behavioral model time constant $\tau_{2A}$ parameter; the contour shows the time constant value is stable and does not changes significantly with either duty cycle or pulse width changes.

Figure **6-10** shows the values for the amplitude fit $c_A$ parameter; it shows a similar trend as parameter $P_{2A}$ where there is not a significant change in the values with changes in pulse width as compared to the changes due to the duty cycle. The value of $c_A$ is very close to one, and it represents an offset in scalar gain (linear voltage gain). The behavior of $c_A$ may be of interest in the study of memory effects on phased arrays, however, that is outside of the scope of this dissertation.

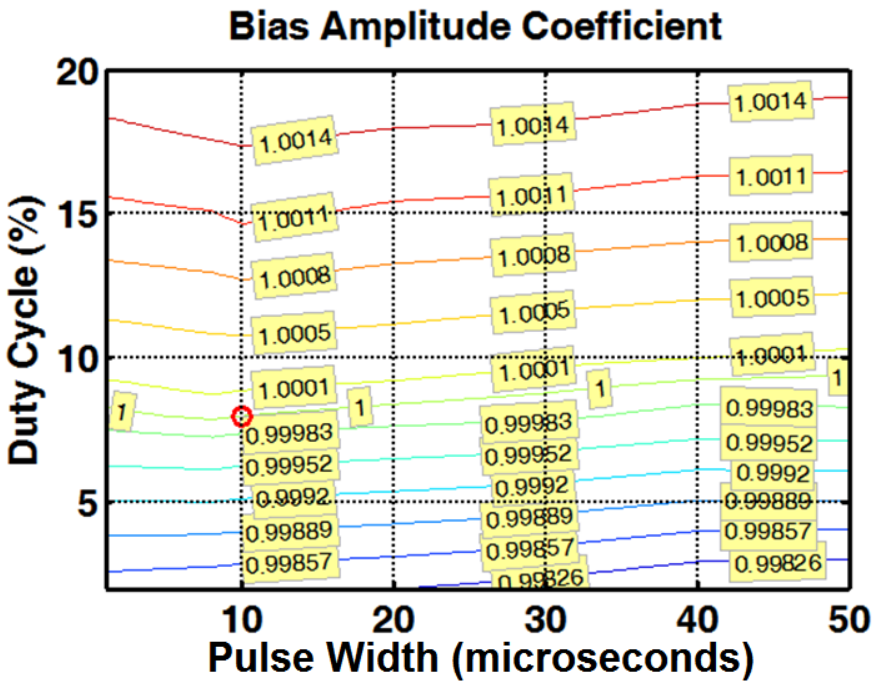


Figure 6-10: Contour for behavioral model $c_A$ parameter; the contour shows that $c_A$ has a strong dependency with duty cycle and a mild non-linearity.

## 6.4 Chapter Summary

This chapter introduced a simple behavioral model capable of replicate the amplifier behavior. The model is based on a Foster network topology. The adequacy of the model was verified by comparing the error between the measured and modeled amplitude transient. Via experimentation, it was determined that the amplitude transient response can be well represented by a two time-constant cascaded Foster network circuit. The phase behavior is more complex and requires three time-constant circuit. The model is later used to implement the predistortion algorithm.

# Chapter 7. Development of a Predistortion Algorithm

This Chapter introduces the concept of digital predistortion as a mechanism to mitigate the transient effects at the output of the power amplifier. The amplitude and phase transients are caused by the use of dissimilar radar waveforms during normal radar operations. These transients affect the system's stability, and thus are detrimental to radar performance. The digital predistortion algorithm presented here effectively cancels the transients in respect to the radar's coherent master oscillator, significantly improving the system stability.

## 7.1 Predistortion Concept

The amplifier behavior shown in Chapters 5 and 6 is repeatable. This means that the response of an amplifier subjected to a waveform sequence will be identical if exposed to the same sequence later in the future. This assumes that other condition such as frequency of operation, power source, and coldplate temperature are kept consistent. It also excludes noise, aging effects and permanent damage to the device. If these conditions are documented and the behavioral model parameters are extracted, then the next time these conditions are fulfilled, the amplifier response will be predicted by the model. Predicting the amplifier behavior provides the opportunity to correct for such behavior.

The behavioral model, replicates the amplitude and phase transients experienced by the amplifier. For each pulse in a CPI, the model provides a single scalar gain and insertion phase coefficient relative to the first pulse in the CPI. The predistortion algorithm applies the inverse of these coefficients to the pulse, so that the average scalar gain and average insertion phase at the output of the amplifier are the same from pulse to pulse.

The predistortion technique does not directly alter the shape of the output pulses in the CPI. Rather it changes the mean value of the amplitude and phase at the input of the amplifier. This counteracts the transient effects introduced by the amplifier. The next few paragraphs will illustrate this concept.

## 7.2 Predistortion Algorithm

The predistortion is conceptually simple; its implementation is complicated due to AM/AM and AM/PM conversion compensation. Figure 7-1 shows a block diagram of the predistortion algorithm. The predistortion algorithm uses the developed behavioral model to calculate the required inverse amplitude and phase transients to negate the effects produced by the amplifier. The coefficients are corrected for AM/AM and AM/PM conversion. Each coefficient is applied to individual pulses in the CPI. The AM/AM and AM/PM conversion is approximated by second order polynomials. The next three subsections will explain the functionality of the blocks within Figure 7-1.

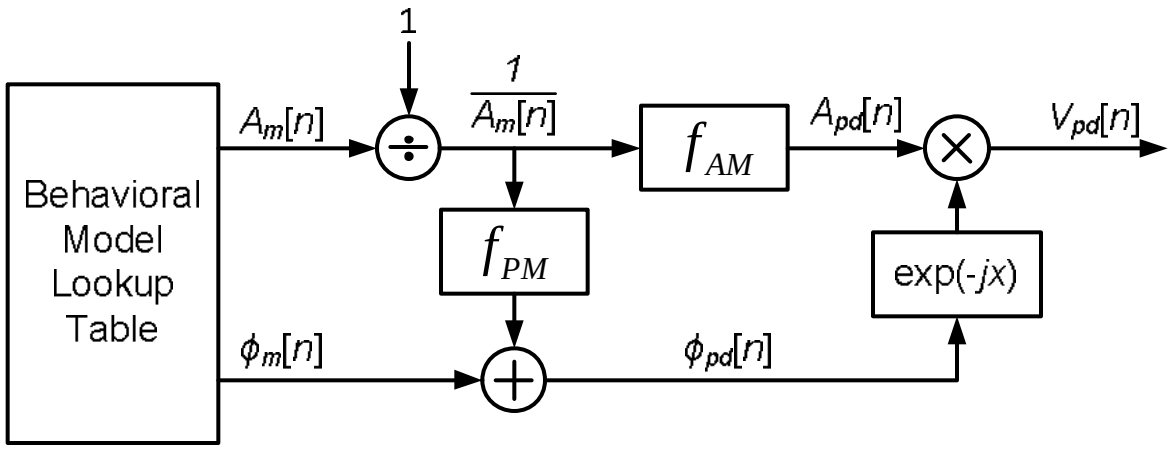


Figure 7-1: Block diagram illustrating the predistortion algorithm. The expected amplifier response is modeled based on parameters stored in a lookup table. The inverse of the amplitude and the negative of the phase are then found. AM and PM modulation compensation are calculated using second-order polynomials.

### 7.2.1 AM/AM and AM/PM Conversion Compensation

In order to implement amplitude predistortion on the transmitted signal it is then necessary to find the inverse of the characterized AM/AM conversion. More specifically, we need to know by how much to change the input power in order to achieve the desired effect at the output and conversely by how much the insertion phase changes based on a desirable change in output power. Figure 7-2 shows the inverse curves for the modulation conversion, found on Section 5.2.3 AM/AM and AM/PM Conversion. The abscissa shows the output power in reference to the maximum PAE operating point. The left vertical axis shows the input power change in decibels. The right vertical axis shows the insertion phase change in degrees. The solid curve illustrates the AM/AM behavior, with input power as a function of output power. The dashed curve illustrates the AM/PM behavior, with insertion phase as a function of output power. As an example, if the output power needs to be reduced by 0.12 dB, the input power must be reduced by 0.75 dB. It will also result on an insertion phase change of over 1.1 degrees.

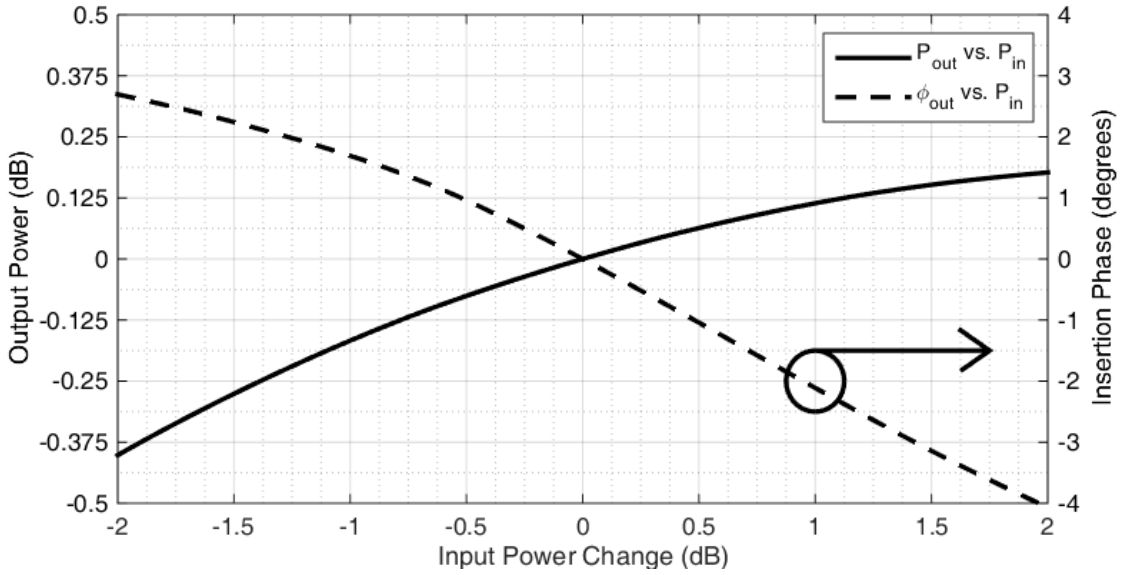


Figure 7-2: AM/AM and AM/PM conversion as a function of RF input power, for a range of input power of ± 2 dB in reference to the nominal operating point.

The AM/AM conversion is approximated by a second order polynomial. The desired output power change is the input argument to the function. The function returns the change in input power to achieve the desired effect:

$$\begin{aligned} V_{in} &= f_{AM}(V_{out}) \\ &= 35.69 \times V_{out}^{\,2} - 65.69 \times V_{out} + 31.00 \end{aligned} \tag{58}$$

where, $V_{out}$ is the desired output change, and $V_{in}$ is the required input change, both in volts.

The AM/PM conversion is also approximated by a second order polynomial. The desired output power change is the input argument to the function. The function returns the resultant change in insertion phase:

$$\begin{aligned} \phi_{out} &= f_{PM}(V_{out}) \\ &= -7.30 \times V_{out}^{\,2} + 13.69 V_{out} - 6.39 \end{aligned} \tag{59}$$

where $\phi_{out}$ is the resulting change in insertion phase due to desired change in output $V_{out}$ in volts.

### 7.2.2 Inverse Amplitude Transient

The modulation conversion curves from Figure 7-2 shows how the output power and insertion phase changes due to changes in input power. The digital predistortion algorithm, however, uses these results in an unconventional way. It requires the input power and insertion phase to be functions of the output power. Thus subscripts were added for clarity; $AM_{OUT}/AM_{IN}$ represents the relationship of the input power to the output power, whereas $AM_{OUT}/PM_{OUT}$ represents the relationship of the insertion phase to the output power. The inverse amplitude transient coefficients with $AM_{OUT}/AM_{IN}$ compensation are found by:

$$A_{pd}[n] = f_{AM}\left(\frac{1}{A_m[n]}\right) \tag{60}$$

where, $A_{pd}$ is the amplitude predistortion coefficient for the $n^{th}$ pulse in the CPI. $A_m$ is the modeled (or measured) amplifier response. The function $f_{AM}(x)$ is a polynomial of second order that describes the $AM_{OUT}/AM_{IN}$ conversion, where $x$ is the output power and $f_{AM}$ returns the input power. $A_{pd}$ represents the desired input power change to the amplifier that will maintain a constant output power from pulse to pulse.

### 7.2.3 Negative Insertion Phase Transient

The negative phase transient coefficients with $AM_{OUT}/PM_{OUT}$ compensation are found by:

$$\phi_{pd}[n] = \phi_m[n] + f_{PM}\left(\frac{1}{A_m[n]}\right) \tag{61}$$

where, $\phi_{pd}$ is the phase predistortion coefficient for the $n^{th}$ pulse in the CPI. The function $f_{PM}(x)$ is a polynomial of second order that describes the $AM_{OUT}/PM_{OUT}$ conversion, where $x$ is the output power and $f_{PM}$ returns the amplifier insertion phase. $-\phi_{pd}$ represents the desired input phase shift to the amplifier that will maintain a coherent phase from pulse to pulse.

These two arrays are combined to form a complex number vector:

$$V_{pd}[n] = A_{pd}[n]e^{-j\phi_{pd}[n]} \tag{62}$$

where, $V_{pd}$ is a vector containing $n$ complex numbers. $V_{pd}$ is then used during waveform synthesis, producing pulses within a CPI that are different from one to another.

### 7.2.4 Predistortion Mechanism for Validation

Recalling Section 4.1.4.2, the switch matrix is a key part in the experiment implementation. It allows for implementation and validation of the predistortion algorithm. Figure 7-3 shows the switch arrangement configured for device characterization. The switch

matrix is configured to alternate the Radar Digital Exciter channels #1 and #2, effectively changing the channel that provide DUT input signals. This configuration connects a sample of the Digital Exciter Channel #1 to the RF Output #1, and Digital Exciter Channel #2 to the RF Output #2. The experiment limits the radar waveforms without predistortion to always be supplied by the Digital Exciter Channel #1.

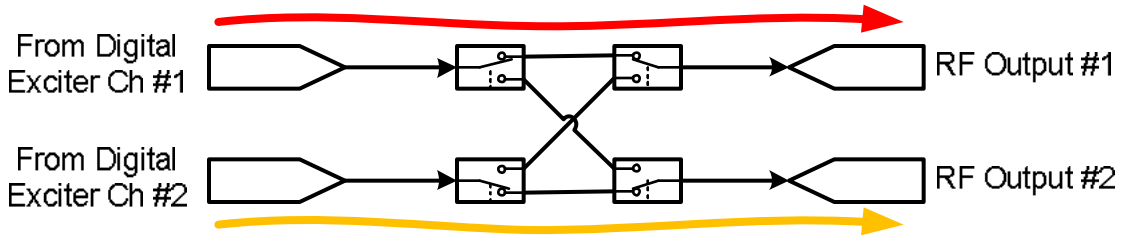


Figure 7-3: Switch Matrix; mechanical RF switches arranged for device characterization.

Figure 7-4 shows the switch arrangement configured for predistortion testing and validation. This configuration connects a sample of the Digital Exciter Channel #1 to the RF Output #2, and Digital Exciter Channel #2 to the RF Output #1. The predistorted radar waveform is supplied by the Digital Exciter Channel #2, along with the other waveforms that form the multifunction sequence. However, these other waveforms are not predistorted.

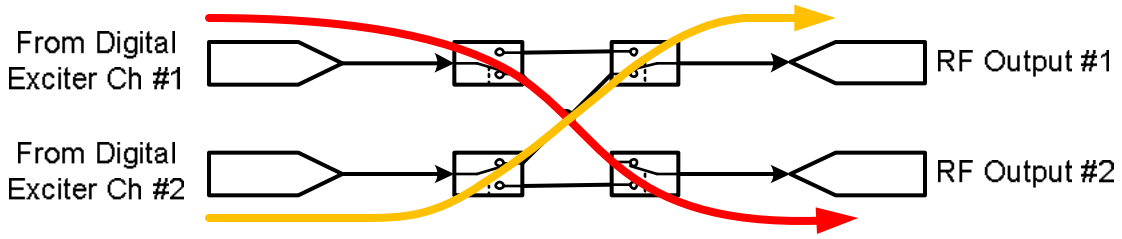


Figure 7-4: Switch Matrix; mechanical RF switches arranged for predistortion testing and validation.

Recalling Chapter 3, Section 3.2.4 Wiener-Hopf Equation; the amplifier transfer function is found via the Wiener-Hopf equation [77], simplified to acquire a single filter coefficient:

$$G = \frac{r_{xy}^{*}(0)}{r_{xx}(0)} \tag{63}$$

where, $r_{xy}(0)$ is the peak of the cross-correlation of the amplified output with the input, and $r_{xx}(0)$ in the peak of the auto-correlation for the input signal. $G$ is a single complex number that denotes the amplifier complex gain.

Each pulse in the sequence has a unique complex gain. These coefficients are arranged in vector form. The resulting gain vector is normalized to the first pulse in the sequence. The complex data is further segregated into amplitude and phase:

$$A[n] = \left| \frac{G[n]}{G[1]} \right| \tag{64}$$

$$\phi[n] = \arg(G[n]) - \arg(G[1]) \tag{65}$$

where, $A[n]$ is the measured scalar gain change, $\phi[n]$ is the measured phase insertion change, and $n$ is the pulse index within a CPI; $n = 1,2,3,\ldots,N$. The trend exhibited by $A[n]$ and $\phi[n]$ thus, defines the amplifier behavior.

Figure 7-5 shows the block diagram of the predistortion operator and amplifier. The figure shows the reference signal x(t) (Digital Exciter Channel #1) being injected into the predistortion block followed by the amplifier. However, during predistortion testing and validation, the switch matrix connects Digital Exciter Channel #2 directly into the amplifier. Since the predistortion coefficients where calculated and applied to the waveforms in Digital Exciter Channel #2, the output of the channel is equivalent to the Digital Exciter Channel #1 convoluted with $V_{pd}$. Thus, connecting Digital Exciter Channel #2 directly into the amplifier is equivalent to the scenario shown in Figure 7-5.

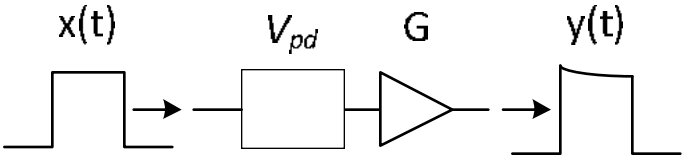


Figure 7-5: Block diagram of predistortion operator and amplifier.

If the same process to find $A[n]$ and $\phi[n]$ is repeated, the ideal result after predistortion is *A = 1* and $\phi$ *= 0*. The combined transfer function $Vpd[n]\times G[n]=1$. The amplitude and phase transients are negated thus, the amplifier output maintains the same output power and remains coherent with respect to x(t).

## 7.3 Predistortion Validation

### 7.3.1 Pulse Envelope

Multifunction waveforms induce amplitude and phase transients across the CPI. As the CPI progresses the transients subside and the difference between pulses become less significant. Figure 7-6 shows the amplitude envelope for all the pulses in CPI 1. Figure 7-7 shows the phase envelope for all the pulses in CPI 1. The further along into the CPI the smaller the variations between pulses, thus improving system stability.

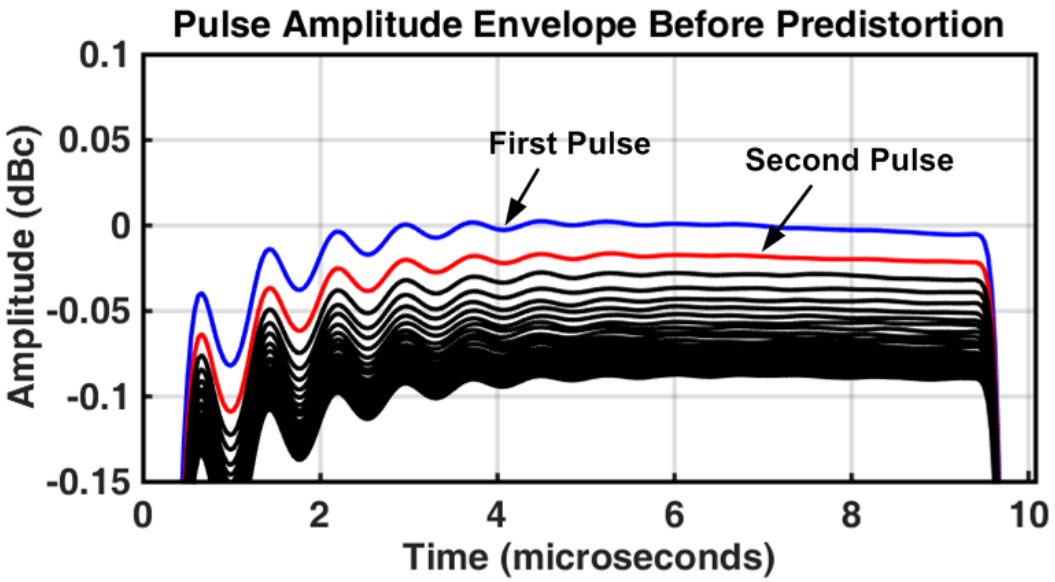


Figure 7-6: Measured envelope for all the pulses in CPI 1 following the multifunction waveform sequence. The graph shows an offset in amplitude.

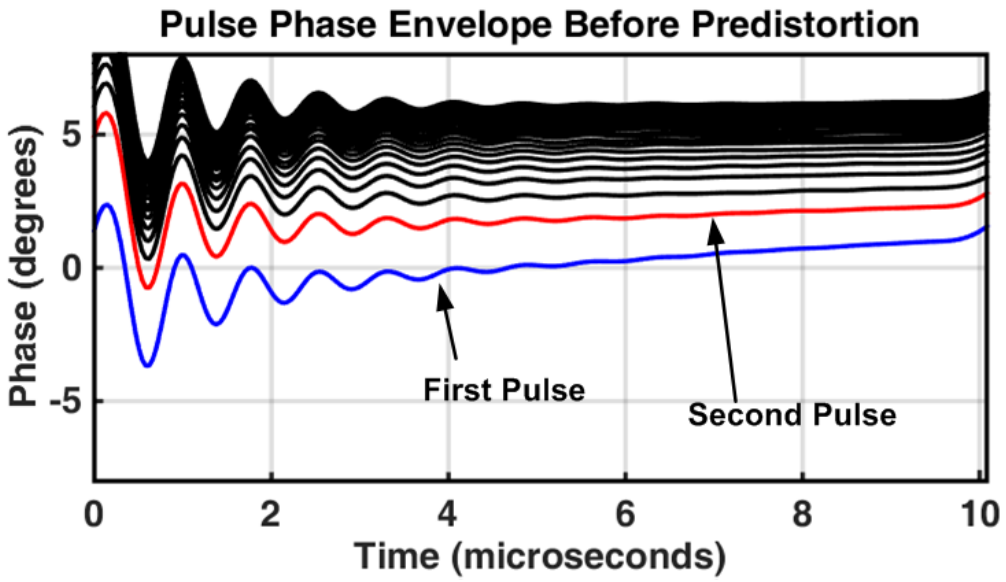


Figure 7-7: Measured phase envelope for all the pulses in CPI 1 following the multifunction waveform sequence. The graph shows an offset in phase.

The measurement technique discussed in Chapter 3 and demonstrated in Chapter 5 is used to measure the amplitude and phase offset between pulses. The predistortion technique then applies the opposite of the transient into the input of the amplifier. Modulation conversion compensation is also used. Figures 7-8 and 7-9 show the amplitude and phase envelope for all the pulses in CPI 1, after predistortion. The predistortion forces the average amplitude and phase for every pulse in the CPI to be the same. The predistortion does not accounts for the pulse shaping. Figure 7-8 shows that all of the amplitude envelopes are virtually identical. However, figure 7-9 shows the shape of the first pulse is different from that the rest of the pulses. This will ultimately affect the P2P stability.

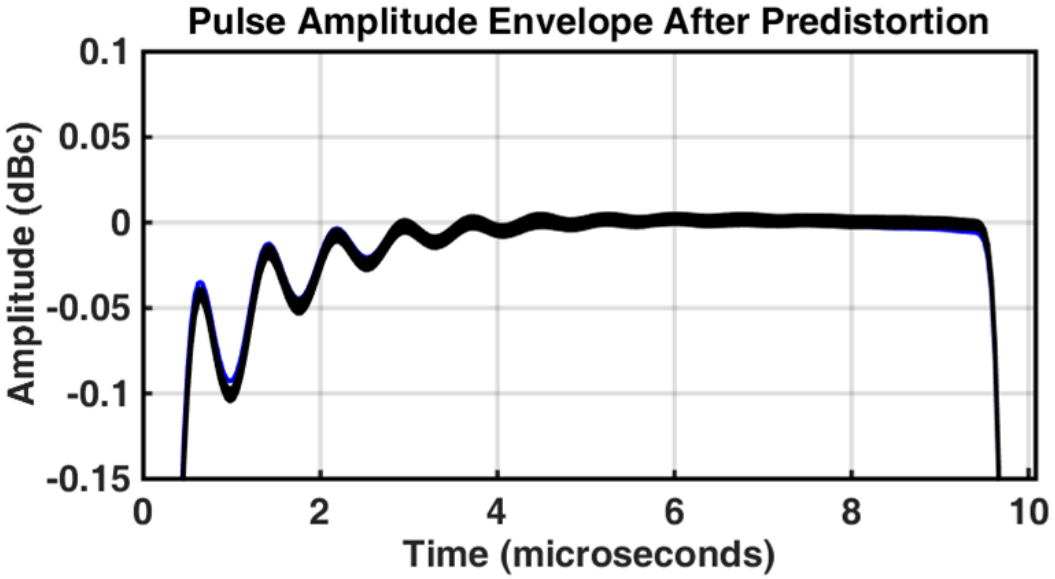


Figure 7-8: Measured envelope, after predistortion, for all consecutive pulses in CPI 1 following the multifunction waveform sequence. The graph shows a significant reduction in the dispersal.

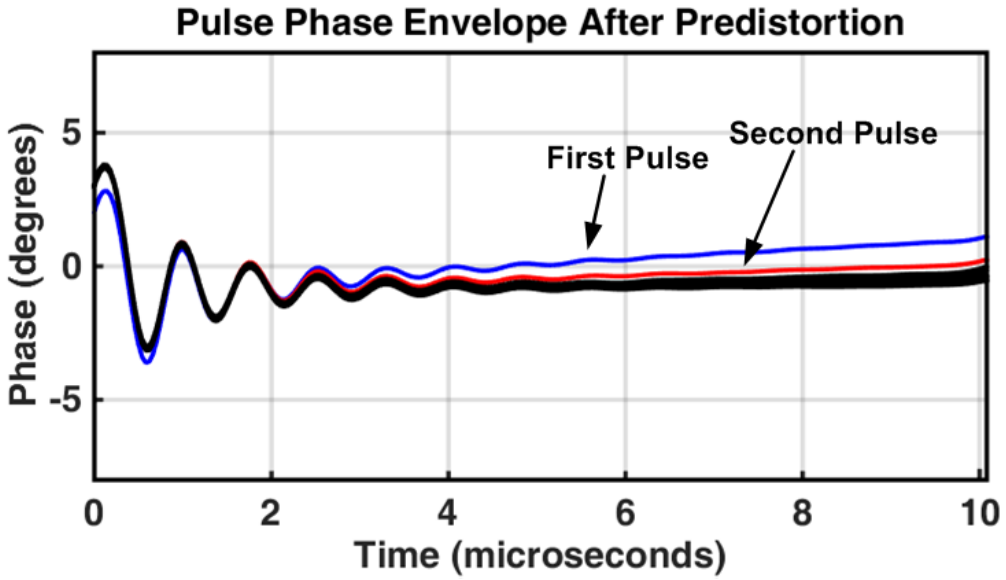


Figure 7-9: Measured phase envelope, after predistortion, for all consecutive pulses in CPI 1 following the multifunction waveform sequence. The graph shows a significant reduction in the dispersal.

Manufacturing variability in each amplifier can result in slightly different behavior across a large number of devices, which is supported by the results obtained in [15, 16]. This may require a unique set of coefficients per amplifier, depending on the Improvement Factor sought.

### 7.3.2 Amplitude and Phase Transient Across CPI

Figure 7-10 shows the amplitude transient both before and after predistortion. Before predistortion the amplitude at the output of the power amplifier fluctuated by almost 0.1 dB across the CPI. After predistortion, the fluctuation was substantially reduced, to essentially the noise floor of the data set.

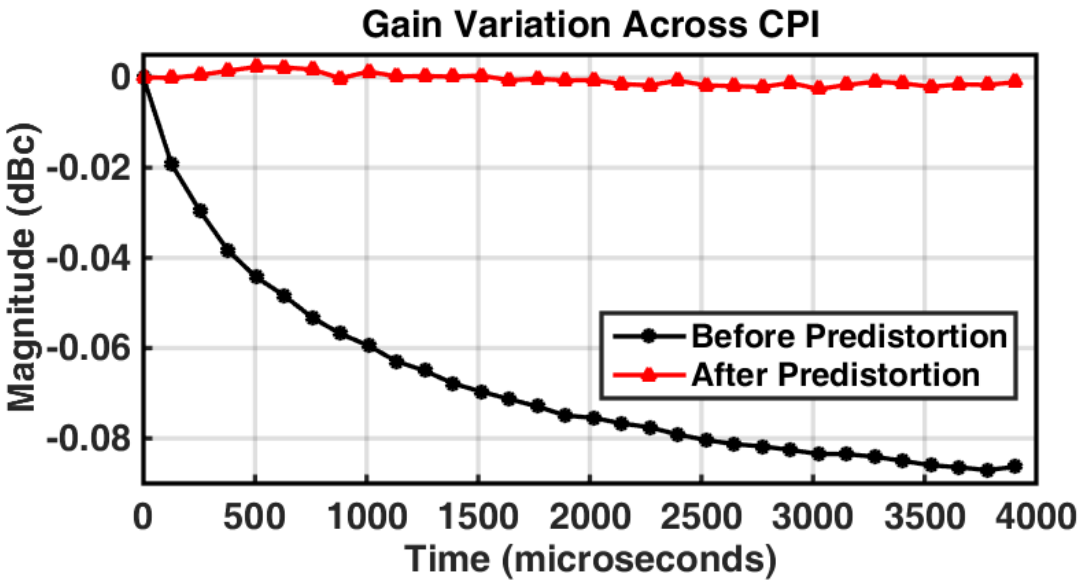


Figure 7-10: Amplitude transient caused by a cooler waveform (CPI 2) preceding the calibration waveform (CPI 1). Before predistortion, the output signal decreased as CPI 1 progressed across the 32 pulses. After predistortion, the output signal is forced to stay constant.

Figure 7-11 shows the insertion phase transient. Before predistortion, the insertion phase transient showed an offset of more than six degrees. After the predistortion, the insertion phase transient was reduced to approximately half a degree. In fact, the phase correction was overshoot due to a less than perfect AM/PM conversion compensation.

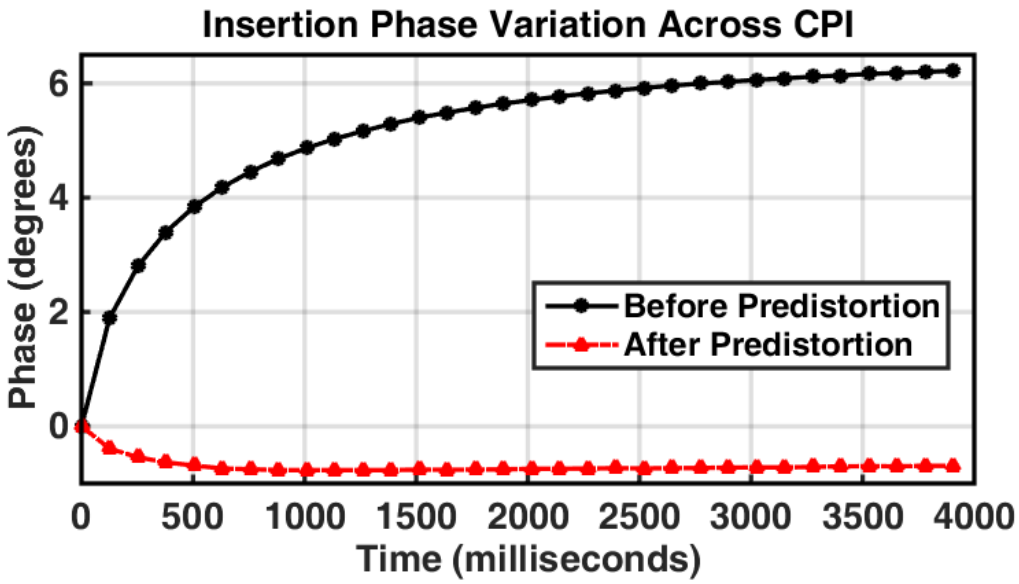


Figure 7-11: Phase transient caused by a cooler waveform (CPI 2) preceding the calibration waveform (CPI 1). Before predistortion, the insertion phase increased as CPI 1 progressed across the 32 pulses. After predistortion, the output phase is forced to stay coherent.

### 7.3.3 MTI Improvement Factor

Earlier in Chapter 5, Section 5.3.3.1, the limit in Improvement Factor due to the amplitude and phase transients was discussed. Figure 7-12 shows the Improvement Factor for the cases before and after predistortion. It is easier to visualize how well the predistortion mitigates the memory effects by looking at the MTI Improvement Factor and determining whether or not it is possible to achieve overall system stability. The MTI Improvement Factor before and after predistortion is shown in Figure 7-12. The transients have been reduced significantly; this allows the Improvement Factor to reach a higher level quicker. As seen in Figure 7-12, the difference between the before and after predistortion is approximately 13 dB for the first two pulses, and 17 dB for the next few pulses. Before predistortion, the threshold for stability was reach at the $12^{th}$ pulse, after predistortion, it was reached at the third pulse. After predistortion, by the $12^{th}$ pulse, the MTI Improvement Factor reaches the limit imposed by the system noise.

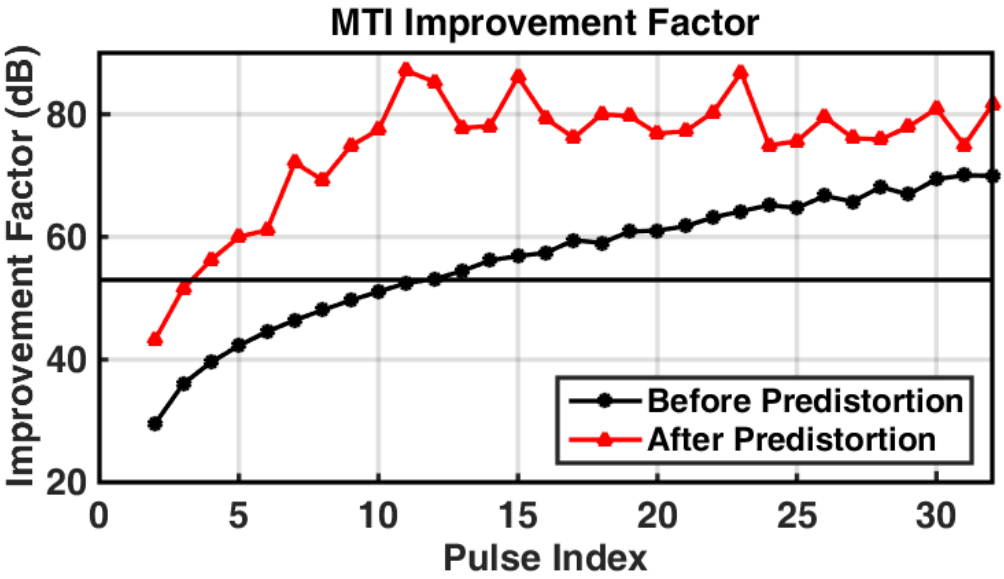


Figure 7-12: MTI Improvement Factor ratio before and after predistortion. Before predistortion, it took 12 pulses to achieve the required stability, after predistortion only three.

### 7.3.4 RMS Pulse to Pulse Stability

Figures 7-13 and 7-15 show the pulse-to-pulse stability for amplitude and phase respectively. The pulse-to-pulse stability is significantly influence by the earlier pulse in the CPI. This is confirmed by removing the leading pulses from the stability calculation. Figure 7-13 show that on average, the amplitude P2P stability for all pulses is -65.1 dB. As pulses one through three are removed from the calculation, the stability improves to -68.1 dB, then -69.8 dB and finally to -71.2 dB.

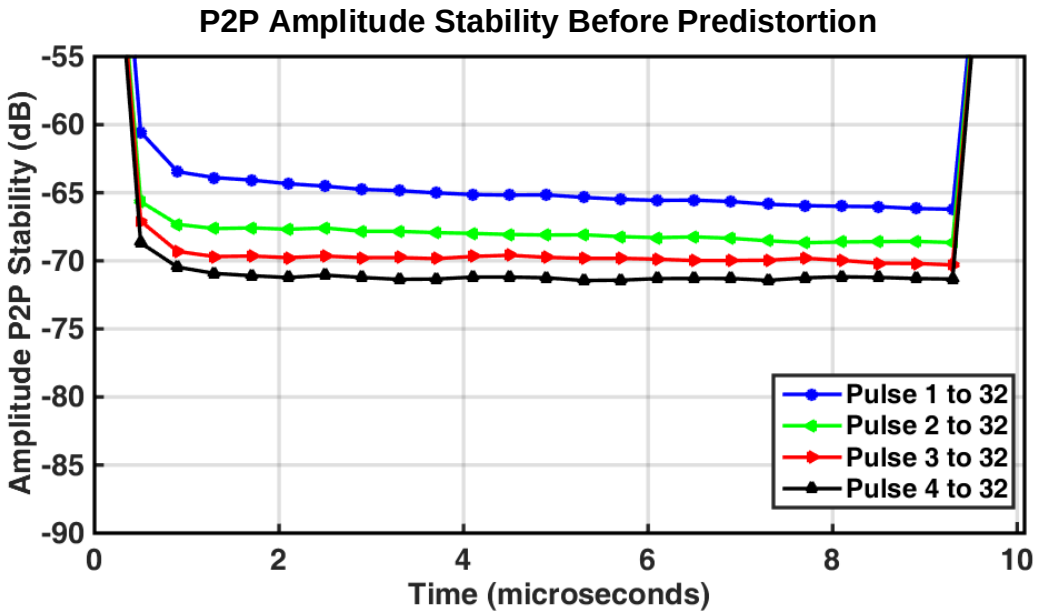


Figure 7-13: P2P amplitude stability before predistortion, showing the relative effect of the first four pulses in the 32 pulses waveform.

Figure 7-14 shows the amplitude P2P stability after predistortion. On average, the stability for all pulses is -80 dB, remaining at that value even after other leading pulses are removed from the calculation. This suggests a limit in the available SNR for the data set. Before predistortion the amplitude P2P stability for all pulses was -65.1 dB. This is a significant improvement of at least 14 dB.

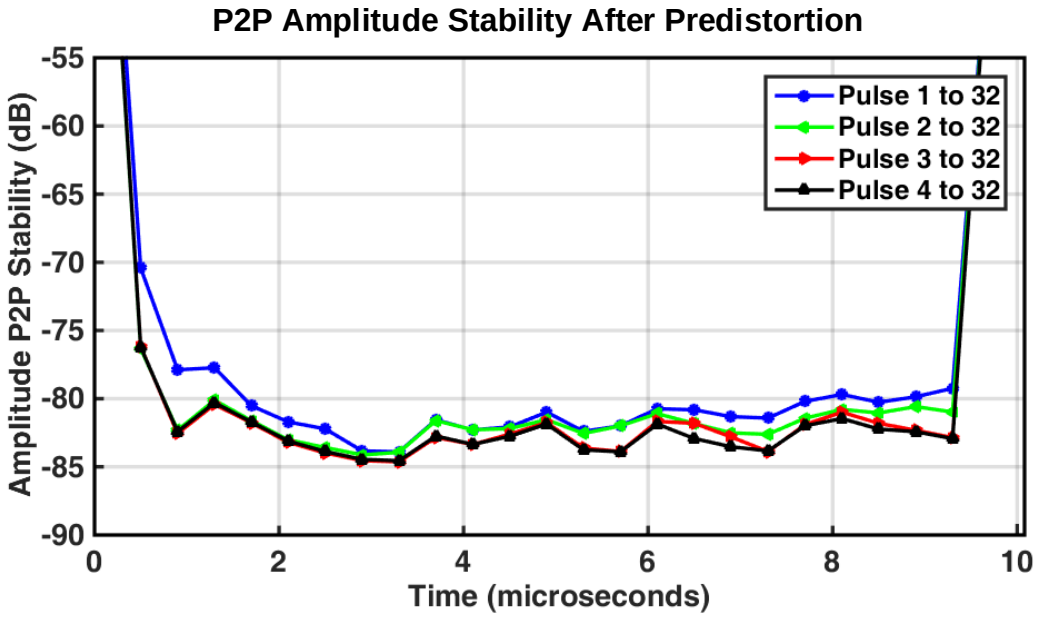


Figure 7-14: P2P amplitude stability after predistortion, showing a significant improvement in stability.

Figure 7-15 show that on average, the phase P2P stability for all pulses is -42.8 dB. As pulses one through three are removed from the calculation, the stability improves to -47.4 dB, then -49.8 dB and finally to -51.8 dB. The P2P stability improves as the leading pulses are removed from the calculation, indicating that earlier pulses have greater variations from the mean. The deviation from a flat line observed in the curve "Pulse 1 to 32" indicates that the shapes of the first pulses are distorted in relationship to the mean.

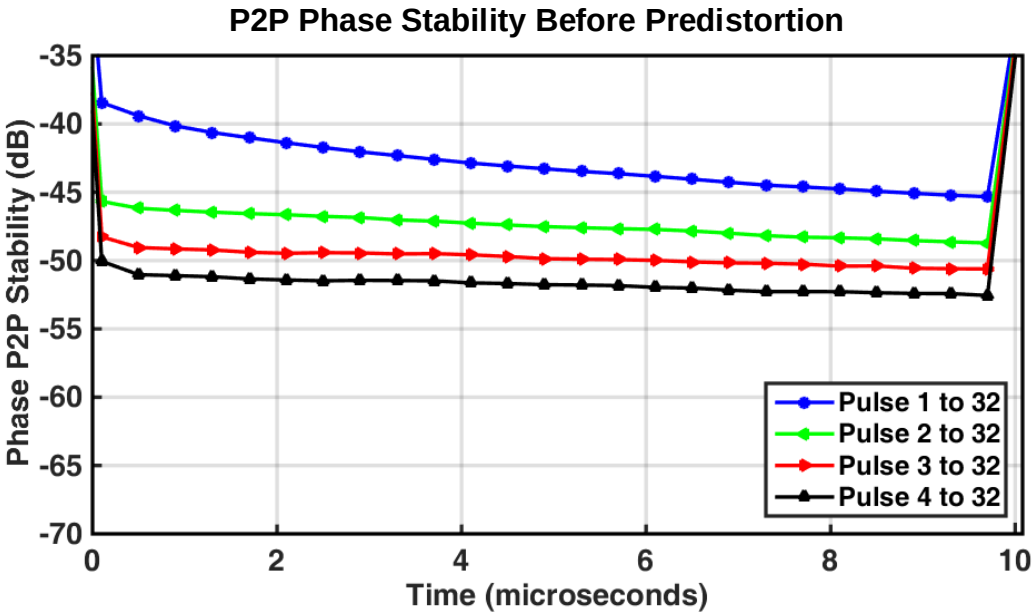


Figure 7-15: P2P phase stability before predistortion, showing the relative effect of the first four pulses in the 32 pulses waveform.

Figure 7-16 show the phase P2P stability after predistortion. The phase P2P stability for all pulses is on average -54.5 dB. As pulses one through three are removed from the calculation, the stability improves to -61.1 dB, then -63.6 dB and finally to -63.9 dB. The P2P phase stability improved by at least 11 dB.

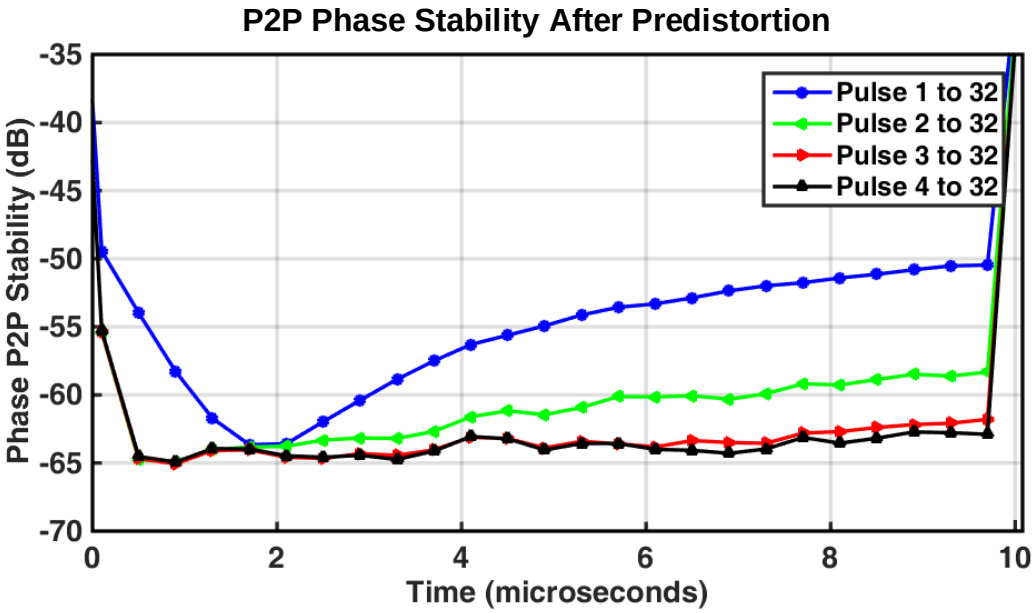


Figure 7-16: Pulse to pulse phase stability after predistortion, showing a significant improvement in stability.

### 7.3.5 Chapter Summary

After predistortion, the RMS method suggests that the first two pulses are the limiting factor in achieving better stability. In Figure 7-16, the curve "Pulse 1 to 32" shows a large discrepancy from the rest of the curves. This denotes that the shape of the first pulse has large variations from the mean pulse in the sequence. The stability reaches a minimum at approximately two milliseconds. The phase envelope for all of the pulses coincides at that time. This corresponds to the predistortion mechanism, where each pulse at the output of the amplifier has equal average amplitude and phase. It also means that to further improve the phase P2P stability without discarding the first or second pulse in the sequence, it will be necessary to account for pulse shaping in the predistortion technique. This is outside of the scope of this investigation. Another limiting factor is the characterization of the AM/AM and AM/PM conversion. The modulation conversion also experiences memory effects. Empirical results suggest that there is a stronger memory effect on the AM/PM than the AM/AM conversion effects.

The MTI Improvement Factor and RMS P2P Stability metrics demonstrate that the proposed predistortion technique can mitigate the transient instability produced by the GaN amplifier when excited with multifunction waveforms. An improvement over stability in the order of 13 to 18 dB was achieved. This is a significant improvement over waiting out the transient, and directly translates into a significant savings of time and energy. For instance, before predistortion, the radar achieved the desired stability after the $11^{th}$ and $12^{th}$ pulses. The first 10 pulses did not meet stability requirements. After predistortion, the radar achieved the desired stability after the third and fourth pulses. The first two pulses did not meet stability requirements. If for example 16 stable pulses are needed to detect a target in the presence of clutter, without predistortion 26 pulses need to be transmitted versus 18 pulses if predistortion is used. This represents a 31% reduction in time, and decrease in consumed energy for the given task.

# Chapter 8. Summary and Conclusion

The incorporation of GaN technology in future radar systems will present new challenges. One of these challenges was identified as interpulse instability, a major factor for Pulse Doppler and MTI radar performance. The characterized behavior showed changes in the device's complex gain over a CPI length. The effect of the phase transient was determined to be two orders of magnitude worse than the amplitude transient with regards to performance degradation. Similar behavior, in terms of duration and magnitude, was reported in [15, 16] for two different GaN Class AB PA designs. Based on the focused context of this study, the duration of the observed transients, and the architecture of the DUT, the self-heating memory effect was identified as the root cause of the observed transient.

A behavioral model was developed to replicate the amplifier's behavior, with a high degree of precision, using a two time-constant Foster network topology to describe the amplitude transient, and three time-constant Foster network topology for the phase transient. The behavioral model was validated by using the inverse of the predicted amplitude and phase transient along with compensation for AM/AM and AM/PM conversion to digitally predistort individual pulses in a CPI. Results clearly showed that the residual transient after predistortion was significantly smaller than the original transient, thus increasing radar system stability. This was confirmed by using the MTI Improvement Factor and RMS P2P stability metrics. The digital predistortion significantly improves the system stability by at least 10 dB in all cases tested, reducing the time required for the system to achieve the desired stability.

Implementing the digital predistortion technique may require radar system architecture modifications or redesigns. In particular, a radar exciter must have enough flexibility to apply amplitude and phase corrections to each individual pulse in a CPI. This concept contradicts the standard practices followed by the radar community, which require identical pulses within a CPI.

## 8.1 Summary of contributions

The work done throughout this research concluding with this dissertation have uncovered four main contributions:

- The first contribution is the development of a new measurement technique to characterize a power amplifier during normal radar operating conditions. The characterization focused on measuring changes in the power amplifier complex gain (power gain and phase insertion) for each pulse in a radar waveform, immediately after a different radar waveform was transmitted.
- The second contribution is the discovery of amplitude and phase transients produced by GaN Power Amplifiers when excited with multifunction waveforms. The root cause of these transients was identified as the self-heating mechanism that produced a electrothermal memory effect. These transients produce interpulse instability in the transmitted waveform, significantly reducing radar system performance.
- The third contribution is the development of a behavioral model capable of replicating the observed transients at a high level of abstractions. The level of abstraction selected was pulse-to-pulse changes in amplitude and phase in the time domain. One important application is to create models to predict radar performance and to assess the impact of these transients on MTI clutter suppression. Another important application is to use the model to mitigate these transients in MTI and pulse Doppler radars to generate predistortion coefficients.
- The fourth contribution is the development of a predistortion algorithm. The algorithm uses the developed behavioral model to determine the expected power amplifier behavior. Within the algorithm, the inverse response needed from the amplifier is calculated, compensating for AM/AM and AM/PM conversion. For a given radar waveform, the algorithm generates a vector of complex coefficient that describes the appropriate amplitude and phase change needed at the input to the power amplifier for each pulse in the waveform.

The developed algorithm provides various advantages over the current state of the art, mainly in the form of more efficient and faster use of radar resources. First, the need to add fill pulses for the sake of interpulse instability is significantly reduced or eliminated because the resulting transmitted pulse is coherent with respect to the radar's master oscillator. Secondly, the radar's power efficiency is increased. There will be less RF energy wasted. Third, there will be considerable time savings. This additional time available to the radar's scheduler results in increased search rate.

All of these advantages are possible by predistorting each individual pulses within a CPI with a unique complex coefficient. The interaction between the unique pulses and the power amplifier are such that the resulting transmitted pulse is coherent with respect to the radar's master oscillator. This allows the radar system to achieve desired system stability in a shorter amount of time.

## 8.2 Future Directions

While the work and results herein addressed some of the issues related to the interpulse instability and transient effects produced by GaN Power Amplifiers under multifunction conditions, there are still a number of topics to be examined:

- Redesign device thermal stack, with the goal of shifting the thermal constant and reducing the thermal gradient. The transient effects could be mitigated by decreasing the temperature difference between layers, effectively shifting the time constants to where it may not affect the CPI. This approach is linked to properties such as thermal resistance and thermal capacitance. This will require the use of thermal analysis tools to correlate the heat transient that occurs in the device with the dissipating power induced by the radar waveform. It will also require additional expertise in material properties, semiconductor architecture and thermal modeling. This task is more suited to semiconductor chip and transistor designers.

- Study performance degradation caused by the interpulse instabilities on Pulse Doppler signal processing with modulated pulses, and Pulse Repetition Frequency (PRF) staggered pulses in MTI radars waveforms. Using the developed measurement technique, the amplifier behavior can be characterized for the various different waveforms. This information is then added to radar performance prediction software tools. This approach requires the development or modification of the above mentioned software tools. To the author's knowledge, these software tools do not have the capability to simulate unique amplitude and phase coefficients for every individual transmit pulse.

- Analysis of performance degradation on synthetic aperture radar. Synthetic aperture radars collect data captures for analysis over relatively long time spans. Excellent time and phase tracking is of vital importance in order to generate the synthetic aperture images. As the transients observed are influenced by preceding waveforms, to include silence, this system may also be affected. As in the case of the MTI radar system where the maximum possible improvement factor was limited by the transient, the synthetic aperture radar performance may also be limited.
- Finding a mathematical operator for the behavioral model. Currently the model parameters are stored in lookup tables. The model parameter values are nonlinear with respect to the preceding waveform pulse width and duty cycle. However, this nonlinearity is well behaved. Preliminary testing suggest that each model coefficient for a particular waveform of interest can be modeled by the use of a third order two-dimensional polynomial function where the input variable for the functions are the preceding pulse width and duty cycle.
- Analysis of transient effects on phased array transmit antenna patterns. The transient effect is not expected to change the antenna main beam, however, it may affect the characteristics of antenna nulls. If a null or area null is desired, the transient effect may prevent the nulls from forming as expected or cause them to change location over time.

# References


[1] R. A. Stapleton and C. G. Tua. (2011) Digital Array Radar Testbed. *Leading Edge*. 8.

[2] S. Cote, "Naval Multi-Function RADAR," in *IEEE Radar Conference*, 2010, pp. 96-101.

[3] K. C. Lauritzen, J. E. Sluz, M. E. Gerwell, A. K. Wu, and S. H. Talisa, "High-Dynamic-Range Receivers for Digital Beam Forming Radar Systems," in *IEEE Radar Conference*, 2007, pp. 55-60.

[4] R. A. Pucel, "Looking Back at Monolithic Microwave Integrated Circuits," *IEEE Microw. Mag.*, vol. 13, pp. 62-76, 2012.

[5] E. D. Cohen, "The MIMIC Program—A Retrospective," *IEEE Microw. Mag.*, vol. 13, pp. 77-88, 2012.

[6] !!! INVALID CITATION !!!

[7] C. F. Campbell, A. Balistreri, M. Kao, D. C. Dumka, and J. Hitt, "GaN Takes the Lead," *IEEE Microw. Mag.*, vol. 13, pp. 44-53, 2012.

[8] C. S. Whelan, N. J. Kolias, S. Brierley, C. MacDonald, and S. Bernstein, "GaN Technology for Radars," in *Proc. Int. Conf. Compound Semiconductor Manuf. Technol.* , Boston, MA, 2012, pp. 1-4.

[9] Y. Wu and P. Parikh, "High-power GaN HEMTs battle for vacuum-tube territory," *Compound Semiconductor*, vol. 12, pp. 21-23, 2006.

[10] S. Dahmani, "Large-Size AlGaN/GaN HEMT Large-Signal Electrothermal Characterization and Modeling for Wireless Digital Communications," in *IEEE Proc. Eur. Solid-State Device Res. Conf.*, 2011.

[11] K. Krishnamurthy, J. Martin, B. Landberg, R. Vetury, and M. J. Poulton, "Wideband 400 W pulsed power GaN HEMT amplifiers," in *IEEE Int. Microw. Symp. Dig.*, 2008, pp. 303-306.

[12] D. A. Gajewski, S. Sheppard, T. McNulty, J. B. Barner, J. Milligan, and J. Palmour, "Reliability of the GaN/AlGaN HEMT MMIC technology on 100-mm 4H-SiC," in *26th Annual JEDEC ROCS Workshop*, Indian Wells, CA, 2011, pp. 1-5.

[13] R. S. Pengelly, S. M. Wood, J. W. Milligan, S. T. Sheppard, and W. L. Pribble, "A Review of GaN on SiC High Electron-Mobility Power Transistors and MMICs," *IEEE Trans. Microw. Theory Techn.*, vol. 60, pp. 1764-1783, 2012.

[14] R. Stevenson, "Preparing GaN for greater military service," *Compound Semiconductor*, vol. 19, pp. 30-34, July 2013 2013.

[15] C. G. Tua, "Measurement technique to assess the impact of RF power amplifier memory effects on radar performance," in *IEEE Radar Conference*, 2012, pp. 0089-0094.

[16] C. G. Tua, "Analysis of High Power RF Amplifier Electro-Thermal Memory Effects on Radar Performance," in *MSS Tri-Service Radar Symp.*, Boulder, CO, 2012, pp. 1-4.

[17] J. Delprato, D. Barataud, M. Campovecchio, G. Neveux, C. Tolant, and P. Eudeline, "Measured and Simulated Impact of Irregular Radar Pulse Trains on the Pulse-to-Pulse Stability of Microwave Power Amplifiers," *IEEE Trans. Microw. Theory Techn.*, vol. 62, pp. 3538-3548, 2014.

[18] F. Fornetti, M. Beach, and J. G. Rathmell, "The application of GaN HEMTs to pulsed PAs and radar transmitters," in *European Conference in Microwave Integrated Circuits*, 2012, pp. 405-408.

[19] T. Thrivikraman, D. Perkovic-Martin, M. Jenabi, and J. Hoffman, "Radar waveform pulse analysis measurement system for high-power GaN amplifiers," in *IEEE Microw. Meas. Conf.*, 2012, pp. 1-4.

[20] S. Leonov, "MTI radar stability measurement error," in *IEEE CIE Proc. Int. Conf.*, 2001, pp. 244-245.

[21] F. Mkadem, M. B. Ayed, S. Boumaiza, J. Wood, and P. Aaen, "Behavioral modeling and digital predistortion of Power Amplifiers with memory using Two Hidden Layers Artificial Neural Networks," in *IEEE Int. Microw. Symp. Dig.*, 2010, pp. 656-659.

[22] J. Vuolevi, J. Manninen, and T. Rahkonen, "Cancelling the memory effects in RF power amplifiers," in *IEEE Int. Symp. Circuits and Systems*, 2001, pp. 57-60 vol. 1.

[23] L. Jong-Wook and K. J. Webb, "A temperature-dependent nonlinear analytic model for AlGaN-GaN HEMTs on SiC," *IEEE Trans. Microw. Theory Techn.*, vol. 52, pp. 2-9, 2004.

[24] J. Mazeau, R. Sommet, D. Caban-Chastas, E. Gatard, R. Quere, and Y. Mancuso, "Behavioral Thermal Modeling for Microwave Power Amplifier Design," *IEEE Trans. Microw. Theory Techn.*, vol. 55, pp. 2290-2297, 2007.

[25] A. S. Tehrani, C. Haiying, S. Afsardoost, T. Eriksson, M. Isaksson, and C. Fager, "A Comparative Analysis of the Complexity/Accuracy Tradeoff in Power Amplifier Behavioral Models," *IEEE Trans. Microw. Theory Techn.*, vol. 58, pp. 1510-1520, 2010.

[26] J. C. Pedro and S. A. Maas, "A comparative overview of microwave and wireless power-amplifier behavioral modeling approaches," *IEEE Trans. Microw. Theory Techn.*, vol. 53, pp. 1150-1163, 2005.

[27] J. B. King and T. J. Brazil, "Nonlinear Electrothermal GaN HEMT Model Applied to High-Efficiency Power Amplifier Design," *IEEE Trans. Microw. Theory Techn.*, vol. 61, pp. 444-454, 2013.

[28] A. Zhu, J. C. Pedro, and T. J. Brazil, "Dynamic Deviation Reduction-Based Volterra Behavioral Modeling of RF Power Amplifiers," *IEEE Trans. Microw. Theory Techn.*, vol. 54, pp. 4323-4332, 2006.

[29] F. Besombes, J. Mazeau, J. P. Martinaud, Y. Mancuso, R. Sommet, S. Mons, *et al.*, "Electro-thermal behavioral modeling of RF power amplifier taking into account load-pull effects for narrow band radar applications," in *IEEE Conf. Microw. Integr. Circuits*, 2011, pp. 264-267.

[30] A. Soury and E. Ngoya, "Handling long-term memory effects in X-parameter model," in *IEEE Int. Microw. Symp. Dig.*, 2012, pp. 1-3.

[31] J. H. K. Vuolevi, T. Rahkonen, and J. P. A. Manninen, "Measurement technique for characterizing memory effects in RF power amplifiers," *IEEE Trans. Microw. Theory Techn.*, vol. 49, pp. 1383-1389, 2001.

[32] A. S. Tehrani, T. Eriksson, and C. Fager, "Modeling of long term memory effects in RF power amplifiers with dynamic parameters," in *IEEE Int. Microw. Symp. Dig.* , 2012, pp. 1-3.

[33] M. Isaksson, D. Wisell, A. Eng, and D. Ronnow, "A study of a variable-capacitance drain network's influence on dynamic behavioral modeling of an RF power amplifier," in *IEEE Microw. Measurement Conf.*, 2007, pp. 1-5.

[34] C. Maziere, A. Soury, E. Ngoya, and J. M. Nebus, "A system level model of solid state amplifiers with memory based on a nonlinear feedback loop principle," in *IEEE Eur. Microw. Conf.*, 2005, pp. 569-572.

[35] B. Fehri and S. Boumaiza, "Systematic estimation of memory effects parameters in power amplifiers' behavioral models," in *IEEE Int. Microw. Symp. Dig.*, 2011, pp. 1-4.

[36] S. Boumaiza and F. M. Ghannouchi, "Thermal memory effects modeling and compensation in RF power amplifiers and predistortion linearizers," *IEEE Trans. Microw. Theory Techn.*, vol. 51, pp. 2427-2433, 2003.

[37] J. Delprato, D. Barataud, M. Campovecchio, G. Neveux, C. Tolant, and P. Eudeline, "Measured and Simulated Impact of Irregular Radar Pulse Trains on the Pulse-to-Pulse Stability of Microwave Power Amplifiers," *Microwave Theory and Techniques, IEEE Transactions on*, vol. 62, pp. 3538-3548, 2014.

[38] A. Reddy, L. Qing, W. K. M. Ahmed, and E. Carey, "Performance analysis of a novel real-time closed-loop technique for non-linearity correction of power amplifiers," in *IEEE Sarnoff Symp.*, 2007, pp. 1-6.

[39] A. Katz and R. Dorval, "Evaluation and correction of time dependent amplifier non-linearity," in *IEEE Int. Microw. Symp. Dig.*, 1996, pp. 839-842 vol.2.

[40] A. Aghasi, A. Ghorbani, and H. Amindavar, "Polynomial Based Predistortion for Solid State Power Amplifier Nonlinearity Compensation," in *IEEE North-East Workshop Circuits and Systems*, 2006, pp. 181-184.

[41] H. Zhifu, G. Xuebang, and C. Shujun, "Electro-thermal model extraction of power GaN HEMT using I-V pulsed and DC measurements," in *IEEE 8th Int. Conf. ASIC*, 2011, pp. 850-853.

[42] P. Aaen, Jaime A. Plá, and J. Wood., *Modeling and Characterization of RF and Microwave Power FETs*: Cambridge University Press, 2007.

[43] A. Prejs, S. Wood, R. Pengelly, and W. Pribble, "Thermal analysis and its application to high power GaN HEMT amplifiers," in *IEEE Int. Microw. Symp. Dig.*, 2009, pp. 917-920.

[44] S. Boumaiza, J. Gauthier, and F. M. Ghannouchi, "Dynamic electro-thermal behavioral model for RF power amplifiers," in *IEEE Int. Microw. Symp. Dig.*, 2003, pp. 351-354 vol.1.

[45] R. Marante, L. Cabria, P. Cabral, J. C. Pedro, and J. A. Garcia, "Temperature dependent memory effects on a drain modulated GaN HEMT power amplifier," in *IEEE Workshop Integrated Nonlinear Microwave and Millimeter-Wave Circuits*, 2010, pp. 75-78.

[46] R. Pengelly and B. Pribble, "Intrinsic Cree GaN HEMT Models allow more accurate waveform engineered PA designs," in *ARMMS April 2013*, Oxfordshire, 2013, pp. 1-31.
[47] H. Kondoh, "An Accurate FET Modelling from Measured S-Parameters," *Microwave Symposium Digest, 1986 IEEE MTT-S International*, pp. 377-380, 2-4 June 1986 1986.
[48] F. Sechi and M. Bujatti, *Solid-State Microwave High-Power Amplifiers* vol. 1. Boston: Artech House, 2009.
[49] D. Wolpert and P. Ampadu, *Managing temperature effects in nanoscale adaptive systems*, 1 ed. vol. 1. New York: Springer Publishing New York, 2012.
[50] M. AKARSU, S. AYDOGU , and O. OZBAS, "Calculation of the electron mobility of GaN semiconductor compound using the Monte Carlo method," *Romanian Journal of Physics*, vol. 50, pp. 869-873, 2005 2005.
[51] P. C. Canfield, S. C. F. Lam, and D. J. Allstot, "Modeling of frequency and temperature effects in GaAs MESFETs," *IEEE J. Solid-State Circuits*, vol. 25, pp. 299-306, 1990.
[52] H. Tokuda, K. Kodama, and M. Kuzuhara, "Temperature dependence of electron concentration and mobility in n-GaN measured up to 1020 K," *Applied Physics Letters*, vol. 96, p. 252103, 2010.
[53] A. M. Darwish, B. D. Huebschman, E. Viveiros, and H. A. Hung, "Dependence of GaN HEMT Millimeter-Wave Performance on Temperature," *IEEE Trans. Microw. Theory Techn.*, vol. 57, pp. 3205-3211, 2009.
[54] A. M. Darwish, A. A. Ibrahim, and H. A. Hung, "Temperature Dependence of GaN HEMT Small Signal Parameters," *International Journal of Microwave Science and Technology*, vol. 2011, pp. 1-4, 2011.
[55] C. Florian, A. Santarelli, R. Cignani, and F. Filicori, "Characterization of the Nonlinear Thermal Resistance and Pulsed Thermal Dynamic Behavior of AlGaN-GaN HEMTs on SiC," *IEEE Trans. Microw. Theory Techn.*, vol. 61, pp. 1879-1891, 2013.
[56] S. Nuttinck, E. Gebara, J. Laskar, B. Wagner, and M. Harris, "RF performance and thermal analysis of AlGaN/GaN power HEMTs in presence of self-heating effects," in *IEEE Int. Microw. Symp. Dig.*, 2002, pp. 921-924 vol.2.
[57] C. Tien-Shun, L. Tsung Yi, and C. Tien-Sheng, "Temperature Dependence of Electron Mobility on Strained nMOSFETs Fabricated by Strain-Gate Engineering," *IEEE Electron Device Lett.*, vol. 33, pp. 931-933, 2012.
[58] V. O. Turin and A. A. Balandin, "Electrothermal simulation of the self-heating effects in GaN-based field-effect transistors," *Journal of Applied Physics*, vol. 100, pp. 054501-054508, 2006.
[59] V. Siklitsky. (2014). *GaN-Gallium Nitride*. Available: http://www.ioffe.rssi.ru/SVA/NSM/Semicond/GaN/index.html
[60] W. Yuh-Renn and J. Singh, "Transient study of self-heating effects in AlGaN/GaN HFETs: Consequence of carrier velocities, temperature, and device performance," *Journal of Applied Physics*, vol. 101, pp. 113712-113716, 2007.
[61] Y. Wang, "Electrical and thermal analysis of gallium nitride HEMTs," Masters Thesis, Physics, California Naval Postgraduate School, Monterey, 2009.
[62] S. Gueye, B. Dakyo, S. Alves, M. Stanislawiak, J.-P. Sipma, M. Olivier, *et al.*, "Insertion phase variation as a function of the voltage switching power supply of LDMSOS and GaN transistors for Radar Stability," in *IET Int. Conf. Radar Systems*, 2012, pp. 1-4.
[63] A. Rabany, L. Nguyen, and D. Rice, "Memory Effect Reduction for LDMOS Bias Circuits," *Microwave Journal Magazine*, vol. 46, pp. 124-130, 2003.
[64] W. Bosch and G. Gatti, "Measurement and simulation of memory effects in predistortion linearizers," *IEEE Trans. Microw. Theory Techn.*, vol. 37, pp. 1885-1890, 1989.
[65] A. Soury, E. Ngoya, and J. M. Nebus, "A new behavioral model taking into account nonlinear memory effects and transient behaviors in wideband SSPAs," in *IEEE Int. Microw. Symp. Dig.*, 2002, pp. 853-856 vol.2.
[66] M. J. Franco, "Bias induced memory effects in RF power amplifiers," ed. Hamilton, New Jersey: LINEARIZER TECHNOLOGIES INC, p. 38.
[67] C. Nguyen, N. X. Nguyen, and D. E. Grider, "Drain current compression in GaN MODFETs under large-signal modulation at microwave frequencies," *IEEE Electron. Lett.*, vol. 35, pp. 1380-1382, 1999.
[68] R. E. Leoni, III, M. S. Shirokov, J. Bao, and J. Hwang, "A phenomenologically based transient SPICE model for digitally modulated RF performance characteristics of GaAs MESFETs," *IEEE Trans. Microw. Theory Techn.*, vol. 49, pp. 1180-1186, 2001.
[69] A. Jarndal, B. Bunz, and G. Kompa, "Accurate Large-Signal Modeling of AlGaN-GaN HEMT Including

Trapping and Self-Heating Induced Dispersion," in *IEEE Symp. Power Semiconductor Devices and IC's*, 2006, pp. 1-4.
[70] J. M. Tirado, J. L. Sanchez-Rojas, and J. I. Izpura, "Trapping Effects in the Transient Response of AlGaN/GaN HEMT Devices," *IEEE Trans. Electron Devices*, vol. 54, pp. 410-417, 2007.
[71] S. C. Binari, P. B. Klein, and T. E. Kazior, "Trapping Effects in GaN and SiC Microwave FETs," *IEEE Proc.*, vol. 90, pp. 1048 - 1058, 2002.
[72] Z.-Q. Fang, D. C. Look, D. H. Kim, and I. Adesida, "Traps in AlGaN/GaN/SiC heterostructures studied by deep level transient spectroscopy," *Applied Physics Letters*, vol. 87, pp. 182115-182118, 2005.
[73] J. Joh, J. A. del Alamo, and J. Jimenez, "A Simple Current Collapse Measurement Technique for GaN High-Electron Mobility Transistors," *Electron Device Letters, IEEE*, vol. 29, pp. 665-667, 2008.
[74] T. Mizutani, Y. Ohno, M. Akita, S. Kishimoto, and K. Maezawa, "A study on current collapse in AlGaN/GaN HEMTs induced by bias stress," *IEEE Trans. Electron Devices*, vol. 50, pp. 2015-2020, 2003.
[75] A. S. Tehrani, C. Haiying, T. Eriksson, and C. Fager, "Complexity analysis of power amplifier behavioral models," in *Integrated Nonlinear Microwave and Millimeter-Wave Circuits (INMMIC), 2010 Workshop on*, 2010, pp. 102-105.
[76] C. G. Tua, T. Pratt, and A. I. Zaghloul, "A Study of Interpulse Instability in Gallium Nitride Power Amplifiers in Multifunction Radars," *IEEE Transactions on Microwave Theory and Techniques*, vol. 64, pp. 3732-3747, 2016.
[77] K. J. Keesman, *System identification : an introduction*. London ; New York: Springer, 2011.
[78] M. I. Skolnik, *Radar handbook*, 3rd ed. New York: McGraw-Hill, 2008.
[79] M. Cicolani, A. Gentile, S. Maccaroni, and L. Marescialli, "Pulse-to-Pulse Stability Characteristics of Robust Design Centered High Performances/Low Cost T/R Module," in *IEEE Eur. Radar Conference*, 2006, pp. 323-326.
[80] C. Salmer, P. Eudeline, and P. A. Rolland, "Pulse to Pulse Stability of Solid State Transmitter Module for Radars Application," in *IEEE Eur. Microw. Conf.*, 1998, pp. 79-84.
[81] P. Siqueira, R. Ahmed, J. W. Wirth, and A. Bachmann, "Variable Precision Two-Channel Phase, Amplitude, and Timing Measurements for Radar Interferometry and Polarimetry," *IEEE Trans. Microw. Theory Techn.*, vol. 55, pp. 2248-2256, 2007.

# Appendix A. **Brief tutorial and example on MTI radar processing**

The purpose of an MTI radar is to separate targets from clutter. Clutter is generally defined as unwanted stationary or slow-moving targets. Trees, geographical features, towers, building, terrestrial vehicles, rain and sea are some examples of clutter; what defines clutter depends on the selected radar function. The technique uses the Doppler frequency associated with a moving target to separate targets from clutter. Stationary targets still exhibit small Doppler shift due to wind, platform movement or motion of a rotating antenna. Slow moving targets such as terrestrial vehicles will have a higher Doppler shift; they can also be rejected by the MTI processor depending on filter characteristics. For clarity only the simplest implementation of an MTI filter will be discussed here.

The radar return includes moving targets, stationary targets and clutter. A single pulse return typically does not contain enough information to measure the Doppler shift. Figure A-1 shows the in-phase output of a coherent receiver (bipolar video) for a single return. This example contains close-in clutter and two point targets farther down range, they are marked in the figure for clarity. Point targets are objects typically smaller than the range resolution of the radar. Not having information a priori will make it difficult or impossible to determine which target is moving.

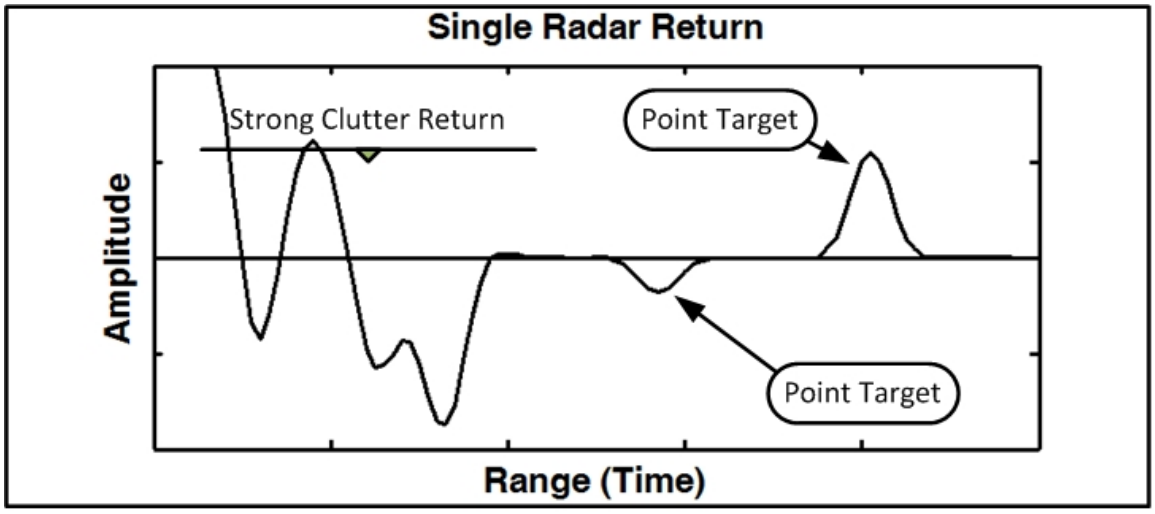


Figure A-1: Coherent receiver in-phase channel output; a single radar return contains clutter and targets.

The Doppler frequency is sampled at a rate of Pulse Repetition Frequency (PRF). PRF is the number of pulses a radar transmits per unit time. Observing the environment at different points in time allows for the separation of stationary targets from moving targets. For any two consecutive pulses received, the stationary target will have similar amplitude and phase. Moving targets will impose a phase change on their return proportional to their radial velocity in respect to the radar. Figure A-2 shows multiple returns; notice the change in amplitude that occurs in the in-phase receiver channel due to phase shift from the moving target. The phase of the target changes on each return, indicating movement.

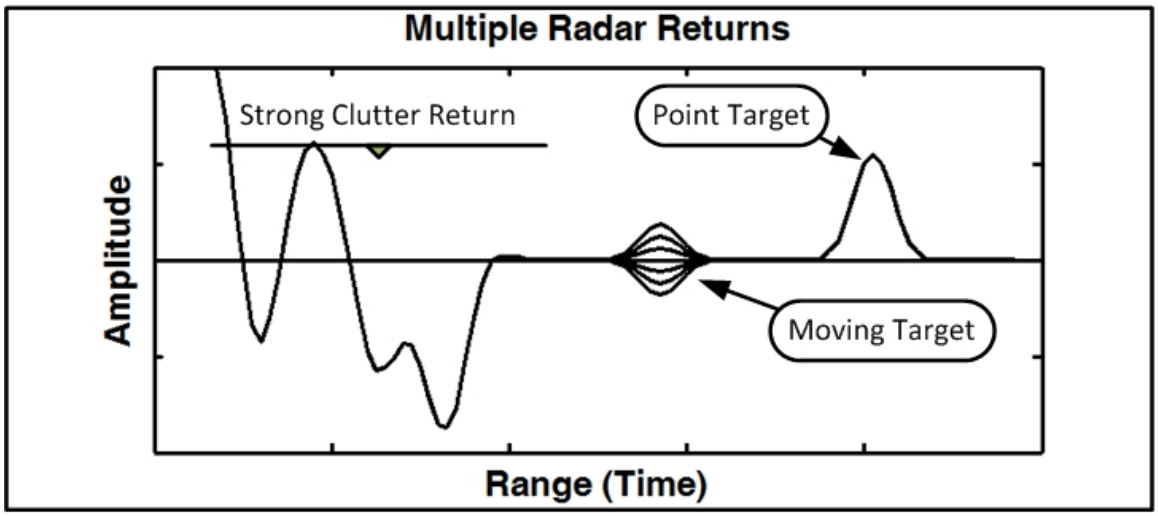


Figure A-2: Coherent receiver in-phase channel output; multiple pulses overlaid to show Doppler Effect on radar return.

One of the simplest ways to detect a moving target from a set of returns is to subtract the second return from the first; this is the most basic implementation of an MTI system. Nowadays this is done in the digital domain, where entire radar returns can be stored for later processing. Figure A-3 illustrates the concept, in which $x[k]$ represent the current received radar return; the previous pulse was stored in memory and delayed by $T = PRI$, where PRI is the Pulse Repetition Interval (the time between pulses).

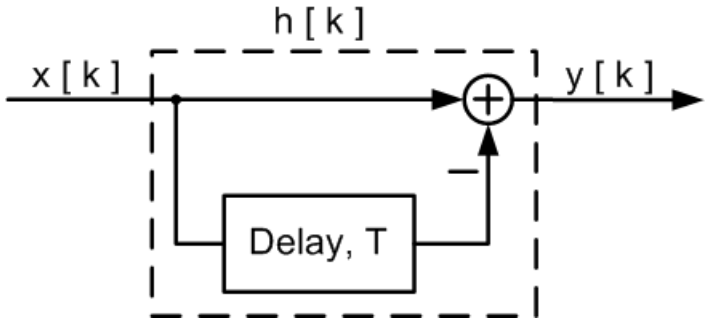


Figure A-3: Single-Delay Pulse Canceller; current received pulse is subtracted from the previous received pulse.

The resulting $y[k]$ illustrated in Figure A-4 contains only the differences between the two pulses; moving targets, noise and system instabilities. The system instabilities concerning this investigation prevent the detection of small targets and desired slow-moving targets due to an increase in the detection threshold.

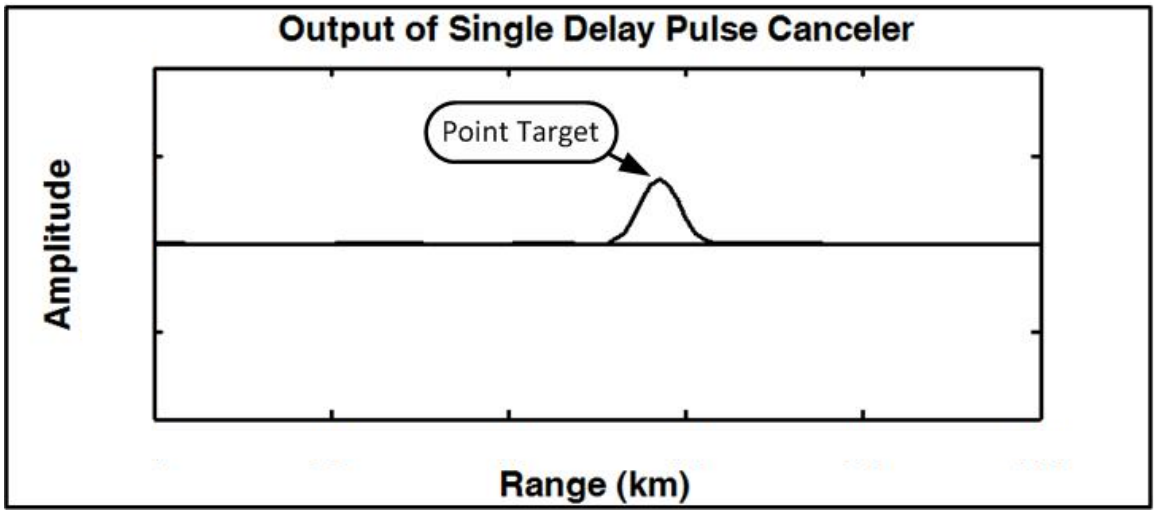


Figure A-4: Output of the Single-Delay Pulse Canceller; only the moving target is visible.

# Appendix B. **Power Amplifier Test Set-up; Hardware Design and Configuration**

The PA test set-up is comprised of several laboratory instrumentation and custom hardware. Figure B-1 shows many of the instruments used in experiment. The next several subsections will describe the function of each of these components.

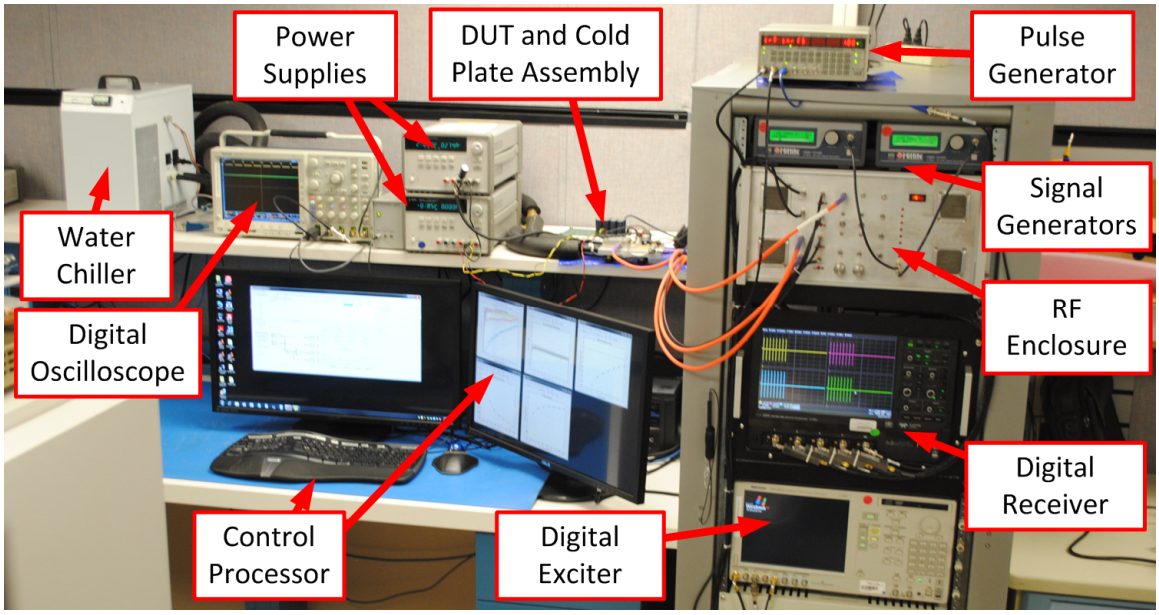


Figure B-1 : Photo of instrumentation used to conduct the experiment.

## Control Processor:

The Control Processor is an industrial rack mounted personal computer running MATLAB™. The MATLAB™ license includes the Instrument Control Toolbox, which facilitate a rapid interface to several instruments. The automation of the required instrumentation involved the creation of MATLAB™ instrument drivers and classes (object oriented programming) to interface with the instruments, also several classes were created for data management. Standard Commands for Programmable Instruments (SCPI) instruction set was

used to remotely control the majority of the instruments. All of the MATLAB™ code associated with the control of the instrumentation, waveform synthesis and data processing was implemented using object oriented classes. This allows for the addition of complex programming routines with minimum impact to previously written code. The flexibility brought by the object oriented programming allows for the addition of multiple identical instruments without interference with each other or complicating the MATLAB code. For instance a second oscilloscope was added to the PA test set-up to capture drain current and drain voltage waveforms.

The Control Processor is used to control all equipment and instrumentation, to create sequences of radar waveforms (CPIs), and to evaluate behavioral model candidate. All the functionality necessary to reproduce radar waveform, capture data and process the amplifier response was programmed into the Control Processor. The Control Processor synthesizes waveforms based on the specifications listed in the Waveform Library File. These waveforms are then uploaded in the Digital Exciter (AWG). The Control Processor is also in charge of managing the data once obtained from the Digital Receiver.

### Radar Digital Exciter:

A two-channel Arbitrary Waveform Generator (AWG) is used as a surrogate Radar Digital Exciter. The Radar Digital Exciter generates the radar waveforms synthesized and scheduled by the Control Processor. A Tektronix AWG5012 Arbitrary Waveform Generator was available for use. This instrument allows for the creation of pulses with arbitrary characteristics. This is a necessary feature for the predistortion technique developed to mitigate the interpulse distortion.

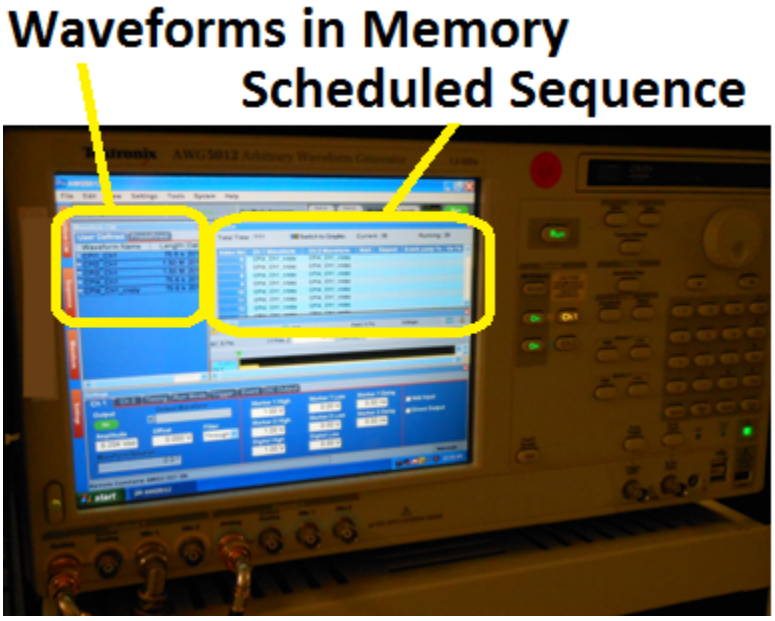


Figure B-2: A Tektronix AWG5012 Arbitrary Waveform Generator is used as a surrogate Radar Digital Exciter.

All the waveforms created from the Waveform Library File are uploaded into the Radar Digital Exciter. This is done by uploading a single pulse for each waveform into the radar exciter. Each pulse is synthesized as a combination of the transmitting pulse and the listening (non-transmitting) portion of the PRI. The waveforms loaded into the Radar Digital Exciter are synthesized to produce an IF of 187.5 MHz at a sampling rate of 600 MS/s. The Radar Digital Exciter can change its output signal power independently on each of the two channels. This allows for an easier system calibration as it facilitates the setup of the DUT operating point and other tests.

**Down-Converter Design:**

The down-converter follows a dual-stage design. Figure B-3 shows a block diagram of the down-converter design. A total of four down-converters were fabricated and installed inside an RF enclosure.

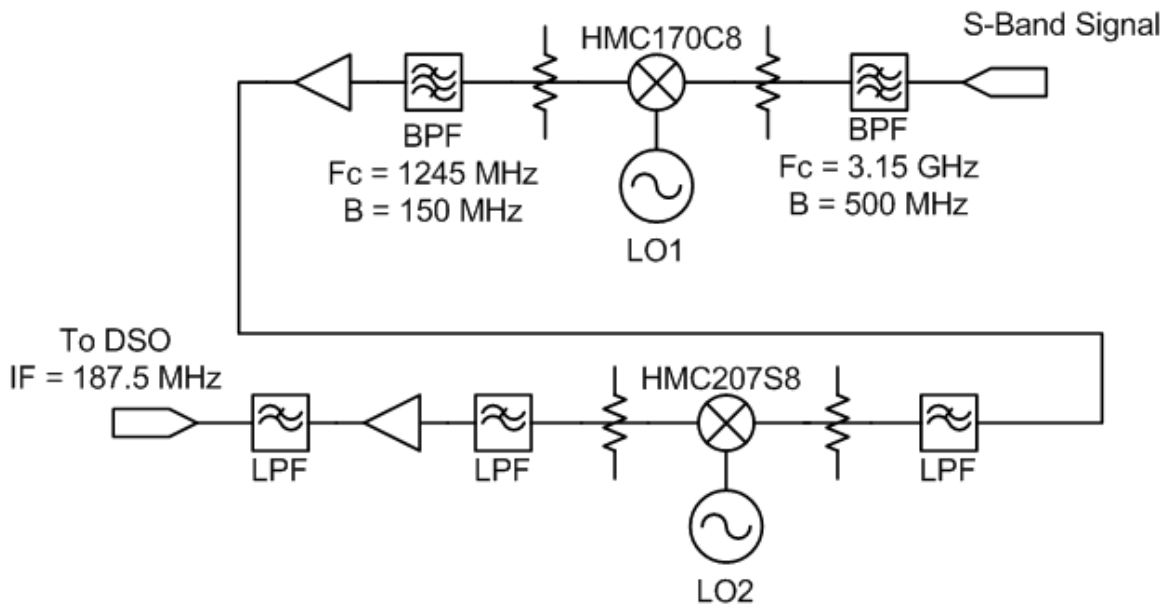


Figure B-3: Block diagram of down-converter design.

Starting at the upper right corner of Figure B-3, the RF signal between 2900 MHz and 3400 MHz enters the down-converter. The input signal is filtered by a Band Pass Filter (BPF) centered at 3150 MHz, with a 3 dB bandwidth of 500 MHz. This filter is used to limit out of band emissions and noise from entering the first downconverter stage. The signal is conditioned by an attenuator before entering the first mixer; this is done to improve impedance matching between components. The mixer's *LO*1 frequency is tuned to translate the expected *RF* signal to a fixed *IF* centered at 1245 MHz. The *LO*1 range is tunable between 4145 MHz and 4645 MHz. Multiple products with frequencies $n \times LO1 \pm m \times RF$ are now at the output of the mixers, where *n* and *m* are integers, typically assumed to be from 0 to 4. The desired product is $IF1 = LO1 - RF$ ; a second BPF is used to filter most of the undesirable products. The BPF is centered at 1245 MHz, with a 3 dB bandwidth of 150 MHz. The signal is then amplified and further conditioned by a Low Pass Filter (LPF) and attenuator before entering the second conversion stage.

The signal centered at *IF*1 now enters the second mixer. The output of the mixer has products with frequencies $n \times LO2 \pm m \times IF1$. The desired product is $IF2 = LO2 - IF1$, where

*LO2* is fixed to 1432.5 MHz and *IF*1 is fixed to 1245 MHz. A LPF is used to filter most of the undesirable products and leave the desirable product now at 187.5 MHz. Further signal amplification and filtering is done prior to the input into the digital receivers. This includes a custom made BPF centered at 187.5 MHz with a bandwidth of 20 MHz.

## Up-Converter Design

The first step translates the signal coming from the Radar Digital Exciter (*IF*2) into a fixed *IF* (*IF*1). The second state translates *IF*2 into a desired *RF*. Figure B-4 shows a block diagram of the up-converter design. A total of two up-converters were fabricated and integrated into the *RF* enclosure.

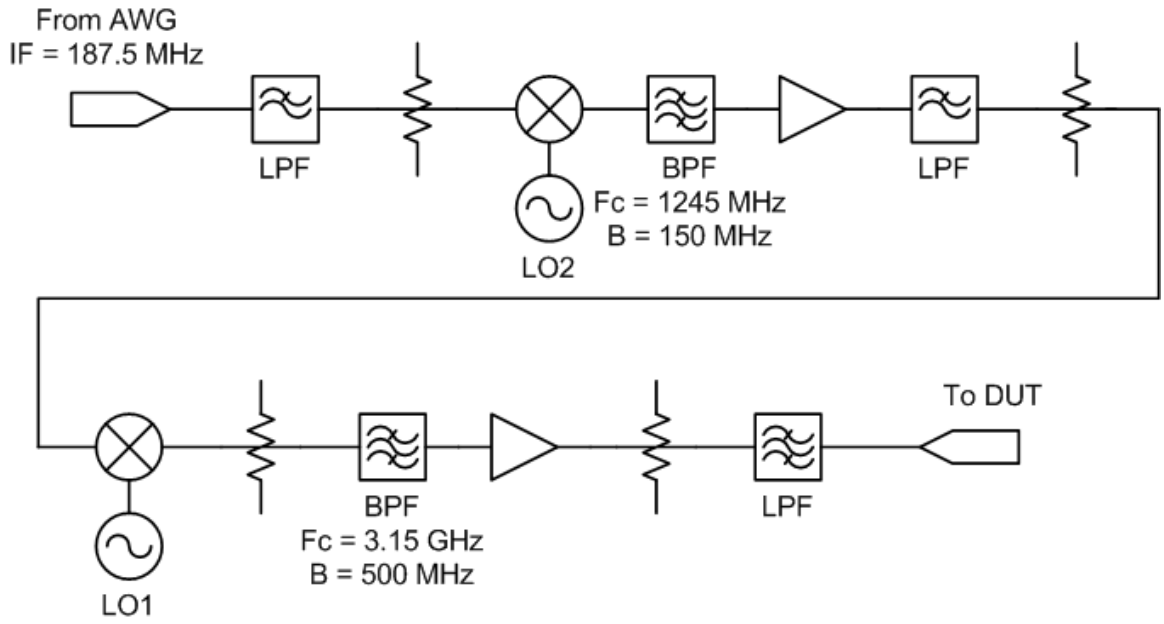


Figure B-4: Block diagram of up-converter design.

As the *IF*2 signal coming from the Radar Digital Exciter (AWG) enters the first up-converter stage, a LPF is used to condition the signal. An attenuator is placed in between the LPF and the first Mixer to help improve the impedance matching between components. The signal then enters the first stage mixer, where the nonlinear device produces multiple frequencies

$n \times LO2 \pm m \times IF2$; the desired product is $IF1 = LO2 - IF2$, where $LO2$ is fixed to 1432.5 MHz and $IF2$ is fixed to 187.5 MHz. A BPF is used to filter most of the undesirable products, leaving only the desirable signal centered at 1245 MHz. The BPF is centered at 1245 MHz with a 3 dB bandwidth of 150 MHz. The signal is then amplified and further conditioned by another LPF and attenuator before entering the second conversion stage.

The IF1 signal now enters the second RF mixer. The nonlinear device produces multiple products with frequencies $(n \times IF1 \pm m \times LO1)$. The desired product is $IF1$-$LO1$, where $IF1$ is fixed to 1245 MHz and LO1 is tunable between 4145 MHz and 4645 MHz. A BPF is used to filter most of the undesirable products, leaving only the desirable product now within the selected RF band between 2900 MHz and 3400 MHz. The BPF is centered at 3150 MHz with a 3 dB bandwidth of 500 MHz. The RF signal is further conditioned by amplification and filtering before it enters the switch matrix.

## Pulse Generator

A Stanford Research Systems Model DG645 Digital Delay Generator is used to coordinate the trigger pulses. The Tektronix AWG5012 (Radar Exciter) has two digital marker outputs per channel, with the same time granularity as its analog outputs. One of the instrument's digital marker outputs is connected to the pulse generator. The pulse generator creates a trigger pulse to initiate data collection for the RF waveforms and DC waveforms.


Figure B-5: Stanford Research Systems Model DG645 Digital Delay Generator is used to coordinate trigger to the Radar Digital Receiver and Digital Oscilloscope

The DG645 is programmed to change the time-location of the trigger pulse sent to the Digital Receiver and Digital Oscilloscope. This allows for data collection of waveforms that are longer than the available Digital Receiver hardware memory. The technique is successful based on the assumption that the amplifier behavior is repeatable. If the Waveform of Interest (WOI) has a duration longer than the available memory for the Digital Receiver and Digital Oscilloscope, then the data is collected using multiple triggers. Each collection is time aligned by the Pulse Generator. The designed software has sufficient logic to determine if the procedure is necessary and how to manage the data after it is collected.

The other marker is used to activate amplifier enable circuitry if available. This feature is not used during testing of the CREE CMPA2735075F device, but it was used during testing of the Aethercomm Model Number SSPA 2.9-3.5-100 and the RFHIC Model Number RRP31250-10 Power Amplifiers. Figure B-6 illustrates the amplifier enable pulse concept. The leading edge of the amplifier enable pulse leads the RF Signal. The falling edge lags the RF Signal. The amplifier enable pulse is programmed to activate the amplifier circuitry $T_E$ microseconds before the RF pulse is transmitted and it lasts $T_E$ after the RF pulse ends.

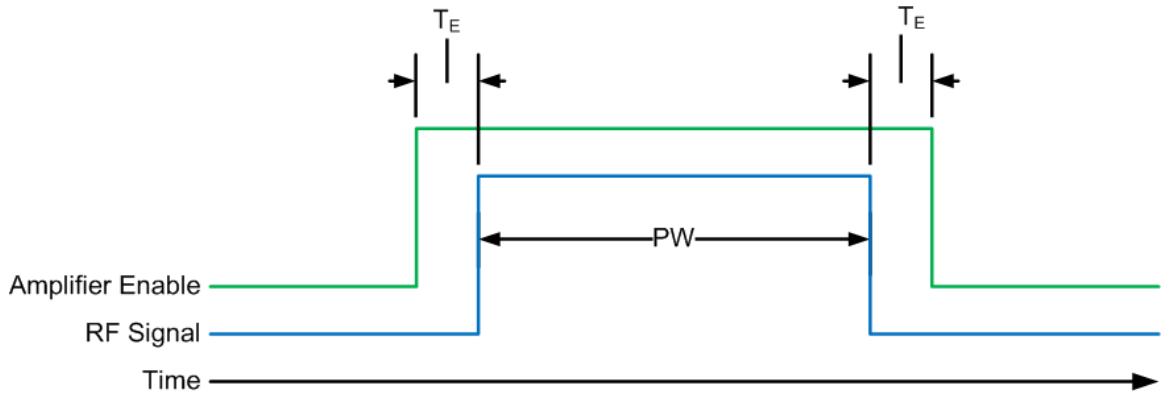


Figure B-6: Amplifier enable pulse concept. The amplifier enable pulse activates the amplifier circuitry **$T_E$** microseconds before the RF pulse is transmitted and it lasts **$T_E$** after the RF pulse ends.

The oscilloscope (digital receiver) horizontal time-scale and memory size are also automatically adjusted to accommodate long CPIs. If the CPI is too long for the available memory, then logic in the instrument control software will coordinate the data collection using multiple captures. This is done primarily by programming the delay in the Pulse Generator. Figure B-7 shows how the trigger pulse moves to capture an entire CPI. Figure B-7 (a) shows a CPI with ten pulses. The Digital Receiver memory is only big enough to capture five complete pulses. The trigger pulse is positioned slightly before the beginning of the CPI and the first five pulses are captured and transferred into the Control Processor memory. In figure B-7 (b), the trigger pulse was shifted in time so that the next time the Digital Receiver is triggered it will capture the remaining pulses that complete the CPI.

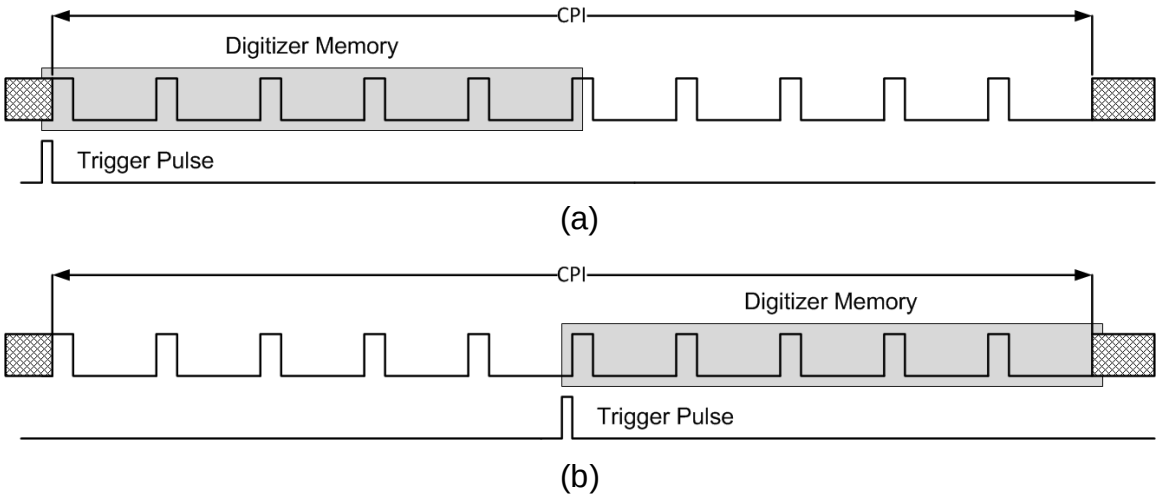


Figure B-7: Shifting trigger pulse to capture long CPI. The digital memory is limited, so the trigger pulse is set to capture the first part of the CPI. Later the trigger pulse is shifted in time to capture the second part of the CPI.

**RF Enclosure:**

The up-converter, down-converter, RF switch network, digital control, internal temperature monitoring, Local Oscillator (LO) distribution manifold and necessary power supplies where integrated inside a 19" rack mounted electronics enclosure (RF Enclosure).

## Switch Matrix:

The Switch Matrix is used to route RF signals into the DUT and the 4-channel Radar Digital Receiver. The signal routing is controlled via mechanical RF switches. These are actuated by a digital interface card controlled over USB.

Figure B-8 shows a block diagram of the switch matrix and calibration manifold. The Digital Exciter Channels 1 and 2 are signals that have been up-converted into RF. The Digital Receivers channels 1 through 4 are signals that will be down-converted before digitizing. The RF Outputs 1 and 2 are the signals that will be injected to the DUTs (amplifiers). The RF inputs 1 and 2 are signals after amplification.

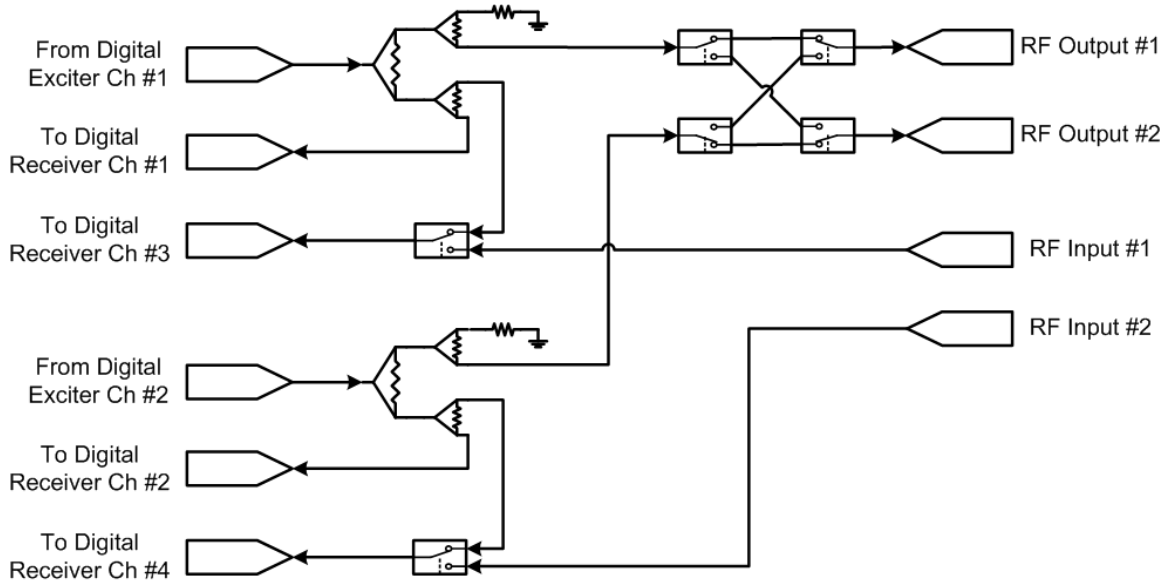


Figure B-8: Block diagram of RF switch matrix

Starting with the signals coming from the two-channel Radar Digital Exciter, each of the outputs is split into four. Only three signal outputs are used, the remaining signals port is terminated with a 50 ohm load. One of the output signals is routed and hardwired directly into one of the Radar Digital Receiver channels. This is necessary to provide a signal sample for

system identification. The Digital Receiver channels 1 and 2 are used exclusively for this purpose.

A mechanical RF switch is located below each of the 1-to-4 ways splitters. Each switch is used to route one of two signals into a Digital Receiver. The signal source routed into Digital Receiver #3 is either a reference signal from the Digital Exciter #1 or a signal from the RF enclosure RF Input #1. Likewise the signal source routed into Digital Receiver #4 is either a reference signal from the Digital Exciter #2 or a signal from the RF enclosure RF Input #2.

Located on the upper right side of the figure is an arrangement of mechanically actuated RF switches. They are configured to alternate the Radar Digital Exciter channel #1 and #2, effectively changing the channel that provides the DUTs input signal. Figure B-9 (a) shows the switch arrangement configured for device characterization. This configuration connects a sample of the Digital Exciter Channel #1 to the RF Output #1, and Digital Exciter Channal #2 to the RF Output #2. Figure B-9 (b) shows the switch arrangement configured for predistortion testing and validation. This configuration connects a sample of the Digital Exciter Channel #1 to the RF Output #2, and Digital Exciter Channel #2 to the RF Output #1.

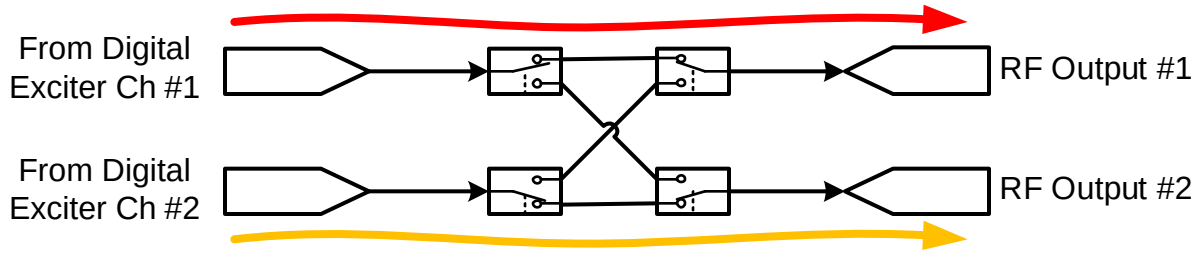


(a) Device characterization

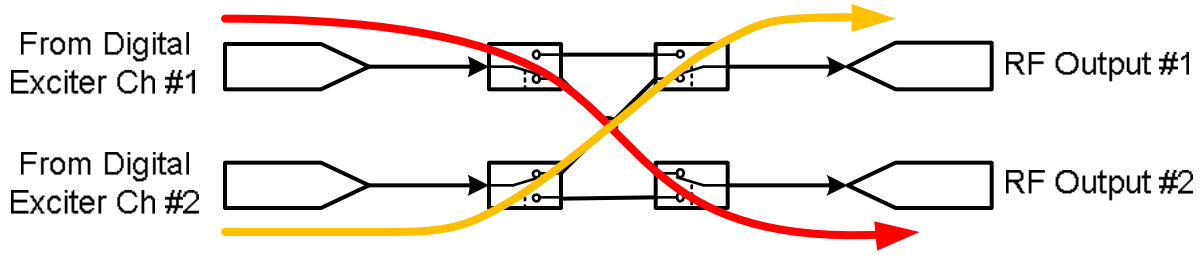


(b) Predistortion testing and validation

Figure B-9: Switch Matrix; mechanical RF switches arrangement used to swap the digital exciter channels to a different RF Output port.

Ultimately the switch matrix is configured in three different ways: 1) Calibration, 2) Device Characterization and 3) Predistortion Test and Validation. Table B-1 shows the RF Enclosure port connections for the three different configurations.

Table B-1: Switch Matrix RF Port Configuration

| Operation Mode | RF Input | RF Output |
|---|---|---|
| Calibration | Digital Exciter #1 | Digital Receiver #1 |
| | | RF Output #1 |
| | | Digital Receiver #3 |
| | Digital Exciter #2 | Digital Receiver #2 |
| | | RF Output #2 |
| | | Digital Receiver #4 |
| Characterization | Digital Exciter #1 | Digital Receiver #1 |
| | | RF Output #1 |
| | RF Input #1 | Digital Receiver #3 |
| | Digital Exciter #2 | Digital Receiver #2 |
| | | RF Output #2 |
| | RF Input #2 | Digital Receiver #4 |
| Predistortion | Digital Exciter #1 | Digital Receiver #1 |
| | | RF Output #2 |
| | RF Input #1 | Digital Receiver #3 |
| | Digital Exciter #2 | Digital Receiver #2 |
| | | RF Output #1 |
| | RF Input #2 | Digital Receiver #4 |

**Local Oscillator:**

Two Hittite HMC-T2100 Signal Generators were used as Local Oscillators (LO) for the up/down-converter stages. Inside the RF Enclosure, the LO signals is divided into 8 equally powered signals. For each of the LOs, two are terminated with a 50 ohm load, while the other six are routed, two for the up-converters and four for the down-converters.

The LO1 is tuned within the frequency range of 4145 - 4645 MHz. The actual frequency needed is automatically calculated by the Control Processor based on the desired center frequency. The LO2 is tuned to the fixed frequency of 1435 MHz. This ensures that the appropriate IF is obtained within the up/down-converter stages.

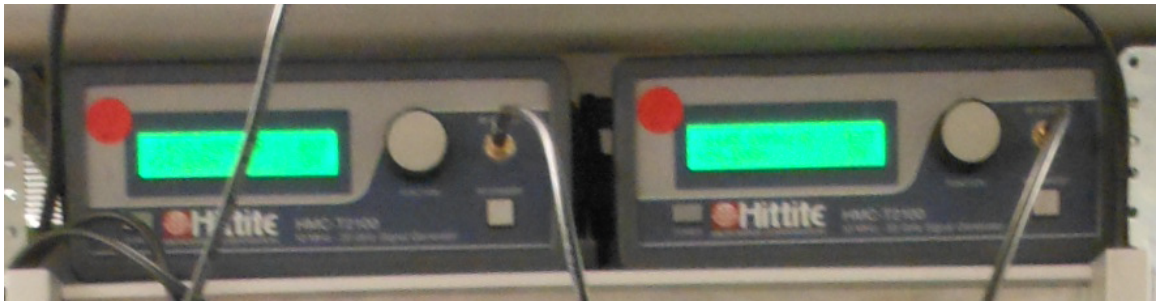


Figure B-10: Signal Generator used as local oscillators for the up and down converters

**Recirculating Water Chiller:**

A MELCOR MRC300 recirculating water chiller is used to keep the DUT at a stable temperature. The chiller temperature set point is changed via software from the Control Processor.

**Radar Receiver:**

A four-channel Digital Storage Oscilloscope (DSO) is used as a surrogate Radar Digital Receiver. Initially a Tektronix DSO4034 oscilloscope was used as surrogate digital receiver. It was later replaced with a Teledyne-LeCroy HDO6054 digital oscilloscope in favor of improved vertical resolution and faster data download. The Radar Digital Receiver digitizes signals after the down-converters. The analog bandwidth is reduced to 20 MHz via band pass filters just before the Digital Receiver. All waveform signals are at a nominal Intermediate Frequency (IF) of 187.5 MHz and are digitized at a sampling rate of 50 mega samples per second. The resulting

digital IF is 12.5 MHz. Digital Downconvertion (DDC) is later used to translate the digital IF into In-phase (I) and In-quadrature (Q), (a.k.a. I/Q data).


Figure B-11: Surrogate Radar Digital Receiver.

## DC Signaling Digitizer:

The amplifier requires an operating point. The point of maximum efficiency was chosen as the best point to get the most power out of the device. Calculating the device efficiency requires a complicated set of measurement, for example a precise knowledge of the RF input power, RF output power and consumed DC power. For this reason drain current waveform and drain voltage waveform measurement capabilities were added to the PA test set-up. The addition was relatively straight forward thanks to the use of object oriented programming; another instance of an oscilloscope for data capture was added.

A Tektronix DSO4034 oscilloscope is equipped with an Agilent N2783A current probe to monitor and digitize the DUT's drain current ($I_D$) waveform. The drain current waveform contains high frequency components due to the pulse signal's short rise and fall time and ringing. A high bandwidth current probe is needed to characterize the current waveform.

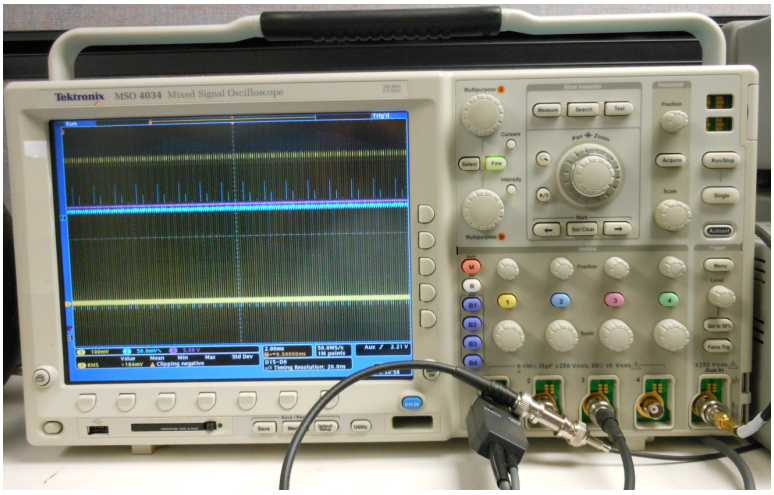


Figure B-12: Digital Oscilloscope used to digitize the DUT's drain voltage and drain current waveforms.

The drain voltage waveform ($V_D$) is also monitored and digitized. The drain voltage waveform is composed of two waveforms captured by the oscilloscope. The first waveform captured using a DC coupled voltage probe, it is later reduced to drain voltage mean value. The second waveform is drain voltage measured using an AC coupled voltage probe. The DC coupled voltage measurement is arithmetically added to the AC coupled voltage measurement before storage.

The two waveforms for current and voltage are saved along with the digitized RF waveforms. With the drain current and drain voltage, the DUT's power draw is approximated. The results are used to compute Power Added Efficiency (PAE).

# Appendix C. **Instrument Class Properties and Methods:**

## Waveform Library File

The information required to construct radar waveforms is stored in a Waveform Library File (WLF). The WLF contains a list of the waveforms to be synthesized during a test event. The number of entries in the waveform file is arbitrary, but should be kept small to conserve system resources and reduce the number of possible waveform combination while conducting an experiment. A description of the properties required for each entry in the WLF is listed in Table C-1. Each waveform must have a unique waveform name, and have independent and arbitrary values for the following properties: Pulse Modulation, Modulation Bandwidth, Pulse Width, Pulse Duty Cycle and Number of Pulses in a waveform.

Table C-1: Waveform Library File; field descriptions

| Field Name: | Description: | Example Value: | Range of values: |
|---|---|---|---|
| index | Waveform entry index, must be unique starting with a one | 1 | Incremental integers starting with 1 |
| name | Waveform name, must be a unique single word | CPI1 | Any unique word without symbols or spaces |
| modul | Pulse modulation, various modulations are supported. | CW | CW, LFM, PSK, NOSIG, AMP_ENABLE, Vramp and Pramp |
| RF_GHz | Waveform RF specified in GHz. Only the first entry in the Waveform Library File is used to initialize the experiment's Local Oscillators. | 3.2 | From 2.9 to 3.4 in 0.01 step increments. |
| IF_MHz | Waveform IF specified in MHz, each waveform can have its own independent frequency. Usable tuning range is hardware-limited to ±10 MHz from nominal. | 187.5 | 187.5 ±10 |
| FS_MHz | Sampling rate for Digital Exciter (AWG) specified in MHz. Only the first entry in the Waveform Library File is use to setup the AWG sampling clock. | 600 | Many possible ranges, consult user's manual. |
| BW_MHz | Pulse bandwidth, specified in MHz. Used only if LFM or PSK is selected as the waveform modulation, otherwise it is set to zero. Available bandwidth is limited by hardware filters at the Digital Receiver input to less than 20 MHz. | 0 | 0 to 20 |
| PW_usec | Pulse width, specified in microseconds. Values are limited by available memory and software checks. | 10 | 1 to 200 |
| DC_perc | Pulse duty cycle, specified in percentage. Values are limited by available memory and software checks | 8 | 1 to 100 |
| Npulses | Number of pulses in a waveform. Values are limited by available memory. | 32 | 1 to 65536 |

The Radar Control Processor is tasked with the synthesis of all the waveforms specified in the Waveform Library file. All the properties associated with a waveform are kept within a Waveform_Class object. The synthesized waveforms will later be loaded into the Radar Exciter (AWG). The exception to this is the synthesis of the WOI, where each pulse in the waveform is assigned to its own Waveform_Class object. Figure C-1 shows the waveform synthesis concept.

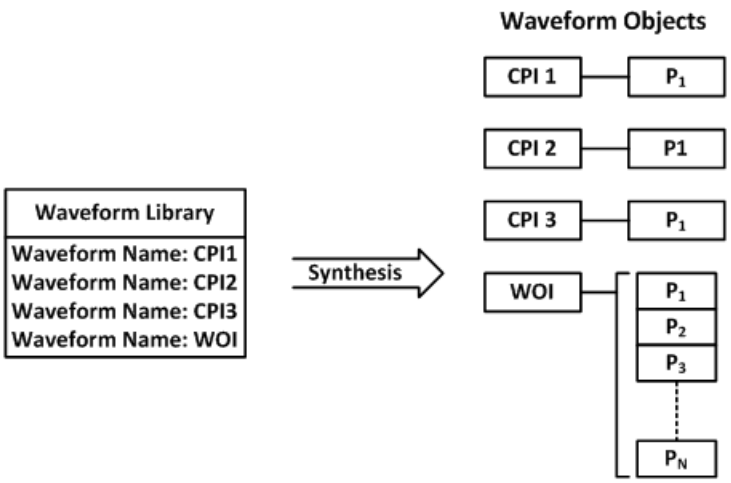


Figure C-1: Waveform Synthesis. From the Waveform Library, multiple waveforms are created into memory, each waveform has unique properties. For normal CPIs, a single pulse is synthesized and uploaded to the AWG. For the WOI, all the individual pulses are synthesized and uploaded.

The Radar Exciter must be able to transmit the waveforms that were synthesized from the waveform library. For typical waveforms a single pulse is synthesized and later uploaded into the Receiver Exciter. Every time the Radar Exciter transmits the waveform the pulses are repeated in a loop to achieve the designed Number of Pulses for the waveform's CPI. Figure C-2 illustrates this concept.

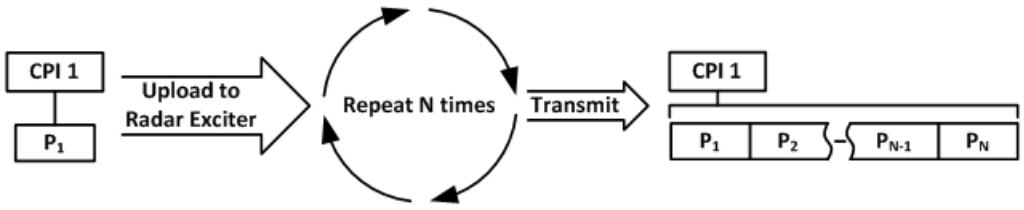


Figure C-2: After waveform creation, a single pulse per waveform is uploaded into the Radar Exciter. The pulse in queued in memory to be transmitted N times to complete a CPI.

## Waveform Sequence:

The experiment requires a minimum of two waveforms be synthesized. However, all the waveforms listed in a waveform library file are loaded to the radar exciter for transmission. The waveform play back order can be changed at will. Figure C-3 illustrates the concept where a waveform library file is used to synthesize a group of waveforms. The number of waveforms listed in a waveform library file and the subsequence reproduction of these by the radar exciter are limited by the hardware memory.

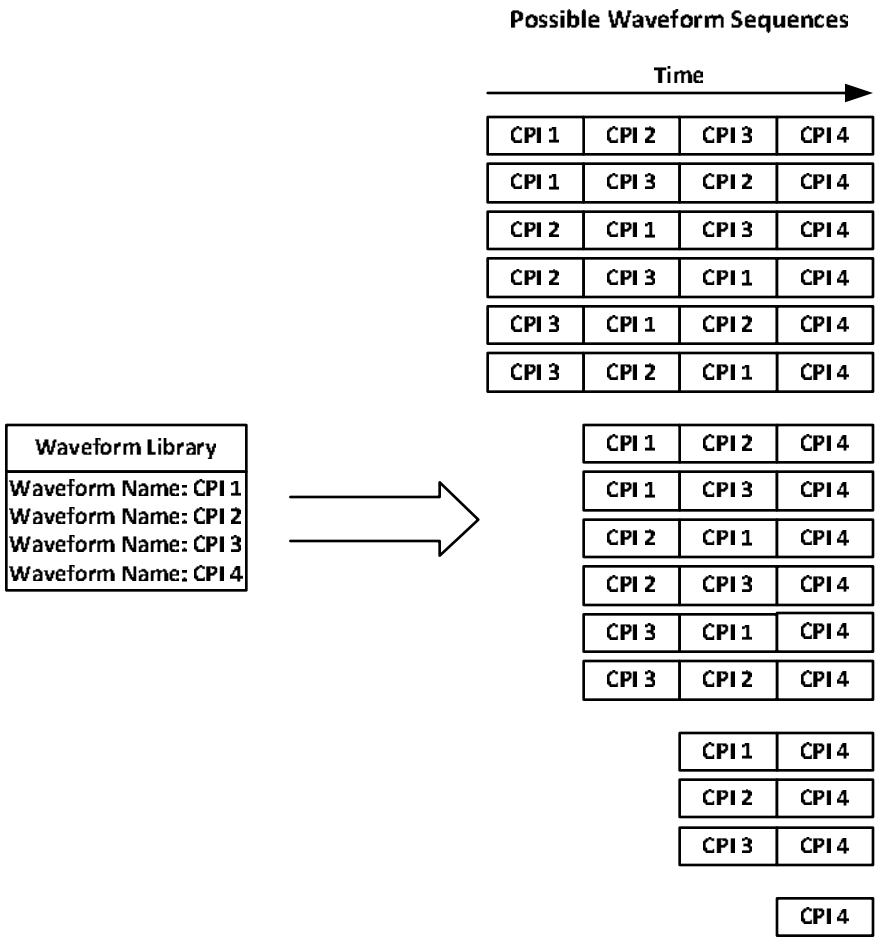


Figure C-3: Possible Waveform Sequences

Due to the length of the observed transient and the desire to control the number of variables in the experiment, the waveforms length is limited. The length is set to guarantee that only the memory effect from the previous waveforms affect the WOI. Figure C-4 illustrate the concept, where the combinations of waveforms are limited. The combination of waveforms necessary to characterize and document the amplifier behavior is reduced.

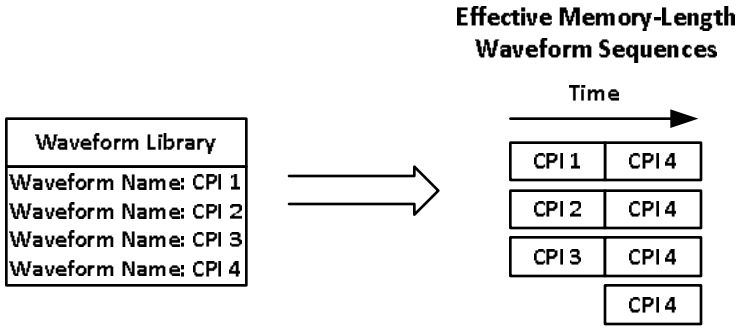


Figure C-4: Effective Waveform Sequence

## Waveform Class Object

Each waveform listed in the Waveforms Library File has a limited set of properties. The waveform synthesis derives several other properties. These properties, including a copy of the synthesized waveform, are stored in a Waveform Class Object. A description of the properties required for each synthesized waveform is listed in Table C-2.

Table C-2: Waveform Object Properties

| Property: | Description: | Data Type: |
|---|---|---|
| **name** | Unique name is assigned to each pulse in a waveform | String of characters |
| **modulation** | Pulse modulation used | String of characters |
| **BW** | Modulation bandwidth (Hz) | Float |
| **FS** | Sampling frequency used by radar exciter (Hz) | Float |
| **IF** | Intermediate frequency used by radar exciter and radar receiver (Hz) | Float |
| **PW** | Pulse width (seconds) | Float |
| **DC** | Pulse duty cycle in fractions | Float |
| **RF** | RF frequency used on test (Hz) | Float |
| **Marker1** | Digital signal produced by the radar exciter to enable or disable power amplifier | Float Array |
| **Marker2** | Digital signal produced by the radar exciter to synchronize digital receiver and pulse generator | Float Array |
| **index** | Used for data indexing purposes | Float |
| **FS_DSO** | Digital receiver sampling frequency (Samples per second) | Float |
| **t_DSO** | Time vector for RF signal (seconds) | Float Array |
| **Xref_ch1** | Digitized channel 1 RF reference signal | Float Array |
| **Xr_ch1** | Digitized channel 1RF signal | Float Array |
| **Xref_ch2** | Digitized channel 2 RF reference signal | Float Array |
| **Xr_ch2** | Digitized channel 2 RF signal | Float Array |
| **Xch1** | Synthetized pulse waveform for radar exciter channel 1 | Float Array |
| **Xch2** | Synthetized pulse waveform for radar exciter channel 2 | Float Array |
| **FS_DSO2** | Sampling frequency for DC waveform digitizer (Samples per second) | |
| **t_DSO2** | Time vector of DC waveforms (seconds) | Float Array |
| **Vd** | Drain voltage digitized waveform (Volts) | Float Array |
| **Id** | Drain current digitized waveform (Amps) | Float Array |
| **pre_amplitude** | Predistortion amplitude coefficient (Linear amplitude) | Float |
| **pre_phase** | Predistortion phase coefficient (Phase in radias) | Float |

## Synthesizing Waveform of Interest:

Upon the waveform synthesis stage, one of the waveforms must be selected as the Waveform of Interest (WOI). This waveform is the only one that will be collected for analysis. Due to the envisioned predistortion algorithm, this waveform synthesis requires the creation of all of the pulses in the waveform, instead of repeating an identical pulse. This will allow for the

predistortion of each individual pulse in a waveform. This also means that reproducing the waveform will occupy more system resources such as memory, as well as increasing the data transfer time between Radar Controller and the Radar Exciter. Figure C-5 illustrates the concept; each created WOI has $N$ synthesized pulses, these are uploaded to the Radar Exciter for transmission. The Radar Exciter arranges the pulses in an ascending order, where $P_1$ is followed by $P_2$ and so on until reaching $P_N$.

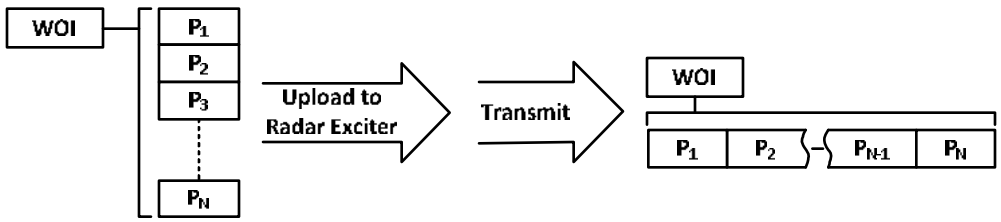


Figure C-5: WOI synthesis and transmission. Each pulse within a WOI is synthesized, uploaded to the Radar Exciter and then transmitted in sequence.

# Appendix D. **Graphical User Interface (GIU):**

A graphical user interface was developed to facilitate data collection and analysis. This interface allows for the loading of Waveform Library Files and the selection of the desired Waveform of Interest (WOI). Figure D-1 shows the GUI as it is initializing the instruments. The upper right corner of the figure includes a progress bar and status message that inform the user of which actions are being taken by the program. In this instance, the status message is indicating the creation of the MRC300 (water recirculating chiller) object. Once all the instruments are interconnected with MATLAB™, the GUI is ready to select a Waveform Library File. The file can be browsed and selected by clicking on the **Load Waveform** pushbutton located at the upper left side of the GUI figure.

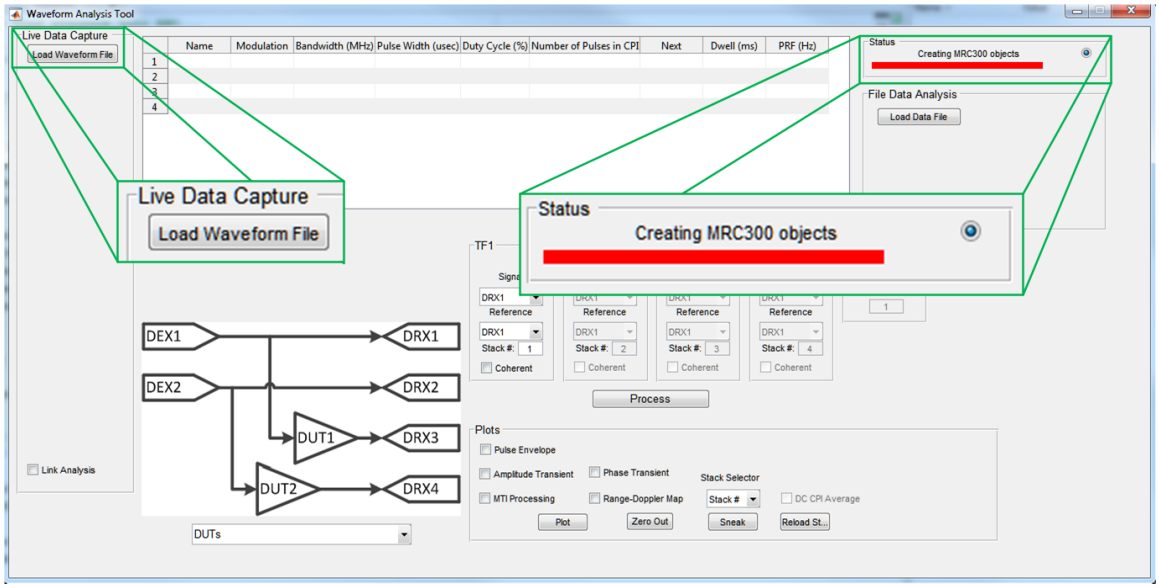


Figure D-1: GUI used for waveform creation, data collection and preliminary data processing.

Figure D-2 highlights the waveform table after the Waveform Library was loaded into the computer memory. A table on the GUI is populated with the waveform properties as specified by the Waveform Library file. The waveforms are not yet synthesized, after clicking on the

Create Waveform push button a dialog box appears asking the user to select the desired Waveform of Interest.

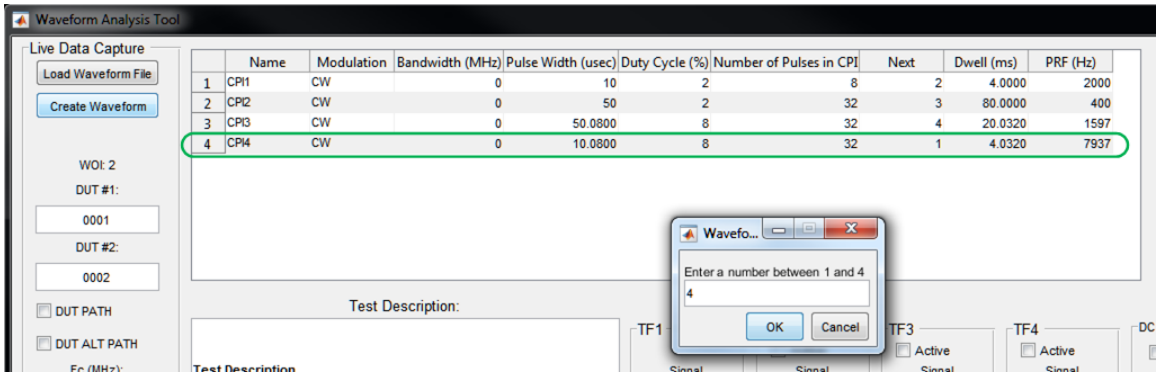

Figure D-2: Waveform properties are loaded into the GUI table.

Figure D-3 shows that waveform number 4 was selected as the WOI. This means that several Waveform_Class objects will be instantiated, one for each waveform in the Waveform Library File. The exception is the WOI; each pulse within this waveform will be assigned to a unique Waveform_Class object. They will be linked so that their order within the CPI is known. At this point all of the waveforms have been synthesized. After synthesis the user can choose to apply any calculated predistortion coefficients into the Waveform_Class objects. By clicking on the **Load AWG** pushbutton, highlighted if Figure D-3, all of the waveforms will be uploaded into the Digital Exciter (AWG).

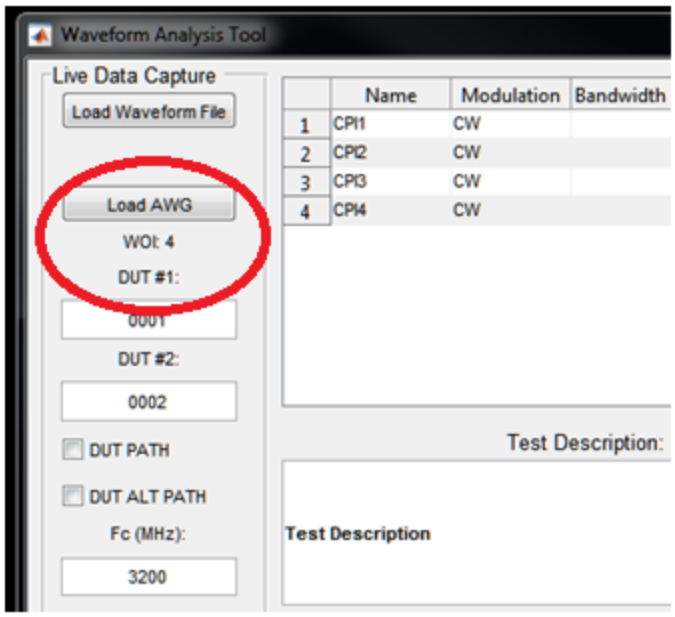


Figure D-3: Waveform 4 was selected as Waveform of Interest for this test event.

Once a waveform is loaded into the Digital Exciter the number of pulses in any of the waveforms can be changed, with the exception of the WOI. Also the order of the waveforms can be altered at any time. WOI must always be in the selected sequence. Figure D-4 shows the GUI waveform table. The waveform number of pulses and order (next column), highlighted in the picture, can be altered by directly type the new values into the GUI. The user must click on **Update Load AWG Scheduler** pushbutton to send the appropriate commands to the instrument.

| | Name | Modulation | Bandwidth (MHz) | Pulse Width (usec) | Duty Cycle (%) | Number of Pulses in CPI | Next | Dwell (ms) | PRF (Hz) |
|---|---|---|---|---|---|---|---|---|---|
| 1 | CPI1 | CW | 0 | 10 | 2 | 8 | 2 | 4.0000 | 2000 |
| 2 | CPI2 | CW | 0 | 50 | 2 | 8 | 4 | 20.0000 | 400 |
| 3 | CPI3 | CW | 0 | 50.0800 | 8 | 32 | 4 | 20.0320 | 1597 |
| 4 | CPI4 | CW | 0 | 10.0800 | 8 | 32 | 2 | 4.0320 | 7937 |

Figure D-4: Waveform number of pulses and order can be change at any time.

The user has the ability to input information relevant to the experiment. Figure D-5 highlights four different fields that can be changed based on particular test conditions. For example multiple amplifiers could be tested. The serial number for each amplifier or some other identifiable information and a test description can be typed directly into the GUI text edit boxes.

Also a circuit diagram can be selected via a drop down menu. Every time data is saved, all of the user inputs and all of the current states of the GUI are saved with the data, including the actual waveform sequence. The same GUI is used offline for data analysis. All of the test descriptions, DUT serial number fields and block diagram are retrieved and displayed by the GUI. At this point data collection is simplified to a simple click on the Data Collection pushbutton. All of the necessary instrument setups and procedures are performed by the GUI and the underlying classes and scripts.

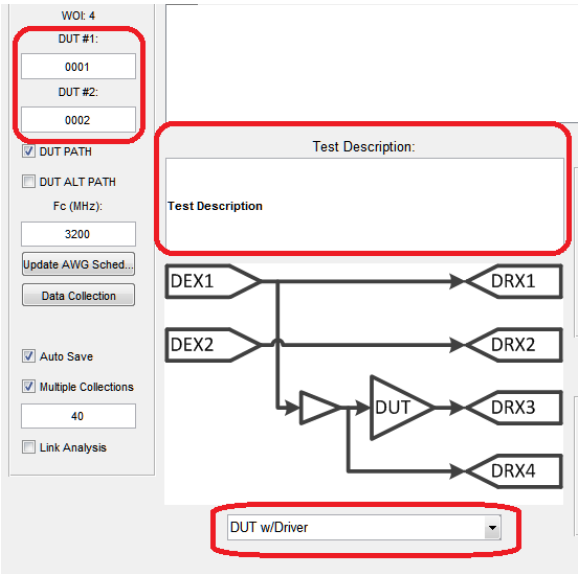


Figure D-5: User data can be added to the GUI.

The control over the Switch Matrix is also done via the GUI. The three modes supported by the GUI are:

Calibration mode: where all of the signals are keep within the RF enclosure. The mode is selected by unchecking the **DUT PATH** check box.

Characterization mode: where signals are sent and received from the DUT. The mode is selected by checking the **DUT PATH** check box.

Predistortion mode; were the Digital Exciter channels are swapped before their signals are routed to the DUTs. The mode is selected by checking the **DUT PATH** and the **DUT ALT PATH** check boxes. This mode is only valid if predistortion coefficient were applied to the WOI, otherwise it is equivalent to the Characterization mode.

There are actually several steps necessary for data collection. The Digital Receiver and Digital Storage Oscilloscope are configured to capture and digitize the RF and DC Waveforms. Sampling rates and memory size are configured prior to data collection. The Digital Receiver and DC Waveform Digitizer are configured (armed) to trigger on the edge of the pulse sent by the Pulse Generator. This pulse marks the beginning of the WOI CPI. The location of all subsequent pulses is known.

The software verifies that a successful trigger occurred. The data collected by the Digital Receiver and the DC Waveform Digitizer are then transferred into the computer memory. The collected data is a continuous sample with duration equal to the WOI CPI. The data is parsed into individual pulses and copied into a Waveform_Class object unique to each pulse in the WOI CPI. Only the time in which the pulse was active in addition to a programmable amount of guard time is stored, the rest of the collected data is discarded. Since the Digital Receiver data is in the form of a digital IF centered at 12.5 MHz, each of the waveforms undergoes digital down-conversion and digital filtering to transfer the data into digital I/Q, before proper signal processing is attempted.

Figure D-6 shows multiple checkboxes design to facilitate the data collection, saving and analysis. Upon verifying that all test parameters are correct, the user can choose to automatically save the captured data into a uniquely named data file. The file name is automatically generated and contains the date and time of when the data was saved. The user can also choose to do multiple back-to-back data collections, automatically save all of the collections, and link each data collection to the analysis. Data processing is performed on the current data set by pressing the Process pushbutton.

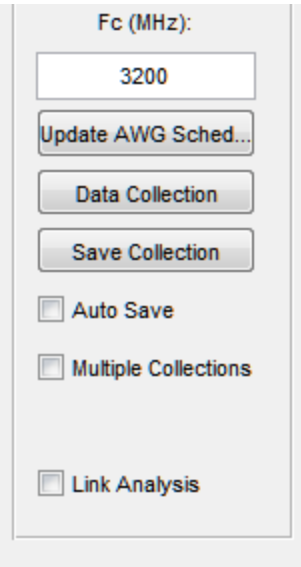


Figure D-6: Data Collection

# Appendix E. **Power Added Efficiency (PAE)**

Another desired data product is the calculation of Power Added Efficiency (PAE). Efficiency is the ratio of the output power minus the input power to the prime power used to drive the power amplifier (dc bias). The efficiency is calculated from measured RF input power, RF output power and DC power drawn. This calculation indicates the power that is dissipated by the device in the form of heat and how effectively the amplifier converts energy into usable RF power.

Figure E-1 shows a simplified block diagram of the power and heat exchanges that occur inside the amplifier. The amplifier has two inputs, one is RF power and the other one is DC Power. It also has two outputs, one is usable RF power and the other one is wasted as heat. A portion of the DC power is converted into wasted heat; the rest is converted into usable RF power.

Figure E-1: Mechanism to illustrate the Power Added Efficiency. Power is introduced into the circuit via the RF input port and the DC bias, power is removed from the circuit via the RF output port and as heat via the mounting flange.

To calculate the PAE the following equation was used:

$$PAE = 100 \times \frac{P_{RF\,out} - P_{RF\,in}}{P_{DC\,in}} \tag{66}$$

where, the $P_{RF\ out}$ is the RF output power, $P_{RF\ in}$ is the RF input and $P_{DC\ in}$ the DC input power.